

POLITECNICO DI TORINO

Master Degree Course in ENVIRONMENTAL ENGINEERING

Master Degree Thesis

Geomorphological, nivo-meteorological and seismic analysis of snow avalanches release areas in Central Italy, January 2017



Supervisors:

Barbara Ing. Frigo
Igor Dott. Geol. Chiambretti

Supervisors' signature

.....

.....

Candidate:

Alessio Gentile

Candidate's signature

.....

A.A. 2018-2019

Summary

ABSTRACT	1
1. SNOW AVALANCHES: GENERAL NOTIONS (HINTS)	2
1.1 SNOW AVALANCHES: DEFINITIONS AND CLASSIFICATIONS	2
1.2 SNOW AVALANCHES CAUSES	7
1.3 WHY STUDY SNOW AVALANCHES AND THEIR PREVENTION?.....	8
2. EARTHQUAKES: GENERAL NOTIONS (HINTS)	10
2.1 RELEASE OF ELASTIC WAVES	10
2.2 SITE EFFECTS AND AMPLIFICATION	11
2.3 ORIGINS, MODELS, AND DEFINITIONS	12
2.4 FAULTS DESCRIPTION.....	13
2.5 CHARACTERISTICS QUANTITIES	14
2.6 QUANTIFICATION SCALES.....	15
2.7 BASIC AND LOCAL SEISMIC HAZARD	16
3. STATE OF THE ART IN MONITORING, CHARACTERIZING AND FORECASTING SNOW AVALANCHES	17
3.1 SNOW AVALANCHES MONITORING, CHARACTERIZING AND FORECASTING METHODS.....	17
3.1.1 <i>Seismic Methods</i>	17
3.1.2 <i>Infrasonic methods</i>	24
3.1.3 <i>Seismic and infrasonic methods compared</i>	28
3.2 INTRODUCTION TO SNOW AVALANCHES TRIGGERED BY EARTHQUAKES	29
3.2.1 <i>General notions, definitions and identification of seismic-induced avalanches</i>	29
3.2.2 <i>Snow avalanches release models with earthquake action</i>	32
4. THE CASE STUDY: CENTRAL APENNINES IN JANUARY 2017	36
4.1 REGIONS OF INTEREST SEISMICITY.....	36
4.2 NIVO-METEOROLOGICAL DATA IN THE PERIOD OF INTEREST	40
4.2.1 <i>Sector 07: "Appennino Umbro-Marchigiano"</i>	41
4.2.2 <i>Sector 04: "Grandi Massicci Appenninici and Appennino Abruzzese"</i>	45
4.2.3 <i>Cumulated snow precipitation</i>	50
4.3 GEOMORPHOLOGICAL ANALYSIS	53
4.3.1 <i>DEM: SRTM (Shuttle Radar Topography Mission)</i>	53
4.3.2 <i>Slope</i>	55
4.3.3 <i>Aspect</i>	57
4.3.4 <i>Curvature</i>	59
4.3.5 <i>Curvature classification (Dikau, 1989)</i>	61
4.3.6 <i>Specific Catchment Area (SCA)</i>	62
4.3.7 <i>Topographic Wetness Index (TWI)</i>	64
4.3.8 <i>Stream power Index (SPI)</i>	65
4.3.9 <i>Convergence Index (CI)</i>	66
4.3.10 <i>Topographic Position Index (TPI)</i>	68
4.4 SNOW AVALANCHES IN CENTRAL APENNINES AND GEOMORPHOLOGICAL, NIVO-METEOROLOGICAL ANALYSIS OF RELEASE AREAS (JANUARY 2017)	70
4.4.1 <i>Total release areas</i>	72
4.4.2 <i>Gran Sasso release areas</i>	74
4.4.3 <i>Gran Sasso, Adriatic side, release areas</i>	75
4.4.4 <i>Gran Sasso, Tyrrhenian side, release areas</i>	77
4.4.5 <i>Laga release areas</i>	78
4.4.6 <i>Laga, Adriatic side, release areas</i>	79
4.4.7 <i>Laga, Tyrrhenian side, release areas</i>	81
4.4.8 <i>Majella release areas</i>	82
4.4.9 <i>Majella, Adriatic side, release areas</i>	83
4.4.10 <i>Majella, Tyrrhenian side, release areas</i>	85
4.4.11 <i>Sibillini release areas</i>	86

4.4.12	<i>Sibillini, Adriatic side, release areas</i>	87
4.4.13	<i>Sibillini, Tyrrhenian side, release areas</i>	89
4.4.14	<i>Sirente Velino release areas</i>	90
4.4.15	<i>Mountain sectors release areas compared</i>	91
4.5	POTENTIAL RELEASE AREAS (PRA) DELINEATION ALGORITHMS.....	98
4.5.1	<i>Maggioni (2004)</i>	99
4.5.2	<i>Bühler et al. (2018)</i>	103
4.6	SEISMIC ANALYSIS OF RELEASE AREAS (JANUARY 2017).....	105
4.6.1	<i>Total release areas</i>	106
4.6.2	<i>Gran Sasso release areas</i>	107
4.6.3	<i>Gran Sasso, Adriatic side, release areas</i>	109
4.6.4	<i>Gran Sasso, Tyrrhenian side, release areas</i>	110
4.6.5	<i>Laga release areas</i>	111
4.6.6	<i>Laga, Adriatic side, release areas</i>	113
4.6.7	<i>Laga, Tyrrhenian side, release areas</i>	114
4.6.8	<i>Sibillini release areas</i>	115
4.6.9	<i>Sibillini, Adriatic side, release areas</i>	116
4.6.10	<i>Sibillini, Tyrrhenian side, release areas</i>	118
4.6.11	<i>Mountain sectors release areas compared</i>	119
4.6.12	<i>Snow avalanches potentially triggered by earthquakes</i>	122
4.7	RIGOPIANO DISASTER (JANUARY 18 TH 2017)	126
4.8	CONCLUSIONS	129
	BIBLIOGRAPHY AND SITOGRAPHY	133
	APPENDIX A	136
	ACKNOWLEDGMENTS - RINGRAZIAMENTI	140

Abstract

This paper concerns the geomorphological, nivo-meteorological and seismic analysis of snow avalanches release areas in Central Italy in January 2017. The whole analysis was performed using GIS supports. The largest magnitude snow avalanches, occurred in the Central Apennines in January 2017, were obtained following a photo-interpretation work carried out on high-resolution satellite images. In particular, the whole perimeter of individual events was mapped. From these, release areas were extracted. Besides, two algorithms for PRA (Potential Release Areas) delineation have been implemented, and their results were compared with real release areas extracted from photo-interpretation work. Starting from DEM SRTM (30 m), the geomorphological analysis of Central Apennines was developed. It led to a statistical characterization of main topographic attributes (elevation, slope, aspect, and curvature) of snow avalanches release areas. Release areas nivo-meteorological analysis was based mainly on data of cumulative snow precipitation, during the period 15th-18th January 2017, deriving from the meteorological model. In particular, the geomorphological and nivo-meteorological analyses were carried out on the totality of release areas and on Sibillini Mountains, Laga Mountains, Gran Sasso Massif, Majella Massif, and Sirente Velino Mountains release areas. For each mountain sector, release areas were also characterized by differentiating between Adriatic and Tyrrhenian side. Seismic characterization was performed taking into account the most relevant earthquakes occurred in the same period and evaluating accelerations that affected snow avalanches release areas. In addition to these earthquakes, release areas have been characterized by PGA reported by the INGV seismic hazard map, considering an exceeding probability of 10% in 50 years. In this case, release areas were analyzed differencing for three selected mountain sectors: Sibillini Mountains, Laga Mountains, and Gran Sasso Massif. Again, for each mountain sector, release areas were characterized by differentiating between Adriatic and Tyrrhenian side. The release model proposed by Pérez-Guillén (2014) cum bibl. was applied for the achievement of a critical acceleration, produced by an earthquake, that could trigger snow avalanches. These calculations were carried out at the scale of the three selected mountain sector, always differentiating between Adriatic and Tyrrhenian side. So, release areas that could be triggered by most relevant earthquakes were identified. Finally, the Rigopiano disaster was analyzed. Also, Rigopiano release area was statistically characterized by the geomorphological, nivo-meteorological and seismic viewpoint. Accelerations suffered by Rigopiano release area were compared with the critical acceleration found for Gran Sasso, Adriatic side sector, to which the snow avalanche belongs. From this comparison, and considering the time gap between the earthquakes and the avalanche, we concluded, with the highest probability, that earthquakes had a marginal role in the detachment of the Rigopiano snow avalanche.

1. Snow avalanches: general notions (hints)

1.1 Snow avalanches: definitions and classifications

Snow avalanche can be defined as a rapid snow mass movement along a slope. This mass movement can also contain other types of materials beyond the snow: rocks, soil, vegetation or ice (Schweizer et al., 2015). Generally, in all snow avalanches, it is possible to recognize three different areas: *release area*, *track zone* and *runout zone*. These areas are defined below and reported in Fig. 1.1. The release area is the place where the phenomenon has its origin. Generally, this is a particularly steep area, also if the critical release angle depends on the snow conditions. The *starting zone* is usually located in snow accumulation zones or near the ridges. The *track zone* is the area between the *release area* and *runout zone*. In this area, snow avalanche reaches maximum speed. It is characterized by high inclination (typically 15° - 30°) and scarce vegetation. Sometimes it is vegetated, but only with shrubs and young age trees and with different species compared to neighboring wooded areas. Track zones are essentially subdivided into two categories described below (see *track shape* paragraph). It is possible to find some track zones formed by the combination of the two categories. The *runout zone* is the place where the avalanche slows down until it stops. In this area the slope angle (typically $< 15^{\circ}$) is close to the static friction angle. It can be a wide terrace, a valley floor or the opposite side of a valley (McClung et al., 2006; Schweizer et al., 2015).



Fig. 1.1 Snow avalanche release area, track zone and runout zone.

Modified after. Source: http://www.lavocedelnordest.eu/wp-content/uploads/2016/12/CauriolFoto_1.jpg

It is crucial, for studying snow avalanches, to define a classification system. Because of the presence of many parameters describing this type of phenomenon, it is difficult to find a single one exhaustive system. For this reason, snow avalanches can be described uniquely using different criteria. They are summarized below.

Release type. There are two release types: point and linear. They are reported in Fig. 1.2. In the first one, failure begins as a small volume ($< 1 \text{ m}^3$; Schweizer et al., 2015) and it produces an avalanche of weak cohesion snow (loose snow avalanche) characterized by the typical inverted cone shape. The involvement of limited volumes generally distinguishes this phenomenon, usually, less than 10^{-4} m^3 (McClung et al., 2006), as a substantially harmless one, though the complete snowpack saturation could cause the involvement of larger volumes increasing snow avalanche dangerousness. The second one type of failure consists of linear fractures which propagate along a weak layer, beneath the slab, and intersect each other, on the snowpack surface, thus isolating a portion of a slab. The weak layer beneath the slab acts as a sliding plane, and the slab avalanche is released. It is characterized by cohesion.

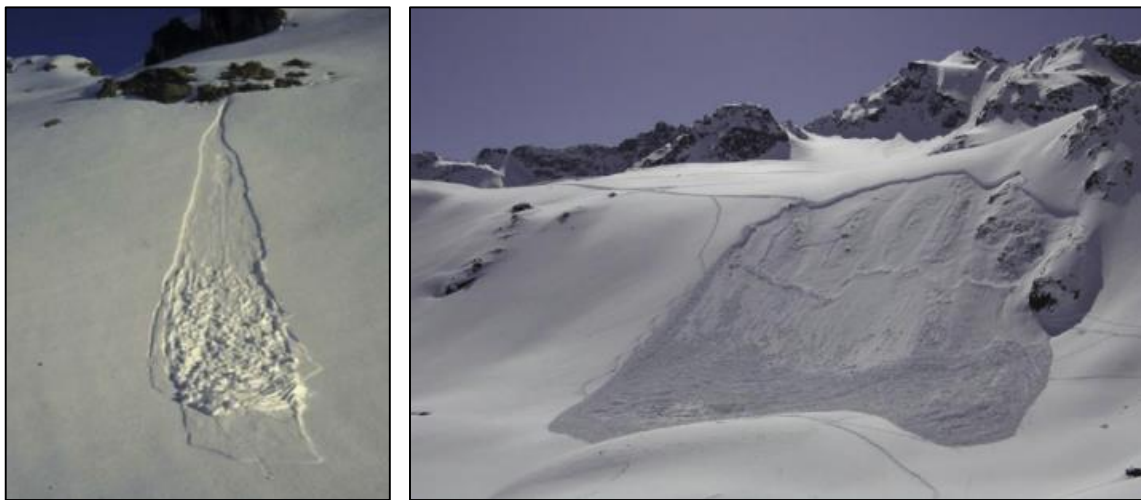


Fig. 1.2 On the left a loose snow avalanche; on the right a slab snow avalanche
 Source: Schweizer, Bartelt, van Herwijnen. *Snow and Ice-Related Hazards, Risks, and Disasters; Chapter 12: Snow Avalanches*, (2015), p.401;

The slab avalanche is the most dangerous and there is, in literature, a specific nomenclature about it. It is reported in Fig. 1.3. Generally, the first fracture affecting the slab originates the sliding plane, called *bed surface*. Subsequently, a fracture perpendicular to the sliding plane, called *crown*, is created. It defines the upper limit of the slab; it lies on the border with the snow that remains in place. In the end, a diagonal shear fracture, called *stauchwall*, is formed in the lower part of the slab, approximately at the same time of *flanks* (left and right sides of the slab) formation (McClung et al., 2006).

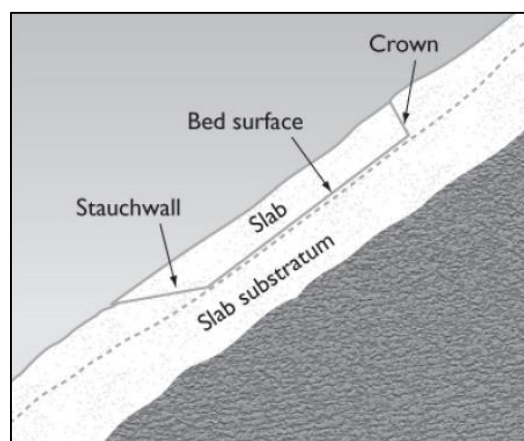


Fig. 1.3 Nomenclature of a typical snow slab in a cross section
 Source: McClung, Schaerer. *The Avalanche Handbook*, 2006

Position of sliding surface. If the failure occurs inside the snowpack, i.e., failure does not affect whole snowpack thickness, a surface layer avalanche is generated. If failure occurs at ground level, a full-depth avalanche is generated and the whole snowpack thickness is involved. These snow avalanches types are reported in Fig. 1.4.



Fig. 1.4 On the left a surface layer avalanche; on the right a full-depth avalanche.

Source left image: <http://www.stradadeiparchi.it/cosa-si-formano-le-valanghe/>

Source right image: Schweizer, Bartelt, van Herwijnen. *Snow and Ice-Related Hazards, Risks, and Disasters; Chapter 12: Snow Avalanches*, (2015), p.408

Snow humidity. Depending on the water content, snow avalanches can be considered wet or dry. In particular, we refer to the ICSI (International Commission on Snow and Ice) classification system reported in Table 1 (Fierz et al., 2009). The first ones are characterized by the presence of water in the snowpack and their movement is typical of a flow. The second ones could also be nubiform or powdery and they consist of three stratified components: dense flowing snow at the bottom, light flowing snow, and powder snow (Schaerer et al., 1980). It is important to underline that flow regimes can be co-present and they could change along the avalanche way. An exemplification of these snow avalanches types is reported in Fig. 1.5.

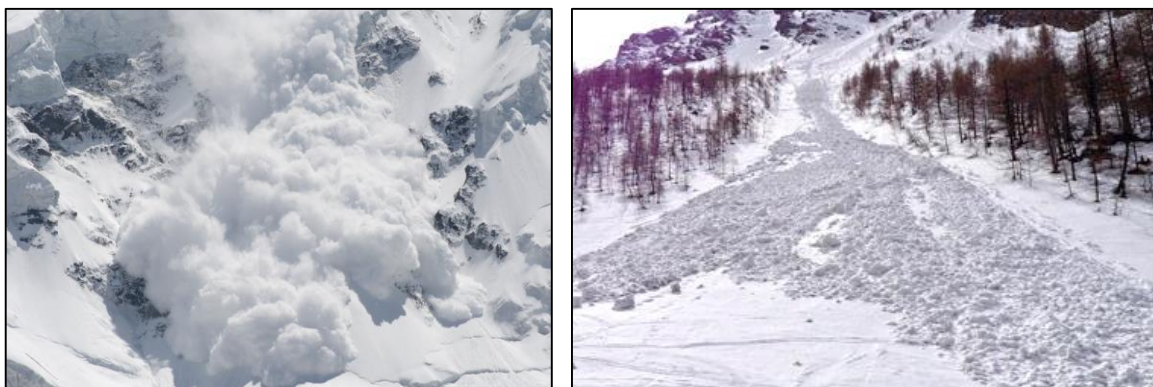


Fig. 1.5 On the left a dry snow avalanche; on the right a wet snow avalanche.

Source left image: <http://cdn-media.ingegneri.info/wp-content/uploads/2017/11/formazione-valanga-1024x576.jpg>

Source right image: http://www.realsnow.it/wpcontent/themes/realsnow/images/snowboard/valanga_bagnata.gif

Table 1 ICSI (International Commission on Snow and Ice) Classification System depending on Water Content.
 Source: Fierz, Armstrong, Durand, Etchevers, Greene, McClung, Nishimura, Satyawali and Sokratov. *The International Classification for Seasonal Snow on the Ground. IHP-VII Technical Documents in Hydrology N°83, IACS Contribution N°1, UNESCO-IHP, Paris, (2009)*

Term	Remarks	Water Content (% by volume)
Dry	Usually T is below 0°C, but dry snow can occur at any temperature up to 0°C. Disaggregated snow grains have little tendency to adhere to each other when pressed together, as in making a snow ball.	0%
Moist	T=0°C. The water is not visible even at 10X magnification. When lightly crushed, the snow has a distinct tendency to stick together.	< 3 %
Wet	T=0°C. The water can be recognized at 10X magnification by its meniscus between adjacent snow grains, but water cannot be pressed out by moderately squeezing the snow in the hands.(Pendular regime)	3-8 %
Very Wet	T=0°C. The water can be pressed out by moderately squeezing the snow in the hands, but there is an appreciable amount of air confined within the pores. (Funicular regime)	8-15 %
Slush	T=0°C. The snow is flooded with water and contains a relatively small amount of air.	> 15 %

Track shape. When the snow avalanche flows inside a channel (for example, formed by the intersection of two mountainsides or by stream riverbed) it is called channeled. If it flows freely on a mountainside, it is called unconfined or slope avalanche and, in this case, the phenomenon is not driven by the topography.



Fig. 1.6 On the left a channeled snow avalanche; on the right a slope snow avalanche.
 Source left image: https://en.wikipedia.org/wiki/Avalanche#/media/File:Avalanche_on_Everest.JPG
 Source right image: http://www.sfu.ca/~yla312/IAT%20235/P04_week%2013/img/avalanche.jpg

The characteristics mentioned above, together with others as roughness and contamination of deposits, were used to define the International Morphological Avalanche Classification (UNESCO, 1981) that considers the three characteristic areas of a snow avalanche: release area, track zone and runout zone. This classification is reported in Table 2. There is also another snow avalanches classification, based on events sizes. The avalanche size classification is reported in Table 3.

Table 2 International Morphological Avalanche Classification (UNESCO, 1981)

Source: Schweizer, Bartelt, van Herwijen. *Snow and Ice-Related Hazards, Risks, and Disasters; Chapter 12: Snow Avalanches*, (2015), p.400

Zone	Criteria	Distinguishing features	Denomination
Release Area	Type of detachment	point detachment (no cohesion)	loose snow avalanche
		linear detachment	slab snow avalanche
	Position of slip plane	within the snowpack	shallow snow avalanche
		at ground level	background snow avalanche
	Liquid water in snow	absent	dry snow avalanche
present		wet snow avalanche	
Track zone	Type of path	slope	slope snow avalanche
		channel	channeled snow avalanche
	Type of movement	snow dust cloud	nubiform snow avalanche
		flowing along ground	flowing snow avalanche
Runout zone	Surface roughness of deposit	Coarse	Coarse deposit
		Fine	Fine deposit
	Liquid water in snow	absent	dry avalanche deposit
		present	wet avalanche deposit
	Contamination of deposit	no visible contamination	Clean avalanche
		visible contamination (debris, soil, branches, trees)	Contaminated avalanche

Table 3 The avalanche size classification. In the "Size" field the new denominations for the avalanches sizes, based on decisions from the 2017 EAWS General Assembly, are reported. The names have been shifted to the previous number, defining category 5 "Extremely large": previously absent item. In this way, it improves the effectiveness of avalanche warnings

Source: Schweizer, Bartelt, van Herwijen. *Snow and Ice-Related Hazards, Risks, and Disasters; Chapter 12: Snow Avalanches*, (2015), p.398

Size	Description	Typical Mass	Typical Path Length	Typical Impact Pressures
1: Small	Relatively harmless to people	< 10 t	10 m	1 kPa
2: Medium	Could bury, injure or kill a person	10 ² t	100 m	10 kPa
3: Large	Could bury a car, destroy a small building or break a few trees	10 ³ t	1000 m	100 kPa
4: Very large	Could destroy a railway car, large truck, several buildings or a forest with an area up to 4 hectares (4000 m ²)	10 ⁴ t	2000 m	500 kPa
5: Extremely large	Largest snow avalanches known; could destroy a village or a forest of 40 hectares	10 ⁵ t	3000 m	1000 kPa

1.2 Snow avalanches causes

It is possible to distinguish two different types of snow avalanches causes: predisposing and triggering.

The first ones are connected with the process that led to the actual conformation of the slope and snowpack: they can be identified in slope inclination, terrain mechanical characteristics, morphology, forests absence, exposure, presence of thick snowpack over a weak layer and meteorological conditions (mainly wind and precipitations).

Slope steepness is surely a predisposing cause of primary importance. As previously mentioned, there is no absolute slope inclination value for which the snow avalanches are released: it depends on snow conditions. The experimental observations, regarding release areas inclination and the relative induced snow avalanches, are reported in Table 4.

Table 4 Experimental observations relating release areas inclination and snow avalanches types
Source: McClung, Schaerer. *The Avalanche Handbook*, (2006)

Release Area Inclination	Related snow avalanches
60°-90°	Avalanches are rare; snow sluffs frequently in small amounts
30°-60°	Dry loose-snow avalanches
45°-55°	Frequent small slab avalanches
35°-45°	Slab avalanches of all sizes
25°-35°	Infrequent (often large) slab avalanches; wet loose-snow avalanches
10°-25°	Infrequent wet snow avalanches and slush flows

A not negligible aspect is given by the forest presence. Trees prevent snow avalanches formation for different reasons: (1) their ability to intercept the snowfall;(2) the reduction of near-surface wind speeds; (3) the modification of the radiation and temperature regimes; and (4) the direct support of the snowpack by stems, remnant stumps, and dead wood (Schweizer et al., 2015). Snowpack is composed by snow layers accumulated over time. Among these layers, it is possible to find a weakness plan with poor mechanical properties compared to adjacent layers. In such layer, which can present different thicknesses, stress and strains are concentrated, and so a failure can occur. Precipitations are a very relevant factor for snow avalanches release because they produce a loading process. As well as precipitations also snow redeposited by wind can produce a process of loading. So, it can create unstable snow deposits. Schaerer (1977) proposed a qualitative Wind Index (WI), reported in Table 5, which allows to identify areas in which snow is accumulated and which can develop release areas. As the index grows, more snow can be accumulated.

Table 5 Qualitative Wind Index indicating snow deposits sizes in release areas (Schaerer, 1977)
Source: McClung, Schaerer. *The Avalanche Handbook*, (2006)

W.I.	Description
1	Start zone completely sheltered by dense surrounding forest
2	Start zone sheltered by open forest or facing prevailing wind direction
3	Start zone on open slope with rolls or other irregularities where drifts can form
4	Start zone on the lee side of a sharp ridge
5	Start zone on the lee side of a wide, rounded ridge or open area where large amounts of snow can be moved by wind

The second ones are represented by the last action which led to snow mass movement: it is essential to underline that, in the occurrence of a snow avalanche, there are many predisposing causes but only one triggering cause. Triggering causes can be subdivided into two types: natural and artificial. Artificial triggering causes are, for example, explosions. Natural triggering causes can be recognized in melting snow, bringing changes in the effective shear strength, and in other causes which generally produce a process of loading: for example, the crossing of skiers, frequent precipitations increasing snow weight, volcanic activities and earthquakes.

In this study, the characteristics of real snow avalanches release areas were analyzed. Among these characteristics, we studied predisposing features such as slope and morphology. Furthermore, we concentrated on the release of snow avalanches considering as triggering cause snowfall accumulation and earthquakes. Before analyzing characteristics of real snow avalanches release areas, it's crucial to digress about the importance of avalanche prevention. So, the state of techniques in avalanches monitoring and forecasting is presented.

1.3 Why study snow avalanches and their prevention?

The deep reason for investigating snow avalanches is that, every year, they produce many accidents and fatalities. For example, from data reported by AINEVA (Associazione Interregionale Neve e Valanghe) about accidents in Italy, considering seasons from 1985-86 to 2017-2018, it is possible to observe the situation reported in Fig. 1.7. In a period of only 33 years, the mean of dead and wounded people is 42 per season. The total number of people caught in snow avalanches, in the considered period, amounts to 3137 of which 1386 (44%) are dead or injured. This number is enormous, and sometimes it is possible to run into particularly disastrous seasons.

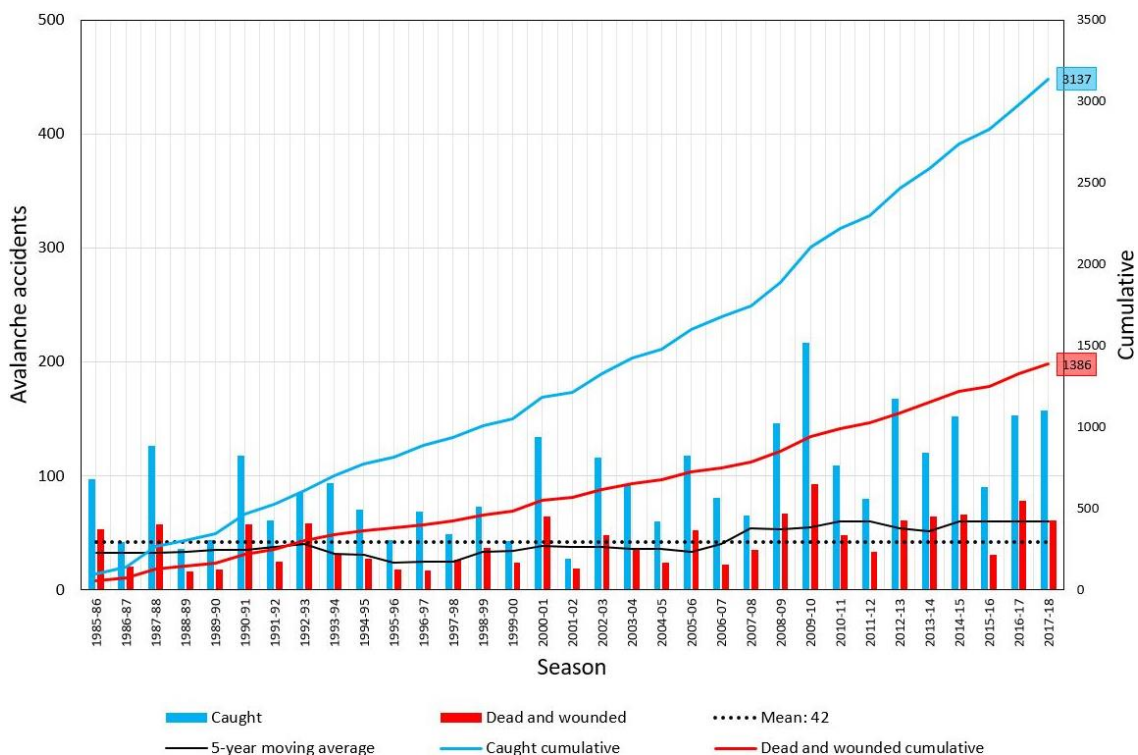


Fig. 1.7 Incidents data caused by snow avalanches in Italy reported by AINEVA considering seasons from 1985-86 to 2017-2018

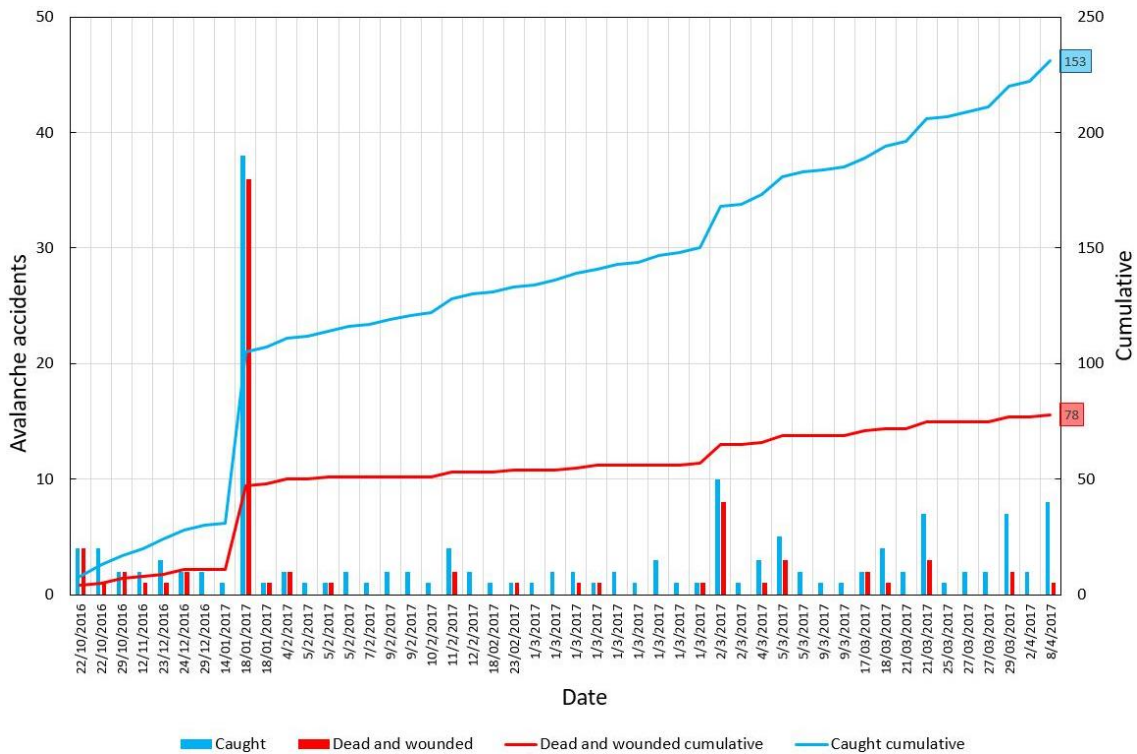


Fig. 1.8 Incidents data caused by snow avalanches in Italy reported by AINEVA considering the 2016-2017 season

Starting from data reported by AINEVA about accidents, it is possible to analyze more in detail, in the period considered, the 2016-2017 season in which a high number of deaths and injuries was recorded. Graph reported in Fig. 1.8 shows that 153 people were caught by snow avalanches: among these people, 78 (51%) were killed or injured. It is also possible to point out that there is a peak of 38 caught people, 29 of whom died and 7 were injured, at the date of January 18th 2017 when a snow avalanche swept the Rigopiano Hotel (Farindola, Abruzzo, Italy). Indeed, such events cause sensation and attract attention, but victims due to snow avalanches are still many every year, despite less memorable events which are, commonly, related to recreational activities.

In addition to the loss of human lives, it is necessary to consider the economic damages caused by a flux reduction of tourists and the possible impracticability of the infrastructures. There are often also considerable material and environmental damages to buildings or infrastructures and forests.

To mitigate the effects of these natural phenomena, in Italy, #ItaliaSicura presented on May 10th 2017, at Chigi Palace, “Il piano nazionale di opere e interventi e il piano finanziario per la riduzione del rischio idrogeologico”. In this plan, through the collaboration of various institutions acting on the territory, a financial requirement map, was created. It was based on data about projects presented on the national territory (update February 2017) that are available from ReNDiS (Repertorio Nazionale degli interventi per la Difesa del Suolo) platform. This map was the starting point for the development of a large action plan to be developed in the mitigation of hydrogeological instability with a natural hazards prevention purpose. The results of this work are reported in Table 6.

Table 6 Number of projects, total cost and resources requested to the State for the mitigation of hydrogeological instability; update February 2017. In evidence data about snow avalanches
 Source: #ItaliaSicura: <http://italiasicura.governo.it/site/home/dissesto/piano.html>

Hydrogeological instability	n° of projects	Total Cost (*10 ⁶ €)	Resources requested to the State (*10 ⁶ €)
Floods	3284	15046	13809.4
Landslides	4828	8144.1	7709.9
Coastal erosion	227	2126.8	1251.9
Mixed	555	2922.5	2778
Snow avalanches	32	125.1	121.6
Other	471	745.5	737.1
TOTAL	9397	29110	26407.9

We can observe that 9397 projects, with a request for funds of 26 billion euros were required, of which 32 projects (0.34%) with a request for funds of 121.6 million euros (0,46%) were required for snow avalanches.

These data must be compared with costs for compensating and repairing damages. #ItaliaSicura states that, since 1945, Italy pays an average of 3.5 billion euros annually for the repair of damages due to hydrogeological instability. From this data it is easy to understand that, from 1945 to 2017, around 250 billion euros were spent on damages due to the various types of instabilities. Assuming that 1 euro spent in prevention saves up to 100 euros in damages repair (source: #ItaliaSicura), it is possible to understand that, by investing in prevention the 3.5 billion that Italy pays on average each year for the disasters, we would avoid 350 billion euros of repair costs: more than spent on damages in about 70 years.

In this perspective of prevention, among interventions that must be carried out and in addition to physical protection works, it is essential to develop methods for monitoring, forecasting and characterizing snow avalanches.

2. Earthquakes: general notions (hints)

2.1 Release of elastic waves

An earthquake (from the Latin *terrae motu* or movement of the earth) is a rapid movement of the earth's surface due to the abrupt release of the energy accumulated inside the Earth in an ideal point called *hypocenter* or *fire*. The point on the ground surface, placed on the vertical of the hypocenter, is called *epicenter* (INGV). Energy travels in the ground in the form of mechanical waves that propagate from the hypocenter in all directions up to the surface. These waves are mainly of two categories: compression or shear. Compression waves (P waves) cause particles to move in the same direction as wave propagation, causing volumetric deformations. Shear waves (S waves) gives origin to particles oscillation perpendicularly to the direction of wave propagation, causing shape deformations. Moreover, these waves have a different propagation speed:

$$v_p = \sqrt{\frac{M}{\rho}} = \sqrt{\frac{\lambda + 2\mu}{\rho}} \quad v_s = \sqrt{\frac{G}{\rho}} = \sqrt{\frac{\mu}{\rho}} \quad (1)$$

Where, v_p and v_s are respectively the propagation velocities of P waves and S waves, M is the edometric module, G is the shear module, ρ is the material density and λ, μ are the Lamé constants. Therefore, if compression and shear waves are generated at the same time and in the same material, the former propagate faster than the latter.

In addition to P and S waves, there are surface waves. They are subdivided into Rayleigh and Love waves. The particles motion, caused by Rayleigh waves, is elliptical within a vertical plane: it is a combination of P and S waves, with variations of both volume and shape. Love waves, instead, cause transverse movements, compared to the wave direction of propagation, in a horizontal plane. The surface waves are less affected by geometric attenuation, so, they disperse their energy less. A schematization of the seismic waves described above is reported in Fig. 2.1.

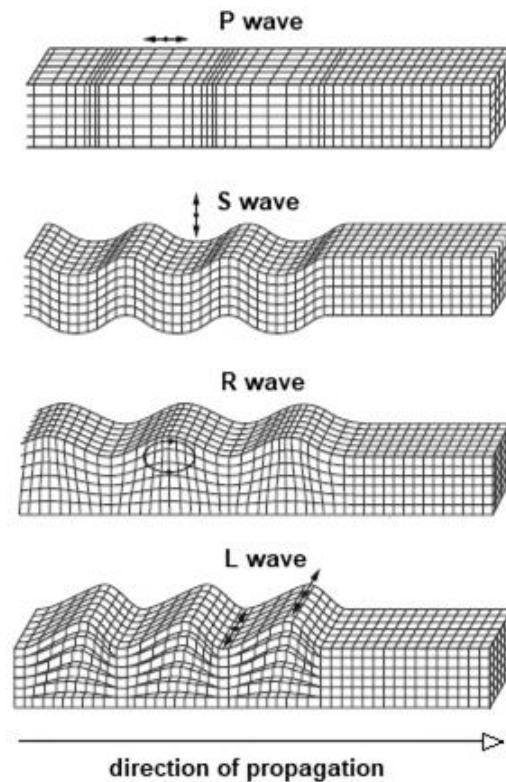


Fig. 2.1 Schematization of seismic waves with indication of particles movements around their equilibrium position

2.2 Site effects and amplification

The wave speed can considerably change depending on the material that is crossed. In fact, in the passage from rock to soil the phenomenon of seismic amplification can occur (stratigraphic amplification). During the passage of the wave through interface areas of different materials, wave transmission and reflection phenomena can occur too. They are governed by a single parameter that relates the amplitude of reflected (A_r) and transmitted (A_t) wave with that of the incident wave (A_i): this parameter is the impedance contrast (α_z):

$$\alpha_z = \frac{\rho_2 v_2}{\rho_1 v_1} \quad A_r = \frac{1 + \alpha_z}{1 - \alpha_z} A_i \quad A_t = \frac{2A_i}{1 + \alpha_z} \quad (2)$$

Where the subscript 1 indicates the medium from which the wave originates, while the subscript 2 indicates the medium in which the wave propagates. Generally, from the depth to the surface, you will encounter more deformable layers that will always tend to amplify the seismic wave. To evaluate this type of amplification, it is possible to use mathematical models or simplified formulas provided by seismic regulations. Among these formulas, there is the evaluation of the average speed for S waves until a depth of 30 m ($v_{s,30}$). On this, the definition of different subsoil categories, to evaluate the amplification, is based. $v_{s,30}$ is defined as follows:

$$v_{s,30} = \sum_{i=1}^m \frac{30}{\left(\frac{h_i}{v_{s,i}}\right)} \left[\frac{m}{s}\right] \quad (3)$$

where h_i is the i -th layer thickness, $v_{s,i}$ is the S wave velocity in the i -th layer and m the total number of layers. By convention, the rigid reference, in which the amplification is absent, was defined as a material having a $v_{s,30} \geq 800$ m/s. Compared to this reference, more the $v_{s,30}$ decreases and more the amplification increases.

It is also possible to come across another amplification type: topographic amplification. The latter has a purely geometric nature and it is, for example, found near the ridges. Here, due to the reflection of the seismic rays, the energy converges towards the ridges. Approximating the incident wave to a plane wave, it is possible to estimate a topographic amplification factor (A_T) equal to:

$$A_T = \frac{2\pi}{\varphi} \quad (4)$$

Where φ is the angle subtended by the two sides that converge in the ridge. Obviously, it is necessary to underline that the two types of amplification work together.

2.3 Origins, models, and definitions

Earthquakes occur because, according to the theory of plate tectonics, there are portions of the Earth's crust in contact with each other that reach a failure condition, generating faults. Along faults, there is a relative sliding of these portions that generates mechanical waves. Faults are classified, according to their orientation and movement type (traction, compression, shear), respectively in *normal*, *reverse* and *transcurrent* faults. The cracks in the Earth's crust release energy according to Reid's elastic rebound theory. According to this theory, the surfaces that move along a fault have roughnesses that show a frictional resistance. Once this resistance is overcome, due to the accumulation of elastic energy, the roughness failure occurs. Therefore, a reciprocal movement of the two flaps in contact, until new roughnesses don't show a frictional resistance to stop the movement, goes on. This theory explains the cyclicity of earthquakes. In addition, it clarifies that a seismic event is characterized by the main shock, which may be preceded by precursor shocks (foreshocks) or followed by aftershocks. About that, it is essential to introduce the concept of seismic sequence. The INGV defines the latter as " ...a series of earthquakes located in the same area and in a certain time interval, characterized by the main shock followed by smaller replicas, which decrease over time in number and magnitude following a typical trend defined as Omori's law (1894)". A particular seismic sequence is constituted by the seismic

swarm defined by Utsu as "a concentration (cluster) of earthquakes in which there is not a single earthquake with a predominant magnitude (predominantly large)".

2.4 Faults description

When stresses are created within the Earth's crust and they exceed the elastic limit, a fracture is generated. When movements are found along the fracture, we speak of a fault. The plane along which the sliding occurs is called the *fault plane* and the two contact blocks are called *lips*. The block that runs above the other is called the *hanging wall*; the other is called *foot wall*. As mentioned above, faults are classified according to their orientation and movement type. Regarding the movement, they are classified into *normal*, *inverse* and *transcurrent*. The normal faults originate because of traction movements, and there is a lowering of the hanging wall compared to the foot wall. The reverse faults originate as a result of compressive movements which cause the hanging wall to slide upwards concerning the foot wall. The transcurrent faults are characterized by a relative movement of the two blocks generated by shear stress. An example of the three types of fault is shown in Fig. 2.2.

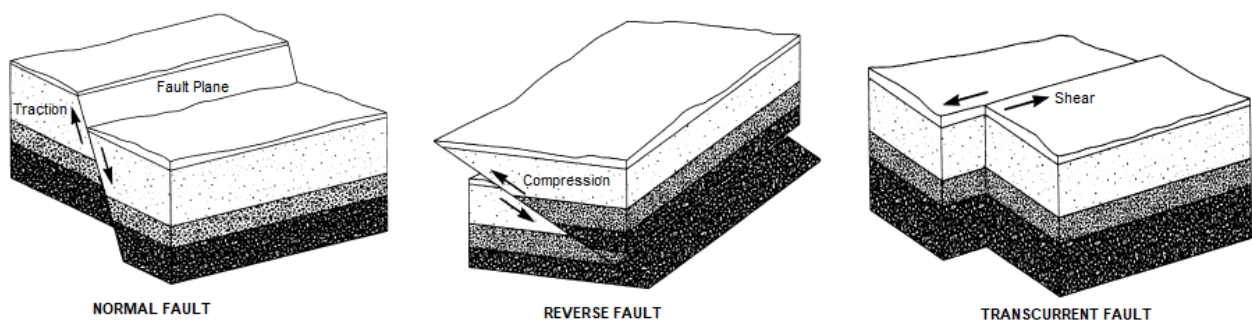


Fig. 2.2 Fault classification based on type of movement

To describe faults on the territory, INGV compiled a database including potential earthquake sources called DISS (Database of Individual Seismogenic Sources). "The Individual Seismogenic Sources are defined by geological and geophysical data and are characterized by a full set of geometric (strike, dip, length, width and depth), kinematic (rake), and seismological parameters (single event displacement, magnitude, slip rate, recurrence interval)" (INGV). The geometrical parameters, described below, are those that make it possible to classify fault for its orientation. A graphic representation of these parameters is shown in Fig. 2.3.

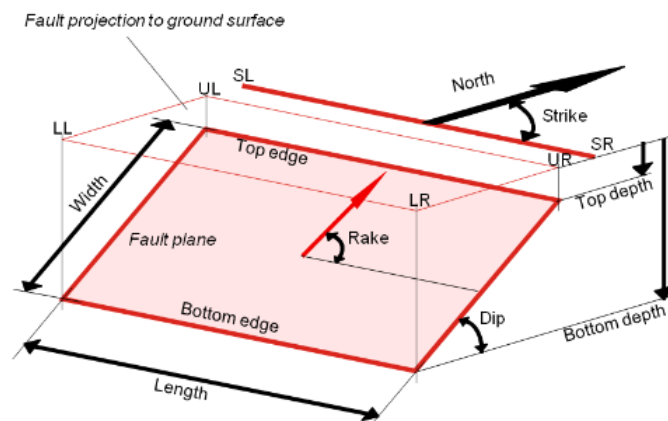


Fig. 2.3 Geometric and kinematic characteristics of an Individual Seismogenic Source
Source: <http://diss.rm.ingv.it/diss/index.php/help/15-individual-seismogenic-sources>

Fault *dip* is the angle between the fault and the horizontal ground surface. Fault *strike* is the direction, relative to North, of the line created by the intersection of the fault plane and the horizontal ground surface. *Rake* is the direction in which the hanging wall moves during rupture. It is measured counterclockwise, on the fault plane, concerning the strike line. In this study, we will refer to CSS (Composite Seismogenic Sources). These are fault systems that embrace an unspecified number of individual sources. They were designed to achieve completeness in the identification of potential earthquake sources, although this implies less accuracy in their description (INGV). DISS reports the composite seismogenic sources on the maps as a projection of the fault system on the Earth's surface, according to the scheme shown in Fig. 2.4.

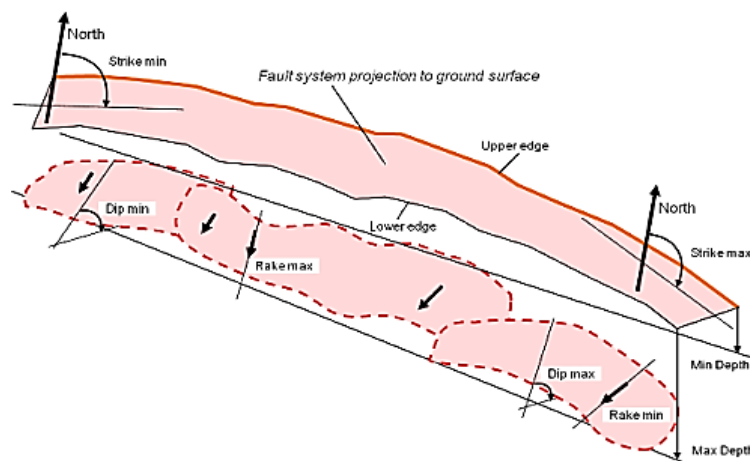


Fig. 2.4 Geometric and kinematic characteristics of a Composite Seismogenic Source.
Source: <http://diss.rm.ingv.it/diss/index.php/help/16-composite-seismogenic-source>

By consulting the ITHACA catalog (ITaly HAZard from Capable faults), it is possible to identify the capable faults. These are faults that can potentially create deformation on the surface. Despite capable faults can also be seismogenic structures, ITHACA catalog cannot be used for a characterization of the seismogenic source in terms of shaking. In fact, superficial faults are not always a continuation of the deep ones. Superficial faults could be provoked by secondary collateral breaks that make the reasoning, about the actual fault ruptures, more complex.

2.5 Characteristics quantities

The quantities that are detected by an earthquake, through seismographs, are mainly acceleration, speed and displacement. They must be recorded in 3 different directions (East-West, North-South, Up-Down) to exhaustively describe the motion. Commonly, accelerometers are used because speeds and displacements can be achieved by integrating the accelerograms. It is necessary to introduce shake parameters because quantities mentioned above vary over time and, therefore, are difficult to use. Not always the maximum value of the time series evaluated can be considered representative, especially in the case of accelerations. Sometimes, in the case of speeds and displacements the difference can be significant, and this makes it possible to capture additional aspects. It is interesting to add a parameter that quantifies duration such as bracketed duration or uniform duration. However, these depend on the value of the chosen threshold. So, it is possible to use the intensity function of the motion:

$$I(t) = \frac{\pi}{2g} \int_0^t a^2(\tau) d\tau \quad (5)$$

This function allows calculating the cumulative acceleration values that will tend to a maximum value, called Arias intensity. This value is like a velocity, and it is associated with the local energy given by the shock at the point where the measuring instrument is located. Normalizing the function, $I(t)$, with respect to the Arias intensity, it is possible to obtain the value of the significant duration. It is equal to the duration in which the maximum energy release is obtained (from 5 to 95%). Since the failure occurs in a point and then it propagates, larger the fault is, more time will pass so that the whole area is affected by the failure.

Another critical shaking parameter is the elastic response spectrum. It describes the effect of the shaking produced by an earthquake at the base of a structure. The elastic response spectrum is defined as the place of the points of the maximum accelerations of a simple oscillator for different periods. A critical parameter of the response spectrum is the PGA (Pick Ground Acceleration). It is read in the response spectrum as the acceleration corresponding to the null period.

Subsequently, it will be explained that the seismic macro-zonation was carried out by mapping the values of PGA considering the exceeding probabilities (P_{VR}) related to the operation limit states and the last limit states for constructions. These PGA values are obtained following the application of laws called GMPEs (Ground Motion Prediction Equations). The GMPEs are empirical laws that, according to the expected magnitude and the site-source distance, allow understanding the effect at the site in terms of a specific motion parameter. These laws are obtained after a seismic data collection, on a regional scale, by seismologists with a subsequent interpolation in graphs showing a specific motion parameter as a function of the epicentral distance. The magnitude and the distance are undoubtedly the two most relevant parameters even if, sometimes, in these laws, informations regarding the type of source (normal, inverse or transcurrent), site effects (stratigraphic amplification and topographic amplification) and the deformability of the ground (dependent on v_s , 30) were also included. The functional form of GMPE derives, therefore, from the interpolation of data and, increasing information on earthquakes recorded over time, these laws are subject to constant changes. Among the most well-known GMPE we have the Ambraseys' law and Sabetta&Pugliese's law.

2.6 Quantification scales

There are several scales for the earthquakes' quantification. Surely the oldest is the Mercalli-Cancani-Sieberg (MCS) scale, reported in Table 7. It defines the macroseismic intensity that grows as the damage increases. This type of scale is not objective. In fact, equal earthquakes in areas with different types of buildings will cause different damages. Even if this scale is not objective, it is nevertheless of fundamental importance to know the earthquakes that occurred in pre-instrumental times. It is, however, possible to find a presumed correlation between the value of perceived intensity and the energy emitted by the earthquake, also defined as magnitude.

Table 7 Mercalli-Cancani-Sieberg intensity scale

Degree	Shock	Description
I	imperceptible	Only sensed by seismic instruments.
II	very light	Only warned by some people in appropriate conditions.
III	light	Warnings from few people. Objects hanging with vibrations similar to those of a car's passage oscillate.
IV	moderate	Warning by many people; trembling of fixtures and crystals, and slight oscillations of hanging objects.
V	rather strong	Also felt by sleeping people; falling objects.
VI	strong	Some slight injury in the shattered buildings and windows.
VII	very strong	Fall of smokestacks, injuries in buildings.
VIII	ruinous	Partial ruin of some building; some isolated victims.
IX	destructive	Total ruin of some buildings and serious injuries in many others; sparse human victims but not numerous.
X	completely destructive	Ruin of many buildings; many human victims; crevasses in the ground.
XI	catastrophic	Destruction of urban agglomerations; many victims; crevasses and landslides in the soil; tsunami.
XII	apocalyptic	Destruction of every artifact; few survivors; soil upheaval; destructive tsunami.

The scale most used today is the Richter or magnitude scale. It is possible to define two types of magnitude: the local magnitude (M_L) and the moment magnitude (M_W) as follows:

$$M_L = \log_{10}(A_{max}) \quad M_W = \frac{\log_{10}(M_0)}{1.5} - 10.7 \quad M_0 = \mu AD \left[\frac{dyne}{cm} \right] \quad (6)$$

Where A_{max} is the maximum amplitude recorded by Wood-Anderson seismometer (located 100 km from the epicenter), μ is the shear module, A is the fault area and D the amount of displacement. M_0 is the seismic moment. It quantifies the released energy. This scale is certainly more objective since the magnitude, representing the energy, is a characteristic of the earthquake and not of the recording. So, there is a one-to-one correspondence: an earthquake corresponds to one and only one magnitude, and vice versa. Keep in mind that the magnitude depends on the seismic moment, which in turn depends on the fault area. Since the significant duration increases with the increase of fault area, it is possible to state that the increase of earthquake magnitude also increases its significant duration.

2.7 Basic and local seismic hazard

The basic hazard is based on a study carried out since 1996 by the INGV. In this study all the seismic sources (i.e., the faults) were considered to realize, by means of the probabilistic method, a mapping with a regular grid of 0.05 ° step. This map shows, for each node, the main shaking parameters on the whole Italian territory in the hypothesis of rigid and plan soil. Therefore, the basic hazard allows identifying and classifying different areas of the national territory, according to the PGA (Pick Ground Acceleration) found. The mapping of the basic hazard is also defined as seismic macro-zonation.

It is emphasized that the seismic macro-zonation was carried out by mapping the PGA or the elastic response spectrum values considering the exceeding probabilities (P_{VR}) relative to operation and last limit states for the constructions. They refer to the performances of constructions when subjected to seismic actions. The exceeding probabilities for the limit states are shown in Table 3.2.1, extracted from NTC (Norme Tecniche per le costruzioni) 2018 and reported below.

Tab 3.2.1 – Probabilità di superamento P_{VR} in funzione dello stato limite considerato

Source: Ministero delle Infrastrutture e dei Trasporti. Aggiornamento delle "Norme tecniche per le costruzioni". Gazzetta Ufficiale della Repubblica Italiana, n. 42 (febbraio 2018) p.45

Stati Limite	P_{VR} : Probabilità di superamento nel periodo di riferimento V_R	
Stati limite di esercizio	SLO	81%
	SLD	63%
Stati limite ultimi	SLV	10%
	SLC	5%

For each limit state it is possible to derive the return period T_R of the earthquake, i.e. the average time between the occurrence of two successive events of entity equal to or higher than an assigned value. The following relationship is used:

$$T_R = -\frac{V_R}{\ln(1 - P_{VR})} = -\frac{C_U \cdot V_N}{\ln(1 - P_{VR})} \quad (7)$$

Where C_U is the coefficient of use. It quantifies the degree of crowding and frequency of human presence. V_N is the nominal life. It represents the number of years in which the structure has to fulfill its function. V_R is the reference life and it corresponds to the product of the two quantities previously described.

The local hazard, or seismic micro-zonation, allows evaluating, starting from macro-zonation, the site effects, i.e., all site conditions that could not be taken into account by the national study carried out by INGV. The local hazard is based on the identification of stable, susceptible to local amplification and unstable areas (landslides, surface breakage caused by faults, dynamic liquefactions).

3. State of the art in monitoring, characterizing and forecasting snow avalanches

3.1 Snow avalanches monitoring, characterizing and forecasting methods

Considering the loss of human lives and economic damages, of which an approximate budget has been made in paragraph 1.3, it is important to study new snow avalanches monitoring, forecasting, and characterizing techniques and keep the already known ones continuously updated. Among the most popular techniques, there are seismic, remote sensing, infrasonic, radar and photographic methods. In this introduction we will mainly focus on seismic and infrasonic methods.

3.1.1 Seismic Methods

Since the end of the 70s, it was known that seismic signals were suitable for detecting snow avalanches. The use of seismic methods is based on vibrations, caused by snow avalanches, that propagate until they reach sensors (geophones) which record them. They can be used for multiple purposes, summarized below, and in particular for characterizing and monitoring snow avalanches.

Snow avalanche signal and environmental noise

To use seismic methods for avalanches study, it is essential to try not to confuse signals produced by the phenomenon with the environmental noise. For this purpose, it is necessary to study signals in time and frequency domain (the last ones obtained using the Fourier transform). van Herwijen et al. (2011) observed that the most energetic signals generated by snow avalanches were generally below 50 Hz, typically 1-30 Hz, with a triangular spectrogram shape (Surinach et al., 2005). On the other hand, most signals energy generated by environmental noise was above 50 Hz. It is important to stress that earthquakes are an exception because the energy is concentrated at low frequencies: just like snow avalanches. Earthquakes can be detected, even automatically, thanks to the comparison with signals in the database (Lacroix et al., 2012). In addition, they can be recognized because the seismogram shows quite clearly the arrival of P and S waves. This is not the case of snow avalanches whose seismograms have the typical spindle shape. Signals derived from snow avalanches can be often confused with those of landslides because they are very similar. Nevertheless, snow avalanches seismograms are smoother and their spectrograms are more regular (Lacroix et al., 2012). Fig. 3.1 shows seismograms and spectrograms, obtained from Lacroix et al. (2012), which highlight differences in signals shape and in the energy content concentration at different frequencies, depending on the considered phenomenon.

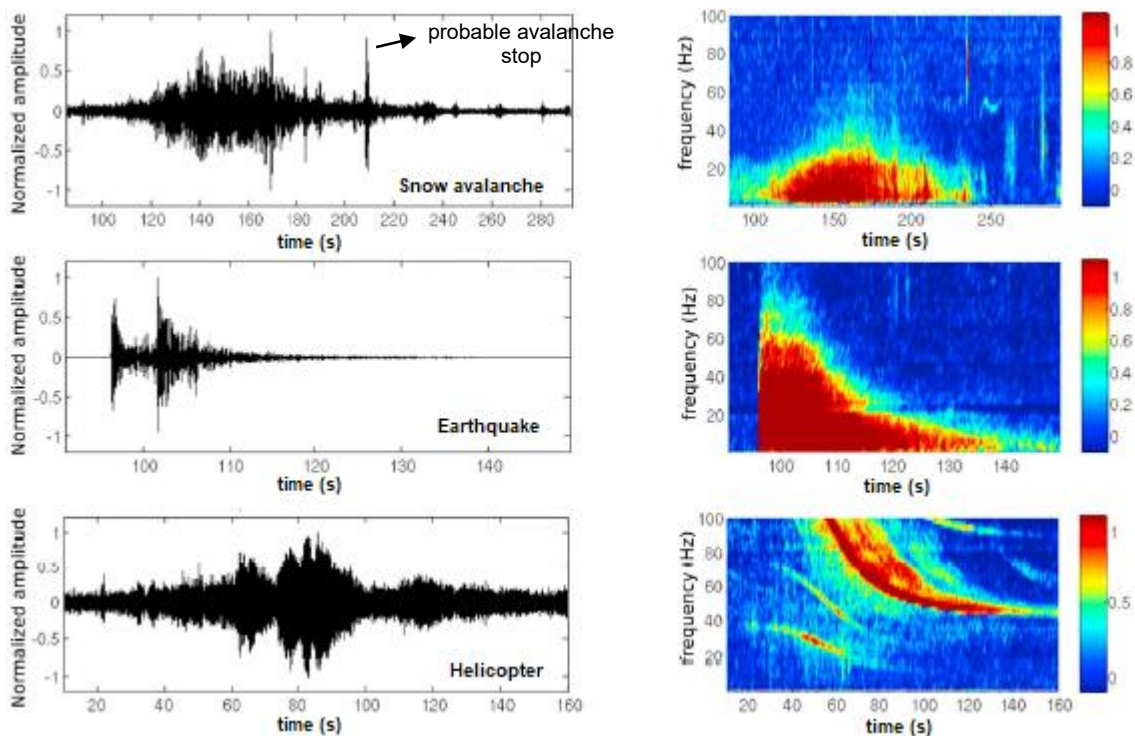


Fig. 3.1 Signals (on the left) and Spectrograms (on the right) generated by snow avalanche, earthquake and a general environmental noise.

Modified after. Source: Lacroix, Grasso, Roule, Giraud, Goetz, Morin, Helmstetter. Monitoring of snow avalanches using a seismic array: Location, speed estimation, and relationships to meteorological variables. Journal of geophysical research 117 (2012) p.3

So, after defining, in general terms, how to distinguish signals produced by snow avalanches from those produced by other phenomena, it is possible to use them to characterize snow avalanches.

Snow avalanche velocity

The immediate way to use seismic signals is the estimation of the snow avalanches frontal velocity. Given the signal obtained from a sensor, it is possible to understand the arrival of the snow avalanche front at the geophone. The instant in which the front reaches the sensor is when the signal shows a decidedly greater amplitude compared to the background noise. It is not easy to identify this moment. Therefore, the standard seismological picking technique can be used. When this technique is difficult to use, because of signal complexity, the cross-correlation procedure can be applied: in this way, the difference between arrival times of the front at two different geophones is obtained (Vilajosana et al., 2007). Consequently, if the signals obtained from two sensors are available, it is possible to obtain easily the advancing speed of the front. For example, in Fig. 3.2, are reported two possible seismic signals (vertical component), obtained from two different geophones and caused by the same snow avalanche.

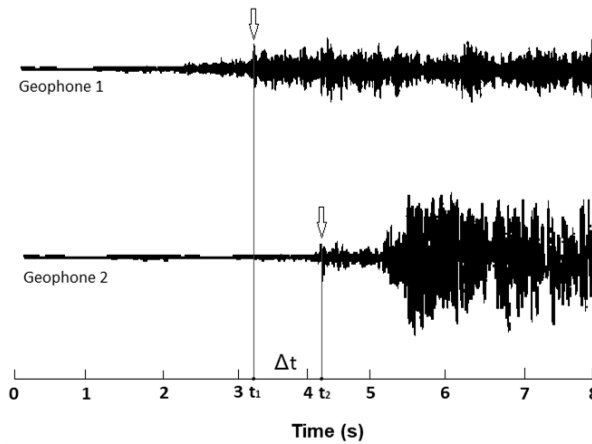


Fig. 3.2 Signals obtained from two geophones and generated by the same snow avalanche. Arrows indicate first time arrival of the front at the sensors (t_1 and t_2). Δt is the difference between t_2 and t_1 .

It is possible to detect the arrival times of the front, t_1 and t_2 (for example obtained with standard seismological technique), respectively to the geophone 1 and 2. Defined d the distance between the two geophones, which are positioned along the snow avalanche trajectory, and defined Δt the difference between the two times indicated above (or obtained directly with the cross-correlation method), it is possible to estimate the front velocity according to the following relation:

$$v_f = \frac{d}{\Delta t} \quad \left[\frac{m}{s} \right] \quad (8)$$

The arrival times of the front, in the case of dry snow avalanches, generally do not reflect the arrival of the powder front. This is caused by an insufficient sensitivity. So, only the arrival of the other two zones front is detected. The passage of various avalanche portions can be also detected in frequency domain. The passage of the front is characterized by a low energy dissipation at frequencies between 1-40 Hz. The passage of turbulent region (only present in dry snow avalanches) is characterized by a high dissipation of energy at low frequencies (<10 Hz). Finally, the passage of the tail, usually denser, presents a spectrum with high frequencies (>10 Hz) with a higher energy dissipation for wet snow avalanches than dry snow avalanches (Pérez-Guillen, Ph.D. Thesis, 2016).

There are also other more sophisticated methods for estimating snow avalanche speed. For example, using beam-forming methods, it is possible to obtain avalanches azimuth, and so, through azimuth time series processing, avalanche velocity can be estimated by linear regression (Lacroix et al., 2012).

Instant of snow avalanche detachment and stop

Previous studies tried to identify in seismic signals what is the exact moment of snow avalanches release, but it is often difficult to identify the waves that really correspond to such instant. Probably, so that sensor perceives the signal, it is necessary to accumulate a certain quantity of snow that is higher than the amount present at the time of detachment (Surinach et al., 2000). This is even more difficult if the avalanche is triggered by an earthquake because, at the release time, the energy due to the earthquake is also present (Pérez-Guillen, Ph.D. Thesis, 2016). It is possible to have information regarding the interruption of the snow avalanche flow from the presence of peaks in the tail of the seismogram, as shown in Fig. 3.1. Probably, these are related to the sudden and violent stop of the avalanche when it reaches the deposition area (Pérez-Guillén et al., 2016).

Snow avalanche path

There are also some features of seismic signals that provide information about the path followed by the avalanche. This information can be found thanks to the study of the signal wave trains (Fig. 3.3). If wave trains have long durations, they are associated with the presence of obstacles along the avalanche descent path. In the absence of obstacles, the wave trains can indicate changes in the avalanche path slope, alterations in the flow or avalanche type, and phenomena associated with the deceleration stage of the avalanche. In the latter case, wave trains have a shorter duration. Another signals characteristic is the following: snow avalanches that traveled the same way show similar seismic signals. This similarity is not found in signals amplitude, but in the seismic energy distribution, in the spectral content and ground motion velocity directions (in vertical and horizontal planes), as shown in Fig. 3.3 (Surinach et al., 2000).

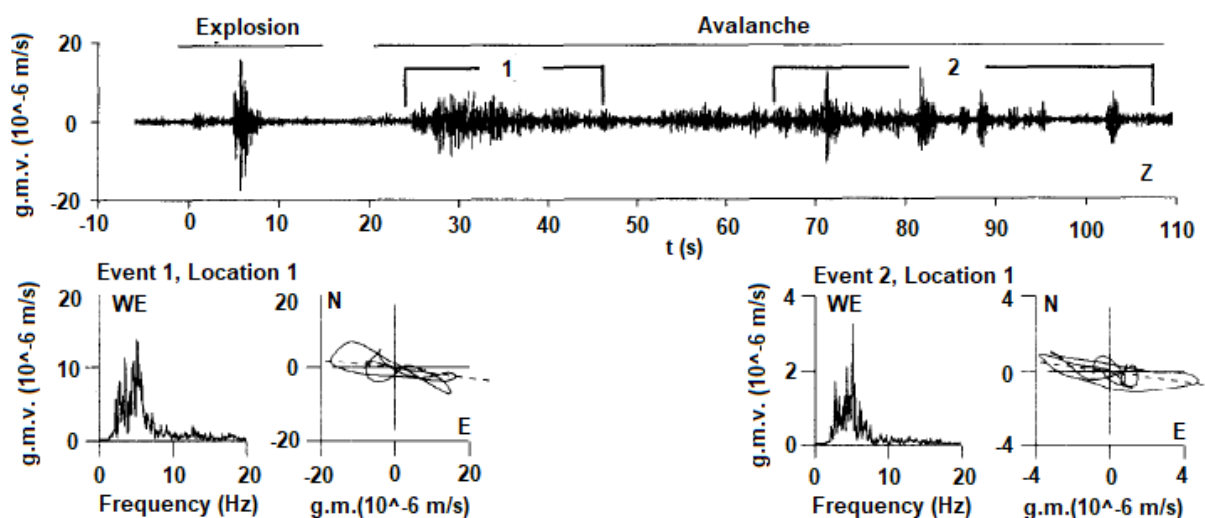


Fig. 3.3 The top graph shows the trend of snow avalanche (triggered by explosion) ground motion velocity (g.m.v. : z component). There are two different types of wave trains: the number 1 indicates longer wave trains associated to changes in slope and obstacles; the number 2 indicates shorter wave trains associated to the avalanche stopping phase. The bottom graphs in figure shows a similarity in spectral content and in ground motion velocity directions (horizontal plane) between 2 events occurred in the same location.

Modified after. Source: Surinach, Sabot, Furdada, Vilaplana. Study of Seismic Signals of Artificially Released Snow Avalanches for Monitoring Purposes. Phys. Chem. Earth (B), 25, n. 9 (2000), p.725

Snow avalanche size

The ground motion velocity module can be related to the size (volume and length) of the avalanche: as the module grows, the size of the avalanche increases (Surinach et al., 2000). Making this consideration, the distance between the snow avalanche and the sensor must always be taken into account. In fact, a small avalanche closer to the sensor can provide a signal with greater amplitudes than a larger avalanche furthest from the sensor. It is necessary to underline that, due to the anelastic attenuation with the distance, there is a limit of detection related to avalanches size (Biescas et al., 2003; Surinach et al., 2001). For evaluating the event size, energy criteria based on seismic energy dissipation (estimated through the knowledge of front speed) can be used (Vilajosana et al., 2007). More recent studies have shown that it is possible to estimate the avalanche size by using the run-out distance as a function of the seismic signal duration. In this case, the avalanche type must be known first. The relationship between the seismic signal duration and the avalanche run-out distance follows a linear function:

$$D = A \cdot T_A \quad [m] \quad (9)$$

Where D (m) is the run-out distance, T_A (s) is avalanche seismic signal duration, and A ($m \text{ s}^{-1}$) is the regression coefficient fitted to the data. By reporting known data on a $D - T_A$ graph and tracing the regression lines, it is possible, for each snow avalanche category, to find the A coefficient value. Therefore, it is possible to estimate avalanche dimensions using equation (9) being known A and T_A . There are also other types of regression but, in these cases, the avalanches size estimation is less dependable (Pérez-Guillén et al., 2016). An example is shown in Fig. 3.4.

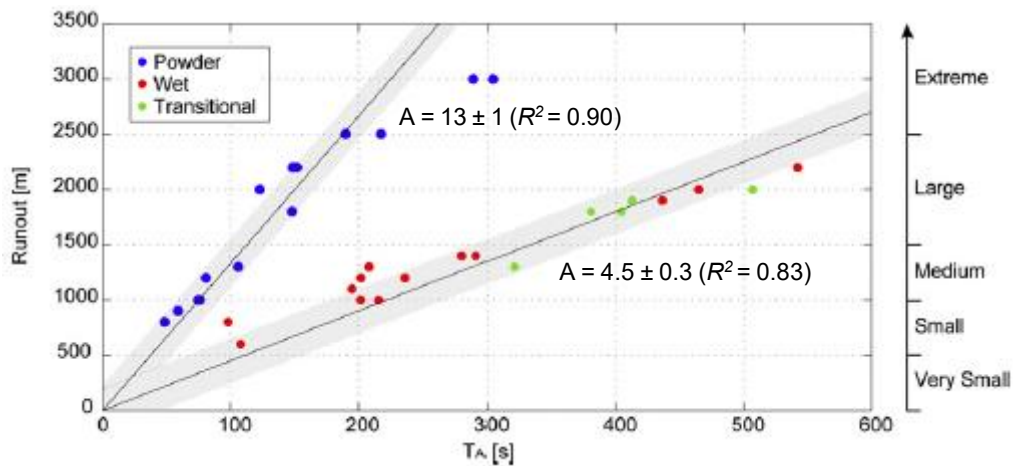


Fig. 3.4 Correlations between the seismic signal duration and run-out distance with indication of A values obtained from data linear regression.

Modified after. Source: Pérez-Guillén, supervised by Surinach Cornet. *Advanced seismic methods applied to the study of snow avalanche dynamics and avalanche formation (Ph.D. Thesis)*, (2016), p.36

Snow avalanche type

The ground motion velocity module can also be an indicator of snow avalanche type. It was shown that avalanches with a similar runout distance produce seismic signals with more or less high amplitudes depending on snow avalanche type: wet or dry respectively. Furthermore, wet-snow avalanches usually generate more extended signals, i.e., with longer duration, compared to dry snow avalanches (Biescas et al., 2003). Another seismogram feature that allows knowing

the snow avalanche type is its shape. For example, loose snow avalanches manifest the typical spindle shape, i.e. the amplitude increases as the snow mass, involved in the phenomenon, increases. Snow slab avalanches, on the other hand, can be identified by the presence in the seismogram of a first arrival that is made to correspond to the fracture occurring in the weak layer. Few times sensors can perceive the energy released by this fracture, unless it occurs at relatively short distances from the sensor. Considering that seismogram, apart from this first arrival, is very similar to that of loose snow avalanches, it is challenging to define a signal that corresponds uniquely to a snow slab avalanche (van Herwijen et al., 2011). However, an example of the two seismogram types is shown in Fig. 3.5. More recent studies have shown that it is possible to understand the avalanche type studying frequencies in which energy is dissipated by mass movement. However, this is only possible if the flow passes directly on the geophone. If it does not happen, all avalanches have similar energy content at low frequencies due to anelastic attenuation. (Pérez-Guillén et al., 2016)

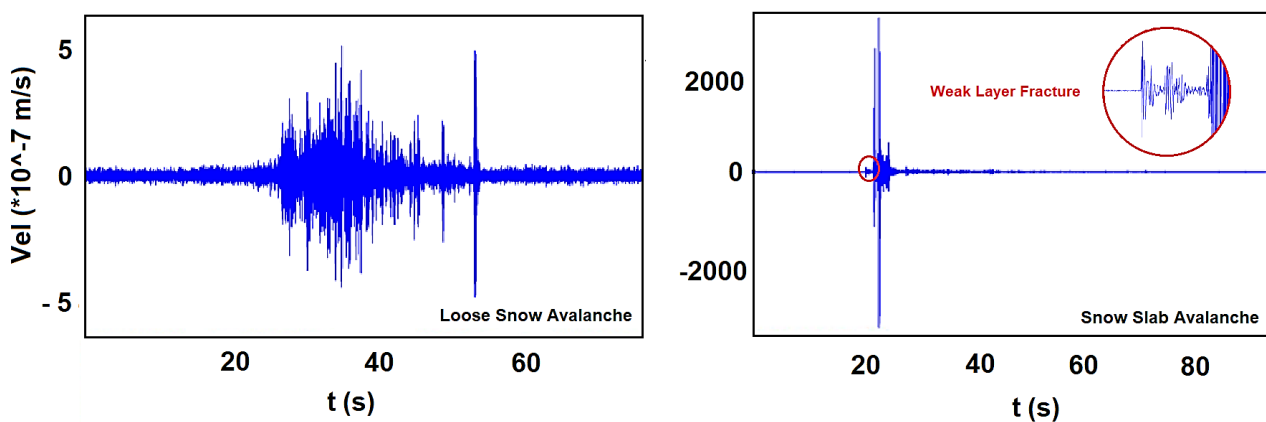


Fig. 3.5 Seismogram of Loose Snow Avalanche (on the left) and Snow Slab Avalanche (on the right). Modified after. Source: van Herwijen, Schweizer. Monitoring avalanche activity using a seismic sensor. *Cold Regions Science and Technology* 69 (2011), p.170 and p.174

Snow avalanche distance from the sensor

Signals can also be used to know the snow avalanche distance from the sensor. In fact, past research showed that snow avalanches frequency content is due to the distance between the mass movement and the geophone (Surinach et al., 2005). It is necessary to observe frequencies in which the greatest energy is present. The reason is that anelastic attenuation depends on frequency: high-frequency signals are attenuated more quickly than those at low frequency. It follows that, if most of the energy is situated at low frequencies, the avalanche release took place far from the sensor; on the contrary if most of the energy is situated at high frequencies (van Herwijen et al., 2011). It must be remembered what we said previously about anelastic attenuation. There are also other methods to locate snow avalanches using first-time picking. When these methods cannot be used, the polarization and beam forming methods can be used (Lacroix et al., 2012).

Site effects

Signals can also be studied to learn about site effects. The presence of these effects is highlighted by a different energy distribution in the 3 signals components, recorded in different places, but generated by the same avalanche.

Forecasting snow avalanches

Seismic data can also be used for forecasting snow avalanches. From these data, it is possible to identify avalanches release times for understanding the periods in which these phenomena are more concentrated and if they show a periodicity. For example, some studies revealed that in the spring season, avalanches show a periodicity corresponding to the daytime hours, as it could be expected intuitively. This information can be validated by data obtained from visual observations. So, it is possible to create catalogs. It is known that the past avalanches activity is correlated with the future one, therefore, it is possible to define prediction models based on the past activity reported in catalogs (van Herwijnen et al., 2016).

Automatic detection

The first seismic methods for the automatic detection of avalanches were based on the comparison of some signal characteristics, observed in time or frequency domain, with those of pre-recorded signals that could be confused with the avalanches (Pérez-Guillen, Ph.D. Thesis, 2016). Subsequently, Besson et al. (2007) proposed an automatic detection method based on the calculation of 10 characteristic parameters ($\alpha_i, i = 1, 2, \dots, 10$) for each event occurring in the same avalanche path. When a new event occurs in the reference avalanche path, it is compared to all known events in the same avalanche path and the proportional error is calculated:

$$E_{jk} = \sum_{i=1}^{10} W_{ik} \left| \frac{\alpha_{ik} - \bar{\alpha}_{ijk}}{\bar{\alpha}_{ijk}} \right|^e ; j = 1, 2, \dots, N_k ; k = 1, 2, \dots, n \quad (10)$$

Where k indicates the reference path, j indicates the event occurred in the referenced path, N_k is the total number of known events in the path, W_{ik} is a factor related to the weight assigned to each parameter. The exponent e is generally considered equal to 2. To understand what kind of phenomenon the new recorded event is related to, the most similar events are taken into consideration and they are compared using the proportional error. At this point, we proceed according to a majority principle: if most of the similar signals identify the new event as a snow avalanche, although there are others that indicate the opposite, the new event is identified as a snow avalanche. If the proportional error value exceeds a certain threshold, it is possible to identify the signal as “unknown” (Besson et al., 2007). Another more sophisticated method for automatic detection of avalanches is presented below. As previously stated, spectrograms generated by avalanches have a typical triangular shape. This shape depends on the anelastic attenuation, the distance between avalanche and geophone and on the mass increasing during the flow. On the basis of this spectrogram shape, automatic detection methods have been developed. One way is to proceed, firstly, with an extraction of spectral attributes from the signal, which allows differentiating classes of seismic signals. Secondly, for each class of interest, it is carried out a probabilistic description of the spectral attributes time series by means of Gaussian distributions. This procedure is called Hidden Markov Model (HMM). Parameters of HMMs created are learned from pre-classified training data. Subsequently, a single reference wave is used to create an ad hoc classifier for the event in question: an avalanche HMM is immediately created allowing the detection. This procedure was successfully developed only for the detection of wet-snow avalanches and it works only when the source-receiver distance is at most equal to 8 times the avalanche length (Hammer et al., 2017).

3.1.2 Infrasonic methods

Infrasonic signals can be used, like seismic signals, for different purposes. In particular, they can be used for monitoring and detecting avalanches phenomena. It was considered useful to use these systems since it was shown how the snow mass movement causes low-frequency acoustic waves.

Snow avalanche signal, environmental noise, and automatic detection

As in the case of seismic methods, also for infrasonic methods, it is essential to be able to distinguish between the signal of interest, associated with the event, and environmental noise. The main element of disturbance during the use of infrasonic methods is the wind action. Of course, different signal detection conditions may occur. The ideal detection condition verifies when there is a strong signal generated by the avalanche and a low disturbance produced by the wind. On the contrary, the most unfavorable condition occurs when there is a weak signal generated by the avalanche and a great disturbance produced by the wind (Scott et al., 2007). An example, given by records of cases described above, is shown in Fig. 3.6 .

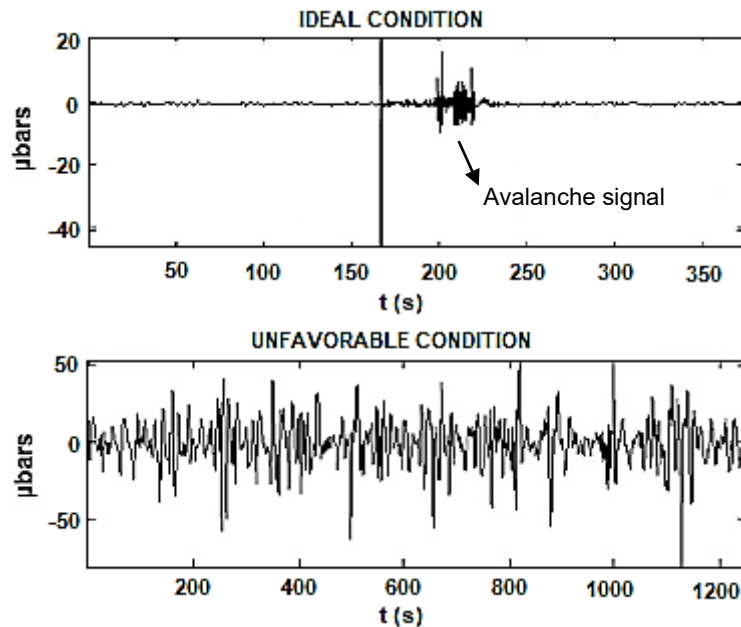


Fig. 3.6 The top graph shows infrasound data (0.1-8.5 Hz) in ideal conditions for avalanche identification; The bottom graph shows infrasound data (0.1-8.5 Hz) in unfavorable conditions for avalanche identification.

Modified after. Source: Scott, Hayward, Kubichek, Hamann, Pierre, Comey, Mendenhall. *Single and multiple sensor identification of avalanche-generated infrasound. Cold Regions Science and Technology 47 (2007) p.161-162*

If the registration occurred in ideal conditions, the avalanche is easily identifiable; in the second case, the identification of the signal coming from the avalanche is challenging, despite the development of single sensor signal processing algorithm (Comey et al., 2004). Environmental noise can make snow avalanches identification difficult directly from the signal. So, techniques based on signals autocorrelation were developed. By applying these techniques to the signals reported in Fig. 3.6, it is possible to obtain the autocorrelation coefficient trend, shown in Fig. 3.7. It is possible to observe how, in ideal conditions, the identification is immediate because the developed algorithms allow, through the application of filters, discarding some energy content, such as that of the explosives, before calculating autocorrelation. Therefore, a single peak due to the avalanche is produced. On the contrary, the calculation of autocorrelation in unfavorable conditions produces different peaks. Surely, the reading of autocorrelation coefficient allows to have a clearer vision of what can represent an avalanche and

what can be environmental noise, but peaks of avalanches and wind can often be very similar and so difficult to distinguish. For this reason, it is useful to have records obtained from different sensors. In fact, under unfavorable conditions, while autocorrelation data of a sensor produces different pronounced peaks, the same operation carried out in a different sensor could better highlight the peak due to the avalanche as shown in Fig. 3.7 (Scott et al., 2007).

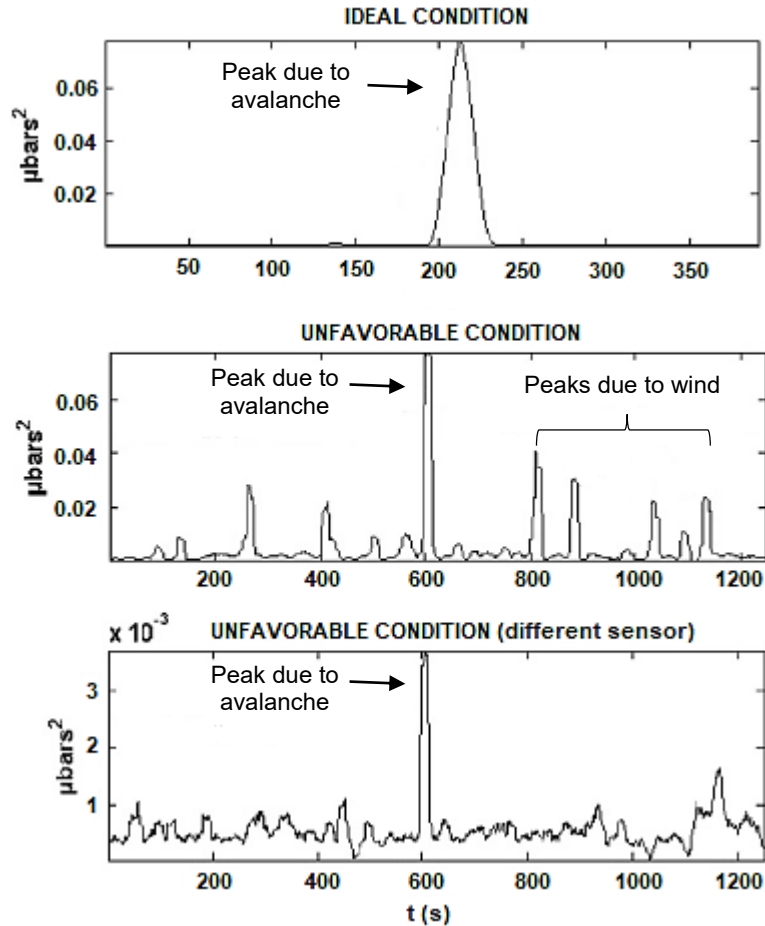


Fig. 3.7 The two top graphs show the autocorrelation coefficient trend related to infrasound data reported in Fig. 3.6. The bottom graph shows the autocorrelation coefficient trend, related to infrasound data, obtained from a different sensor, but for the same event occurred in unfavorable conditions. Peak due to the avalanche is confirmed at 600 s. Modified after. Source: Scott, Hayward, Kubichek, Hamann, Pierre, Comey, Mendenhall. Single and multiple sensor identification of avalanche-generated infrasound. *Cold Regions Science and Technology* 47 (2007) p.162-163

Nowadays it is known that, for robust identification of the avalanches, it is necessary to have data coming from different sensors. In fact, instead of calculating autocorrelation of data, obtained in one sensor, it is possible to cross-correlate signals obtained from different sensors. In the case of cross-correlation, it is also possible to discern ambient noise, such as explosions, using filtering techniques (Scott et al., 2007). More recent studies allow the signal to be discriminated by noise through the application of multi-channel correlation methods (Ulivieri et al., 2011). The parameter that allows distinguishing the signal from the noise is the residual time (ΔT_n). Having an array composed of n sensors, for each triplet of sensors, it is possible to calculate the residual time, as indicated by the following expression:

$$\Delta T_n = |\Delta t_{ij} + \Delta t_{jk} + \Delta t_{ki}| \quad (11)$$

Where Δt_{ij} is the delay between infrasound recorded at sensors i and j . The calculation of the residual time is repeated for all the triplets and then an average residual time is calculated. If the latter is lower than a threshold value, which depends on the opening of the array and on the frequency of the signal, avalanche detection is considered valid (Ulivieri et al., 2011). Avalanches common detection and classification methods are generally characterized by the extraction of some salient characteristics of signals (as back-azimuth, apparent velocity or event duration). For each of these characteristics, threshold values are normally assigned and, on the basis of these values, events detection and classification are carried out. Thuring et al. (2015) showed that these techniques often originate false and/or missed detections. For this reason, a machine learning-based approach was developed. This type of algorithm allows, through the input of training data, optimizing the decision margins, taking into consideration also the possible mutual dependencies of the parameters extracted from the signal. In particular, raw data are pre-processed before the features extraction. After this, part of the data is used for the algorithm training. Subsequently, the classifier is optimized through a cross-validation procedure. Classification can be achieved after applying a filter (Thuring et al., 2015).

Snow avalanche front velocity

Some recent studies have shown how, from the infrasound signals, it is possible to estimate the avalanche front velocity. During the path followed by the avalanche there is a continuous migration of back azimuth. It identifies the direction from where the signal is coming from. A possible trend of the back-azimuth angle, over time, is reported in Fig. 3.8.

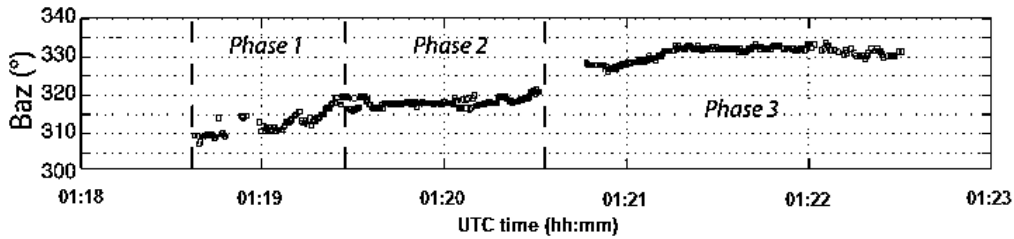


Fig. 3.8 Possible back azimuth angle trend over time with identification of 3 path phases followed by the avalanche. Modified after. Source Marchetti, Ripepe, Ulivieri, Kogelnig. *Infrasound array criteria for automatic detection and front velocity estimation of snow avalanches: towards a real-time early-warning system. Nat. Hazards Earth Syst. Sci* 15 (2015) p. 2548

It is possible to see that the chart is divided into 3 phases. The first phase is dominated by the infrasound produced by the avalanche front and the angle variation is related to the path followed by the front. The second phase shows a constant trend due to the rapid change of slope. The third phase is related to a source that extends horizontally. Therefore, it represents the stopping phase in the deposition area. Since it is possible to correlate the back azimuth variations with the front positions, then it is possible to obtain information related to the front velocity. In fact, given the absolute coordinates (x_i, y_i, z_i) of successive points that will be met by the avalanche, it is possible to calculate the reciprocal, horizontal (h_i) and vertical (l_i), distances and the theoretical back azimuth angle (azi_i), as shown by the following relations:

$$\left\{ \begin{array}{l} h_i = \sqrt{(x_i - x_{i-1})^2 + (y_i - y_{i-1})^2} \\ l_i = \sqrt{(z_i - z_{i-1})^2 + h_i^2} \\ azi_i = \tan^{-1} \left(\frac{x_i - x_a}{y_i - y_a} \right) \end{array} \right. \quad (12)$$

Where x_a and y_a are the coordinates of the central element of sensors array. By comparing the theoretical values with those obtained from the infrasonic signal, it is possible to understand the position of the front along the path. Therefore, converting the azimuth angles to the front positions occupied over time, it is possible to obtain the instantaneous speed of the front (Marchetti et al., 2015).

Snow avalanche localization

The delay time in the arrival of avalanche signal, evaluated at different sensors (obtained from the lag values of pair-wise cross-correlation coefficients), together with data about sensors geometry disposition can be employed to form aggregate beam patterns. The resulting beams make it possible to estimate the signal source position, i.e., the localization of the avalanche. As the amount of available data grows, the accuracy in the estimation of the location increases and the beam presents a smaller opening (Scott et al., 2007). An example of source localization is reported in Fig. 3.9 that shows a typical detection map.

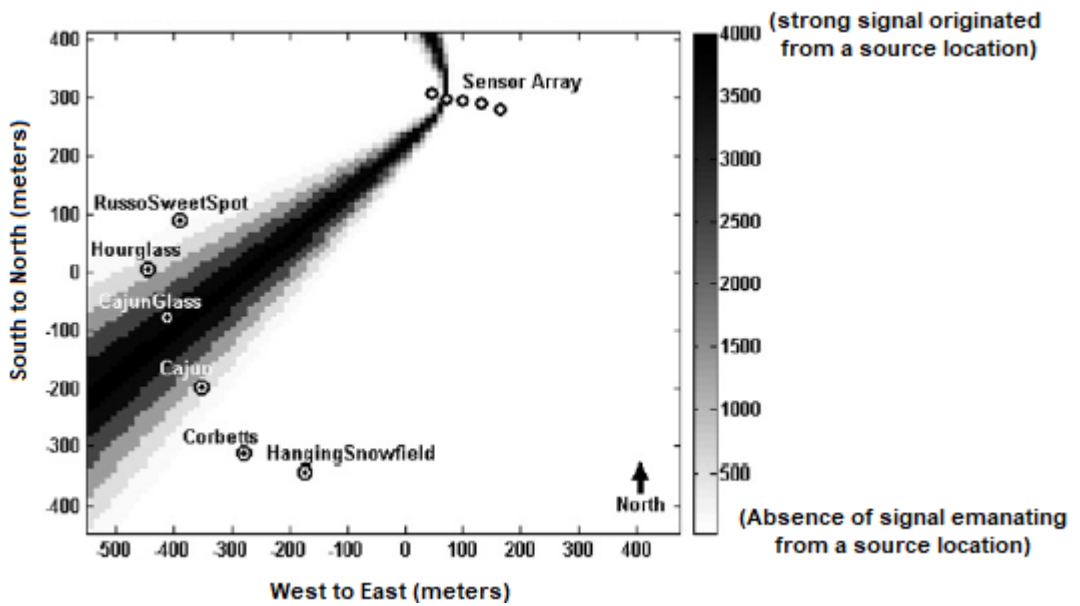


Fig. 3.9 Detection Map for snow avalanches localization. In this case, from data processing obtained from the sensor array, it is very likely that the signal was generated by the detachment of the avalanche Cajunglass. Distance from the sensor can be evaluated on the detection map.

Modified after. Source: Scott, Hayward, Kubichek, Hamann, Pierre, Comey, Mendenhall. Single and multiple sensor identification of avalanche-generated infrasound. *Cold Regions Science and Technology* 47 (2007) p.167

Other information related to the source localization can be obtained thanks to the calculation of the propagation back-azimuth (α) and apparent velocity (c) as indicated by Ulivieri et al. (2011). The first one shows the origin direction of the signal; the second one is related to the wave incidence angle and, therefore, to the source height. These parameters can be calculated using the system of equations reported below, assuming a planar wavefront and a constant wave propagation velocity between two sensors of the array. The system to be solved is:

$$\begin{cases} \frac{L_{ij} \cos(\beta_{ij} - \alpha)}{\Delta t_{ij}} = c_{ij} \\ \frac{L_{ik} \cos(\beta_{ik} - \alpha)}{\Delta t_{ik}} = c_{ik} \end{cases} \quad (13)$$

Where i, j, k , indicate the three elements of the triplet, β_{ij} is the angle between the North direction and the one connecting i and j sensors, α is the angle between the North direction and the wave propagation direction, c_{ij} is the apparent

velocity between i and j sensors and L_{ij} is the distance between two sensors. By hypothesis, apparent velocity is the same among all sensor pairs, therefore $c_{ij} = c_{ik}$: it is possible to solve the system. The apparent speed depends on the wave incidence angle (γ) and on the sound propagation speed in the air, which in turn depends on temperature and humidity, according to the relation: $c = \frac{c_{air}}{\gamma}$. From this expression, it is possible to understand the source altitude. In fact, small incidence angles correspond at high speeds and therefore high altitude sources; vice versa in the case of small speeds. (Ulivieri et al., 2011)

3.1.3 Seismic and infrasonic methods compared

Finally, it is possible to compare the seismic and infrasonic methods. As already mentioned, avalanches can have different flow regimes and are made up of different parts. It is known, from past studies, that seismic signals are generated mainly by the densest portion of the avalanche due to friction with the basal surface; the turbulent powder cloud generates infrasonic signals. A comparison between infrasonic and seismic signals, obtained for the same phenomenon, could be useful for understanding the flow regime. In fact, wet snow avalanches generate high amplitudes in seismic registrations; vice versa, powder snow avalanches generate lower seismic amplitudes, but higher infrasonic amplitudes. Another aspect to underline is that, despite the seismic waves are attenuated a lot due to anelastic attenuation and to geometric diffusion, depending mainly on the source-receiver distance, infrasonic waves are not affected by attenuations for distances up to 5 km. For these reasons, it was found that infrasonic methods are more suitable in detecting the initial phase of the avalanche. In fact, the movement is perceived earlier than seismic sensors. The latter are more suitable for detecting the final phase of the phenomenon. The avalanche stopping phase is only detected by seismic sensors, probably because the powder cloud is drastically reduced, while increasing dense flow and friction. Therefore, for the same avalanche monitored by seismic and infrasonic methods, it is observed, with the phenomenon development, an infrasonic amplitude decrease and a seismic amplitude increase. The combination of seismic and infrasonic measurements is also useful for understanding accurately and exhaustively the real duration of the phenomenon. A comparison between a seismic and an infrasound signal, recorded for the same avalanche, is shown in Fig. 3.10. In short, it is possible to observe a complementarity of the two methods which can together provide an excellent potential for monitoring snow avalanches (Kogelnig et al. 2011).

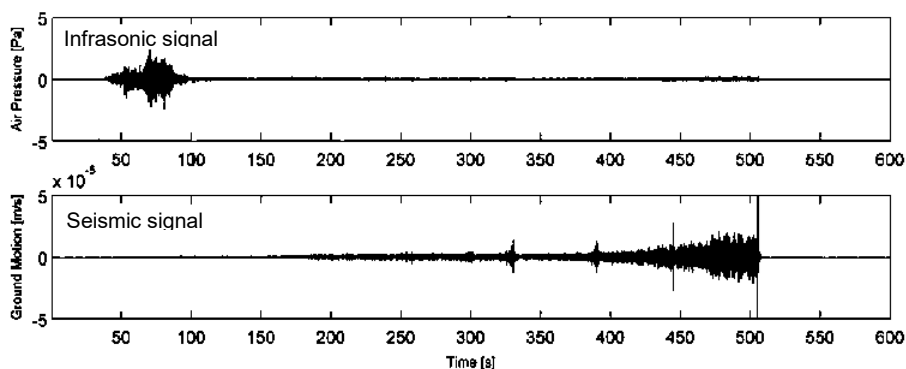


Fig. 3.10 Comparison between a seismic and an infrasound signal recorded for the same avalanche. Modified after. Source: Kogelnig, Surinach, Vilajosana, Hubl, Sovilla, Hiller and Dufour. On the complementarity of infrasound and seismic sensors for monitoring snow avalanches. *Nat. Hazards Earth Syst. Sci* 11 (2011) p.2366

3.2 Introduction to snow avalanches triggered by earthquakes

3.2.1 General notions, definitions and identification of seismic-induced avalanches

Global spatial extension of seismic-induced snow avalanches

Earthquakes can be a possible triggering factor of snow avalanches and a large area, even up to hundreds of kilometers, around the epicenter may be subjected to a shake sufficient to cause the snow cover to break (Podolskiy et al. 2010, II). Past studies have shown that, in all the world, areas that can be subject to avalanches, defined as areas with snow cover > 30 cm, slope > 17 ° and rise of 20-30 m, are about 6.2% of the entire Earth's surface. Instead, earthquakes verified in regions where active faults are present. Faults are normally known and mapped. From the overlap of such data, it has been possible to evaluate areas that may incur in seismic-induced snow avalanches corresponding to 3.1% of the total land area. Despite this, in the last century, documented cases of this type are very few (Podolskiy et al. 2010, I). In general, the relationship that exists between the snow avalanches release and the earthquakes depends on the hypocentral distance, the local conditions (geological, topographical, stability of the snowpack) and on the seismic source characteristics that are amplitude, frequency and duration (Pérez-Guillén et al. 2014).

What is a "snow avalanche triggered by an earthquake"

It is often difficult to understand when the triggering factor of a snow avalanche is effectively an earthquake. First of all, it is necessary to define what is meant by "avalanche triggered by an earthquake". It is possible to identify co-seismic snow avalanches, whose release occurs more or less at the same timing of the earthquake. Moreover, there are snow covers that, due to an earthquake that produced stress changes, have irremediably compromised their stability. In this case, snow avalanches release occurs a certain period of time after the earthquake (Podolskiy et al. 2010, I). This could also be caused by secondary aftershocks following the main shock. If the snowpack, due to the main shock, is close to limit equilibrium conditions, it is very likely that a secondary shock, even a minor one, can completely make it unstable. If the shear stress, caused by accelerations arriving from the earthquake, is higher than the shear strength of a point within the weak layer inside the snowpack, a necessary condition for the rupture is verified. This shear stress increases as the acceleration increases. The latter depends on the earthquake magnitude, the hypocentral distance and on-site effects (Pérez-Guillén et al. 2014). Moreover, it is possible to observe the amplification of the shear stress depending on the inertial loading. Therefore, it results to be greater where the acceleration is higher (Podolskiy et al. 2010, I).

Identification of earthquakes-induced snow avalanches

To understand if an earthquake induced a snow avalanche, an approximate determination of the avalanche release time and the knowledge of seismic waves arrival time to the site are required. As already mentioned, the snow avalanche release time identification, in the case that an earthquake occurred too, is difficult to determine precisely because of the signals overlapping. An excellent approach to the problem was followed by Pérez-Guillén et al. 2014: a comparison was made between seismic and infrasonic signals of earthquakes, which are thought to cause avalanches, and others in which no releases occurred. Below, in Fig. 3.11, are shown seismic and infrasonic signals, registered at the same station, of two earthquakes: the first one triggered a snow avalanche; the second one didn't cause any release. Where the earthquake didn't cause releases, seismic and infrasonic signals are well correlated. In particular, correspondence is found between the arrival of the P waves and the increase in amplitude of the infrasound signal, as

well as it is found in amplitude decreasing of both signals over time. A different behavior was found in the comparison of seismic and infrasonic signals for the event in which the avalanche was released. Firstly, the increase in amplitude due to the arrival of the P waves is not found in the infrasound sequence, but this may be due to the low signal-to-noise ratio and to the low energy of the earthquake. Secondly, while the seismic signal decreases in amplitude, with the passage of time, the infrasound signal, on the contrary, increases its amplitude. The latter phenomenon is probably caused by the reception, at the sensor, of the infrasound generated by the passage of the avalanche.

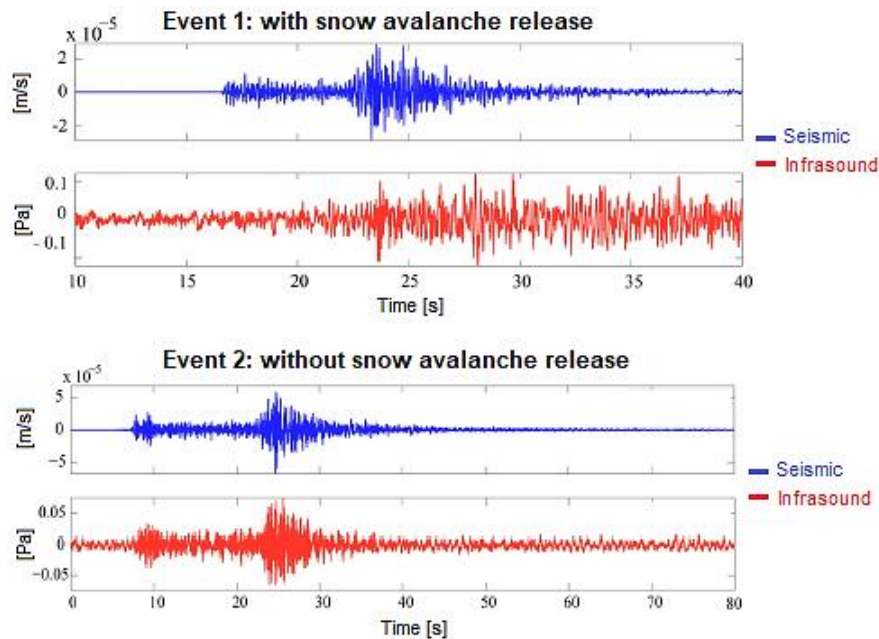


Fig. 3.11 Seismic and infrasonic signals, registered at the same station, of two earthquakes: Event 1 has triggered an avalanche, Event 2 has not caused any release.

Modified after. Source: Pérez-Guillén, Tapia, Furdada, Suriñach, McElwaine, Steinkogler, Hiller. Evaluation of a snow avalanche possibly triggered by a local earthquake at Vallée de la Sionne, Switzerland. *Cold Regions Science and Technology* 108 (2014): p.154-155

The importance of snowpack stability and loading factors

Another important observation that emerged from the study of Pérez-Guillén et al. 2014 is that the earthquake alone is not enough to cause detachment: also other conditions must coexist. In fact, with the same characteristics of earthquake, in some cases the avalanches release was found, in other cases not. It follows that the evaluation of snowpack stability conditions is fundamental. It is expected that as the seismic event magnitude increases, both the total number of avalanches and the area subject to avalanche phenomena increase too. At the same time, it is known that snow stability plays a significant role. In fact, if a snow avalanche was identified at a distance d from the epicenter, it does not necessarily mean that other avalanches occurred in a distance $< d$ (Podolskiy et al. 2010, I). The shaking produced by the earthquake causes a rapid large scale loading, usually oriented normal to the shear plane, which, depending on the snow stratigraphy, can lead to the slabs release (Podolskiy et al. 2010, I, Pérez-Guillén et al. 2014). Other factors to take into consideration are the uniform and gradual loading caused by snowfall and the surface heating phenomena that can lead to some changes in shear strength.

Surely, it is critical to take into account the weather conditions, since extreme events, with high return times, can significantly increase the risk of avalanches, especially when combined with the presence of earthquakes (Fujita et al. 2017). To obtain information on snow stratigraphy, simulations using snow cover models are often implemented as well as data from the avalanche bulletins and/or from other available stations. Among the well-known snow cover models there are the Meteoblue model and the SNOWPACK model. The substantial difference between the two is that the former is a meteorological model that provides information only about snowfall height from data deriving from precipitations. This model is used when there is a deficiency of data from stations. The SNOWPACK model, on the other hand, allows reconstructing snowpack stratigraphy starting from real data recorded directly in weather stations.

Parallelism with earthquake-induced landslides magnitude

To understand some aspects related to snow avalanches triggered by earthquakes, we referred to earthquake-induced landslides. Some studies have shown that, as the earthquake magnitude increases, the maximum distance from the epicenter, in which a landslide occurs, raises too. For landslides, it was also verified that as the magnitude of the seismic event increases, both the total number of landslides and their area increase too. Relationships for correlating the number of landslides and their area with earthquakes magnitude were found in semi logarithmic graphs. They present the following form:

$$\log X = a \cdot M - b \quad (14)$$

Where X is the variable concerned (total number of landslides (N) or their area (A)), M is the magnitude, a and b are the correlation coefficients. Similar behavior is expected in the case of snow avalanches (Podolskiy et al. 2010, I, cum bibl.).

A further comparison was made regarding magnitude values that trigger landslides and those triggering snow avalanches. From literature, the upper limit for triggering a landslide, close to the source ($d = 0$), is a magnitude equal to 4. At the same time, the lower limit was equal to 2.9 (Podolskiy et al. 2010, I, cum bibl.). Podolskiy et al. (2010, I) proposed a higher upper limit, about the initiation of landslides, but a smaller lower limit, about the initiation of snow avalanches (compared to the limit found for landslides). This limit magnitude (considering a mine site) was assumed to be 1.9, corresponding to a PGA of 0.03 g.

The importance of geological surroundings

It is essential to take into consideration the effect that deep geological conditions could have on seismic waves. Generally, site effects, and therefore amplification phenomena, are taken into account considering the value of v_s , 30 that, as explained in paragraph 2.2, is calculated with the S waves speed in the first 30 m of depth. This is due to the fact that data, at greater depths, are often not available. However, some studies showed the significant influence of deep geological features (Bulajic et al. (2018) cum bibl.). Thanks to the use of a GMPE (Ground Motion Prediction Equation), created by Bulajic et al. (2013), it is possible to calculate the PGA taking into account the shallow and deep geological conditions. Bulajic et al. (2018) showed that PGA values obtained considering deep geological data were amplified from 30% to 70% compared to those in which such data were not considered. Moreover, different scenarios, with the same shear strength and snow density, were considered. Subsequently, the possible detachment areas were mapped when the geological conditions were taken into account and when they were not. It was observed that, regardless of the snow density and the shear strength, the release areas increased when deep geological

conditions were considered. Consequently, it must be remembered that when this information is not available, an underestimation of the PGA, as well as the release areas, is obtained (Bulajic et al., 2018).

3.2.2 Snow avalanches release models with earthquake action

Podolskiy and others (2010) model

Over the years, studies tried to understand how the action of the earthquake can affect the stability of the snow cover. Among these studies, Podolskiy and others (2010, II) developed a release model obtained from laboratory tests. In particular, they proceeded to create artificial snow samples, with a weak layer, and to carry out tests using a shaking table. Tests were realized considering different table inclinations and different degrees of freedom (one degree of freedom: horizontal direction; two degrees of freedom: both horizontal and vertical directions). Conventionally, the tensions are considered negative, while the compressions are positive. From tests, it was observed that fractures occurred either in the lower part of the sample, or along the weak layer or in both positions, but at different times. Since the shaking table was monitored with a camera, it was possible to see when the failures occurred. It was observed that fractures originated, in most cases, when the shaking-table trajectory reached the farthest point, on the same side where the slope is oriented, and when the platform reverses direction (Podolskiy et al. 2010, II). In this point, shear and tensile forces reach the maximum value. Considering that at this point the greatest force is reached, the greatest acceleration, defined a_p , is reached too. It is possible to calculate the inertial force (F), applied to the snow sample, and dividing it by the shear plane area (A). So, the critical shear strength (τ_{ap}) is obtained:

$$F = m_f a_p g \quad \tau_{ap} = \frac{F}{A} = \frac{m_f a_p g}{A} \quad (15)$$

Where m_f is the mass of fractured snow and g is the gravitational acceleration. After the calculation of the inertial force, it is possible to calculate the normal and tangential stresses acting on the failure surface A in the 3 cases reported below (Fig. 3.12).

In the case a) there is no presence of shaking, therefore the normal (σ_n) and tangential (τ_n) tensions, along with sliding surface A , are generated by the weight of the block itself (they are both assumed positive):

$$\tau_n = \frac{m_f g \sin(\alpha)}{A} \quad \sigma_n = \frac{m_f g \cos(\alpha)}{A} \quad (16)$$

In case b), in addition to weight action, the acceleration due to the earthquake, and therefore the inertial force, is taken into account. In this case, the normal (σ_t) and tangential (τ_{st}) tensions, acting on the sliding surface A , become:

$$\tau_{st} = \tau_n + \tau_{ap} \cos(\alpha) = \frac{m_f g \sin(\alpha) + m_f a_p g \cos(\alpha)}{A} \quad (17.1)$$

$$\sigma_t = \sigma_n - \tau_{ap} \sin(\alpha) = \frac{m_f g \cos(\alpha) - m_f a_p g \sin(\alpha)}{A} \quad (17.2)$$

In this case, in addition to the shear stress, that tends to slide the block downwards, there is also normal stress that tends to move it away from the slope.

In the case c) the inertial force has the same module, same direction but it has the opposite way compared to case b). The normal (σ_c) and tangential (τ_{sc}) tensions, acting on the sliding surface A, are:

$$\tau_{sc} = -\tau_n + \tau_{ap} \cos(\alpha) = \frac{-m_f g \sin(\alpha) + m_f a_p g \cos(\alpha)}{A} \quad (18.1)$$

$$\sigma_c = \sigma_n + \tau_{ap} \sin(\alpha) = \frac{m_f g \cos(\alpha) + m_f a_p g \sin(\alpha)}{A} \quad (18.2)$$

In this phase, the block presents normal and tangential tensions which lead to keeping it adherent to the slope.

Applying this model to a real case, it is possible to obtain the critical value of m_f , being known the critical shear strength, the peak acceleration, slope inclination, and the sliding surface area, merely inverting the equation (17.1):

$$m_f = \frac{\tau_{st} A}{g(\sin(\alpha) + a_p \cos(\alpha))} \quad (19)$$

Being the snow density (ρ) known, it is possible to estimate the critical snow thickness above the sliding surface (typically coinciding with the weak layer):

$$h_{cr} = \frac{m_f}{\rho A} = \frac{\tau_{st}}{g \rho (\sin(\alpha) + a_p \cos(\alpha))} \quad (20)$$

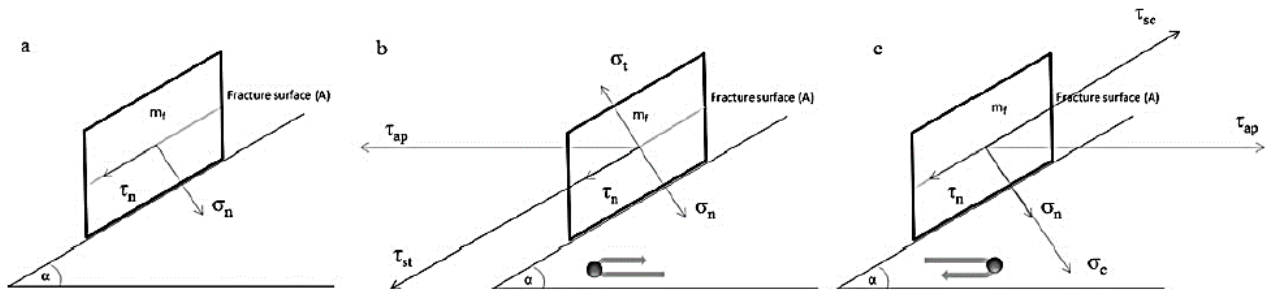


Fig. 3.12 a) Calculation of normal and tangential stresses in absence of shaking b) Calculation of normal and tangential stresses when the shaking-table reaches the farthest point, on the same side where the slope is oriented c) Calculation of normal and tangential stresses when the shaking-table reaches the opposite position compared to the case b).

Source: Podolskiy, Nishimura, Abe, Chernous. *Earthquake-induced snow avalanches: II. Experimental study. Journal of Glaciology* 56, n. 197 (2010) p.453

Stability index of Hiroki Matsushita et al. (2013)

Matsushita et al. (2013) evaluated the stability of the snowpack considering the action of the earthquake. They began the analysis, as Podolskiy et al. (2010, II), starting from the snowpack conditions in the absence of the earthquake, thus defining the following stability index (SI), calculated with reference to a natural slope, reported in Fig. 3.13:

$$SI = \frac{\Sigma_s}{\sigma_n \sin \psi} \quad (21)$$

where Σ_s is the shear strength of the weak layer, σ_n is the weight of the block above the weak layer divided by its surface (it can also be calculated as the product of snow density (ρ), gravity acceleration (g) and snow thickness (D) above the weak layer: $\sigma_n = \rho g D$ [N/m^2]) and ψ is the inclination of the slope. Obviously, the denominator presents the component of the weight acting along the weak layer.

At this point, it is possible to update the stability index (SI_E) adding the contribution given by the action of the earthquake. Given that the acceleration generated by the earthquake is considered only in its horizontal component, as shown in Fig. 3.13, the following expression for stability index is obtained:

$$SI_E = \frac{\Sigma_s}{\sigma_n(\text{sen}\psi + a \text{cos}\psi)} \quad (22)$$

Where a is the degree of horizontal acceleration, defined as the ratio of the acceleration generated by the earthquake to the acceleration of gravity (g) (Matsushita et al. 2013 cum bibl.). Below are shown, in Fig. 3.13, two reference schemes for the calculation of stability indexes previously reported:

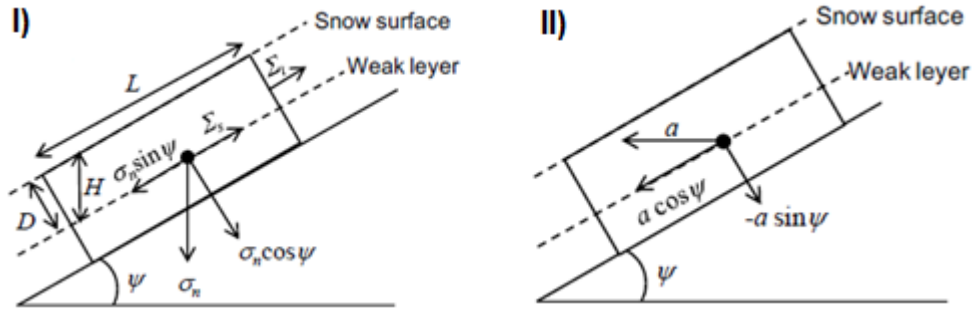


Fig. 3.13 Schemes for the calculation of the stability index. I) Normal and tangential actions acting on the weak layer under natural conditions II) Normal and tangential components of the acceleration, due to the earthquake, acting on the weak layer.

Modified after. Source: Matsushita, Ikeda, Ito, Matsuzawa, Nakamura. Avalanches induced by earthquake in North Tochigi prefecture on 25 February 2013. International Snow Science Workshop. Grenoble – Chamonix Mont-Blanc, (2013), p.1126

It is possible to make explicit the safety index, reported in equation 22, taking a cue from the safety factor in case of soil slopes in and from the equilibrium of stresses inside the snowpack (Matsushita et al. 2013 cum bibl.). Making these considerations the safety index (equation 23) can be expressed as:

$$SI'_E = \frac{CL + \sigma_n L(\text{cos}\psi - a \text{sen}\psi)\text{tan}\phi + \Sigma_t D}{\sigma_n(\text{sen}\psi + a \text{cos}\psi)} \quad (23)$$

Where C [N/m^2] expresses the cohesion between the grains and it can be considered equal to the SFI (Shear Frame Index) (Matsushita et al. 2013 cum bibl.), ϕ is the internal friction angle, L is the length of the snow layer above the weak layer (Fig. 3.13.I), Σ_t [N/m^2] is the shear strength of the weak layer. The latter can be defined by the following relation in the case of rounded grains (Matsushita et al. 2013 cum bibl.):

$$\Sigma_t = 3.40 \cdot 10^{-4} \rho^{3.24} \quad (24)$$

It is possible to observe that the shear strength in equation 23 was expressed in the same form as the Mohr-Coulomb failure criterion (Matsushita et al. 2013 cum bibl.), namely:

$$\Sigma_s = C + \sigma_n \tan \varphi \quad (25)$$

Stability factor of C. Pérez-Guillén et al. (2014) and Newmark analysis

Other studies concerning the stability of the snowpack have been carried out by Pérez-Guillén et al. (2014). They developed a release model, which takes into account earthquake action, studying the relationship between the shear strength of the snowpack, at the weak layer, and the shear stress acting on it. They, therefore, defined the following stability factor (S):

$$S = \frac{\tau_f}{\tau + \Delta\tau} \quad (26)$$

where τ_f is the shear strength, τ is the shear stress due to the weight of the snow slabs above the weak layer and $\Delta\tau$ is the additional shear stress due to the earthquake (Pérez-Guillén et al., 2014). This model was conceived as a safety factor: failure occurs when the denominator is equal (limit equilibrium) or higher than the numerator.

Assuming the x-direction as the direction in which the weak layer develops, the shear stress ($\tau_x(t)$), acting on the weak layer, can be described as the sum of the weight (x component) of the different snow layers above it, to which the stress along x, caused by earthquake acceleration ($a_x(t)$), is added (Pérez-Guillén et al., 2014):

$$\tau_x(t) = \sum_i \rho_i h_i \cdot (g \cdot \sin(\alpha) + a_x(t)) \quad (27)$$

where ρ_i and h_i are the density and height of each layer, α is the inclination of the slope and g is the gravitational acceleration. It is possible to observe the dependence of the shear stress over time. It follows that the maximum shear stress is obtained at the time for which maximum acceleration (PGA) occurs (Pérez-Guillén et al., 2014):

$$\tau_{xMAX}(t) = \sum_i \rho_i h_i \cdot (g \cdot \sin(\alpha) + a_x(t_{PGA})) \quad (28)$$

For shear strength different expressions can be used depending on layers composition: decomposing forms (τ_I) or faceted crystals (τ_{II}). The expressions were obtained by Jamieson and Johnson (Pérez-Guillén et al., 2014 cum bibl.):

$$\tau_I = 14.5 \cdot 10^3 \left(\frac{\rho}{\rho_{ice}} \right)^{1.73} \quad (29.1)$$

$$\tau_{II} = 18.5 \cdot 10^3 \left(\frac{\rho}{\rho_{ice}} \right)^{2.11} \quad (29.2)$$

Where ρ is the layer density and ρ_{ice} is the ice density. These expressions were used to calculate the stability factor respectively in the case of shallow (S_s) and deep (S_d) snow avalanche release (Pérez-Guillén et al., 2014).

$$S_s = \frac{\tau_I}{\tau_{max}} \quad (30.1)$$

$$S_d = \frac{\tau_{II}}{\tau_{max}} \quad (30.2)$$

Finally, it is possible to use the Newmark method to define the cumulative displacement (D) of a block, due to the earthquake acceleration, as follows (Pérez-Guillén et al.,2014):

$$D = \iint (a(t) - a_c) dt^2 \quad (31)$$

Where $a(t)$ is the acceleration of the earthquake at time t , a_c is the critical acceleration. The latter can be expressed, by combining the parameters described above, as follows (Pérez-Guillén et al.,2014):

$$a_c = (S - 1) \cdot g \cdot \text{sen}(\alpha) \quad (32)$$

4. The case study: Central Apennines in January 2017

The present study will deal, for Appennino Umbro-Marchigiano and Appennino Abruzzese, the geomorphological and nivo-meteorological analysis of snow avalanches release areas surveyed in January 2017, through photo-interpretation, by Ph.D. Igor Chiambretti, AINEVA Technical Director. Also, release areas were characterized on the basis of the PGA reported by the seismic hazard map. Subsequently, we tried to understand which accelerations were felt by these areas during some earthquakes that occurred during the 18th January 2017. Also, we tried to define, as a result of statistics made from GIS elaborations, which are the possible releases triggered by earthquakes. To have a well-defined border, the study area is contained within the administrative limits of Abruzzo, Lazio, Marche, Molise and Umbria regions. It is emphasized that the elaborations that will be carried out have reliability only on a regional scale.

4.1 Regions of interest seismicity

To carry out the processing described above, we started by searching for regions of interest seismicity. The seismic basic hazard map, provided by the INGV, which shows the PGA values (50th percentile), according to a regular grid of 0.02° (planar distance of about 3 km), for a given exceedance probability (P_{VR}) in a given reference life (V_R), was taken into consideration. Fig. 4.1 exhibits, for regions of interest, the seismic basic hazard map with PGA values for an exceedance probability of 10% in 50 years.

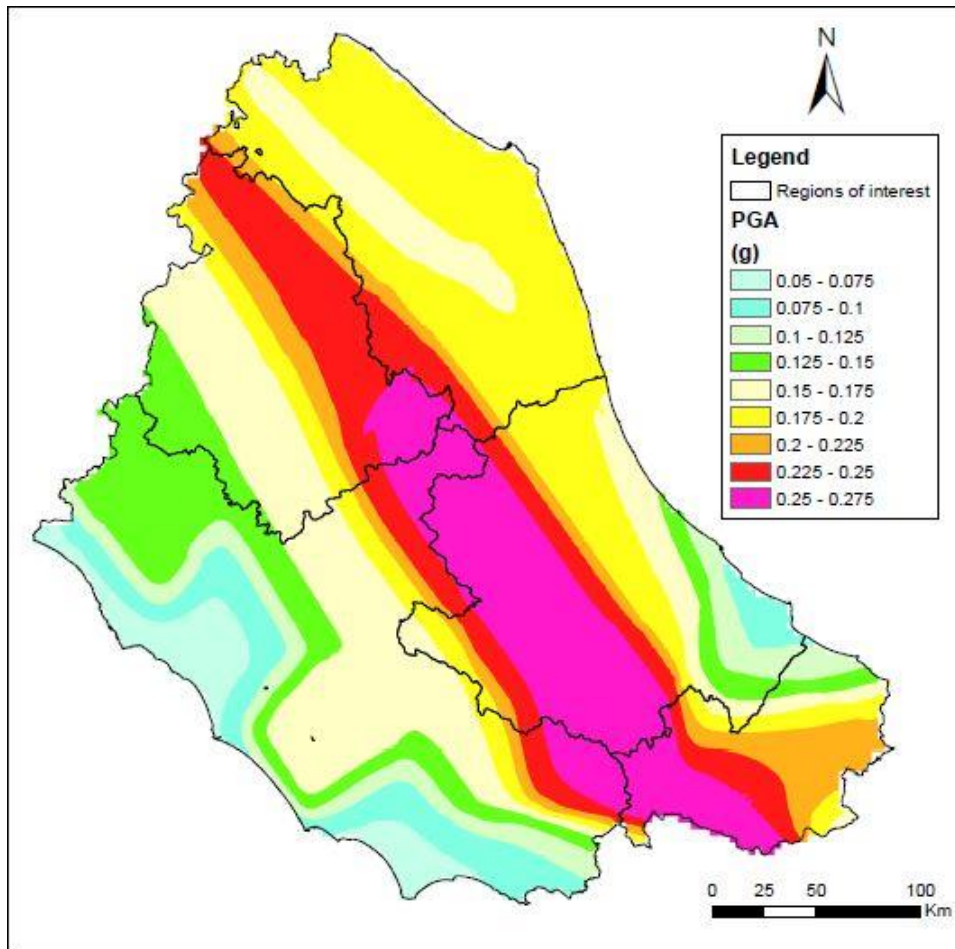


Fig. 4.1 Seismic basic hazard map for regions of interest: PGA (50th percentile) for a exceedance probability of 10% in 50 years. Note: The figure was obtained by mapping the standard values of a_g (50th percentile), with a regular step of 0.02 °, found on the INGV website: <http://zonesismiche.mi.ingv.it/elaborazioni/>.

It is possible to observe how the Apennine area, located in the central portion of the map, show PGA values included between 0.175 and 0.275 g. According to the Ordinance of March 20, 2003, n.3274, Italy was divided into 4 seismic zones as shown in Table 8. It follows that the Apennine area, being in seismic zones 1 and 2, is a strongly seismic area with the highest PGA values. This is because the Apennine arch of Central Italy, as reported by DISS in version 3.2.1, completed in July 2016 and published in April 2018, presents a high concentration of CSS.

Table 8 Definition of seismic zones according to the ordinance of March 20, 2003, n.3274

zone	horizontal acceleration with an exceedance probability of 10% in 50 years
1	> 0.25
2	0.15 - 0.25
3	0.05 - 0.15
4	< 0.05

In Fig. 4.2 the seismic basic hazard map, with an exceedance probability of 10% in 50 years, to which the CSS, reported by the DISS, were superimposed, is shown. Each CSS presents an identification code (ID Source) that allows its recognition. Name and characteristics of each CSS are reported in Table 9.

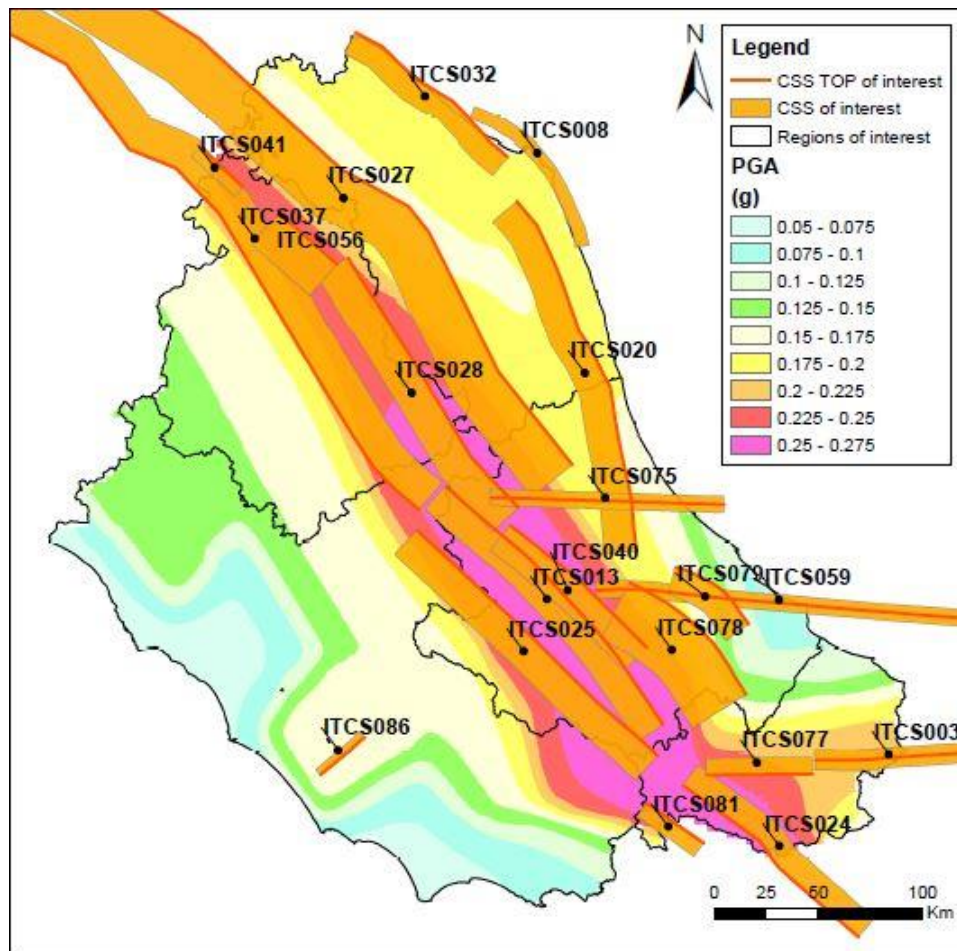


Fig. 4.2 Seismic basic hazard map for regions of interest (PGA (50th percentile) for an exceedance probability of 10% in 50 years) to which the CSS, reported by DISS (version 3.2.1; Source: <http://diss.rm.ingv.it/diss/index.php/DISS321>), were superimposed. Each CSS presents an identification code (ID Source) that allows its recognition. Information for each CSS is reported in Table 9.

Table 9 Characteristics of each CSS in the study area. Note: the information shown in the table are fewer than those available from the database (Source: <http://diss.rm.ingv.it/diss/index.php/DISS321> (exported from CSS shapefile Attribute Table))

IDSource	SourceName	Min Depth [Km]	Max Depth [Km]	Strike Min (°)	Strike Max (°)	Dip Min (°)	Dip Max (°)	Rake Min	Rake Max
ITCS003	Ripabottoni-San Severo	6	25	250	270	75	90	180	220
ITCS008	Conero onshore	3	6.5	110	160	30	45	80	100
ITCS013	Borbona-L'Aquila-Aremogna	2	14	130	150	40	60	260	280
ITCS020	Southern Marche	3.5	13	140	175	35	50	80	100
ITCS024	Miranda-Apice	1	14	300	330	50	60	260	280
ITCS025	Salto Lake-Ovindoli-Barrea	1	14.5	130	150	40	65	260	280
ITCS027	Bore-Montefeltro-Fabriano-Laga	12	22	90	160	20	55	70	110
ITCS028	Colfiorito-Campotosto	2.5	14	130	150	35	55	260	280
ITCS032	Pesaro-Senigallia	3	7.5	105	145	25	35	80	100
ITCS037	Mugello-Citta' di Castello-Leonessa	0.5	8	280	330	25	40	260	280
ITCS040	Barisciano-Sulmona	1	14	120	140	40	65	260	280
ITCS041	Sansepolcro	1	5	130	140	40	50	260	280
ITCS056	Gubbio Basin	2	7	120	140	15	25	260	280
ITCS059	Tocco Casauria-Tremiti	11	20	80	100	65	90	170	230
ITCS075	Campotosto Lake-Montesilvano	11	20	80	100	65	90	170	230
ITCS077	Pescolanciano-Montagano	11	25	260	280	60	80	220	240
ITCS078	Deep Abruzzo Citeriore Basal Thrust	8	18	120	150	20	30	80	100
ITCS079	Shallow Abruzzo Citeriore Basal Thrust	3	8	110	150	20	40	80	100
ITCS081	Venafrò	1	13	120	130	60	70	260	280
ITCS086	Castelli Romani	5	11	220	230	60	80	260	280

The seismic framework was completed searching for earthquakes that occurred in these regions in the year 2017. Earthquakes have been recovered from the database ITACA (Italian Accelerometric Archive rel. 2.3) which reports events data from 1972 to 2017 allowing to search using different filters. An identifying ID, different from the original one, was attributed to each earthquake. The earthquakes location is shown in Fig. 4.3, while their characteristics are reported in Table 10.

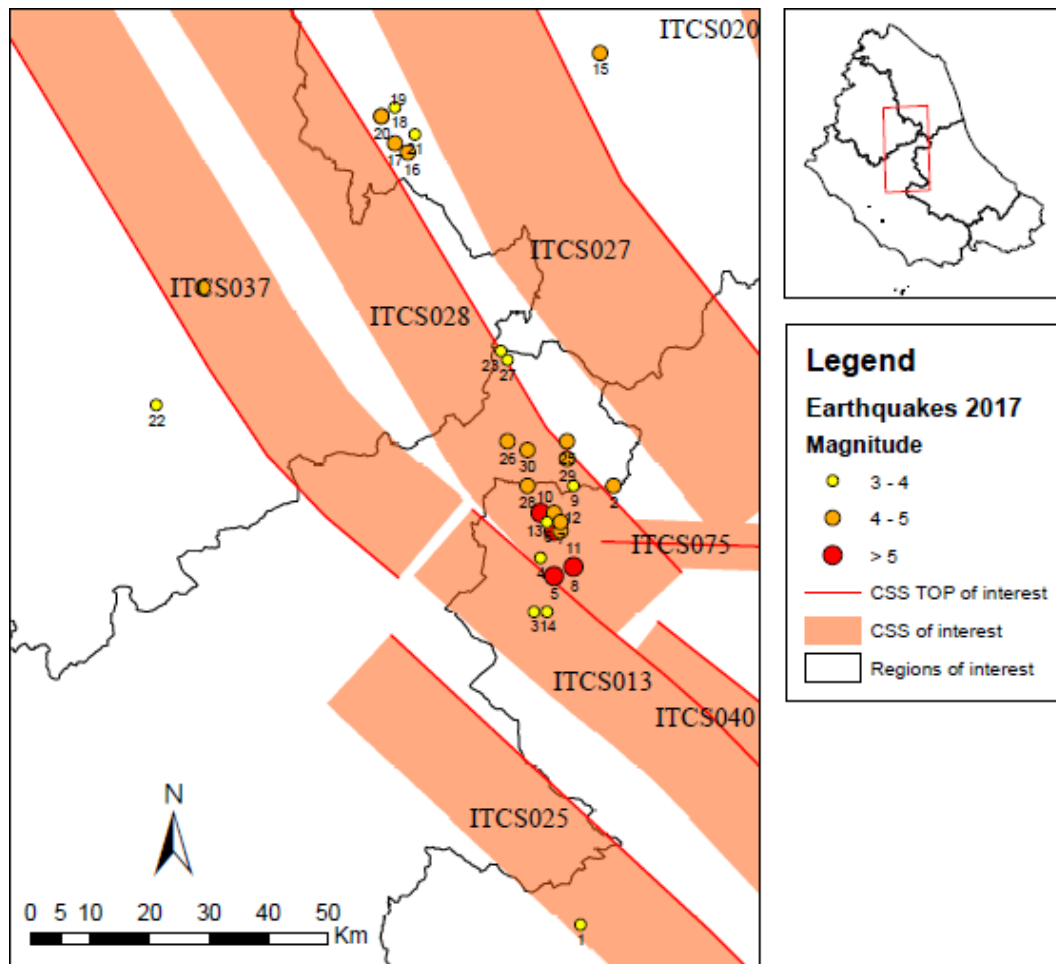


Fig. 4.3 Earthquakes occurred within the regions of interest (2017), superimposed on CSS. The earthquakes representation is different depending on the magnitude. An identifying ID, different from the original one, has been attributed to each earthquake. Information for each earthquake is reported in Table 10.

Table 10 Information for each earthquake recovered from the database ITACA in the study area (2017). Note: the information shown in the table are fewer than those available from the database (Source: <http://itaca.mi.ingv.it>). The earthquakes that occurred in January 2017 (17/30 total) are shown in red. Among these, 4 earthquakes have $M_w \geq 5$ (ID: 5, 8, 12, 13)

ID	Event id (ITACA)	mm/dd/yy	hh:min:sec	Region	Epicenter	z [km]	M_L	M_W
1	EMSC-20170910_0000129	09/10/17	7:58:10 PM	Abruzzo	Tagliacozzo	8.0	4.0	-
2	EMSC-20170722_0000016	07/22/17	2:13:07 AM	Abruzzo	Campotosto	20.0	4.3	-
3	EMSC-20170409_0000007	04/09/17	1:52:28 AM	Abruzzo	-	5.0	4.0	-
4	EMSC-20170220_0000016	02/20/17	3:13:30 AM	Abruzzo	Montereale	11.0	4.0	-
5	EMSC-20170118_0000119	01/18/17	1:33:37 PM	Abruzzo	Montereale	10.0	5.1	5
6	EMSC-20170118_0000077	01/18/17	12:01:17 PM	Abruzzo	-	13.7	3.4	-
7	EMSC-20170118_0000048	01/18/17	10:39:24 AM	Abruzzo	Capitignano	11.0	4.1	-
8	EMSC-20170118_0000037	01/18/17	10:25:26 AM	Abruzzo	Montereale	8.9	5.3	5.4
9	EMSC-20170118_0000049	01/18/17	10:24:16 AM	Abruzzo	Amatrice	10.0	4.0	-
10	EMSC-20170118_0000051	01/18/17	10:16:39 AM	Abruzzo	Montereale	10.7	4.6	-

11	EMSC-20170118_0000059	01/18/17	10:15:33 AM	Abruzzo	Capitignano	9.8	4.7	-
12	EMSC-20170118_0000034	01/18/17	10:14:12 AM	Abruzzo	Capitignano	9.1	5.4	5.5
13	EMSC-20170118_0000027	01/18/17	9:25:42 AM	Abruzzo	Montereale	9.2	5.3	5.1
14	EMSC-20170105_0000083	01/05/17	7:52:59 PM	Abruzzo	Barete	10.0	3.3	-
15	EMSC-20170624_0000039	06/24/17	8:30:09 AM	Marche	Penna San Giovanni	20.0	4.1	-
16	EMSC-20170427_0000119	04/27/17	9:19:43 PM	Marche	Visso	8.0	4.1	-
17	EMSC-20170427_0000114	04/27/17	9:16:59 PM	Marche	Visso	9.0	4.2	-
18	EMSC-20170203_0000032	02/03/17	5:40:34 AM	Marche	Pieve Torina	8.0	3.9	-
19	EMSC-20170203_0000018	02/03/17	4:10:05 AM	Marche	Monte cavallo	7.1	4.4	4.2
20	EMSC-20170203_0000016	02/03/17	3:47:55 AM	Marche	Monte cavallo	6.0	4.1	-
21	EMSC-20170105_0000041	01/05/17	11:34:18 AM	Marche	-	10.0	3.3	-
22	EMSC-20170209_0000098	02/09/17	9:58:27 AM	Umbria	Spoletto	9.0	4.0	-
23	EMSC-20170105_0000079	01/05/17	6:38:32 PM	Umbria	Norcia	11.0	3.1	-
24	EMSC-20170102_0000021	01/02/17	3:36:14 AM	Umbria	Spoletto	7.5	4.1	3.9
25	EMSC-20171203_0000085	12/03/17	11:34:11 PM	Lazio	Amatrice	0.0	4.6	-
26	EMSC-20170630_0000001	06/30/17	12:25:17 AM	Lazio	Amatrice	12.0	4.1	-
27	EMSC-20170121_0000027	01/21/17	9:35:55 AM	Lazio	Accumoli	10.3	3.8	3.7
28	EMSC-20170118_0000199	01/18/17	7:32:32 PM	Lazio	Amatrice	12.6	4.3	4.2
29	EMSC-20170118_0000154	01/18/17	3:16:13 PM	Lazio	Amatrice	10.2	4.3	4.3
30	EMSC-20170118_0000053	01/18/17	11:07:39 AM	Lazio	Amatrice	10.3	4.3	4.1

4.2 Nivo-meteorological data in the period of interest

As already mentioned, it is critical to take into consideration the weather conditions and the state of the snowpack. In this regard, the Meteomont service bulletins were consulted. In particular, the bulletins of the Appennino Umbro-Marchigiano (07 sector) and Grandi Massicci Appenninici and Appennino Abruzzese (04 sector) sectors were consulted. Identification of investigated sectors is reported in Fig. 4.4. Dates of greatest interest are January 14th to 18th, 2017, because, during this period, there was an intense avalanche activity. Sibillini Mountains, Monti della Laga, Gran Sasso Massif, Majella Massif and Matese Massif were the mountain sectors mainly concerned (Chiambretti at al., 2017).



Fig. 4.4 Investigated Meteomont sectors.

Modified after. Source: <http://www.meteomont.gov.it/infoMeteo/jsp/mwablx803.jsp>

4.2.1 Sector 07: “Appennino Umbro-Marchigiano”

Below is reported the description of snow conditions for the “Appennino Umbro-Marchigiano” sector in the period of interest. The following evaluations are carried out on a synoptic-regional scale.

On January 14th, 2017, the snowpack, moderately consolidated on many steep slopes, consisted of wet snow layers up to the ground. In the release areas, snow settled on wind crusts, which can act as a weak interface. Such situation can cause avalanches with low overload. On January 15th, 2017, fresh and dry snow layers were deposited over the pre-existing wind crusts. Once again, the snowpack was moderately consolidated on many steep slopes. On January 16th, 2017, due to abundant snowfalls accompanied by strong wind the presence of soft wind slabs was highlighted over the pre-existing wind crusts. The snowpack was already weakly consolidated and mostly unstable on many slopes. The greatest danger was connected to the wind activity which reworked the fresh snow distribution loading the downwind slopes. On January 17th, 2017, the snowpack conditions were similar to those of the previous day, but due to the widespread snowfalls, of moderate and strong intensity, the snowpack thickness increased. At the highest elevations, the wind activity persisted. On January 18th, 2017, the situation was still very similar to the previous day. As a result of wind activity, the slabs releases, medium or large, on the western and southern slopes, were possible also with weak overload. (summarized from Meteomont bulletins).

In this area, there are two subsectors: “Appennino Marche Settentr.” and “Appennino Marche Merid.-Sibillini”. For these subsectors, the bulletin provides snow height (line) and snow avalanches hazard data (histogram), reported in Fig. 4.5, for days of interest.

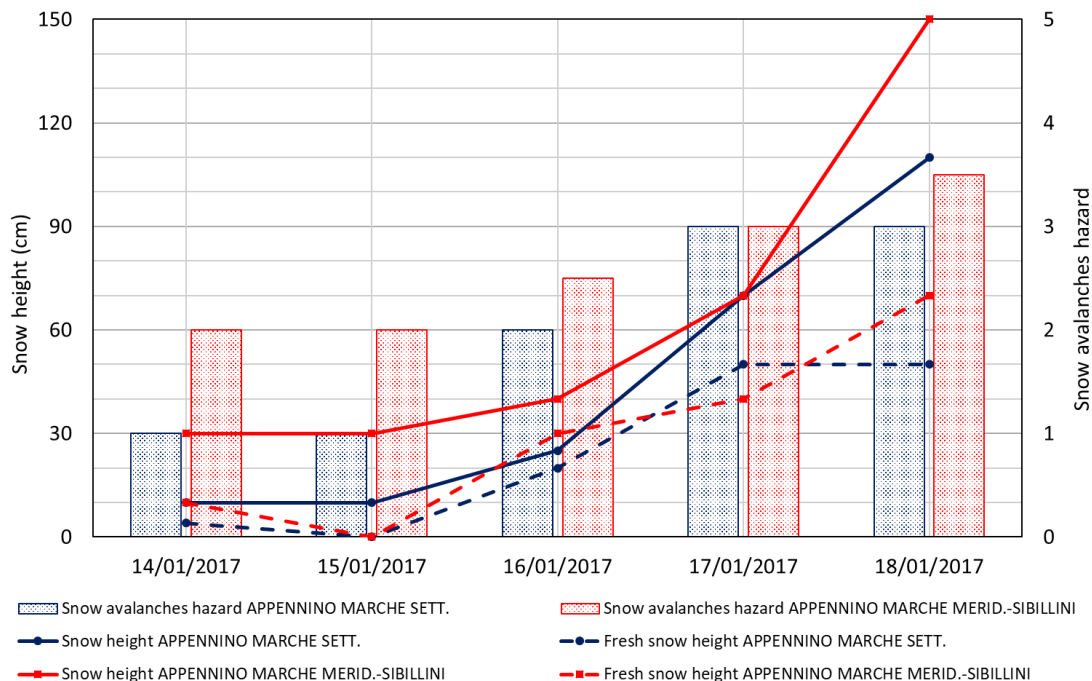


Fig. 4.5 Snow height (line) and snow avalanches hazard data (histogram), for days of interest, in “Appennino Marche Settentr.” and “Appennino Marche Merid.-Sibillini” sub-sectors.

European scale of avalanche hazard degree: 1- weak 2- moderate 3- marked 4- strong 5- very strong

Source: Graph obtained from data of Meteomont bulletins: <http://www.meteomont.gov.it/infoMeteo/caricaPaginaStorici.do>

It is possible to observe the increasing snow height (fresh and not), as well as the snow avalanches hazard level, from January 14th to 18th, 2017.

Inside the daily bulletin, there are forecasts, concerning the values of temperature, winds, and precipitation, regarding the two following days. For each bulletin consulted, to improve data reliability, only the forecast for the following day was considered. Therefore, the forecast for the second following day is entrusted to the following bulletin. Starting from forecasted data, it is possible to understand temperature, freezing level and wind trend for days of interest. These quantities are shown in the following graphs.

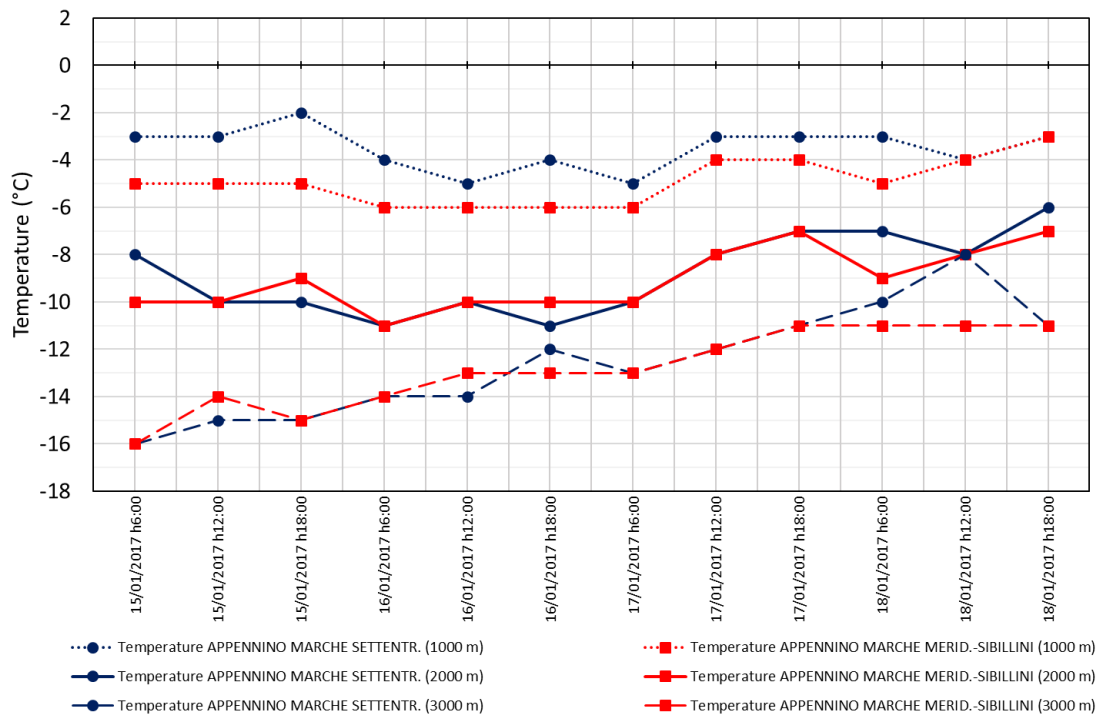


Fig. 4.6 Forecasted data for temperatures at 1000, 2000 and 3000 m, in the days of interest, in "Appennino Marche Settentr." and "Appennino Marche Merid.-Sibillini" subsectors. Source: Graph obtained from data of Meteomont bulletins: <http://www.meteomont.gov.it/infoMeteo/caricaPaginaStorici.do>

Fig. 4.6 shows temperatures trend (at the altitude of 1000, 2000 and 3000 m) in the two subsectors. At 1000 m, on January 16th, temperatures tended to decrease by few degrees in both subsectors, while they returned to their initial values on January 18th, with a two-degree increase in the subsector "Appennino Marche Merid.-Sibillini". On average, there was an increase in temperature from January 15th to 18th at 2000 and 3000 m. This increase was particularly evident at 3000 m.

Fig. 4.7 shows freezing level trends¹, in subsectors analyzed, for the days of interest. Freezing level is the altitude value at which temperature is zero Celsius degrees and above which temperature is always below zero Celsius degrees. A similar trend is observed in both subsectors. In particular, we observe a first decrease of freezing level from January 15th to 17th h: 6.00, from which an increase was expected until January 18th. Values reached on this last date are similar to the initial ones for the "Appennino Marche Settentr." subsector, while they are higher in the other one. Moreover, freezing level of "Appennino Marche Merid.-Sibillini" subsector is always above than the other one. On average, the difference between sectors increases from January 15th to 18th, going from 100 m up to 400 m.

¹ The bulletin presents an altitude range within which it is possible to find the freezing level. For convenience, we have shown the freezing level trend considering the average value of the indicated range. The real value of the freezing level could be above or below the indicated value, up to ±100 m.

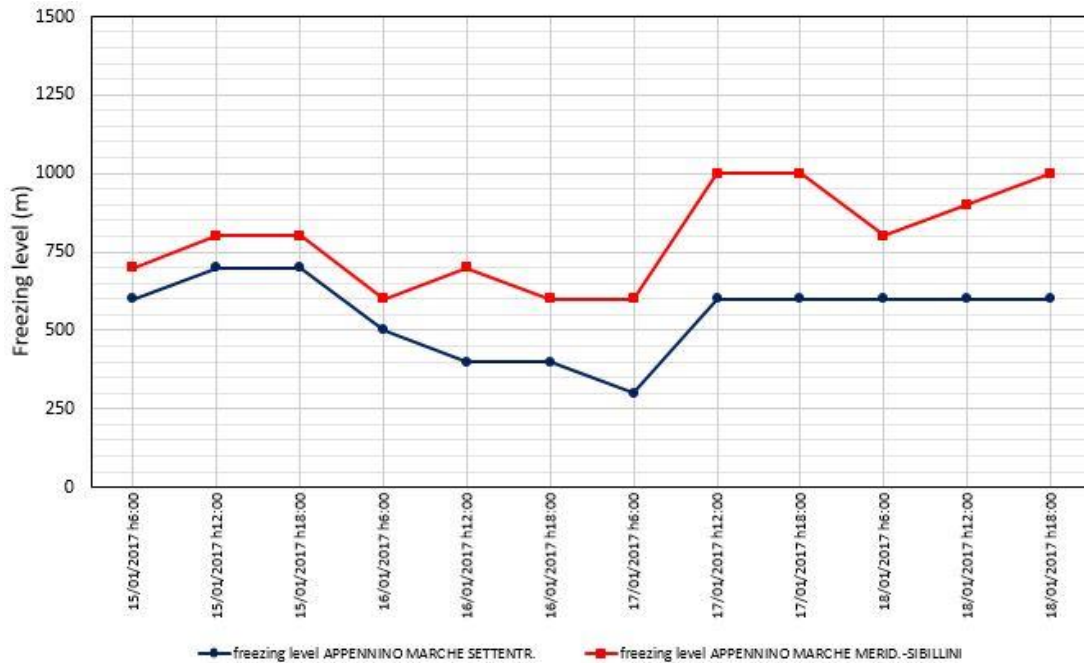


Fig. 4.7 Forecasted data for freezing level, in the days of interest, in "Appennino Marche Settentr." and "Appennino Marche Merid.-Sibillini" subsectors
 Source: Graph obtained from data of Meteomont bulletins: : <http://www.meteomont.gov.it/infoMeteo/caricaPaginaStorici.do>

The following figures show wind speed (line) and direction (dots) data, in the two subsectors, for the days of interest, at altitudes of 1000, 2000 and 3000 m (Fig. 4.8, Fig. 4.9, Fig. 4.10). Compared to the bulletin, wind speed, expressed in knots, was converted to Km/h, while the wind direction was expressed in degrees.

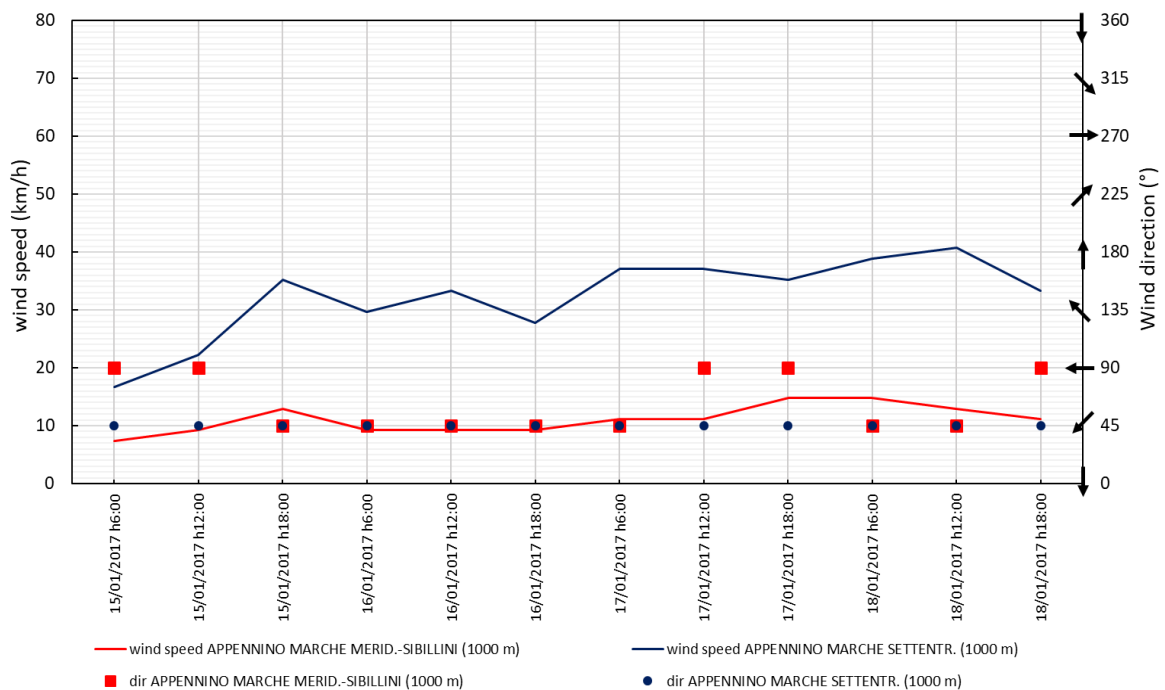


Fig. 4.8 Forecasted data for wind speed (line) and wind direction (dots) (1000 m), in the days of interest, in "Appennino Marche Settentr." and "Appennino Marche Merid.-Sibillini" subsectors
 Wind direction Legend: 0: N 45: N-E 90: E 135: S-E 180: S 225: S-W 270 W 315: N-W 360: N
 Source: Graph obtained from data of Meteomont bulletins: : <http://www.meteomont.gov.it/infoMeteo/caricaPaginaStorici.do>

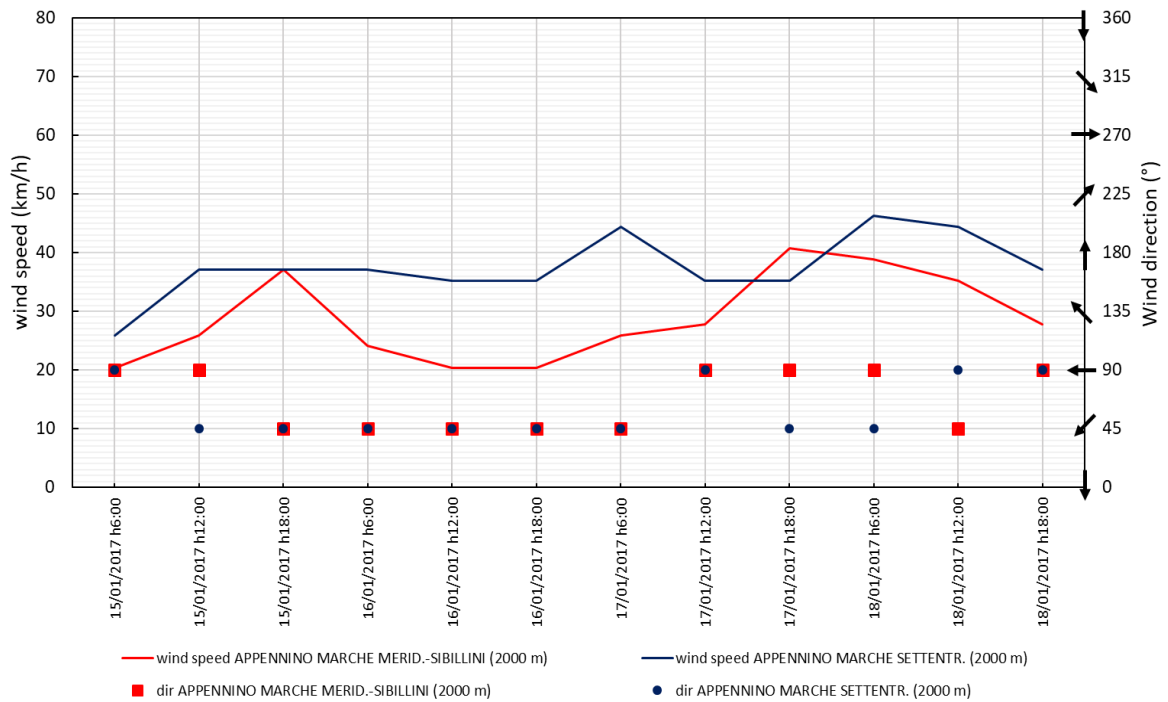


Fig. 4.9 Forecasted data for wind speed (line) and wind direction (dots) (2000 m), in the days of interest, in "Appennino Marche Settentr." and "Appennino Marche Merid.-Sibillini" subsectors.

Wind direction Legend: 0: N 45: N-E 90: E 135: S-E 180: S 225: S-W 270 W 315: N-W 360: N

Source: Graph obtained from data of Meteomont bulletins: <http://www.meteomont.gov.it/infoMeteo/caricaPaginaStorici.do>

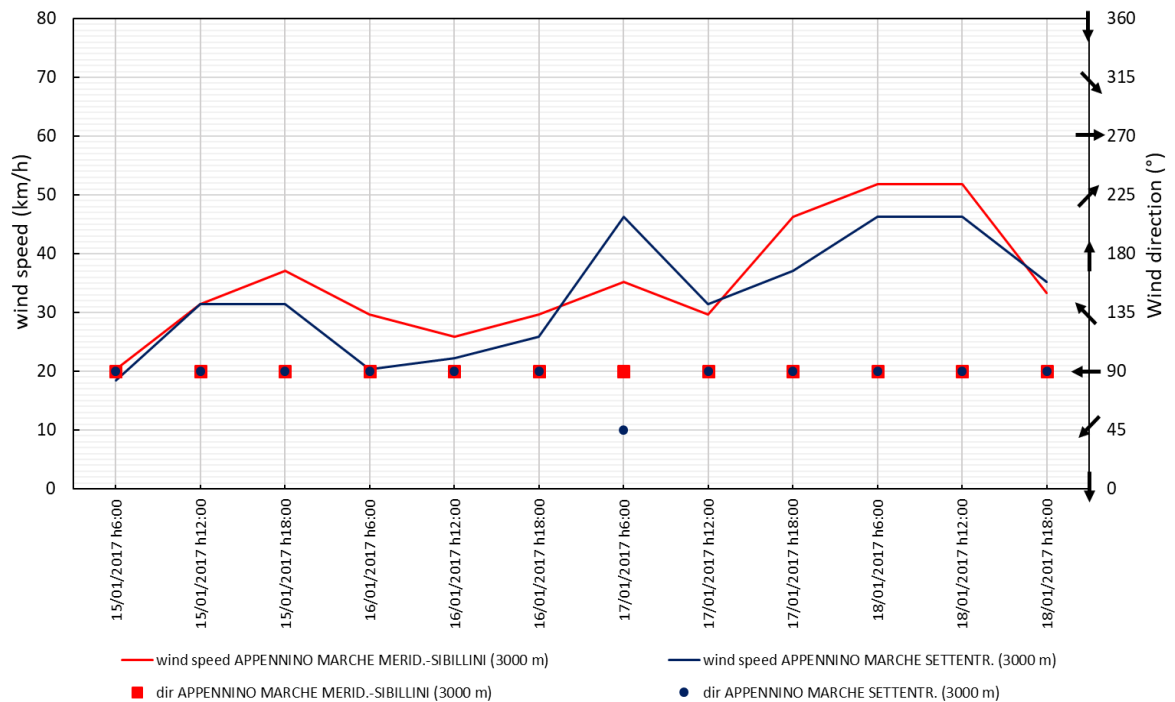


Fig. 4.10 Forecasted data for wind speed (line) and wind direction (dots) (3000 m), in the days of interest, in "Appennino Marche Settentr." and "Appennino Marche Merid.-Sibillini" subsectors

Wind direction Legend: 0: N 45: N-E 90: E 135: S-E 180: S 225: S-W 270 W 315: N-W 360: N

Source: Graph obtained from data of Meteomont bulletins: <http://www.meteomont.gov.it/infoMeteo/caricaPaginaStorici.do>

At an altitude of 1000 m (Fig. 4.8), a very different wind speed is observed in the two subsectors. The trend was found to be approximately constant, with slight variations in the "Appennino Marche Merid.-Sibillini" subsector, while it was more variable and with greater intensity (about 3 times higher) in the other subsector. Vice versa, the wind blew in both cases mainly from North-East, although in the initial phase of the day January 15th and in the final phase of the days January 17th and 18th the wind blew mainly from East. At an altitude of 2000 m (Fig. 4.9), in the "Appennino Marche Settentr." subsector, wind speeds did not change much, compared to those expected at an altitude of 1000 m. On the contrary, in the other subsector, wind speeds grew considerably, more than doubling. Excluding the end of January 15th, the entire January 16th and the beginning of January 17th, in which a prevailing wind direction (North-East), in both sectors, was found, on the other days, wind provenance varied in both sectors between North and North-East. At an altitude of 3000 m (Fig. 4.10), wind speeds were very similar in two sub-sectors and slightly higher than those expected at 2000 m. Moreover, there was a marked intensity increasing on January 18th for the "Appennino Marche Merid.-Sibillini" subsector. It was found that, at this altitude, wind, in both sectors and throughout the whole period of interest, blew mainly from East.

4.2.2 Sector 04: "Grandi Massicci Appenninici and Appennino Abruzzese"

Below is reported the description of snow conditions for "Grandi Massicci Appenninici and Appennino Abruzzese" sector in the period of interest. The following evaluations are carried out on a synoptic-regional scale.

On January 14th, 2017, the snowpack consisted of melt and freeze crusts, hard and soft, alternating with loose snow layers over moderately consolidated layers. The avalanche hazard grew in areas where wind activity redistributed the snowpack, with the formation of great accumulations. Small spontaneous surface loose snow avalanches, were observed. On January 15th, 2017, the snowpack situation was almost identical to that found the previous day. On January 16th, 2017, the snowpack was composed by fresh and dry snow layers with weak cohesion over moderately consolidated layers. The snowpack was generally moderately consolidated. On January 17th 2017, the snowpack was weakly consolidated and mostly unstable on all steep slopes: fresh and dry snow was above weakly consolidated layers. On January 18th, 2017, the snowpack situation was almost identical to that found the previous day. (summarized from Meteomont bulletins).

In this area, there are four subsectors: "Laga-Gransasso-Terminillo", "Maiella", "Appennino Centro-meridionale" and "Appennino Molisano". For these sectors, the bulletin provides snow height (line) and snow avalanches hazard data (histogram), for days of interest, reported in Fig. 4.11. It is possible to observe the increasing snow height, as well as the snow avalanches hazard level, from January 14th to 18th 2017., There was a fresh snow height increasing up to January 16th, while between January 16th and 17th there was a fresh snow thickness decreasing in all subsectors. The achieved values will remain constant even on January 18th 2017.

As previously stated, inside the daily bulletin there are forecasts regarding the two following days. Also in this case, to improve data reliability, for each daily bulletin consulted, only the forecast for the following day was considered. The forecast for the second following day is entrusted to the following bulletin. Therefore, starting from forecasted data, it is possible to understand temperature, freezing level and wind trend for days of interest. These quantities are shown below.

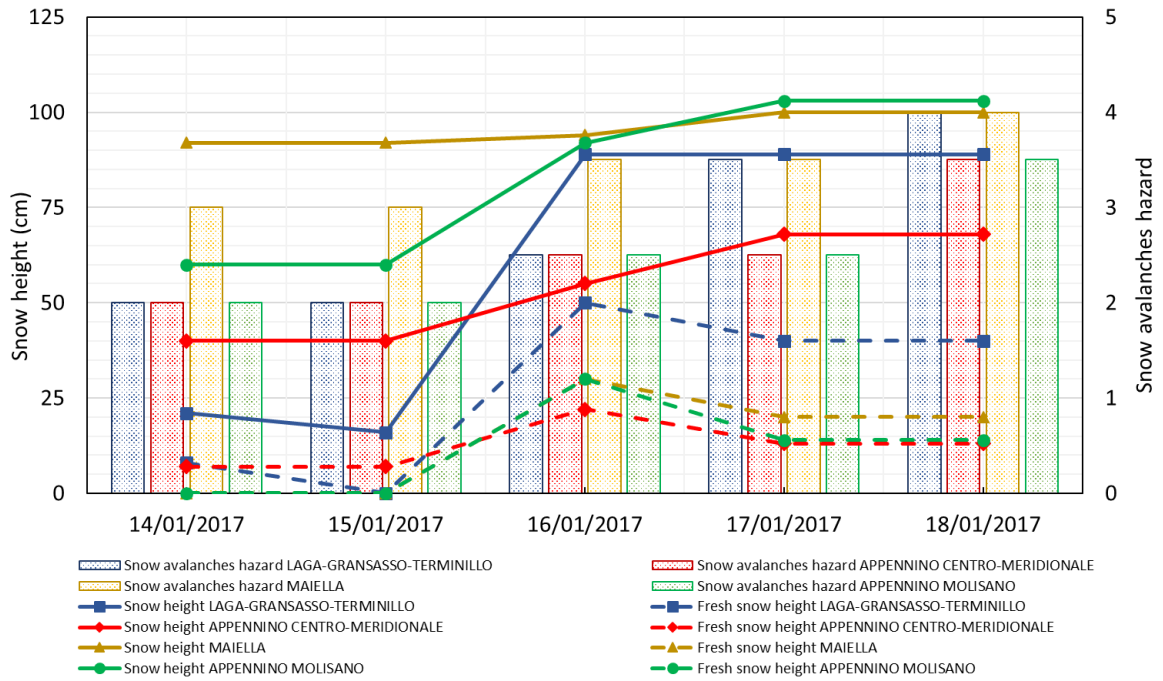


Fig. 4.11 Snow height (line) and snow avalanches hazard data (histogram), on days of interest, in “Laga-Gransasso-Terminillo”, “Maiella”, “Appennino Centro-meridionale” and “Appennino Molisano” subsectors
 European scale of avalanche hazard degree: 1- weak 2- moderate 3- marked 4- strong 5- very strong
 Source: Graph obtained from data of Meteomont bulletins: <http://www.meteomont.gov.it/infoMeteo/caricaPaginaStorici.do>

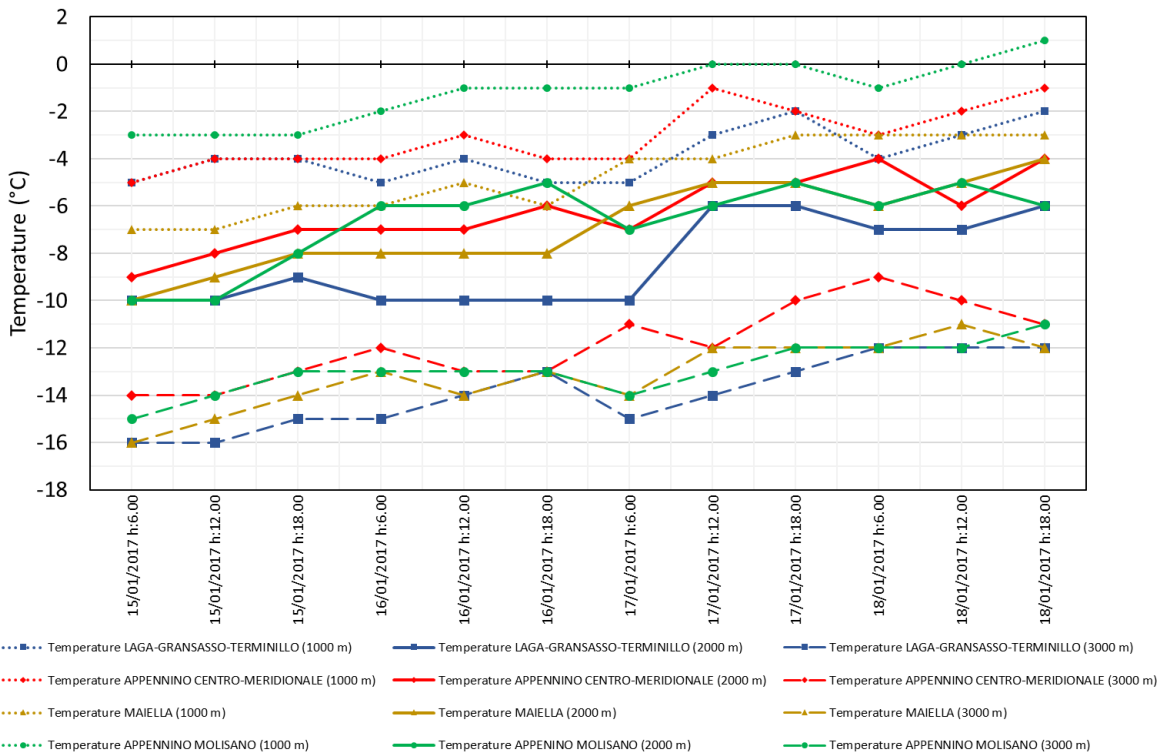


Fig. 4.12 Forecasted data for temperatures at 1000, 2000 and 3000 m, in the days of interest, in “Laga-Gransasso-Terminillo”, “Maiella”, “Appennino Centro-meridionale” and “Appennino Molisano” subsectors
 Source: Graph obtained from data of Meteomont bulletins: <http://www.meteomont.gov.it/infoMeteo/caricaPaginaStorici.do>

Fig. 4.12 shows the temperatures trend (at the altitude of 1000, 2000 and 3000 m) in the four subsectors. The overall temperature trend, at all altitudes and for all subsectors, was a gradual increasing from January 15th to 18th. Concerning the initial value, in all subsectors and at all altitudes, there was a 4-5 °C average increase during the period of interest. For all the altitudes, except for 1000 m, it was found that "Laga-Gransasso-Terminillo" subsector was the one with the lowest temperatures. At 1000 m the "Maiella" subsector had the lowest temperatures. The highest temperature values, at all altitudes, were mainly found in "Appennino Molisano" and "Appennino Centro Meridionale" subsectors.

Fig. 4.13 shows freezing level trend, in subsectors analyzed, for days of interest. The same considerations, relating to the analysis of the freezing level data of Meteomont bulletins, previously carried out for the "Appennino Umbro-Marchigiano" sector, and reported in note 1, are repeated. A similar trend was observed in considered subsectors. It is noted that lower freezing levels values were shown by "Laga-Gransasso-Terminillo" subsector while, among the remaining subsectors, no one had predominant values concerning the others. It is also observed that, except for the "Maiella" subsector, in the other cases there was a sort of periodicity, of about 12 hours, in the trend. However, on average, from January 15th to 18th, a freezing level growth was observed in all subsectors.

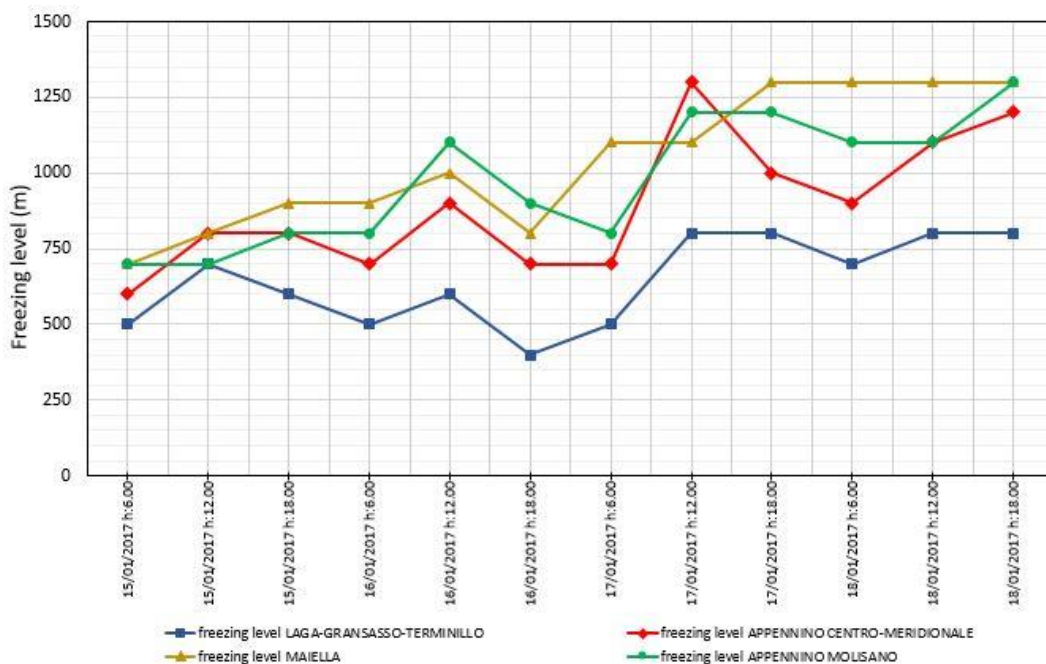


Fig. 4.13 Forecasted data for freezing level, in the days of interest, in "Laga-Gransasso-Terminillo", "Maiella", "Appennino Centro-meridionale" and "Appennino Molisano" subsectors. Source: Graph obtained from data of Meteomont bulletins: <http://www.meteomont.gov.it/infoMeteo/caricaPaginaStorici.do>

The following figures show wind speed (line) and direction (dots) data, in the investigated subsectors, for the days of interest, at altitudes of 1000, 2000 and 3000 m (Fig. 4.14, Fig. 4.15, Fig. 4.16). As already mentioned, compared to the bulletin, wind speed, expressed in knots, was converted to Km/h, while the wind direction was expressed in degrees.

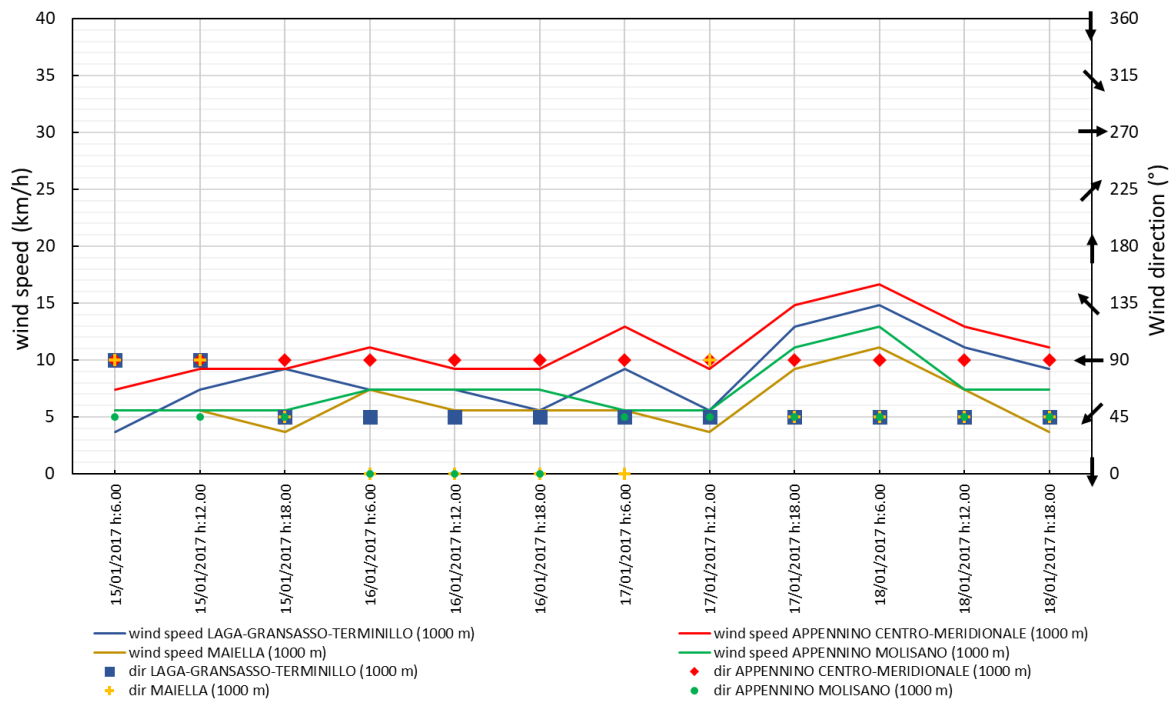


Fig. 4.14 Forecasted data for wind speed (line) and wind direction (dots) (1000 m), in the days of interest, in “Laga-Gransasso-Terminillo”, “Maiella”, “Appennino Centro-meridionale” and “Appennino Molisano” subsectors.

Wind direction Legend: 0: N 45: N-E 90: E 135: S-E 180: S 225: S-W 270 W 315: N-W 360: N

Source: Graph obtained from data of Meteomont bulletins: <http://www.meteomont.gov.it/infoMeteo/caricaPaginaStorici.do>

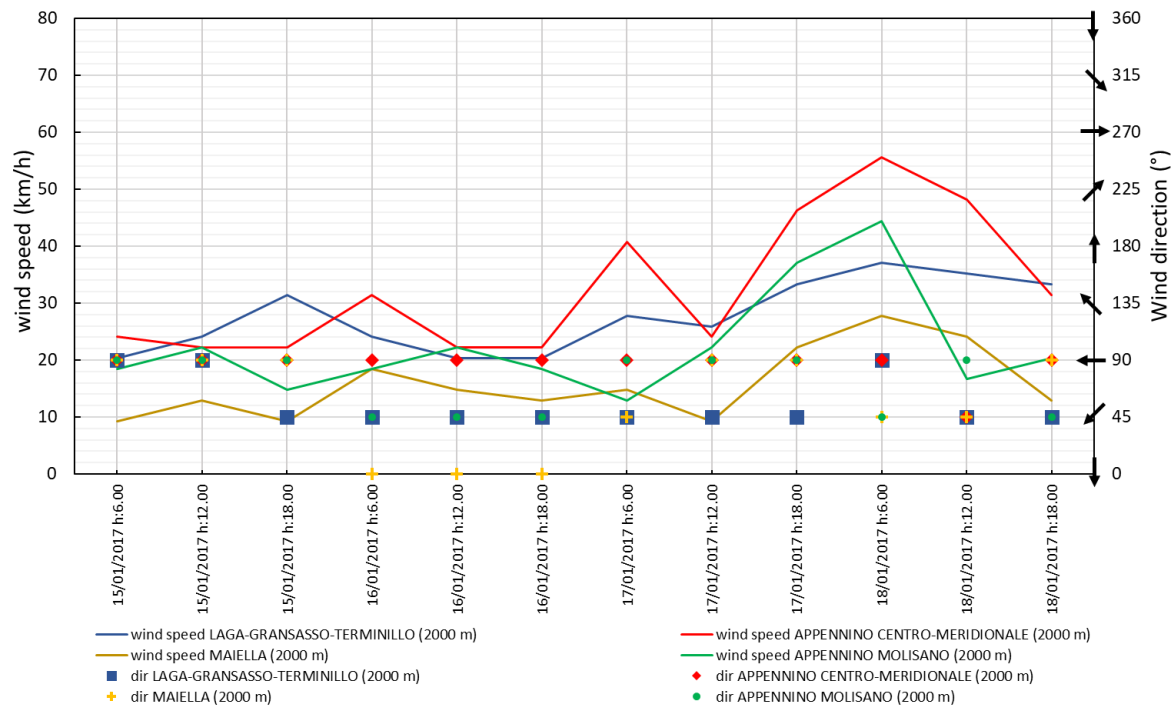


Fig. 4.15 Forecasted data for wind speed (line) and wind direction (dots) (2000 m), in the days of interest, in “Laga-Gransasso-Terminillo”, “Maiella”, “Appennino Centro-meridionale” and “Appennino Molisano” subsectors.

Wind direction Legend: 0: N 45: N-E 90: E 135: S-E 180: S 225: S-W 270 W 315: N-W 360: N

Source: Graph obtained from data of Meteomont bulletins: <http://www.meteomont.gov.it/infoMeteo/caricaPaginaStorici.do>

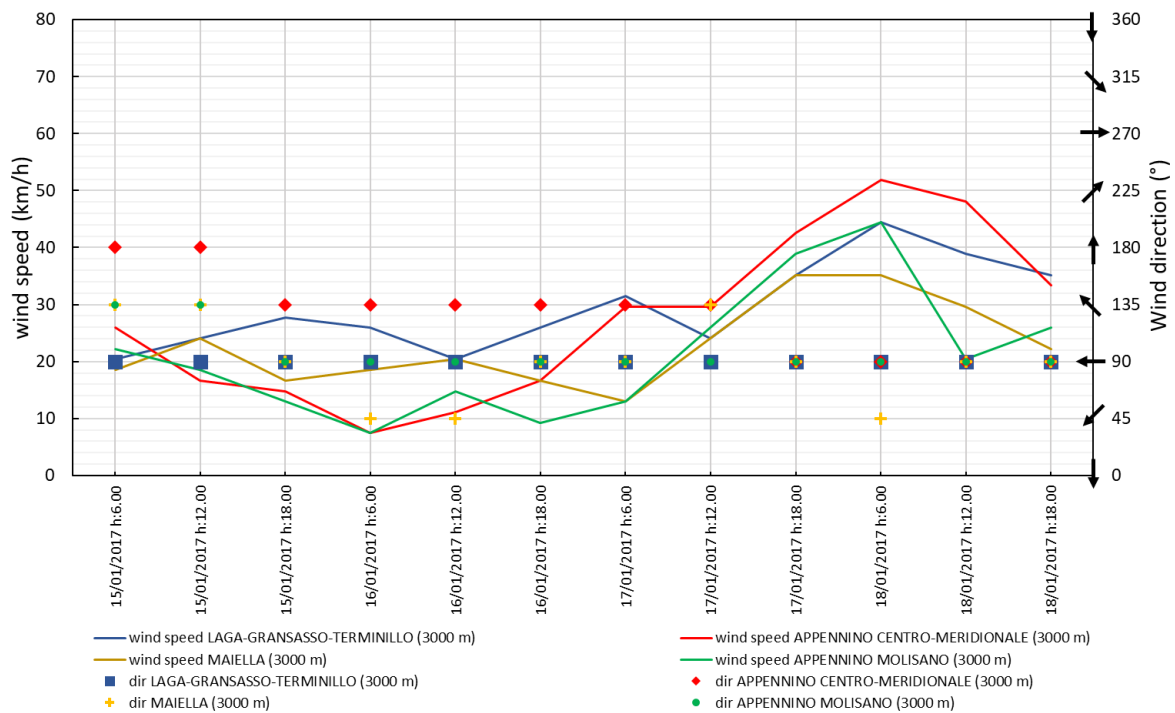


Fig. 4.16 Forecasted data for wind speed (line) and wind direction (dots) (3000 m), in the days of interest, in "Laga-Gransasso-Terminillo", "Maiella", "Appennino Centro-meridionale" and "Appennino Molisano" subsectors. Wind direction Legend: 0: N 45: N-E 90: E 135: S-E 180: S 225: S-W 270 W 315: N-W 360: N Source: Graph obtained from data of Meteomont bulletins: <http://www.meteomont.gov.it/infoMeteo/caricaPaginaStorici.do>

At an altitude of 1000 m (Fig. 4.14), in the investigated areas, wind speeds were very similar to each other. The highest values were found in the "Appennino Centro Meridionale" subsector, while the smaller ones were found in the "Maiella" sub-sector. There was a visible wind speed increasing in all sub-sectors between January 17th and 18th, followed by a rapid decreasing at the end of the last day. Throughout the whole period, the "Appennino Centro Meridionale" subsector presented a wind that blew mainly from East, while in the "Laga-Gransasso-Terminillo" subsector the wind blew mainly from the North-East. In the remaining two subsectors, it changed direction roughly every day and, in both sectors, on January 16th and 18th, the wind blew northward and north-east respectively. At an altitude of 2000 m (Fig. 4.15), there was a wind speed trend similar to that already seen above. In the "Laga-Gransasso-Terminillo", "Appennino Centro Meridionale" and "Maiella" subsectors continuous speed increases and decreases were observed throughout the whole period. The trends were in phase. On the contrary, in the "Appennino Molisano" subsector, the trend was in phase opposition, except on the day January 18th in which there was a sudden increase. In the "Appennino Centro Meridionale" subsector the wind blew mainly from East, while in "Laga-Gransasso-Terminillo" subsector it blew mainly from North-East. In the other subsectors, daily, there were continuous changes in wind direction. At an altitude of 3000 m (Fig. 4.16), The same trend was observed in all the subsectors: moderate or low intensity up to h:12.00 on January 17th, from which there was a sudden speed increasing. It was followed by a rapid speed decreasing at the end of January 18th. In the "Appennino Centro Meridionale" subsector a prevalent wind direction, from South-East, up to January 16th was recorded; subsequently, the prevailing direction was East. The latter was the main direction, in the other sectors, during the entire period of interest.

4.2.3 Cumulated snow precipitation

In addition to data retrieved from bulletins, it was possible to consult the fresh snow cumulative values, for the period January 15th to 18th, 2017, and for regions of interest (courtesy of Ph.D. Igor Chiambretti). It is emphasized that in Meteomont bulletins, in addition to the previously reported information, there are data of snow height, cumulative snow in 24 h and minimum and maximum temperature recorded in some stations. These data are fundamental because they are real data and not forecasted data. The main problem is that, in the period considered, stations with available data are not always the same and, moreover, they are very thinned away on the territory. Such data can be useful at the local scale, but they are virtually unusable on a regional scale. Given the lack of data availability in many stations, the cumulative values were calculated thanks to the application of a meteorological model (Moloch) and compared with NASA satellite images (Chiambretti et al., 2018). These values have been reported in Fig. 4.17. During the considered period, the average cumulative values, at 1500 m, were between 150 and over 300 cm on the Adriatic slopes and around 100-150 cm on the Tyrrhenian slopes. Locally, the cumulative values were higher, also reaching 500 cm. (Chiambretti et al., 2018).

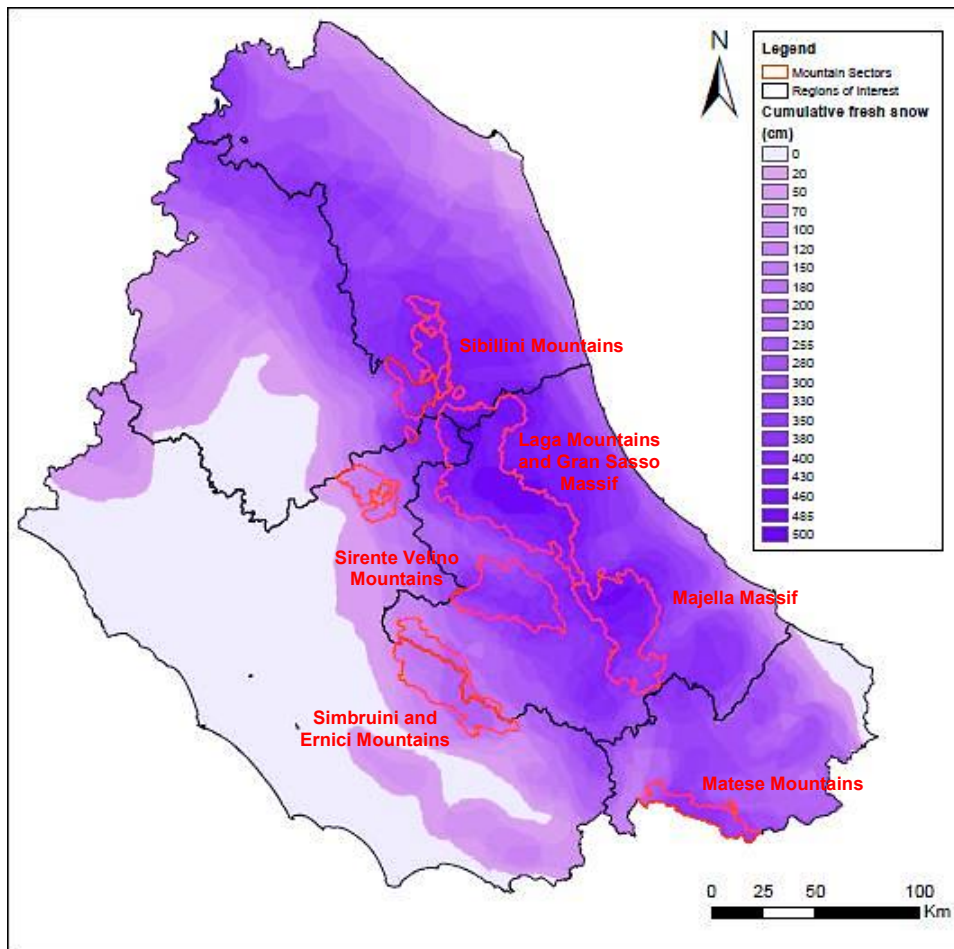


Fig. 4.17 Fresh snow cumulated values [cm] for the period January 15th-18th 2017 in regions of interest and indication of main mountain sectors. Data derived from Moloch model and compared with NASA satellite images. Source: Image obtained from cumulative precipitation raster data (courtesy of Ph.D. Igor Chiambretti) and cut out for regions of interest.

To better understand how the perturbation developed, the cumulative snow height frequency values were calculated for the main mountain sectors affected by the snow avalanches. The mountain sectors considered are Gran Sasso Massif and Laga Mountains, Majella Massif, Matese Mountains, Sibillini Mountains, Simbruini and Ernici Mountains and Sirente Velino Mountains. To identify different mountain sectors the SIC-ZPS official catalog, reported by Geoportale Nazionale, was used. Frequency graphs of cumulative snow height, calculated for previous mountain sectors, are shown in Fig. 4.18. For comparing the distributions obtained, for each of them a boxplot has been created and compared to all the others. The comparison between the different boxplots is shown in Fig. 4.19.

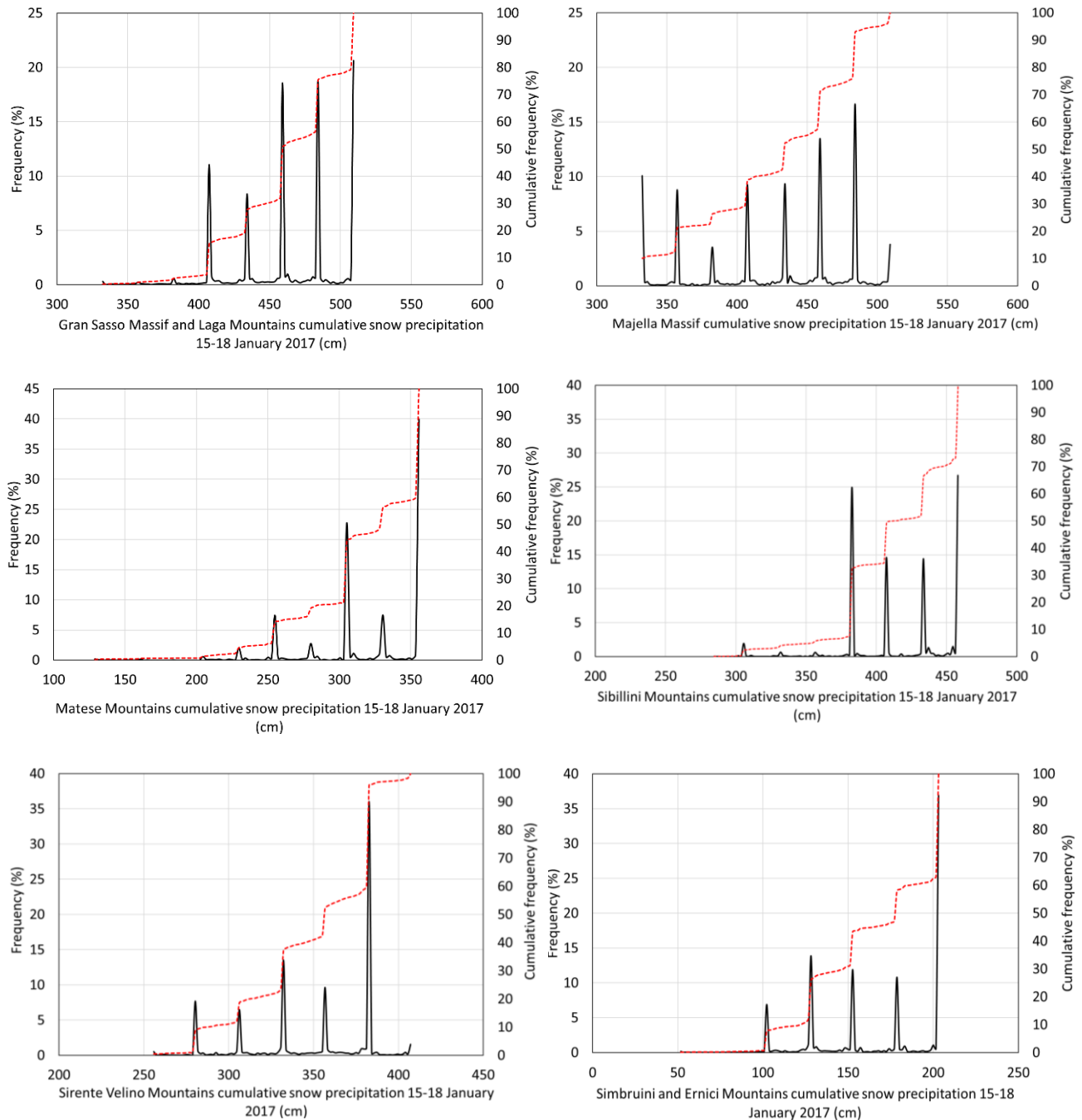


Fig. 4.18 Frequency graphs of cumulative snow height calculated for main mountain sectors affected by snow avalanches

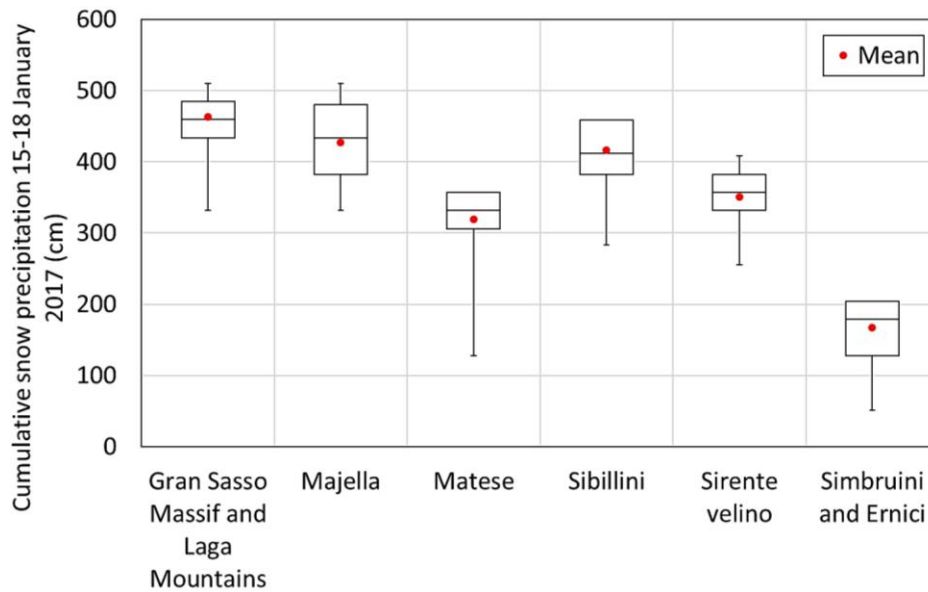


Fig. 4.19 Cumulative snow height boxplot (minimum, 1st quartile, median, 3rd quartile, maximum and mean) for main mountain sectors affected by the avalanche phenomena

It is observed that the mountainous areas mainly affected by the perturbation are Laga Mountains, Gran Sasso and Majella Massifs. In these sectors the average cumulative value is between 400 and 500 cm, but the maximum values also exceed 500 cm. The minimum values are just under 350 cm. Sibillini follows: in this case, the average cumulative value is located just above 400 cm. The maxima in this area are more contained, but still between 400 and 500 cm. In all these sectors, most of the cells present very high cumulative values and this can be considered as the main reason for which in these sectors the highest concentration of avalanches was found. To this, the predisposing conditions such as slopes, exposure and curvature of these areas must be added. These factors will be taken into consideration subsequently for the characterization of snow avalanches release areas. In this study also the earthquake will be investigated as a possible cause of snow avalanches release. In Matese and Sirente Velino Mountains, there are still high values of cumulative snow height, but still lower than sectors already listed. In the Matese Mountains the maximum values are just above 350 cm, while the minimum values fall to about 130 cm. In Sirente Velino the maximum and minimum values are higher, and the average value is around 350 cm. Finally, there is the Simbruini and Ernici mountain sector where the lowest cumulative values were found, in fact, the cumulative snow height values are between 50 and 200 cm. In these last 3 sectors also snow avalanches were less frequent. Overall, it is observed that the mountain areas most affected by the perturbation are the eastern ones. This aspect will be deepened in the characterization of release areas. For the mountain sectors most affected by snow avalanches, the release areas will be characterized from the meteorological point of view considering both the Adriatic side and the Tyrrhenian side. We proceeded in this way to understand if the snow deposition has mainly affected a certain mountain sector side and, if so, we will try to research the reason.

Before characterizing release areas, it is necessary to perform the geomorphological analysis for the study area by calculating different topographic attributes. Subsequently, it will be possible to extract obtained values exclusively for release areas. In this way, it will be possible to proceed to the statistical characterization for these areas. These aspects will be deepened after.

4.3 Geomorphological analysis²

4.3.1 DEM: SRTM (Shuttle Radar Topography Mission)

DEM (Digital Elevation Model) can be considered as a statistical surface that estimates the altitude value at a point starting from measured data, obtained with a repetitive and regular pattern, and only in some equidistant points. Generally, DEM is a raster product in which each cell is characterized by 3 coordinates: two spatial coordinates and one coordinate indicating altitude value. DEM represents the trend of the Earth's surface elevation including the natural elements and the human-made artifacts. DEM obtained from SRTM (Shuttle Radar Topography Mission) was used in this study. In particular, NASA Version 3.0 SRTM³ (SRTM Plus), with 30 m resolution, was used. This data was obtained thanks to the collaboration of various international space agencies, using the radar interferometry method. Topographic data from other sources were used to fill the gaps ("voids") in earlier versions of SRTM data (The SRTM Collection User Guide, 2015). The altitude values are obtained starting from the phase difference between signals sent by satellite and signals returning to the aerial platform, which depend on the distance to the ground. Subsequently, the database must be completed by filling "voids" with processing data carried out on other DEMs. This last operation, consisting of shifting, resampling and interpolating data, can introduce artifacts in some topographic features (The SRTM Collection User Guide, 2015). It is possible to observe the presence of such artifacts, for example, in the extract of the slope raster, reported in Fig. 4.20, and obtained starting from SRTM DEM. Anyway, an accurate description of the SRTM version 3.0 processing can be found in The SRTM Collection User Guide (2015), while radar interferometry is explained in Rosen and others (2000) (The SRTM Collection User Guide, 2015).

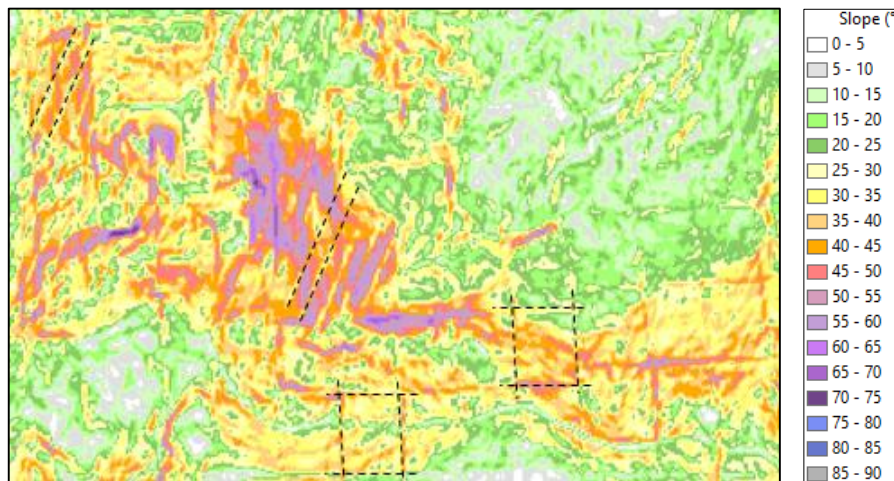


Fig. 4.20 Slope raster extract. Some artifacts produced starting from the SRTM DEM are highlighted with treated lines.

In this case, slope values obtained along these artefacts do not represent the true slope values of the topographic surface. Consequently, the final result presents the background noise. It is possible to use some filtering techniques to improve the shape of the surface, even if the background noise will always be present (Wilson

² All geomorphological analysis rasters were obtained with SAGA GIS Tools and using a Kernel of 3x3 (cell unit). Geomorphological structures greater than this window couldn't be correctly classified. Used kernel was dimensioned according to the average size of structures of interest.

³ It was decided to use the SRTM DEM since the open source data available for the entire national territory present inferior quality. Furthermore, it would be difficult to combine DEM data from different regions because they are obtained with different resolutions and methods.

and Gallant, 2000). In this case, no filtering techniques were used. The quality of DEM must be evaluated about the use that must be made of it. In this case it was considered that, for a regional-scale analysis, the DEM SRTM could be used without being filtered, but carrying out the common preprocessing operations. Firstly, appropriate corrections were made so that SRTM DEM nodes were arranged in system units and therefore at a constant distance (meters), rather than at constant angles (degrees). Subsequently, the Wang & Liu algorithm was used to identify and fill the depressions of the DEM surface. This is accomplished by preserving a minimum slope (and thus elevation difference) between cells (SAGA-GIS Module Library Documentation). In this case, a minimum slope gradient of 0.1 was maintained. The method basically consists of raising the height of some cells to a minimum value that can guarantee the flow in the adjacent cells. This operation is performed to eliminate errors in the DEM, for example when a cell is surrounded by adjacent cells with higher altitude values or when a cell presents negative values. Below, in Fig. 4.21, the difference between the FILLED DEM, obtained after the application of the Wang & Liu algorithm, and the raw SRTM DEM is reported.

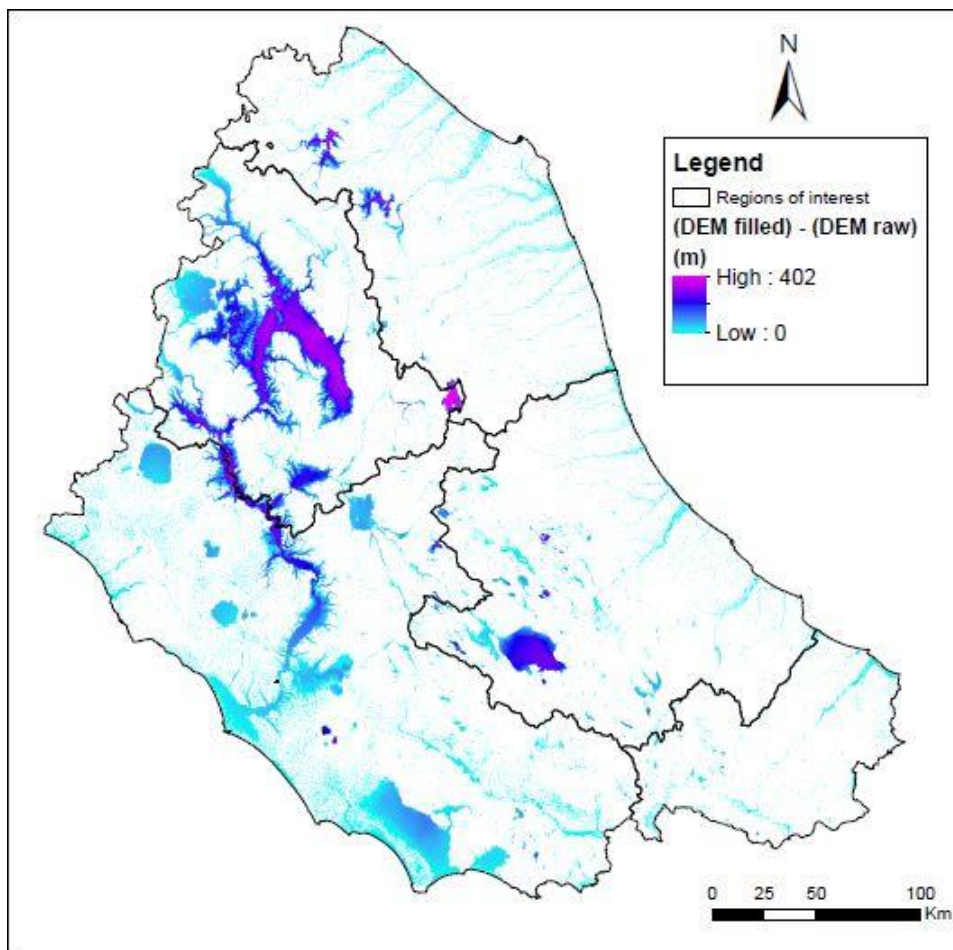


Fig. 4.21 Difference between the FILLED DEM, obtained after the application of the Wang & Liu algorithm, and the raw SRTM DEM

After completion of the SRTM DEM preprocessing procedure, the DEM portion of interest was identified. In this regard, note the perimeter of avalanches occurred in the Apennines in 2017, it was decided to apply an altitude filter equal to 500 m. Therefore, only the areas above this altimetric threshold were considered. In this way, the input DEM to perform the geomorphological analysis was obtained, and it is reported in **Attached 1**.

Elevation frequency graph for the input DEM, used to perform the geomorphological analysis, is reported in Fig. 4.22. It is possible to observe that the median falls around 840 m, so 50% of the cells have values between 500 and 840 m, while the remaining 50% have values between 840 and 2914 m. Moreover, about 65% of the cells have values below 1000 m, another 33% have values between 1000 and 2000 m, while the remaining 2% have values above 2000 m. The average height of the whole area is around 950 m.

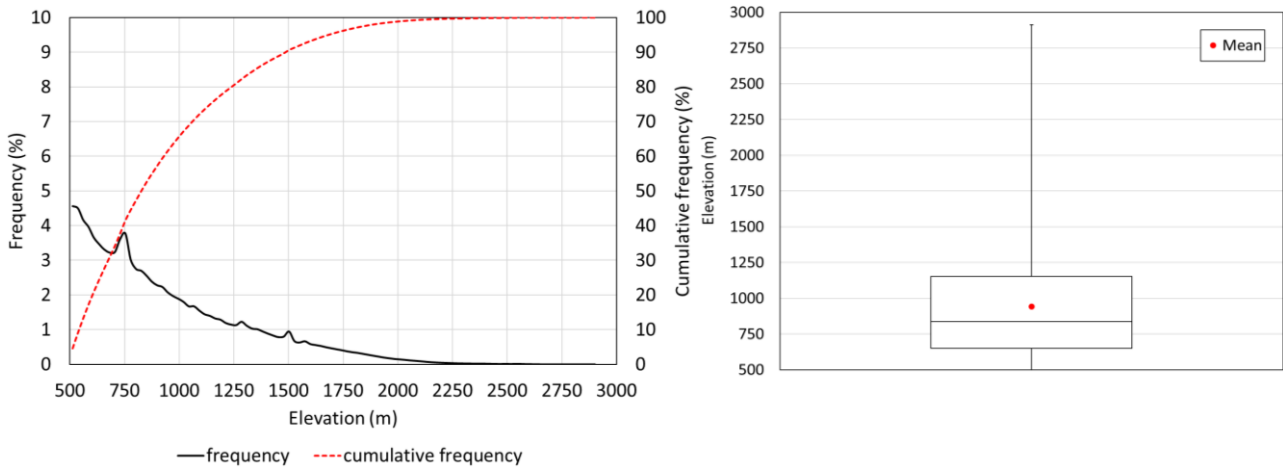


Fig. 4.22 Frequency values of input DEM, used to perform the geomorphological analysis, and relative boxplot (minimum, 1st quartile, median, 3rd quartile, maximum and mean)

4.3.2 Slope

Slope measures the rate of change of elevation in the direction of steepest descent (Wilson and Gallant, 2000). Substantially, it consists in a plane tangent to a specific point of the surface whose angle can be calculated concerning the horizontal: it is, therefore, the first derivative of the surface in the steepest direction. The slope can be calculated with different methods. In this study, the Zevenbergen and Thorne (1987) and Horn (1981) methods were used. Typically, the Zevenbergen and Thorne algorithm works well for low-resolution data and very large areas, while the Horn algorithm works well for medium resolution areas and articulated morphology. For calculating slope, the following formula is used:

$$Slope_{deg} = \text{atan} \left(\sqrt{\left(\frac{\delta z}{\delta x}\right)^2 + \left(\frac{\delta z}{\delta y}\right)^2} \right) \quad (33)$$

Depending on the algorithm used, the long x and long y gradients are calculated differently. About Fig. 4.23, to obtain slope in "e" cell, the Zevenbergen and Thorne (1987) algorithm uses only the 4 DEM cells along the cardinal directions (cells b, d, h, f) and gradients assume the following expressions:

$$G = \frac{\delta z}{\delta x} = \frac{f - d}{2 \cdot \Delta x} \quad H = \frac{\delta z}{\delta y} = \frac{b - h}{2 \cdot \Delta y} \quad (34)$$

In Zevenbergen and Thorne algorithm, the two gradients reported in equation (34) correspond to the parameters G and H of an equation, reported below, describing a surface that passes precisely through the altitude values of the 9 cells considered for the calculation.

$$Z = Ax^2y^2 + Bx^2y + Cxy^2 + Dx^2 + Ey^2 + Fxy + Gx + Hy + I \quad (35)$$

These parameters can be obtained from the 9 cells elevation data through Lagrange polynomials (Zevenbergen and Thorne, 1987). The Horn algorithm (1981), instead, always about Fig. 4.23, uses all 8 DEM cells adjacent to the cell "e" (a, b, c, d, f, g, h, i cells), but with a different weight: 2 for cardinal cells and 1 for diagonal cells. Consequently, gradients are expressed as follows:

$$\frac{\delta z}{\delta x} = \frac{(c + 2f + i) - (a + 2d + g)}{8 \cdot \Delta x} \qquad \frac{\delta z}{\delta y} = \frac{(a + 2b + c) - (g + 2h + i)}{8 \cdot \Delta y} \quad (36)$$

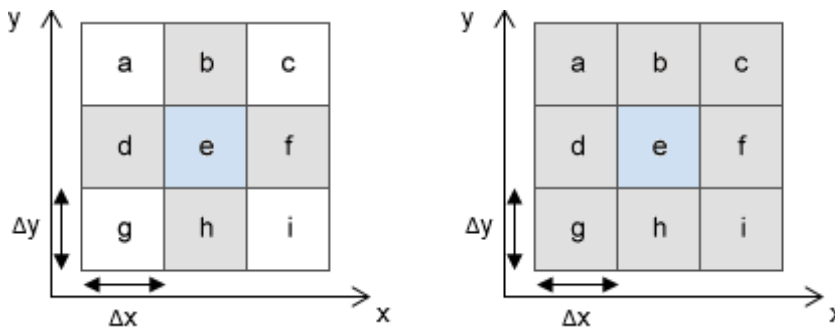


Fig. 4.23 3x3 Kernel for the slope calculation in the "e" cell; Δx and Δy are the pixel raster dimension. On the left, grey color indicates cells used in Zevenbergen and Thorne algorithm. On the right, grey color indicates cells used in Horn algorithm. Modified after. Source: <http://desktop.arcgis.com/en/arcmap/10.3/tools/spatial-analyst-toolbox/how-slope-works.htm>

In Fig. 4.24 are shown the frequency values obtained from slope rasters difference. It is possible to observe that about 70% of the values obtained from the difference is equal to 0. Therefore, the two algorithms provide, in most cases, a substantially equal slope value. Moreover, the distribution has a slight asymmetry whereby the Zevenbergen and Thorne algorithm returned higher slope values than Horn in about 20% of the total cells, while the Horn algorithm returned higher values

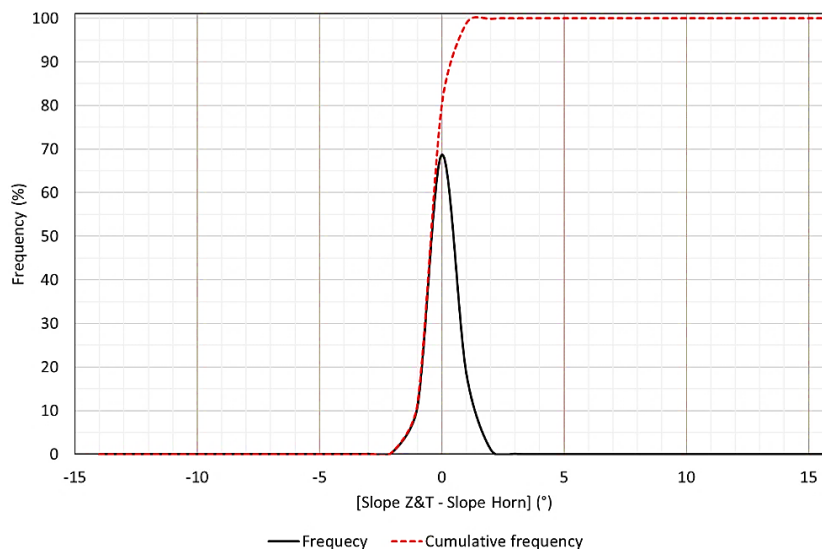


Fig. 4.24 Frequency values of slope rasters difference (Slope Z&T – Slope Horn)

than Z&T in about 10% of the total cells. However, more than 99% of the cells have a slope variation of less than or equal to 2 degrees; only 0.3% of the cells have higher variations which do not exceed 16 degrees. Given the limited difference obtained from the application of the two algorithms, it was decided to continue the geomorphological analysis, calculating slope dependence parameters, using slope obtained with Zevenbergen and Thorne method. Slope frequency graph, obtained with the Zevenbergen and Thorne and Horn methods, is reported in Fig. 4.25. This graph further highlights the minimum difference between values obtained with the two algorithms. From such information it is possible to understand the acclivity of the considered area. The slope range starts from 0° up to 69°. About 12% of total cells have a slope between 30° and 60°: this range is conventionally identified as the one in which it is possible to find snow avalanches release areas. Almost 90% of the cells have slope values lower than 30°, and only 0.1% have values higher than 60°. Slope raster obtained by the application of Z&T algorithm is reported in **Attached 1**.

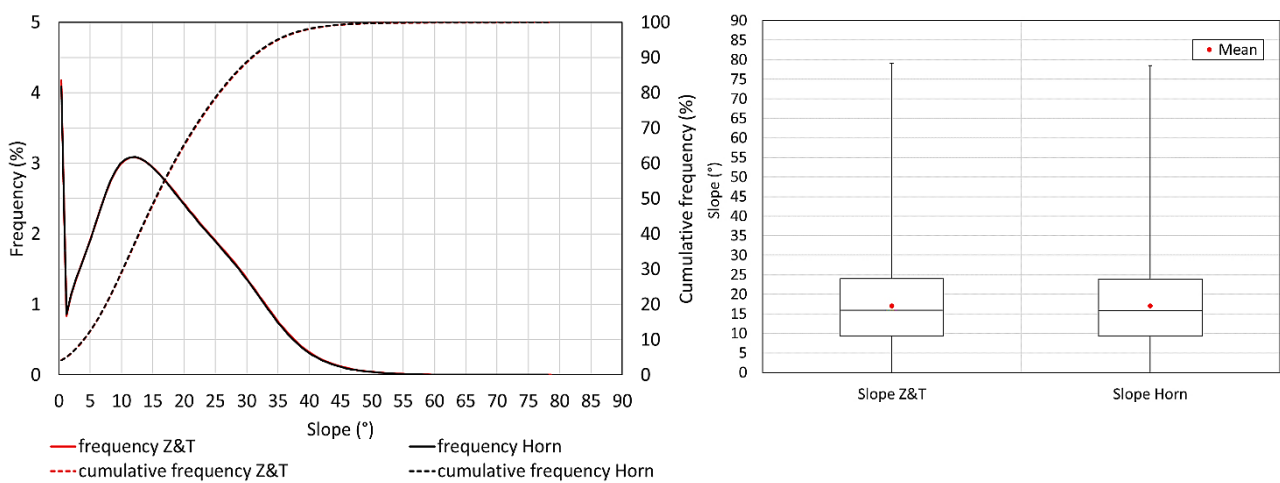


Fig. 4.25 Frequency values. of Slope Z&T and Slope Horn rasters and relative boxplots (minimum, 1st quartile, median, 3rd quartile, maximum and mean)

4.3.3 Aspect

Aspect is the orientation of the line of steepest descent, and it is usually measured in degrees clockwise from North (Wilson and Gallant, 2000). Aspect is therefore substantially the direction, respect to North, in which the slope is calculated. Therefore, depending on the method used for calculating slope, change the method used for calculating aspect. For this last calculation, the following formula is used:

$$\theta = \arctan \left(\frac{-\frac{\delta z}{\delta y}}{-\frac{\delta z}{\delta x}} \right) \quad (37)$$

The signs of the numerator and denominator of equation (37) determine in which quadrant θ lies. Depending on the algorithm used, also in this case, the long x and long y gradients are calculated differently. If the Zevenbergen and Thorne method was used for the slope calculation, then gradients are calculated as in equations (34). If the Horn method was used for the slope calculation, then gradients are calculated as in equations (36). In both cases, expressions refer to

Fig. 4.23. In Fig. 4.26 are shown the frequency cells values obtained from aspect rasters difference. It is possible to observe that about 30% of the values, obtained from the difference, is equal to 0; therefore, in these cells the two algorithms provide an equal aspect value. In any case, more than 98% of cells have variations in aspect smaller than or equal to 10 degrees. This variation does not bring substantial changes to the aspect value. About 1.5% of the cells, on the other hand, exhibit variations in aspect above 10 degrees. Overall, the results obtained have a good matching despite having been calculated with different algorithms. Aspect raster obtained by the application of Z&T algorithm is reported in **Attached 1**.

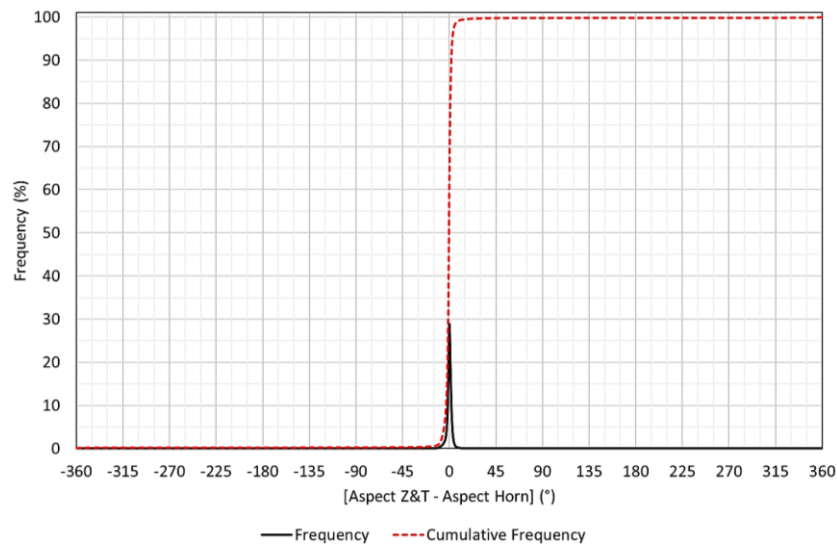


Fig. 4.26 Frequency values of aspect rasters difference (Aspect Z&T – Aspect Horn)

Aspect frequency graph, obtained with the Zevenbergen and Thorne and Horn methods, is reported in Fig. 4.27. From this graph it is possible to understand how, even for the aspect, the values obtained with the two algorithms are absolutely comparable. In particular, from the cumulative frequency values, it is observed that there is no preponderant exposure value. This is also because the survey scale is vast. A minimum prevalence is found for values between 180° and 270°, presented in about 27% of the cells. In the other quadrants the percentages found vary between 20 and 25% of the total cells.

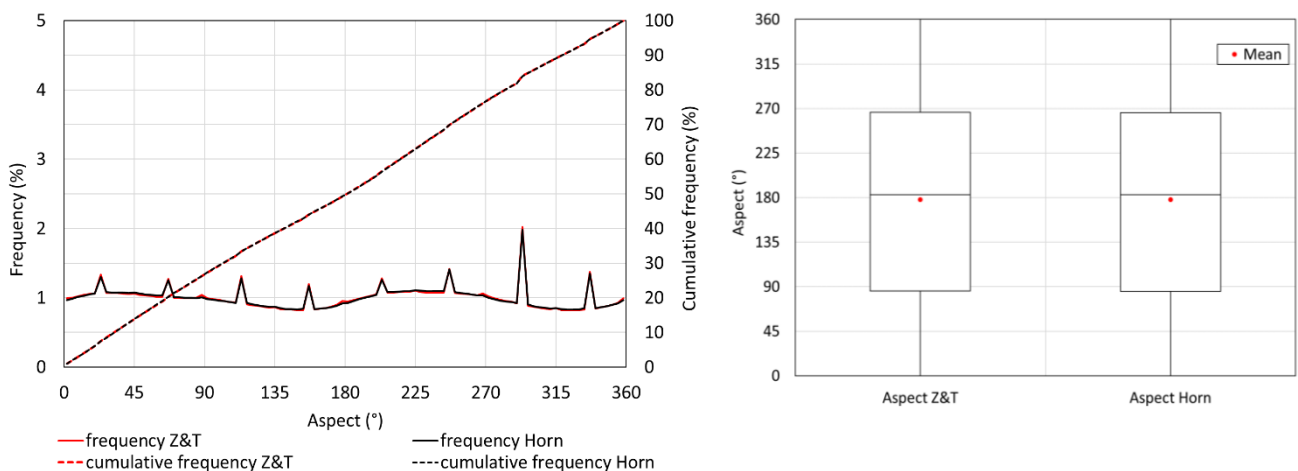


Fig. 4.27 Frequency values of aspect Z&T and aspect Horn rasters and relative boxplots (minimum, 1st quartile, median, 3rd quartile, maximum and mean)

4.3.4 Curvature

Curvature attributes are based on second derivatives and they consist in the rate of change of a first derivative such a slope or aspect, usually in a particular direction (Wilson and Gallant, 2000). Consequently, for every cell and in any direction, the curvature is calculated as the second derivative of Z , expressed in equation (35) (Zevenbergen and Thorne, 1987). Curvature was calculated using the Zevenbergen and Thorne method which defines it as follows:

$$Curvature = \frac{\delta^2 Z}{\delta S^2} = 2(D \cos^2 \varphi + E \sin^2 \varphi + F \cos \varphi \sin \varphi) \quad (38)$$

Where S is in the aspect direction (θ), φ represents the generic direction and D, E, F are the parameters of the equation (35). As mentioned above, they can be obtained from the 9 cells elevation data, through Lagrange polynomials (Zevenbergen and Thorne, 1987), assuming the following values (in relation to Fig. 4.23):

$$\Delta x = \Delta y = L, \quad D = \left[\frac{\frac{d+f}{2} - e}{L^2} \right], \quad E = \left[\frac{\frac{b+h}{2} - e}{L^2} \right], \quad F = \left[\frac{-a+c+g-i}{4L^2} \right] \quad (39)$$

The two main directions in which the curvature is calculated are the direction of aspect ($\varphi = \theta$), returning the value of profile curvature, and the direction perpendicular to that of aspect ($\varphi = \theta + \frac{\pi}{2}$), returning the value of plan curvature (Zevenbergen and Thorne, 1987). It is important to study these two types of curvature since the profile curvature provides indications on the accelerations or decelerations of the gravitational flow, while the plan curvature provides indications on the convergence or divergence of this flow (Curvature function- Help | ArcGIS for Desktop). Profile and Plan curvature are then calculated as follows:

$$PROFC = -2(D \cos^2 \theta + E \sin^2 \theta + F \cos \theta \sin \theta) = \frac{-2(DG^2 + EH^2 + FGH)}{(G^2 + H^2)} \quad (40)$$

$$PLANC = 2(D \sin^2 \theta + E \cos^2 \theta - F \sin \theta \cos \theta) = \frac{2(DH^2 + EG^2 - FGH)}{(G^2 + H^2)} \quad (41)$$

Where G and H are defined in equation (34), while D, E, F are defined in equation (39). Obviously, equations (38), (40) and (41) are directional derivatives and do not provide the true curvature value. The mathematical definition of curvature (expressed in radians / m, where [m] indicates the unit of measurement of altitude) is a function of both the first derivatives and the second derivatives, as shown below (Zevenbergen and Thorne, 1987):

$$K = \frac{\left(\frac{\delta^2 Z}{\delta S^2} \right)}{\left\{ 1 + \left(\frac{\delta Z}{\delta S} \right)^2 \right\}^{\frac{3}{2}}} \quad (42)$$

After having expressed curvature in the conventional dimension, since it generally has small values, it is good to multiply the equations used for the calculation by a factor equal to 10^2 . In this way, the unit of measurement of the curvature is 1/100 m (Zevenbergen and Thorne, 1987). Curvature rasters obtained by the application of previous calculations are reported in **Attached 1**.

Subsequently, the conventions used to define the concavity or convexity of the cells in which the curvature is calculated are described. For the profile curvature, a positive value indicates that the surface is upwardly convex at that cell, a negative value indicates that the surface is upwardly concave at that cell, while a value of zero indicates that the surface is linear (Curvature function- Help | ArcGIS for Desktop adapted). For the plan curvature, a positive value indicates the surface is laterally convex at that cell, a negative value indicates the surface is laterally concave at that cell, while a value of zero indicates the surface is linear (Curvature function- Help | ArcGIS for Desktop adapted). Below is shown in Fig. 4.28 a schematization of the conventions used.

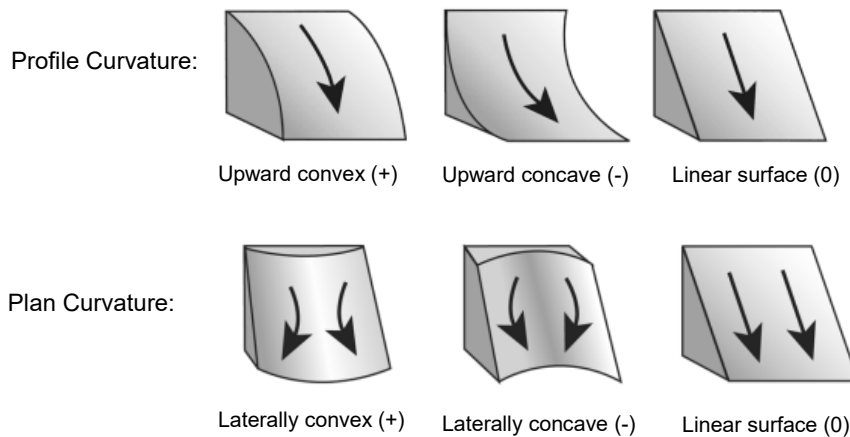


Fig. 4.28 Schematization of the conventions used for profile and planar curvature calculation. Modified after. Source: <http://desktop.arcgis.com/en/arcmap/10.3/manage-data/raster-and-images/curvature-function.htm>

Planar and profile curvature frequency graph, obtained with Zevenbergen and Thorne method, is reported in Fig. 4.29. Frequency distribution of Plan curvature values is substantially symmetrical to 0. Therefore, this means that concave and convex structures are present in equal quantities in the perpendicular direction of steepest descent. On the contrary, the frequency distribution of profile curvature values is slightly asymmetrical, and about 70% of total cells has a negative value. Therefore, this means that concave structures are higher than convex ones in the direction of steepest descent.

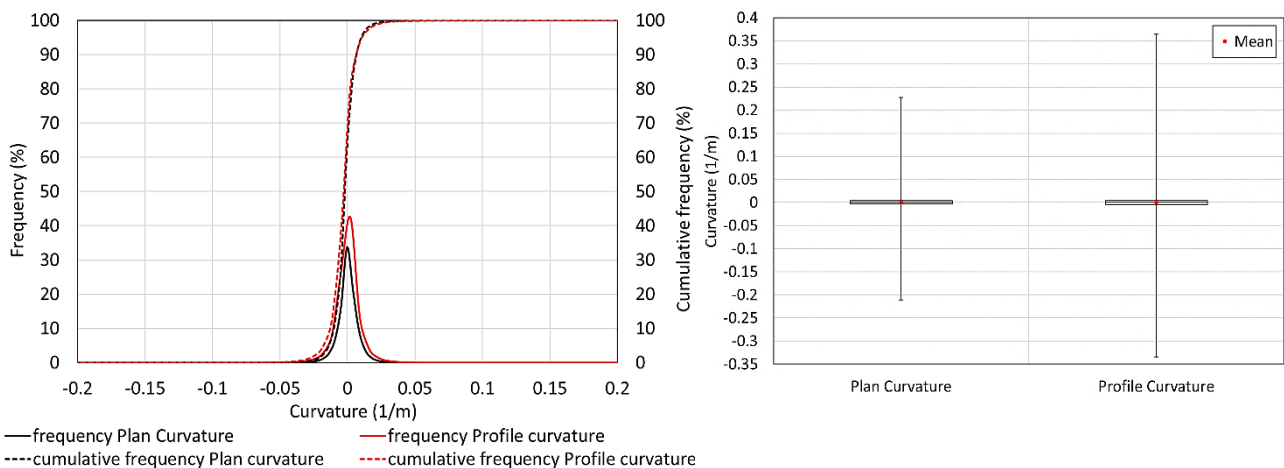


Fig. 4.29 Frequency values of profile and plan curvature rasters obtained with Zevenbergen and Thorne method and relative boxplots (minimum, 1st quartile, median, 3rd quartile, maximum and mean)

4.3.5 Curvature classification (Dikau, 1989)

From the curvatures, it is possible to obtain a geomorphometric classification of the slope shapes. Many authors have proposed classification criteria, but Dikau's (1989) approach is the most used. It is based, for slopes, on 9 basic shapes obtained from the combination of the profile and planar curvature. There are also 6 basic forms evaluated by the combination of maximum and minimum curvature in the flat areas, but in this study flat areas have not been classified. In Fig. 4.30 a) the exemplary diagram of the forms classified by Dikau (1989) for the slopes is shown. Extracts of plan and profile curvature rasters, for the same area, from which Dikau's classification is obtained, are reported below in Fig. 4.30 b). Negative values represent concave structures, while positive ones represent convex structures.

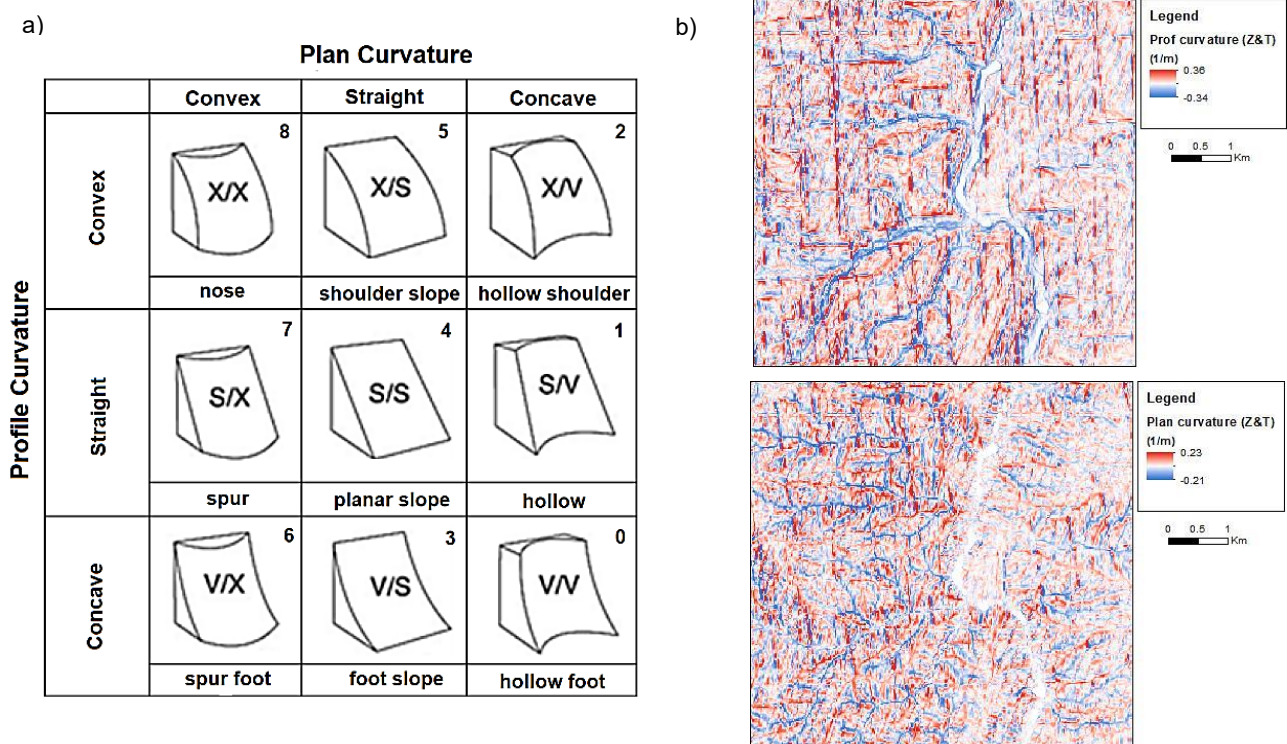


Fig. 4.30 a) Diagram of the forms classified by Dikau (1989) for the slopes. b) Extracts of profile and plan curvature rasters Modified after. Source: <https://pdfs.semanticscholar.org/8ce2/6a7a1f003d5e032155292d6eb4b62f8fee21.pdf> pag.5

Each form is identified by two letters separated by a "/". The first letter refers to the profile curvature, while the second letter refers to the plan curvature. The possible letters are X, S, V which respectively mean convex, concave and planar. In Fig. 4.30 a), the number at the top right of each quadrant represents the value that the algorithm attributes to the cells that present that particular geomorphometric shape. Curvature classification raster obtained by Dikau criterion application is reported in **Attached 1**. The graph of the frequency of the geomorphometric forms is shown below in Fig. 4.31. It is emphasized that even the flat areas have been classified in category 4 as a degenerate case of the planar slope. Following the application of the Dikau criterion, in the area of interest about 30% of the cells were classified as hollow foot, a 3% as hollow and 10% as hollow shoulder. A 4% of the cells have been classified as a foot slope, while a 3% as a shoulder slope. A 10% of the cells have been classified as spur foot, while a 3% as a spur. Another 30% was classified as a nose. Finally, there are about 5% of cells classified as planar slope, but within this percentage, there are also flat areas. It follows that the prevailing structures in the area are hollow foot and nose, covering over 60% of the total area.

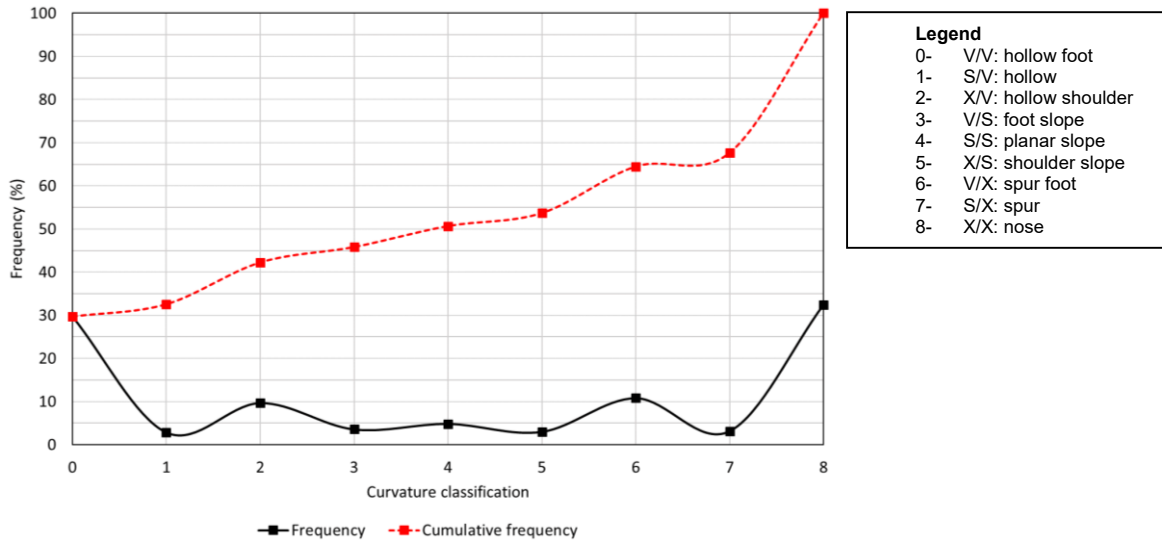


Fig. 4.31 Frequency of the geomorphometric forms classified through Dikau (1989) criterion

4.3.6 Specific Catchment Area (SCA)

Upslope contributing area or total catchment area (TCA), is the area above a certain length of contour that contributes flow across the contour l . This parameter is therefore crucial because it allows understanding the dimensions of the area in which precipitation can be conveyed (Gruber at al., 2008). Therefore, TCA is calculated from the number of cells that feed the flow to the cell of interest. A multiple flow direction (MFD) method was used to calculate the total catchment area. In particular, the method used is known as the TOPMODEL approach (Quinn et al., 1991; Freeman, 1991). This method has been used since, unlike the single-neighbor flow algorithms, it is possible to model a divergent flow, i.e., when a cell drains adjacent cells (Gruber at al., 2008). Single-neighbor flow algorithms solve the problem of divergent flow by arbitrarily assigning a drainage direction. On the contrary, the TOPMODEL approach defines, for each cell adjacent to the one considered, a fraction of central cell flow that will proceed towards the adjacent cells (Gruber at al., cum bibl.). This fraction is defined as follows:

$$\Delta A_i = A \cdot \frac{\tan(\beta_i)^v \cdot L_i}{\sum_{j=1}^n (\tan(\beta_j)^v \cdot L_j)} \quad (43)$$

where n is the total number of outflow directions (considering only the cells with an altitude lower than the central one) indexed with the letter j , ΔA_i is the flow portion, expressed in cells area, which passes into the adjacent i -th downhill cell, A is the total upslope area accumulated in the central cell, β_i is the slope in the outflow direction and L_i is the contour length of the i -th direction. (Quinn et al., 1991) The contour lengths, that are roughly equal to the size of a cell (Wilson and Gallant, 2000) were weighed differently for the cardinal and diagonal cells. In the first case a weight factor of 0.5 was used, while in the second case a weight factor of 0.35 was used (Gruber at al., 2008). The exponent v allows to control the dispersion. As v increases, the flow increases in maximum slope direction. Quinn's TOPMODEL approach used $v = 1$, but Freeman suggested using $v = 1.1$ (Gruber at al., 2008). It was decided to use this last value (SAGA GIS default value). Total catchment area raster obtained by TOPMODEL approach is reported in **Attached 2**. Since values variation range is very wide, a logarithmic (\log_{10}) scale has been used for a better

visualization of the TCA. The graph of the frequency of the TCA is shown below in Fig. 4.32 a). For a better representation, also in this graph, TCA was represented by calculating its logarithm (\log_{10}). It is possible to observe that, about 75% of the cells, have a TCA value between 10^3 and 10^4 m². Approximately 3% of the cells have TCA values above 10^5 m², while the remaining 22 % have values between 10^4 and 10^5 m². An extract of the TCA raster is reported below in Fig. 4.32 b). It is observed that valleys reveal highest contributing areas ($> 10^4$ m²), while lower values are found in ridges ($< 10^3$ m²). The majority of the cells (10^3 - 10^4 m²), therefore, fall in intermediate zones between ridges and valleys. It is therefore observed that TCA grows from ridges to valleys.

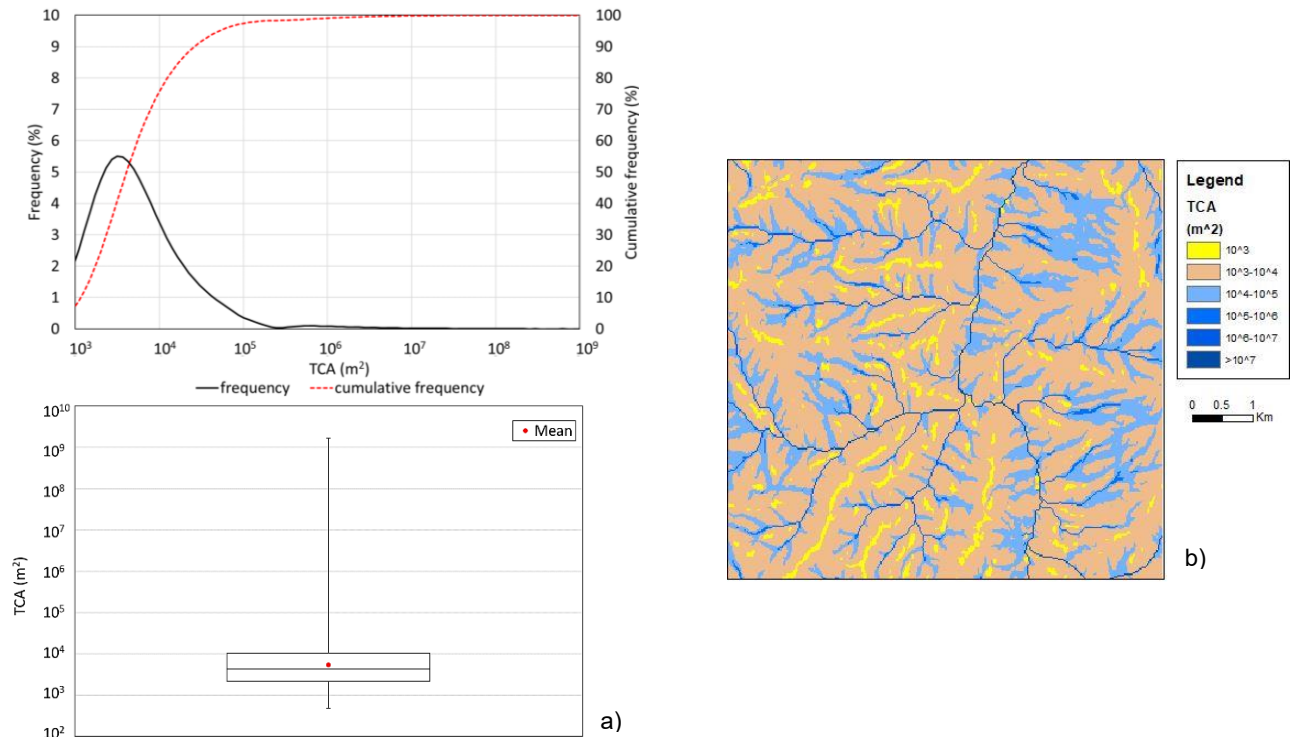


Fig. 4.32 a) Frequency of TCA obtained with TOPMODEL approach and relative boxplot (minimum, 1st quartile, median, 3rd quartile, maximum and mean) b) An extract of the TCA raster

The specific catchment area (SCA), as reported below, is the ratio of the total catchment area (TCA) to the contour length (or flow width) w (Wilson and Gallant, 2000):

$$SCA = \frac{TCA}{w} \left[\frac{m^2}{m} \right] \quad (44)$$

The specific catchment area has been calculated because, starting from it, two important indices can be obtained: Topographic Wetness Index (TWI) and Stream Power Index (SPI). SCA raster, obtained with Quinn et al. 1991 method, is reported in **Attached 2**. Also in this case, since values variation range is extensive, a logarithmic (\log_{10}) scale has been used for a better visualization of the SCA raster. The graph of the frequency of SCA is shown below in Fig. 4.33 a). For a better representation, its logarithm (\log_{10}) was calculated. It is possible to observe that about 50% of the cells have values lower than 10^2 m²/m. Another 40% of the cells have values between 10^2 and 10^3 m²/m, while the remaining cells, about 10%, have values above 10^3 m²/m. An extract of the SCA raster (same area considered for TCA) is reported below in Fig. 4.33 b).

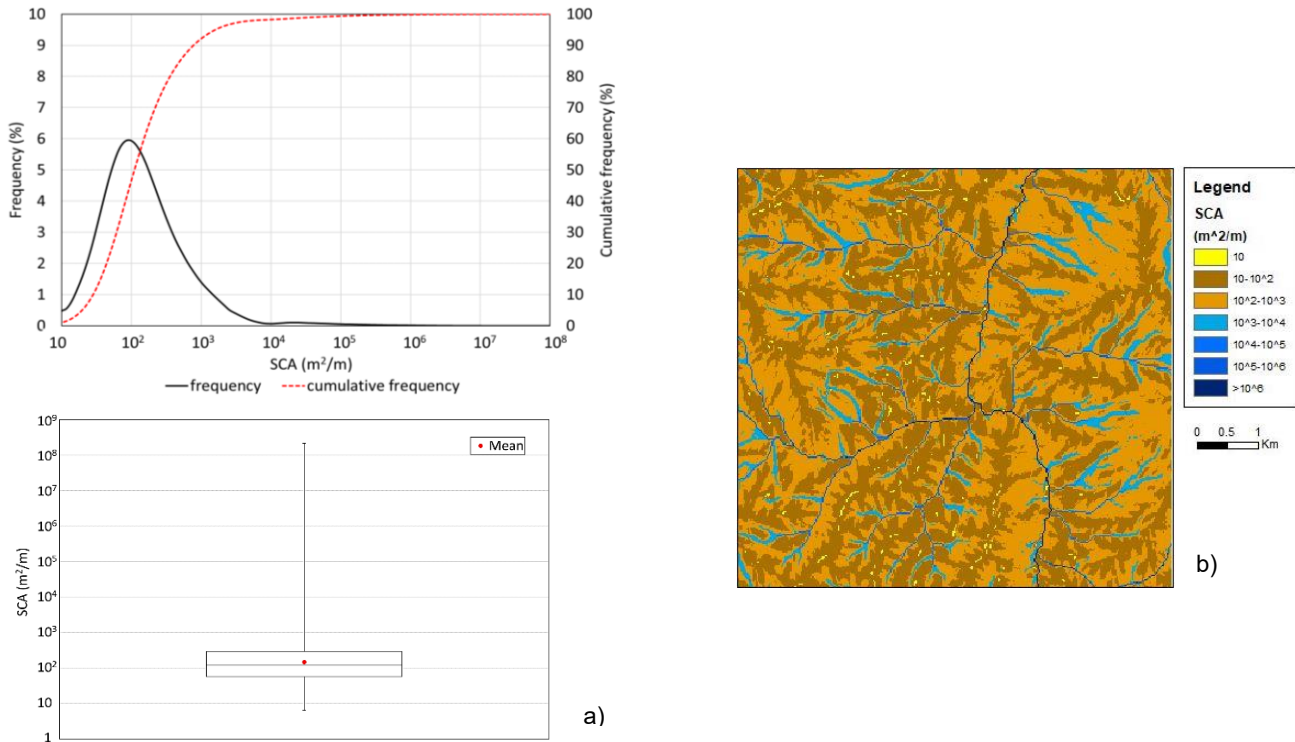


Fig. 4.33 a) Frequency of SCA obtained with TOPMODEL approach and relative boxplot (minimum, 1st quartile, median, 3rd quartile, maximum and mean) b) An extract of the SCA raster

4.3.7 Topographic Wetness Index (TWI)

Topographic Wetness Index (TWI) was defined because it was found that, in areas where SCA is high, and the slope is low, i.e., flat areas, the flow was distributed according to random type assignments, despite the application of an MFD method (Boehner et al., 2006). Assuming a steady-state condition and homogeneous ground conditions (transmissivity = 1), the saturation in the flat areas can be predicted by the Topographic Wetness Index (TWI), which is defined as the natural logarithm of the ratio of SCA to the slope (β) tangent (Wilson and Gallant, 2000):

$$TWI = \ln\left(\frac{SCA}{\tan\beta}\right) \quad (45)$$

It is noted that the TWI is a function of Specific Catchment Area and slope. High TWI values represent valleys and high potential of saturation, while low TWI values represent ridges and a low potential of saturation. Cells with the same TWI value, albeit at different scales, are hydrologically similar, i.e., they have a similar hydrologic response (USGS: Alabama Water Resources Conference, 2007). Topographic Wetness Index raster, obtained by TOPMODEL approach, is reported in **Attached 2**. The graph of the frequency of TWI is shown below in Fig. 4.34. It is possible to observe that about 21% of the cells show TWI values lower than 5: these values highlight crests and therefore a low saturation potential. Another 72% reveal TWI values between 5 and 10, i.e., areas with intermediate saturation potential, while the remaining 7% of the cells report TWI values higher than 10. The latter represent valleys, having a high saturation potential. TCA and TWI raster extracts, for the same area, are reported in Fig. 4.35 a) and b). As already mentioned, this comparison highlights the limits of the algorithm used for calculating TCA, which, in flat areas, presents difficulty in flow distribution. TWI algorithm does not present this problem by correctly defining flat areas degree of saturation.

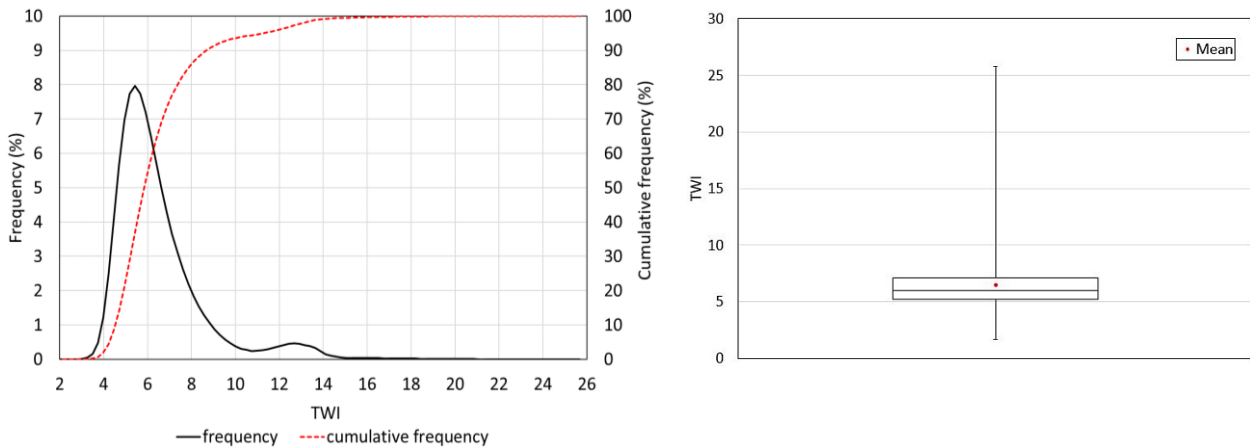


Fig. 4.34 Frequency of TWI obtained with TOPMODEL approach and relative boxplot (minimum, 1st quartile, median, 3rd quartile, maximum and mean)

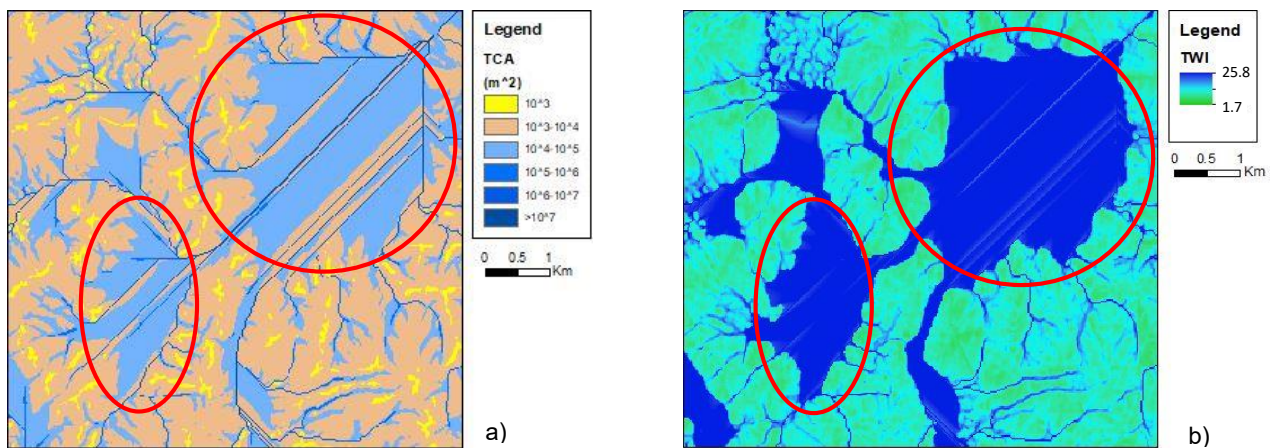


Fig. 4.35 Comparison between a) TCA and b) TWI raster extracts, for the same area. Two flat areas are indicated in red circles

4.3.8 Stream power Index (SPI)

The Stream Power Index (SPI) is an index linked to the erosive power of the water flow. Stream power can be defined as follows (Moore et al., 1991):

$$\Omega = \rho g q \tan \beta \left[\frac{J}{m^2 s} \right] \quad (46)$$

Where ρg is the unit weight of water, q is the discharge per unit channel width (Moore et al., 1991) and β is defined as in TWI. The stream power, basically, represents the power of a watercourse, or better, the work that the watercourse can perform (understood, for example, as the sediment transport) in the unit of time (Goudie, 2004). Equation (46) calculates watercourse power per unit channel area. Along with channel, this quantity tends to have low values at the highest and lowest parts of the river basin because, respectively, there are small discharges and small slope values. The highest stream power values are reached in the intermediate areas of the basin (Goudie, 2004). Since q is proportional to the Specific Catchment Area (SCA) it is possible to use the Stream Power Index (SPI), defined as the product of SCA and slope tangent, as shown in equation (47), like a measure of the stream power.

$$SPI = SCA \cdot \tan \beta \left[\frac{m^2}{m} \right] \quad (47)$$

As the SPI grows, therefore, the water flow energy grows, and different morphologies can be created as a result of solid transport. Stream Power Index raster, obtained by multiple flow direction method, is reported in **Attached 2**. The graph of the frequency of SPI is shown below in Fig. 4.36 a). For a better representation, its logarithm (ln) was calculated. It is observed that about 40% of the cells have SPI values lower than 20 (e^3): these cells represent not suitable zones for erosion. Approximately 58% of the cells have SPI values between 20 (e^3) and 1096 (e^7), which are respectively mildly erodible areas and erodible areas. The remaining cells, about 2%, have SPI values higher than 1096 (e^7) and they represent highly erodible areas. In the extract of the SPI raster (same area considered for TCA and SCA), reported in Fig. 4.36 b), it is possible to observe how the most erodible zones coincide with valleys and with mountainsides where there are both high TCA and slope values. Near ridges, the SPI values are reduced because the TCA and, therefore the SCA, have small values.

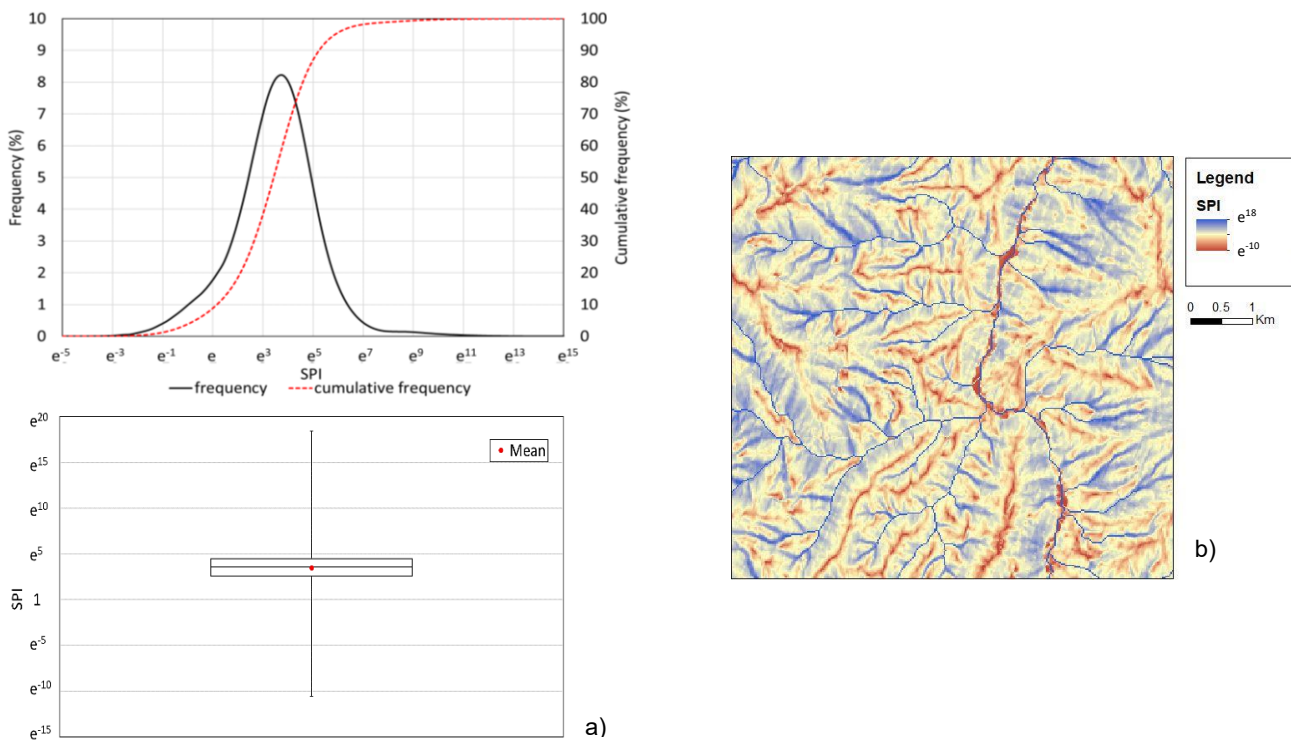


Fig. 4.36 a) Frequency of SPI obtained by multiple flow direction method and relative boxplot (minimum, 1st quartile, median, 3rd quartile, maximum and mean) b) An extract of the SPI raster

4.3.9 Convergence Index (CI)

Convergence Index (CI) is a parameter used to define the structures that show convergence, i.e., channels, and those that show divergence, i.e., ridges. The method used for calculating CI is based on aspect cells values, and it uses a 3x3 kernel. CI is evaluated by the degree of agreement between the ideal convergence matrix (3x3) aspect values and real aspect values within the considered matrix. Specifically, if we want to calculate the CI in the central cell of the considered 3x3 matrix, the index is calculated as the average, on the 8 cells adjacent to the central one, of the angles θ_i , measured counterclockwise, between the real aspect direction of the i-th cell and the ideal convergence direction for that same cell, to which 90° are subtracted. Below, in Fig. 4.37 a), is shown a schematization for the calculation of the convergence index for a 3x3 matrix. Formula for CI analytical calculation is reported in equation (48):

$$CI = \left(\frac{1}{8} \sum_{i=1}^8 \theta_i \right) - 90^\circ \quad (48)$$

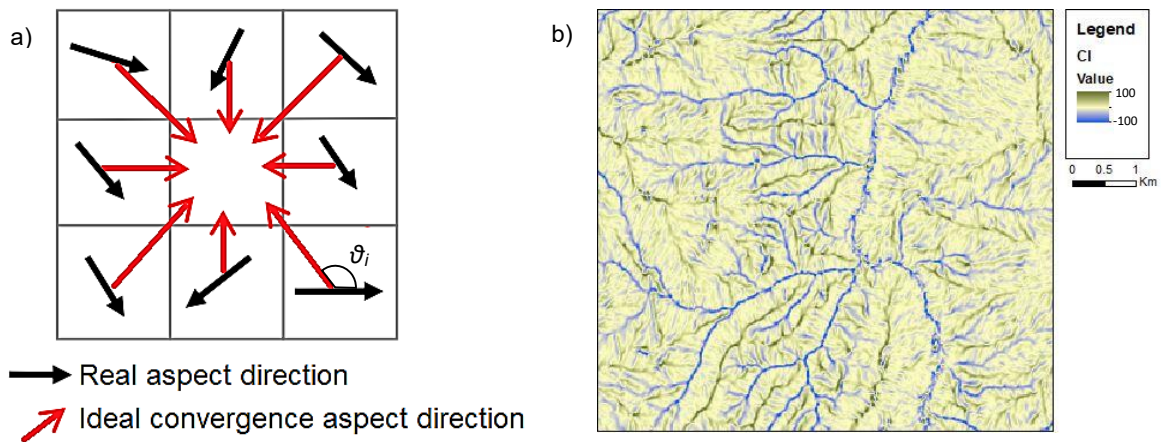


Fig. 4.37 a) Schematization for the calculation of the convergence index (3x3 matrix) b) An extract of the CI raster Modified after. Source: Thommeret, Bailly, Puech. Robust Extraction of Thalwegs Networks from DTMs for Topological Characterisation: A Case Study on Badlands. Proceedings of Geomorphometry 2009. Zurich, Switzerland, (2009) p.219

With the formula reported in the equation (48) the range of variation of this index go from 90° (completely divergent areas) to -90° (entirely convergent areas). In this case, the used algorithm, reports CI on a scale between -100 and 100 multiplying by a factor equal to 10/9. Cells that have a CI value equal to zero represent areas without curvature (Thommeret et al., 2009). Convergence Index raster, obtained by Aspect method, is reported in **Attached 2**. The graph of the frequency of CI is shown below in Fig. 4.38. It is observed that about 10% of the total cells have a value equal to 0, even if the cells having a CI in the neighborhood of 0 (from -2 to 2) are about 20%. These cells are substantially linear, i.e. without curvature. Approximately 45% of the cells have values below -2 which represent convergent structures as channels, while the remaining 35% shows values higher than 2, which represent divergent structures such as the ridges. In the extract of the CI raster (same area considered for TCA and SCA), reported in Fig. 4.37 b), it is possible to observe these structures. Comparing the value of CI in this extract with that of the TCA it is possible to notice that the zones having a major contributing area have a negative CI (convergent areas), while the zones having a lower TCA have a positive CI (divergent areas).

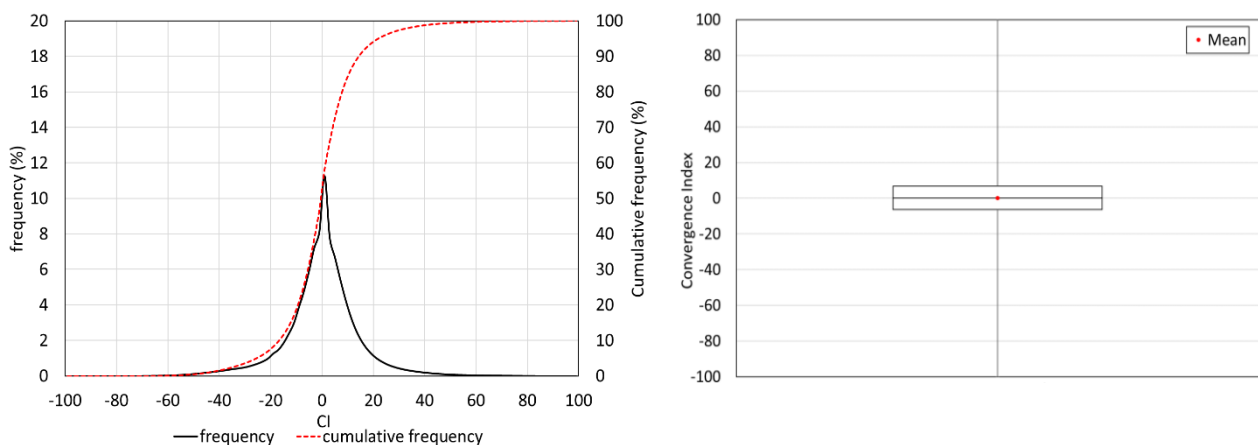


Fig. 4.38 Frequency of CI obtained by Aspect method and relative boxplot (minimum, 1st quartile, median, 3rd quartile, maximum and mean)

4.3.10 Topographic Position Index (TPI)

The Topographic Position Index (TPI) compares the altitude value of a cell with that of cells around it, within a given distance called the neighborhood size (n.s.). Substantially, by changing the neighborhood size value, typically expressed in map units, it is possible to identify geomorphological structures at different scales. Also in this case the two primary structures that can be recognized are ridges and valleys. It is essential to define the scale of computation because, a large-scale structure can turn out to be a ridge, but on a small scale it could even present itself as a valley. This concept is exemplified in Fig. 4.39.

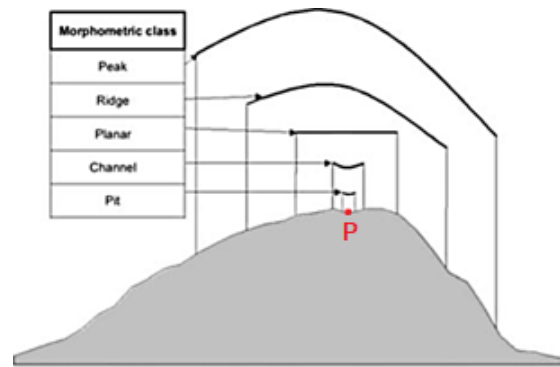


Fig. 4.39 Different morphometric structures identified when the neighborhood size varies around the point P. Modified after. Source: <http://citeseerx.ist.psu.edu/viewdoc/download?doi=10.1.1.127.9302&rep=rep1&type=pdf> p.109

In practice, as reported in equation (49), the TPI is calculated as the difference between the altitude value of the cell i -th and the average of the elevation values of all n cells, around the considered one, which fall within the specified neighborhood size.

$$TPI = DEM_i - \left(\frac{\left(\sum_{j=1}^n DEM_j \right)}{n} \right)_{neighborhood\ size} \quad (49)$$

From this definition it is possible to understand that positive TPI values define ridges, since the considered cell i -th has higher elevation values than mean of surrounding cells, while negative TPI values define valleys, since the considered cell i -th has lower elevation values than the average of the surrounding cells. Cell i -th with TPI value close to 0 represents flat area because the considered cell i -th presents roughly the same elevation value of the average of the surrounding cells. Topographic Position Index raster, obtained using different neighborhood sizes, is reported in **Attached 3**. Specifically, considered neighborhood sizes correspond to 50, 100, 150, 200, 250 and 450 m. In Fig. 4.40, TPI raster extracts for the same area are reported. Each extract corresponds to a different neighborhood size. Different outputs, passing from a n.s. of 50 m to one of 450 m, were observed. Broadly speaking, main structures are not subject to upheaval, but we note that for small n.s. artifacts are much more evident. For large n.s., they are less evident because they are blunted by the values of the surrounding cells. The graph of the frequency of TPI is shown below in Fig. 4.41. It is possible to see that for 50 m n.s., about 30% of the cells have a value of 0 (flat areas), while the remaining cells are equally distributed between positive and negative values (symmetrical distribution). Progressively we observe a sprawl of the distribution such that a decreasing of 0 value cells is observed. In particular, as n.s. grows, we observe a decrease in positive cells (ridges) and an increase of negative cells (valleys). For n.s. of 450 m, in fact, excluding the cells equal to 0, about 60% of the remaining ones show negative values, while 40% have positive values.

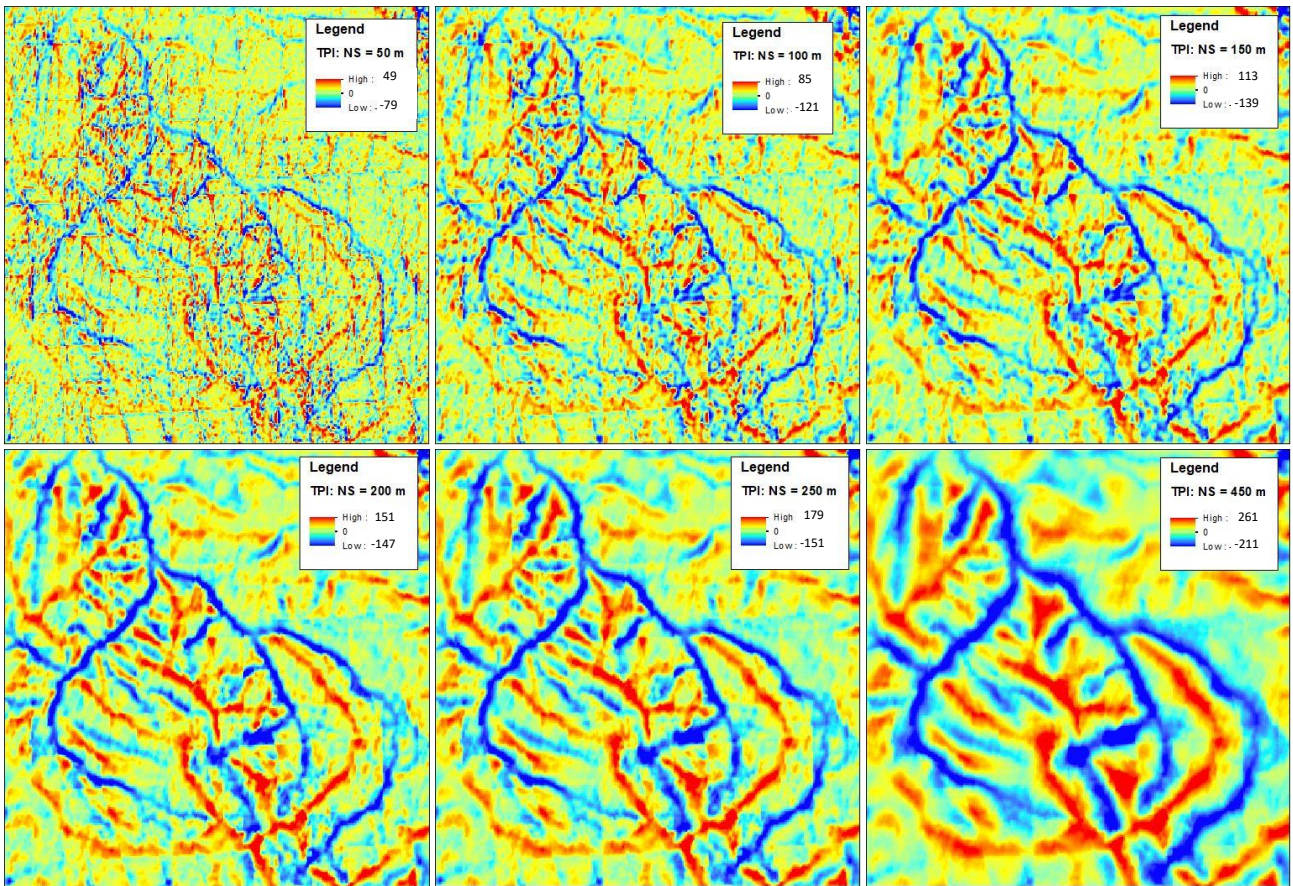
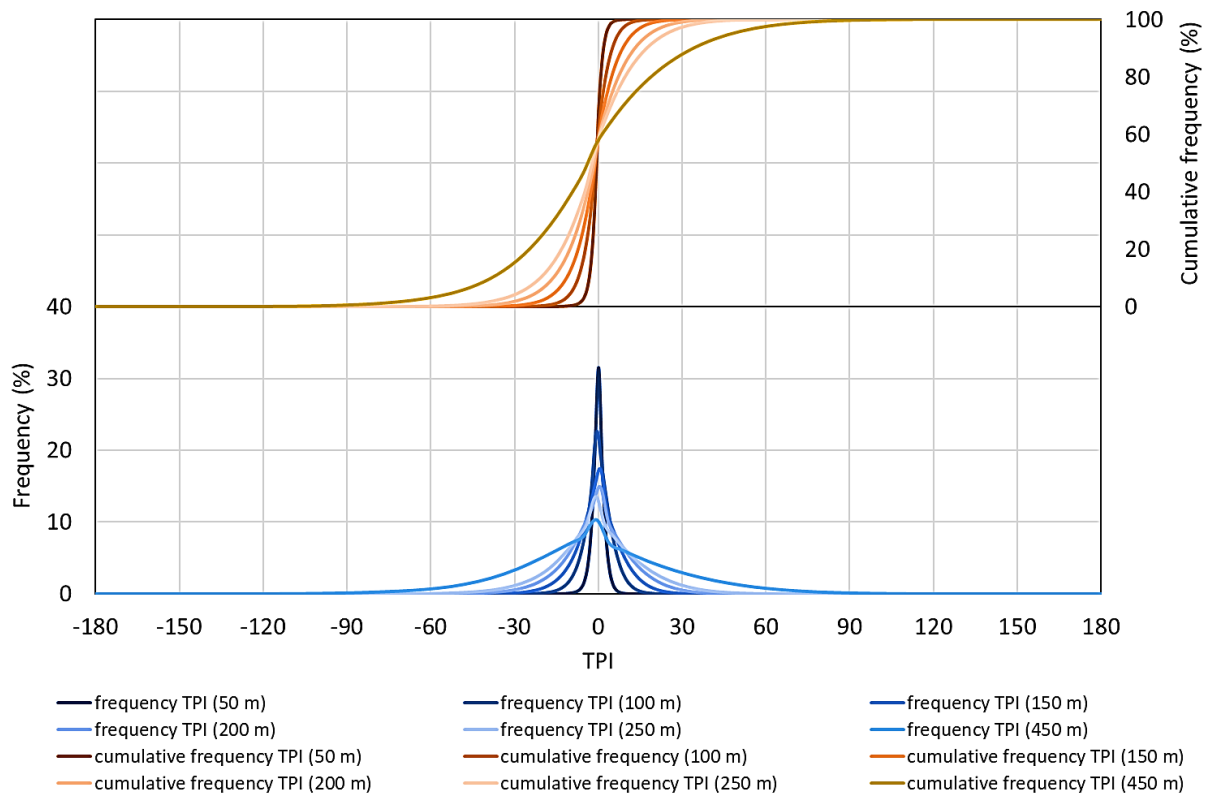


Fig. 4.40 TPI dependence on the scale of investigation. TPI raster extracts of the same area. Each extract corresponds to a different neighborhood size (reported in Legend)



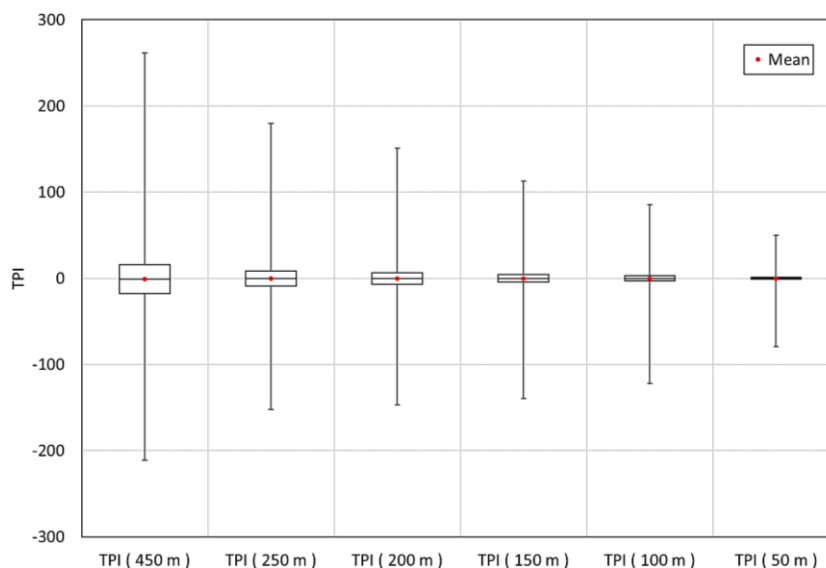


Fig. 4.41 Frequency of TPI obtained for different neighborhood sizes (previous page) and relative boxplots (minimum, 1st quartile, median, 3rd quartile, maximum and mean)

4.4 Snow avalanches in Central Apennines and geomorphological, nivo-meteorological analysis of release areas (January 2017)

Thanks to a work of photo-interpretation, carried out by Ph.D. Igor Chiambretti on high resolution satellite images, it was possible to obtain the perimeter of snow avalanches, with greater magnitude, occurred in the Apennines (January 2017). It is anticipated that the timing of such avalanches is not known. This is underlined since this data could be handy for understanding a possible correlation between snow avalanches and earthquakes. The mountain sectors concerned, as already mentioned, are Sibillini Mountains, Laga Mountains, Gran Sasso Massif, Majella Massif and Sirente Velino Massif. In order to identify different mountain sectors the SIC-ZPS official catalog, reported by Geoportale Nazionale, was used. Overall, 514 snow avalanches were identified. Surely the mountain areas mainly affected by the events are Gran Sasso, Laga and Majella Massifs where more than half of the total events occurred. Gran Sasso and Laga Massifs counted 259 snow avalanches, while in Majella Massif 125 releases verified. Furthermore, in the complex of Sibillini Mountains, 65 releases have been identified and 30 in Sirente Velino complex. There are also some areas less affected by snow avalanches, such as the Simbruini and Ernici Mountains, where occurred 11 events, Pizzuto-Alvagnano Mountains where 6 events have been mapped, Matese mountains that counts 5 events and, finally, 1 event in both Reatini and Monte Ceresa mountains. There are still 11 events that do not fall inside an official SIC-ZPS area. Seven of these events, however, were located in the Sibillini mountains because of their nearness. These observations are summarized in Table 11 and in Fig. 4.42. It is emphasized that, for simplicity of treatment, some SIC-ZPS have been merged. In this case, the table shows the identification codes of individual areas that have been merged to count the events and for calculating areas sectors. The first observation about the data is that, in this specific meteorological contest, mountain sectors with comparable areas can present a very different number of events. Comparing, for example, Simbruini and Ernici mountains data with those of Majella Massif, it is possible to see that their areas are roughly the same, but in the Majella Massif there are 10 times more events. It follows that zones subjected to snow avalanches are not homogeneously distributed on the territory, but there are areas more predisposed to this type of phenomenon.

Table 11 Considered mountain sectors with the indication of code ZPS-SIC, area and number of events.

Denomination	Code ZPS-SIC	Area (Km ²)	Total Area (km ²)	n° events
Gran Sasso and Laga Massifs	IT7110128	1433.11	1433.11	259
Majella Massif	IT7140129	740.82	740.82	125
Sibillini Mountains	IT5210071	179.32	445.43	72
	IT5340014	37.75		
	IT5330029	266.11		
Sirente Velino Mountains	IT7110130	591.34	591.34	30
Simbruini and Ernici Mountains	IT6050008	520.99	719.85	11
	IT7110207	198.86		
Pizzuto-Alvagnano Mountains	IT5210067	13.94	13.94	6
La Gallinola -Monte Miletto - Monti del Matese	IT7222287	250.02	250.02	5
Reatini Mountains	IT6020005	234.83	234.83	1
	IT6020007	31.86		
Ceresa Mountain	IT5340011	10.24	10.24	1
Others	-	-	-	4

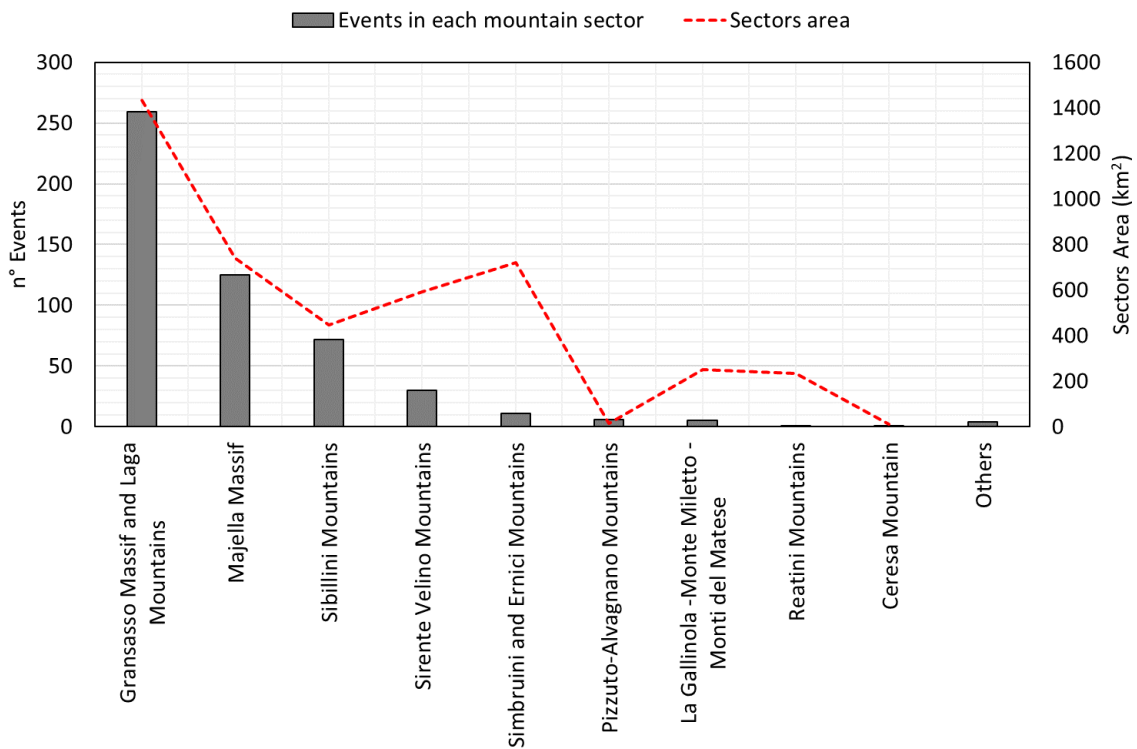


Fig. 4.42 Lack of correlation between number of events and area of the mountain sector considered.

Snow avalanches perimeters were mapped on the Apennine range, and mountain sectors partition, are reported in **Attached 4**. Precisely because areas subjected to snow avalanches are more concentrated in some zones, it is necessary to understand what are their characteristics. As already defined in paragraph 1.1, a snow avalanche is primarily composed of 3 parts: release area, track zone and runout zone. Among these three parts, the most interesting, in order to understand detachment causes, is the release area. For this reason, release areas were extracted from mapped snow avalanches (example reported in Fig. 4.43). On the

basis of the latter, it was possible to perform a statistical analysis of the main topographic attributes (elevation, slope, aspect and curvatures) and cumulative snow precipitation. This analysis was developed both on the entire area of interest and on mountain sectors with the higher release areas concentration. Each mountain sector was further subdivided into Adriatic and Tyrrhenian side, to ascertain any differences. The statistical analysis was performed on the totality of release areas cells falling into the interested mountain sector. Therefore, reasoning was made on a large scale and not considering every single release area.

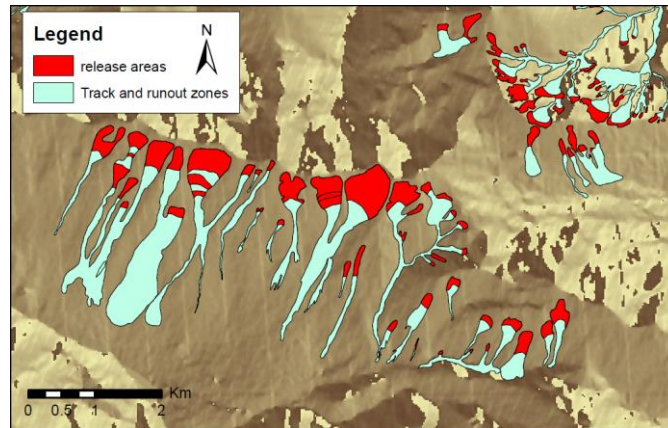
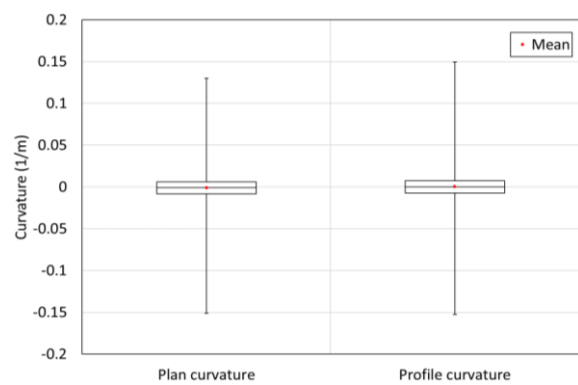
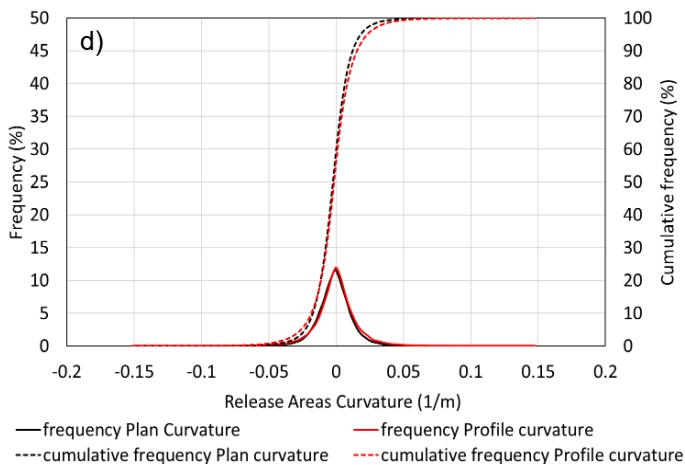
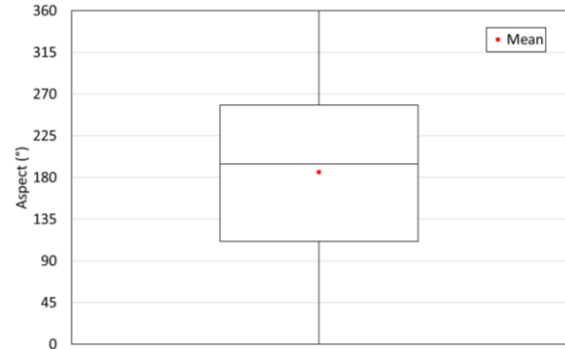
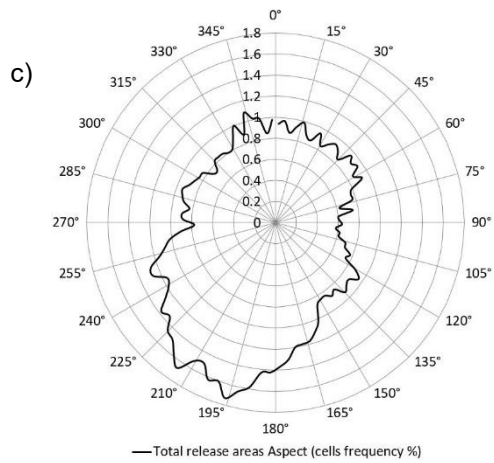
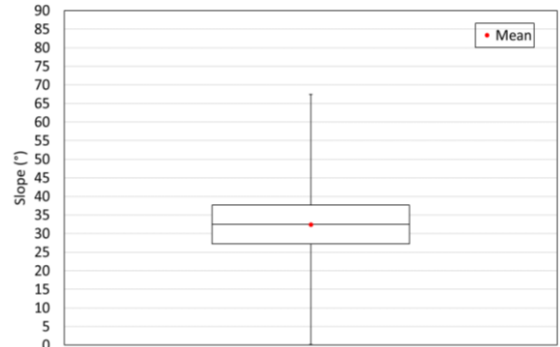
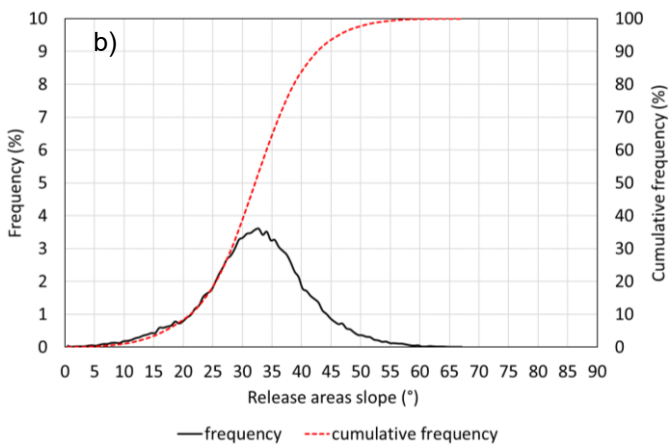
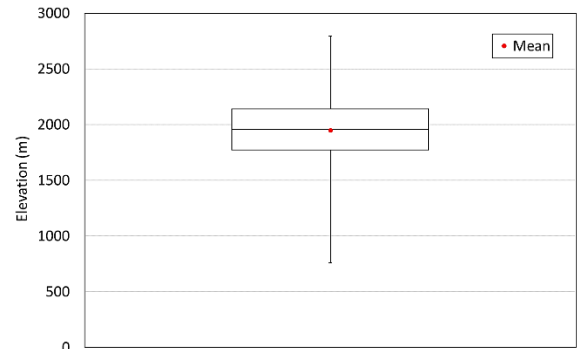
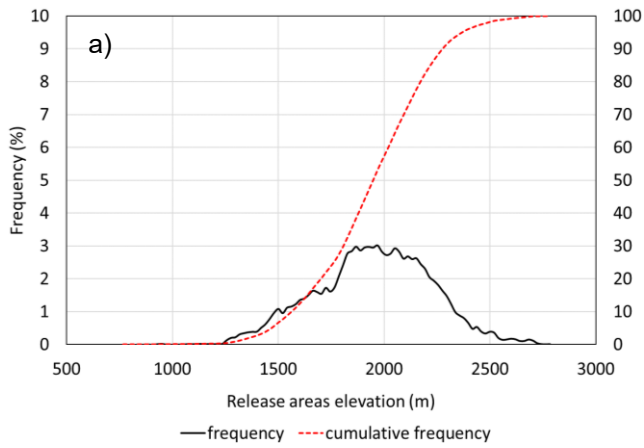


Fig. 4.43 Example of release areas extraction from snow avalanches obtained by photo-interpretation

4.4.1 Total release areas

The statistical analysis carried out for all release areas extracted, taking into account the totality of mountain sectors, is shown below. Fig. 4.44 a) shows the distribution of release areas elevation. Firstly, it is observed that detachment areas are found in a range of altitudes between 750 and 2800 m. As was foreseeable, therefore, detachment areas are found at high altitudes and well above the value chosen as the altimetric filter (500 m). The majority of cells, about 70%, present values between 1700 and 2200 m. Fig. 4.44 b) shows the distribution of release areas slope. The latter is included in a range from 0° to 68°. The median is located just above 30°. About 70% of the cells manifests values between 28° and 60°, which is the optimal range for which detachment is believed to occur. The remaining cells, about 30%, present values lower than 30°. Most likely, these values below 28°-30° are due to a DEM low quality. In Fig. 4.44 c) the release areas aspect distribution is reported. About 21% of the cells show an exposure between 0° and 90° (N → E), about 24% of the cells have exposure values between 90° and 180° (E → S), a 35% of the cells has values between 180° and 270° (S → W), while the remaining 20% shows exposure values between 270° and 360° (W → N). Release areas, therefore, manifest a prevalence aspect in correspondence of 3rd quadrant values (180°-270°). Fig. 4.44 d) shows the Plan and Profile curvatures frequencies distribution for all release areas. It is observed that profile and plan curvature are almost symmetrical with respect to 0, therefore, in the aspect direction, and in the perpendicular direction, the found structures are about 50% concave and about 50% convex. This data must be critically evaluated. What is expected in correspondence to release areas is a prevalence of concave areas, which are more powerful in accumulating snow. The result obtained, in fact, is indeed subject to error since the curvature corresponds to the second derivative of DEM. For release areas, the frequency distribution of the cumulative snow precipitation, during the period January 15th-18th 2017, was also evaluated and reported in Fig. 4.44 e). It is observed that in these areas the cumulative snowfall varies in a range between 150 and 510 cm. Furthermore, during the 3 days considered, snow depth values greater than 463 cm were found in half areas.



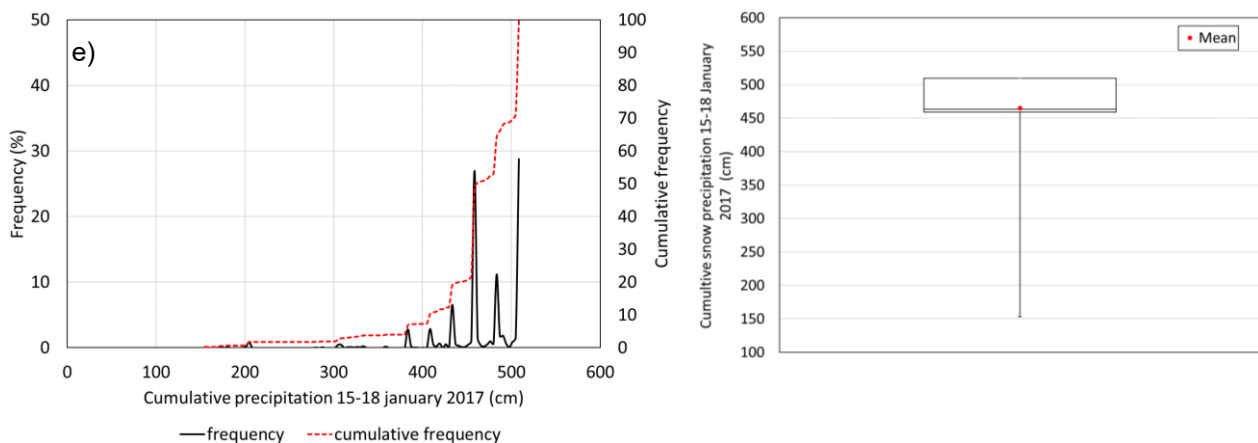


Fig. 4.44 Statistical analysis of the main topographic attributes a) elevation, b) slope, c) aspect and d) curvature (previous page) and e) cumulative snow precipitation carried out for release areas extracted from mapped snow avalanches

4.4.2 Gran Sasso release areas

The statistical analysis carried out for release areas extracted in Gran Sasso Massif is shown below in Fig. 4.45. Fig. 4.45 a) shows the distribution of release areas elevation in the interested mountain sector. Firstly, it is observed that detachment areas are found in a range of altitudes between 925 and 2805 m. It is observed that about 49% of the cells have height values between 1000 and 2000 m. The remaining 51% shows values above 2000 m. Fig. 4.45 b) shows the distribution of release areas slope in Gran Sasso Massif. Slopes are included in a range from 1° to 67°. The median is located around 33°. About 76 % of the cells manifests values between 28° and 60°, which is the optimal range for which detachment is believed to occur. The remaining cells, about 24%, present values lower than 28°. Most likely, these values below 28° depending DEM low quality. Fig. 4.45 c) shows the Plan and Profile curvatures frequencies distribution for Gran Sasso Massif release areas. In detail, it is observed that about 10% of the cells have profile curvature values equal to 0, i.e. flat areas in the direction of maximum slope. The concave areas (negative values) are about 51% while the convex areas (positive values) are about 39%. With regard to Plan curvature, release areas present, in the direction perpendicular to the aspect, a 10% of flat cells, a 56% of concave cells and a 34% of convex cells. Thus a prevalence of concave cells in Plan curvature is observed. This data must be critically evaluated because of error propagation through second derivatives starting from a DEM low-quality. For release areas, the frequency distribution of the cumulative snow precipitation, during the period January 15th-18th 2017, is reported in Fig. 4.45 d). It is observed that in these areas the cumulative snowfall varies in a range between 408 and 510 cm. Furthermore, snow depth values greater than 510 cm were found in half areas. In Fig. 4.45 e) the release areas aspect distribution is shown. The main aspect presented by release areas is S-W (about 30 % of total cells shows values in 3rd quadrant), but there are also a 25 % of cells in 4th quadrant, a 23 % of cells in 1st quadrant and a 22% in 2nd quadrant. During the days of interest, the perturbation mainly came from north-east/east with an average wind speed, at 2000 m, of 28 km/h. Nevertheless, it is observed that release areas exposures are distributed almost homogeneously in the four quadrants with a slight prevalence in the third quadrant, corresponding to the direction in which the wind blew.

Gran Sasso Massif was subdivided into the Adriatic side and the Tyrrhenian side for which the same frequency analysis was performed. The statistical analysis carried out for different sides is reported in the following paragraphs.

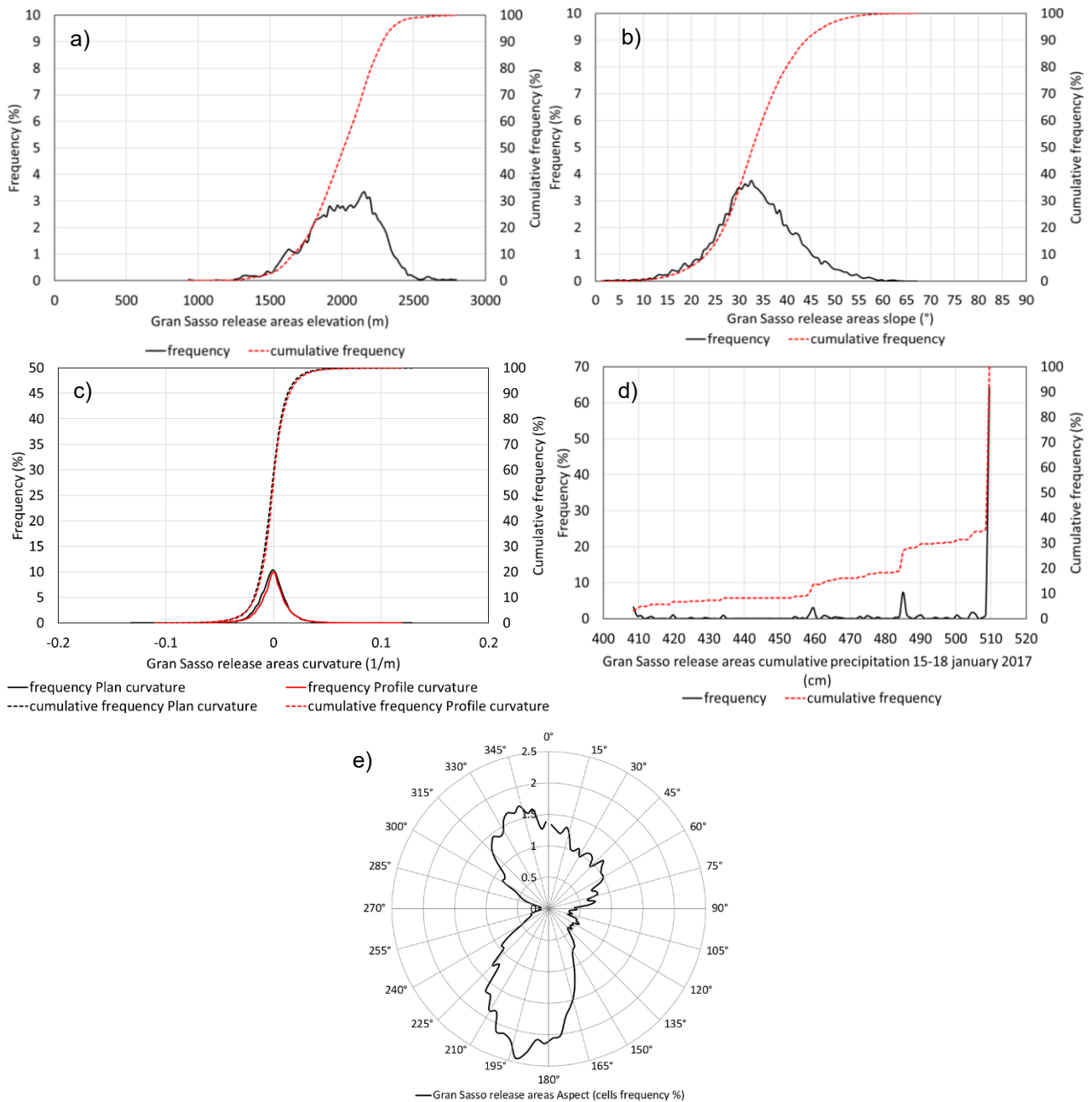


Fig. 4.45 Statistical analysis of the main topographic attributes a) elevation, b) slope, c) curvature d) cumulative snow precipitation and e) aspect carried out for Gran Sasso release areas extracted from mapped snow avalanches

4.4.3 Gran Sasso, Adriatic side, release areas

The statistical analysis carried out for release areas extracted in Gran Sasso Massif, Adriatic side, is shown below in Fig. 4.46. Fig. 4.46 a) shows the distribution of release areas elevation in the interested side of the mountain sector. It is observed that detachment areas are found in a range of altitudes between 925 and 2805 m. It is observed that almost 54% of the cells have height values between 1000 and 2000 m. The remaining 46% shows values above 2000 m. Fig. 4.46 b) shows the distribution of release areas slope in Gran Sasso Adriatic Massif. Slopes are included in a range from 1° to 67°. The median is located around 35°. About 75% of the cells manifests values between 28° and 60°, which is the optimal range for which detachment is believed to occur. The remaining cells, about 25%, present values lower than 28°. Most likely, these values below 28° depending on low quality DEM. Fig. 4.46 c) shows the Plan and Profile curvatures frequencies distribution

for Gran Sasso Adriatic release areas. In detail, it is observed that about 8% of the cells have profile curvature values equal to 0, i.e., flat areas in the direction of maximum slope. The concave areas (negative values) are about 42% while the convex areas (positive values) are about 50%. With regard to Plan curvature, release areas present, in the direction perpendicular to the aspect, a 9% of flat cells, a 54% of concave cells and a 37% of convex cells. Thus a prevalence of concave cells in Plan curvature is observed. As mentioned, this data must be critically evaluated. For release areas, the frequency distribution of the cumulative snow precipitation, during the period January 15th-18th 2017, is reported in Fig. 4.46 d). It is observed that in these areas the cumulative snowfall varies in a range between 409 and 510 cm. Furthermore, snow depth values greater than 510 cm were found in half areas. In Fig. 4.46 e) the release areas aspect distribution is shown. The main aspect presented by release areas is reported in two quadrants: about 43% of total cells shows values in 4th quadrant (N/N-W), but there is also a 40 % of cells that present values in 1st quadrant (N/N-E).

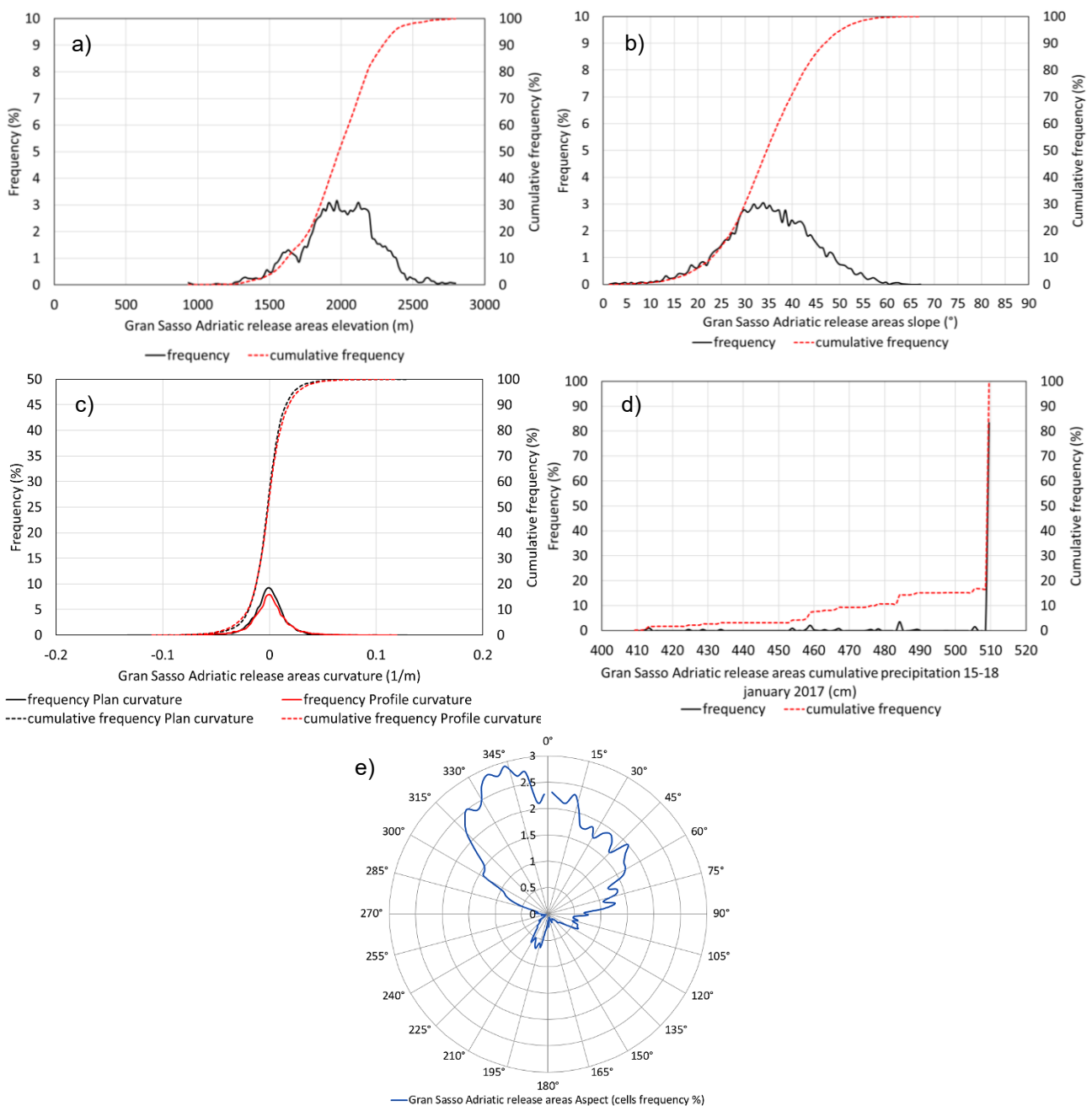
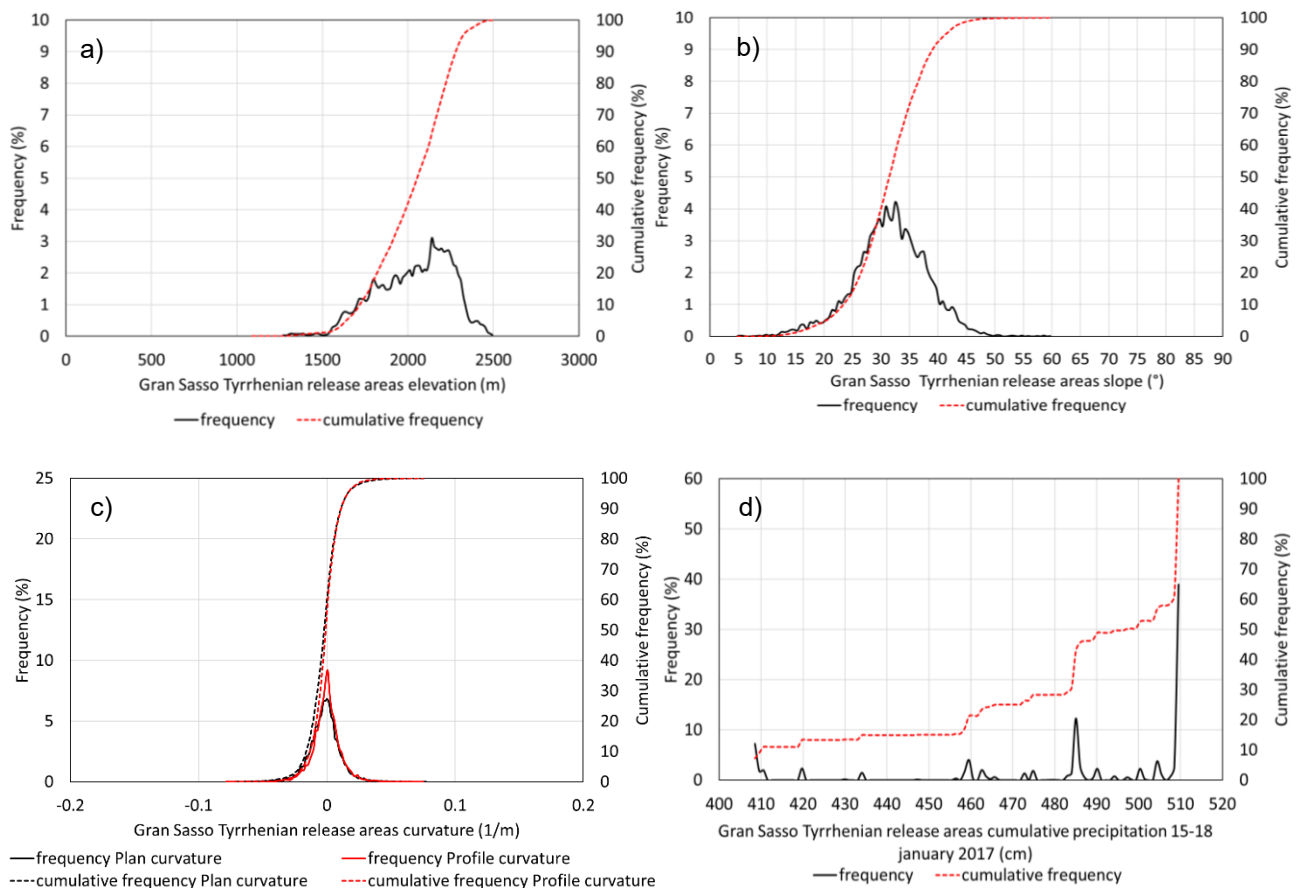


Fig. 4.46 Statistical analysis of the main topographic attributes a) elevation, b) slope, c) curvature d) cumulative snow precipitation and e) aspect carried out for Gran Sasso Adriatic release areas extracted from mapped snow avalanches

4.4.4 Gran Sasso, Tyrrhenian side, release areas

The statistical analysis carried out for release areas extracted in Gran Sasso Massif, Tyrrhenian side, is shown below in Fig. 4.47. Fig. 4.47 a) shows the distribution of release areas elevation in the interested side of the mountain sector. It is observed that detachment areas are found in a range of altitudes between 1085 and 2500 m. It is observed that almost 42% of the cells have height values between 1085 and 2000 m. The remaining 58% shows values above 2000 m. Fig. 4.47 b) shows the distribution of release areas slope in Gran Sasso Tyrrhenian Massif. Slopes are included in a range from 5° to 60°. The median is located around 32°. About 72% of the cells manifests values between 28° and 60°, which is the optimal range for which detachment is believed to occur. The remaining cells, about 28%, present values lower than 28°. These values below 28° depending on low quality DEM. Fig. 4.47 c) shows the Plan and Profile curvatures frequencies distribution for Gran Sasso Tyrrhenian release areas. In detail, it is observed that about 9% of the cells have profile curvature values equal to 0, i.e., flat areas in the direction of maximum slope. The concave areas (negative values) are about 50% while the convex areas (positive values) are about 41%. With regard to Plan curvature, release areas present, in the direction perpendicular to the aspect, a 7 % of flat cells, a 54% of concave cells and a 39% of convex cells. Thus a prevalence of concave cells in Plan curvature is observed. This data must be critically evaluated because of error propagation through second derivatives starting from a low quality DEM. For release areas, the frequency distribution of the cumulative snow precipitation, during the period January 15th-18th 2017, is reported in Fig. 4.47 d). It is observed that in these areas the cumulative snowfall varies in a range between 408 and 510 cm. Furthermore, snow depth values greater than 497 cm were found in half areas. In Fig. 4.47 e) the release areas aspect distribution is shown. The main aspect presented by release areas is reported in two quadrants: about 56% of total cells shows values in 3rd quadrant (S/S-W), but there is also a 41% of cells that present values in 2nd quadrant (S/S-E).



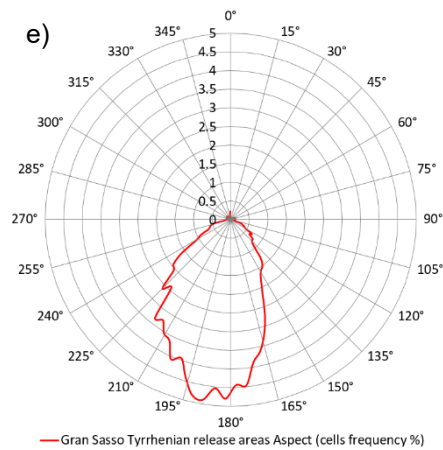


Fig. 4.47 Statistical analysis of the main topographic attributes a) elevation, b) slope, c) curvature d) cumulative snow precipitation (previous page) and e) aspect carried out for Gran Sasso Tyrrhenian release areas extracted from mapped snow avalanches.

4.4.5 Laga release areas

The statistical analysis carried out for release areas extracted in Laga Mountains is shown below in Fig. 4.48. Fig. 4.48 a) shows the distribution of release areas elevation in the interested mountain sector. Firstly, it is observed that detachment areas are found in a range of altitudes between 940 and 2400 m. It is observed that 40% of the cells have height values between 1000 and 2000 m. The remaining 60% shows values above 2000 m. Fig. 4.48 b) shows the distribution of release areas slope in Laga mountains. Slopes are included in a range from 3° to 65°. The median is located around 31°. About 62% of the cells manifests values between 28° and 60°, which is the optimal range for which detachment is believed to occur. The remaining cells, about 38%, present values lower than 28°. Most likely, these values below 28° depending on low quality DEM. Fig. 4.48 c) shows the Plan and Profile curvatures frequencies distribution for Laga release areas. It is observed that about 10 % of the cells have profile curvature values equal to 0, i.e. flat areas in the direction of maximum slope. The concave areas (negative values) are about 34% while the convex areas (positive values) are about 56 %. With regard to Plan curvature, release areas present, in the direction perpendicular to the aspect, a 10 % of flat cells, a 60% of concave cells and a 30% of convex cells. Thus a prevalence of concave cells in Plan curvature is observed. As already mentioned above, this data must be critically evaluated. For release areas, the frequency distribution of the cumulative snow precipitation, during the period January 15th-18th 2017, is reported in Fig. 4.48 d). It is observed that in these areas the cumulative snowfall varies in a range between 459 and 510 cm. Furthermore, snow depth values greater than 486 cm were found in half areas. In Fig. 4.48 e) the release areas aspect distribution is shown. The main aspect presented by release areas is S-W (about 46 % of total cells shows values in 3rd quadrant), but there is also a 24 % of cells that present values in 4th quadrant. During the days of interest, the perturbation mainly came from north-east/east with an average wind speed, at 2000 m, of 28 km/h. It is therefore observed that most of release areas have opposite aspects with respect to the origin direction of the wind.

Laga mountain sector was subdivided into the Adriatic side and the Tyrrhenian side for which the same frequency analysis was performed. The statistical analysis carried out for different sides is reported in the following paragraphs.

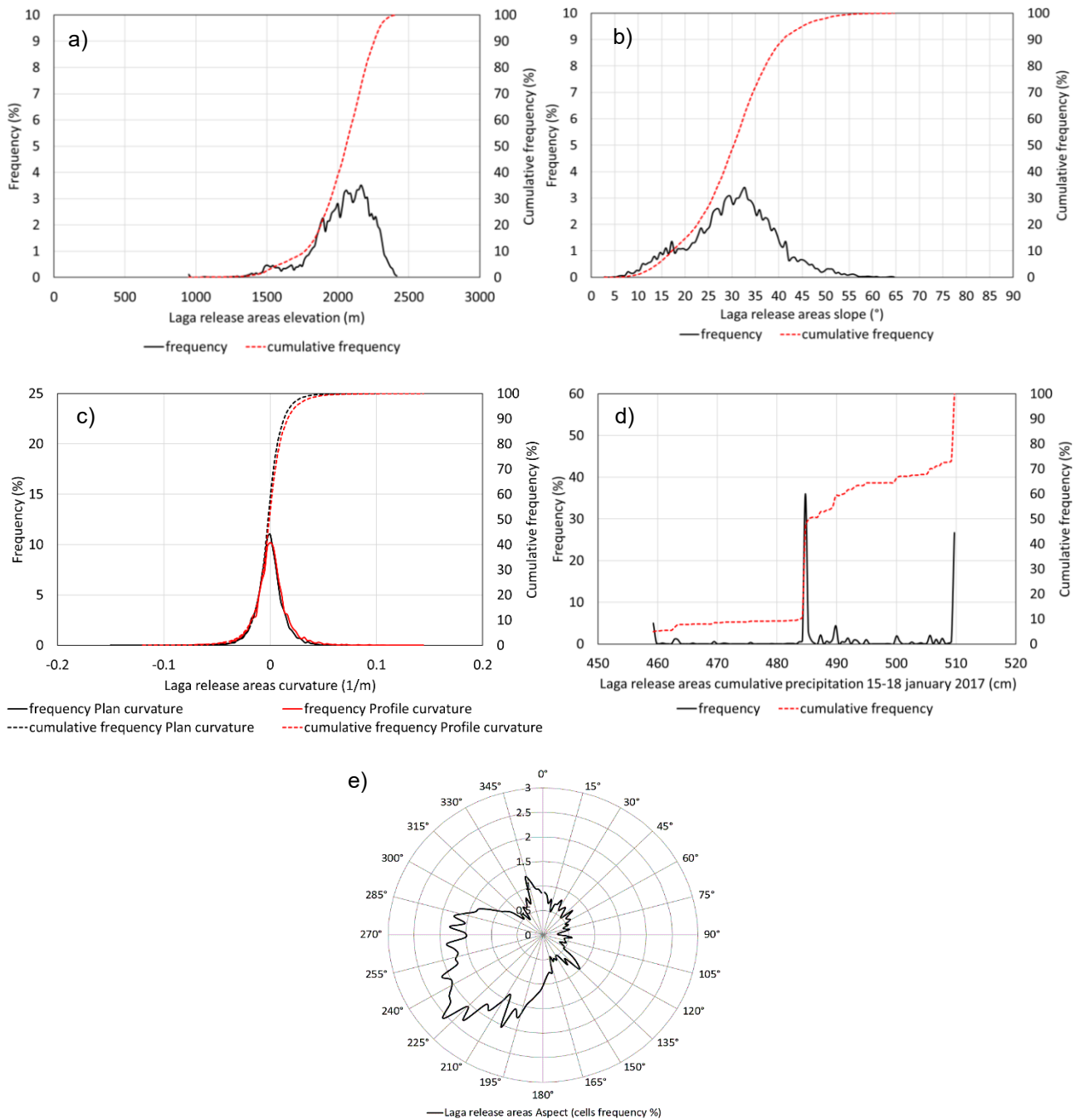


Fig. 4.48 Statistical analysis of the main topographic attributes a) elevation, b) slope, c) curvature d) cumulative snow precipitation and e) aspect carried out for Laga release areas extracted from mapped snow avalanches

4.4.6 Laga, Adriatic side, release areas

The statistical analysis carried out for release areas extracted in Laga Mountains, Adriatic side, is shown below in Fig. 4.49. Fig. 4.49 a) shows the distribution of release areas elevation in the interested side of the mountain sector. It is observed that detachment areas are found in a range of altitudes between 940 and 2400 m. It is observed that almost 89% of the cells have height values between 1000 and 2000 m. The remaining 11% shows values above 2000 m. Fig. 4.49 b) shows the distribution of release areas slope in Laga Adriatic mountains. Slopes are included in a range from 5° to 65°. The median is located around 34°. About 74 % of the cells manifests values between 28° and 60°, which is the optimal range for which detachment is believed to occur. The remaining cells, about 26 %, present values lower than 28°. Most likely, these values below 28° depending on low

quality DEM. Fig. 4.49 c) shows the Plan and Profile curvatures frequencies distribution for Laga Adriatic release areas. In detail, it is observed that about 7 % of the cells have profile curvature values equal to 0, i.e., flat areas in the direction of maximum slope. The concave areas (negative values) are about 47% while the convex areas (positive values) are about 46 %. With regard to Plan curvature, release areas present, in the direction perpendicular to the aspect, a 5 % of flat cells, a 60% of concave cells and a 35 % of convex cells. Thus a prevalence of concave cells in Plan curvature is observed. As mentioned, this data must be critically evaluated. For release areas, the frequency distribution of the cumulative snow precipitation, during the period January 15th-18th 2017, is reported in Fig. 4.49 d). It is observed that in these areas the cumulative snowfall varies in a range between 459 and 510 cm. Furthermore, snow depth values greater than 510 cm were found in half areas. In Fig. 4.49 e) the release areas aspect distribution is shown. The main aspect presented by release areas is N-E (about 57 % of total cells shows values in 1st quadrant), but there is also a 20 % of cells that present values in 2nd quadrant and a 15% of cells in 4th quadrant.

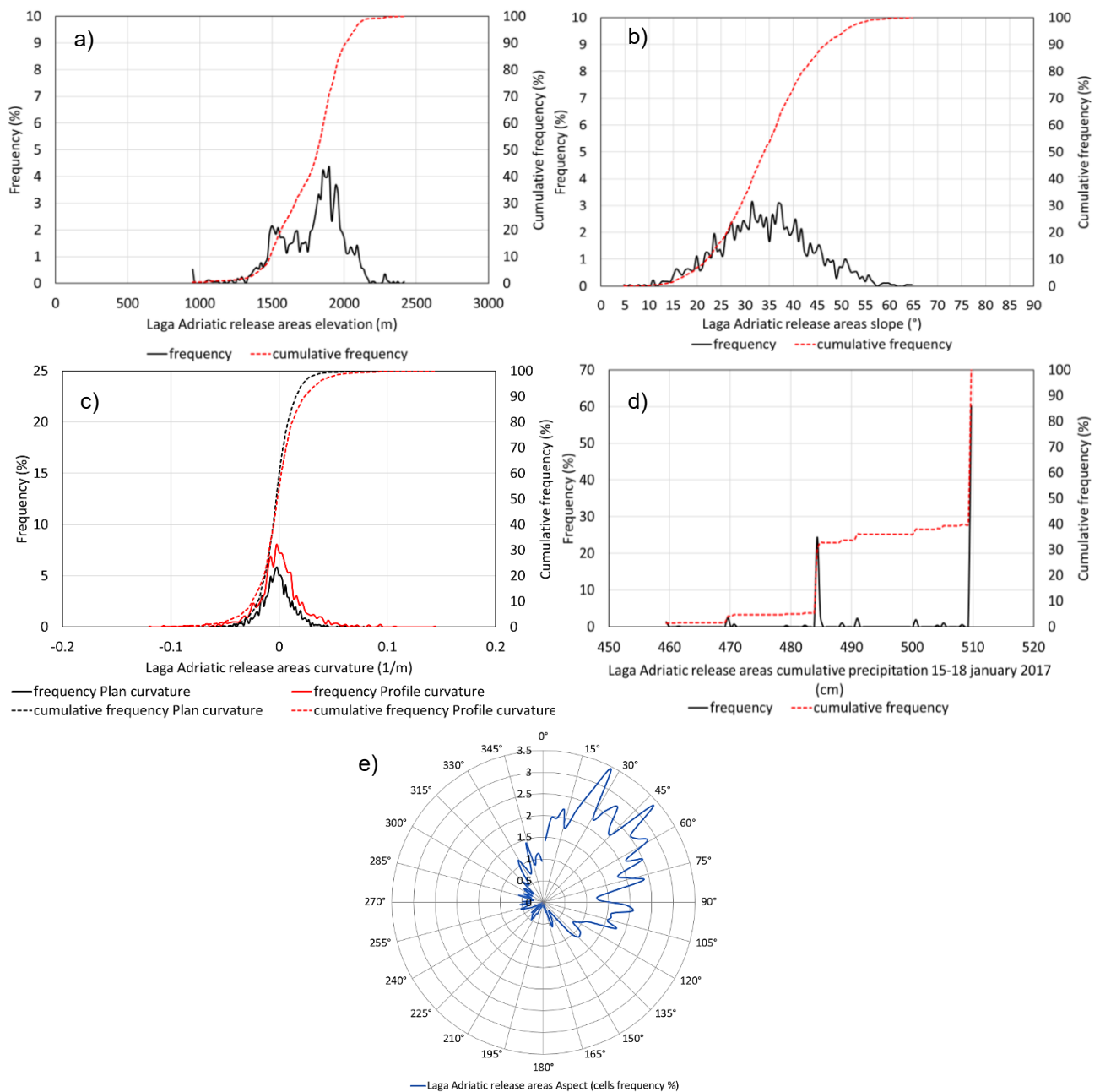
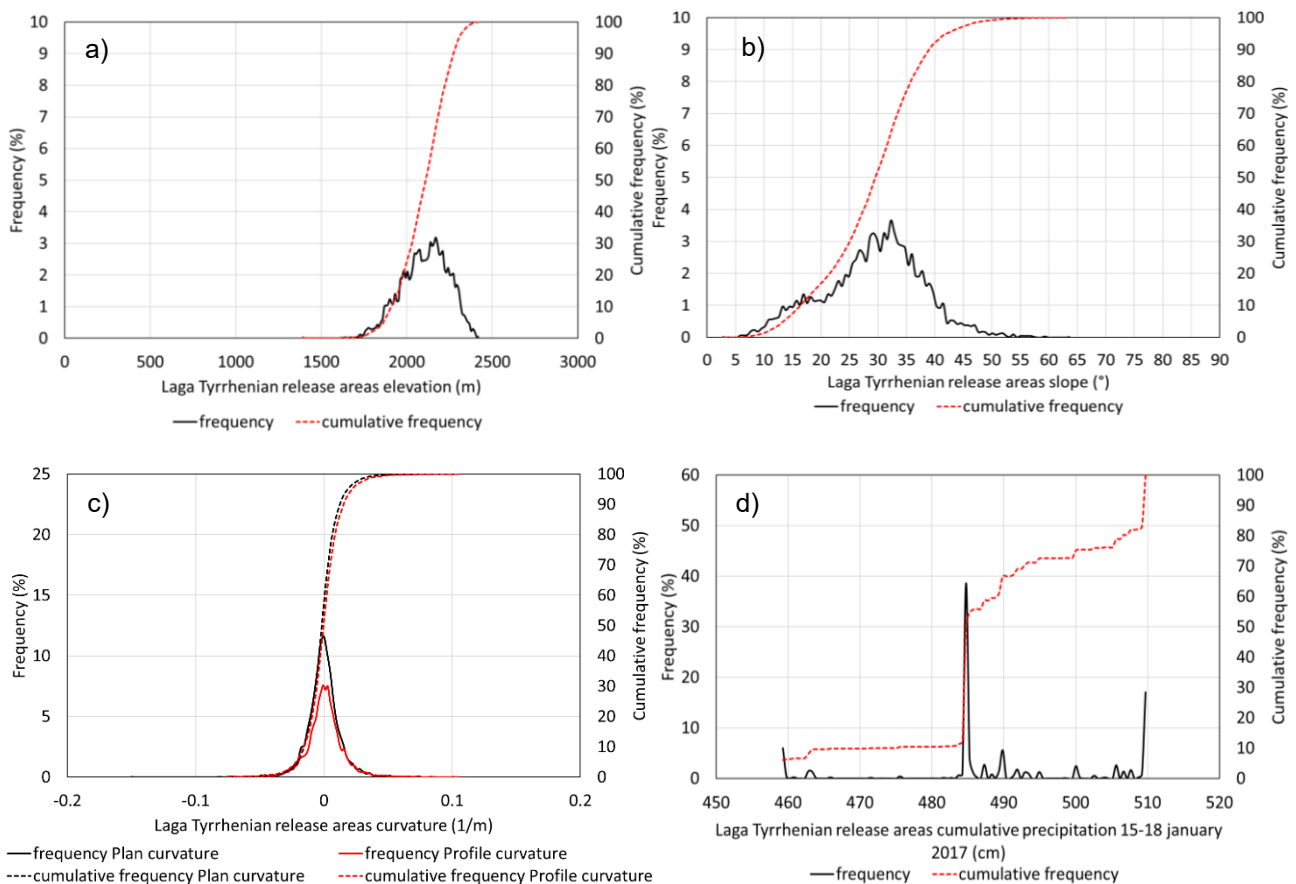


Fig. 4.49 Statistical analysis of the main topographic attributes a) elevation, b) slope, c) curvature d) cumulative snow precipitation and e) aspect carried out for Laga Adriatic release areas extracted from mapped snow avalanches

4.4.7 Laga, Tyrrhenian side, release areas

The statistical analysis carried out for release areas extracted in Laga Mountains, Tyrrhenian side, is shown below in Fig. 4.50. Fig. 4.50 a) shows the distribution of release areas elevation in the interested side of the mountain sector. It is observed that detachment areas are found in a range of altitudes between 1390 and 2420 m. It is observed that almost 25% of the cells have height values between 1390 and 2000 m. The remaining 75% shows values above 2000 m. Fig. 4.50 b) shows the distribution of release areas slope in Laga Tyrrhenian mountains. Slopes are included in a range from 3° to 64°. The median is located around 30°. About 58 % of the cells manifests values between 28° and 60°, which is the optimal range for which detachment is believed to occur. The remaining cells, about 42 %, present values lower than 28°. These values below 28° depending on low quality DEM. Fig. 4.50 c) shows the Plan and Profile curvatures frequencies distribution for Laga Tyrrhenian release areas. In detail, it is observed that about 8% of the cells have profile curvature values equal to 0, i.e., flat areas in the direction of maximum slope. The concave areas (negative values) are about 41% while the convex areas (positive values) are about 51%. With regard to Plan curvature, release areas present, in the direction perpendicular to the aspect, a 10 % of flat cells, a 57% of concave cells and a 33 % of convex cells. Thus a prevalence of concave cells in Plan curvature is observed. This data must be critically evaluated because of error propagation through second derivatives starting from a low quality DEM. For release areas, the frequency distribution of the cumulative snow precipitation, during the period January 15th-18th 2017, is reported in Fig. 4.50 d). It is observed that in these areas the cumulative snowfall varies in a range between 459 and 510 cm. Furthermore, snow depth values greater than 485 cm were found in half areas. In Fig. 4.50 e) the release areas aspect distribution is shown. The main aspect presented by release areas is S-W (about 57 % of total cells shows values in 3rd quadrant), but there is also a 26% of cells that present values in 4th quadrant and a 15% of cells in 2nd quadrant.



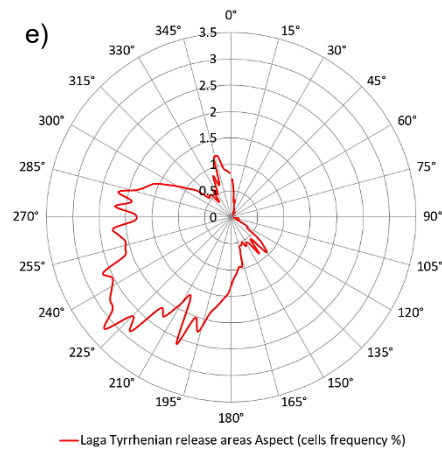


Fig. 4.50 Statistical analysis of the main topographic attributes a) elevation, b) slope, c) curvature d) cumulative snow precipitation (previous page) and e) aspect carried out for Laga Tyrrhenian release areas extracted from mapped snow avalanches.

4.4.8 Majella release areas

The statistical analysis carried out for release areas extracted in Majella Massif is shown below in Fig. 4.51. Fig. 4.51 a) shows the distribution of release areas elevation in the interested mountain sector. Firstly, it is observed that detachment areas are found in a range of altitudes between 757 and 2740 m. It is observed that 49% of the cells have height values between 1000 and 2000 m. The remaining 51% shows values above 2000 m. Fig. 4.51 b) shows the distribution of release areas slope in Majella Massif. Slopes are included in a range from 2° to 64°. The median is located around 33°. About 68% of the cells manifests values between 28° and 60°, which is the optimal range for which detachment is believed to occur. The remaining cells, about 32%, present values lower than 28°. Most likely, these values below 28° depend on low quality DEM. Fig. 4.51 c) shows the Plan and Profile curvatures frequencies distribution for Majella Massif release areas. In detail, it is observed that about 8% of the cells have profile curvature values equal to 0, i.e., flat areas in the direction of maximum slope. The concave areas (negative values) are about 41% while the convex areas (positive values) are about 51%. With regard to Plan curvature, release areas present, in the direction perpendicular to the aspect, a 6% of flat cells, a 52% of concave cells and a 42% of convex cells. Thus a prevalence of concave cells in Plan curvature is observed. This data must be critically evaluated because of error propagation through second derivatives starting from a low quality DEM. For release areas, the frequency distribution of the cumulative snow precipitation, during the period January 15th-18th 2017, is reported in Fig. 4.51 d). It is observed that in these areas the cumulative snowfall varies in a range between 382 and 506 cm. Furthermore, snow depth values greater than 459 cm were found in half areas. In Fig. 4.51 e) the release areas aspect distribution is shown. The main aspect presented by release areas is S-W (about 45% of total cells shows values in 3rd quadrant), but there are also a 24 % of cells in 1st quadrant, and a 20% of cells in 4th quadrant. During the days of interest, the perturbation mainly came from east/north/north-east with an average wind speed, at 2000 m, of 16 km/h. It is therefore observed that most of the release areas have opposite aspects with respect to the origin direction of the wind.

Majella Massif was subdivided into the Adriatic side and the Tyrrhenian side for which the same frequency analysis was performed. The statistical analysis carried out for different sides is reported in the following paragraphs.

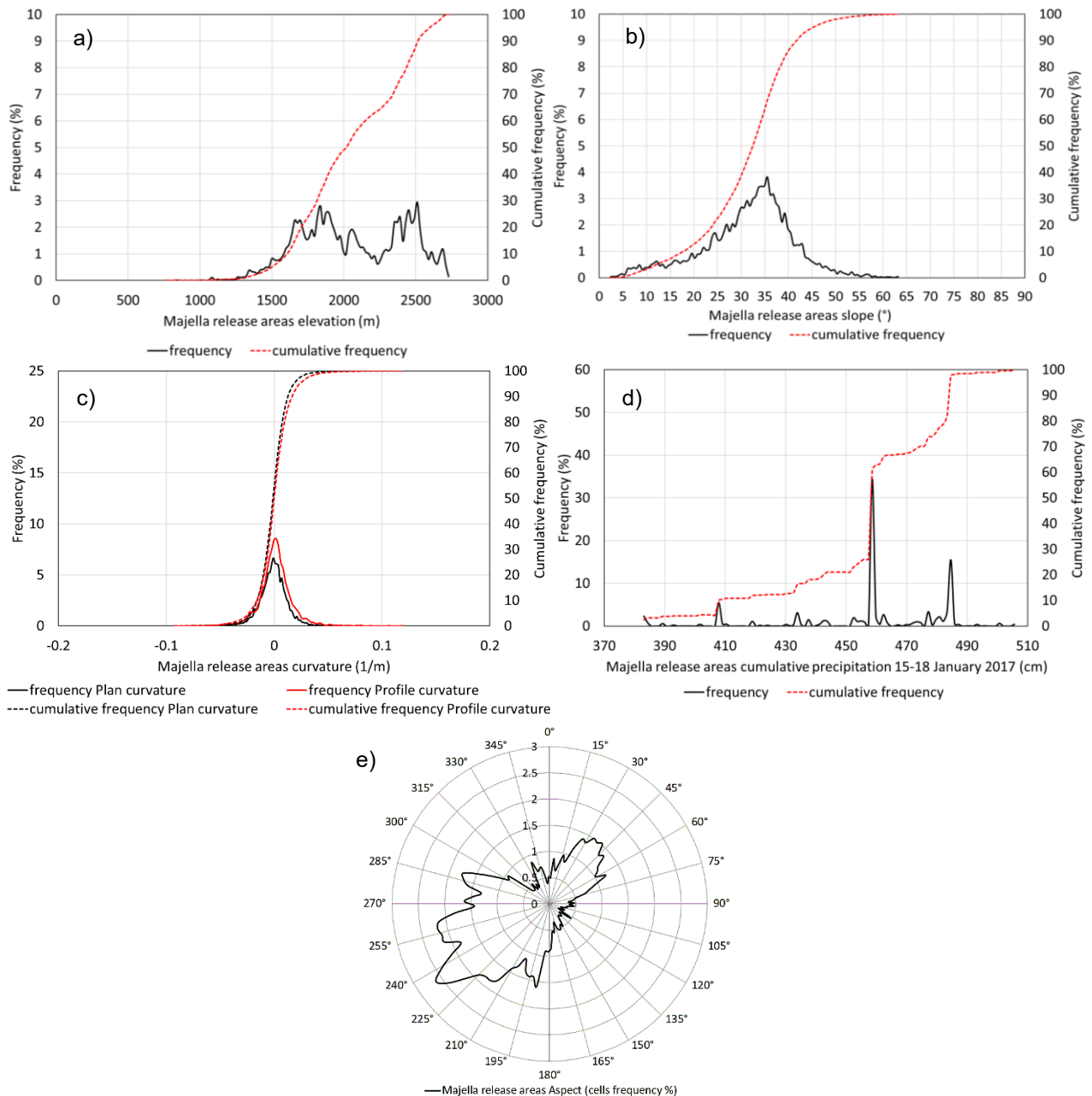


Fig. 4.51 Statistical analysis of the main topographic attributes a) elevation, b) slope, c) curvature d) cumulative snow precipitation and e) aspect carried out for Majella release areas extracted from mapped snow avalanches

4.4.9 Majella, Adriatic side, release areas

The statistical analysis carried out for release areas extracted in Majella Massif, Adriatic side, is shown below in Fig. 4.52. Fig. 4.52 a) shows the distribution of release areas elevation in the interested side of the mountain sector. It is observed that detachment areas are found in a range of altitudes between 1190 and 2740 m. It is observed that almost 47% of the cells have height values between 1190 and 2000 m. The remaining 53% shows values above 2000 m. Fig. 4.52 b) shows the distribution of release areas slope in Majella Adriatic Massif. Slopes are included in a range from 2° to 64°. The median is located around 31°. About 59% of the cells manifests values between 28° and 60°, which is the optimal range for which detachment is believed to occur. The remaining cells, about 41%, present values lower than 28°. Most likely, these values below 28° depending on low DEM quality. Fig. 4.52 c) shows the Plan and Profile curvatures frequencies distribution

for Majella Adriatic release areas. In detail, it is observed that about 8% of the cells have profile curvature values equal to 0, i.e. flat areas in the direction of maximum slope. The concave areas (negative values) are about 42% while the convex areas (positive values) are about 50%. With regard to Plan curvature, release areas present, in the direction perpendicular to the aspect, a 7% of flat cells, a 53% of concave cells and a 40% of convex cells. Thus a prevalence of concave cells in Plan curvature is observed. As mentioned, this data must be critically evaluated. For release areas, the frequency distribution of the cumulative snow precipitation, during the period January 15th-18th 2017, is reported in Fig. 4.52 d). It is observed that in these areas the cumulative snowfall varies in a range between 384 and 506 cm. Furthermore, snow depth values greater than 463 cm were found in half areas. In Fig. 4.52 e) the release areas aspect distribution is shown. The main aspect presented by release areas is N-E (about 42% of total cells shows values in 1st quadrant), but there are also a 23% of cells in 4th quadrant, and a 20% of cells in 3rd quadrant.

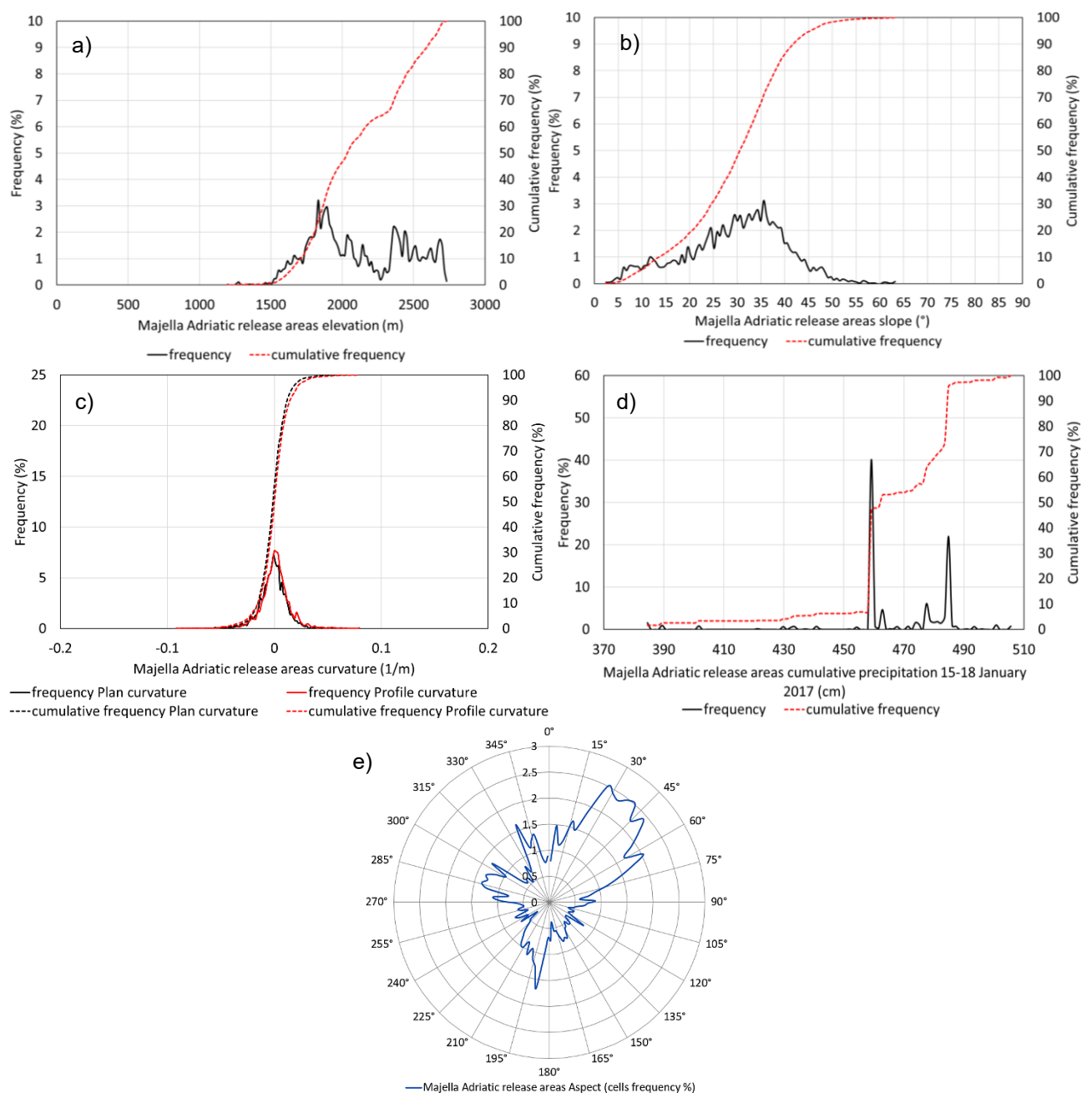
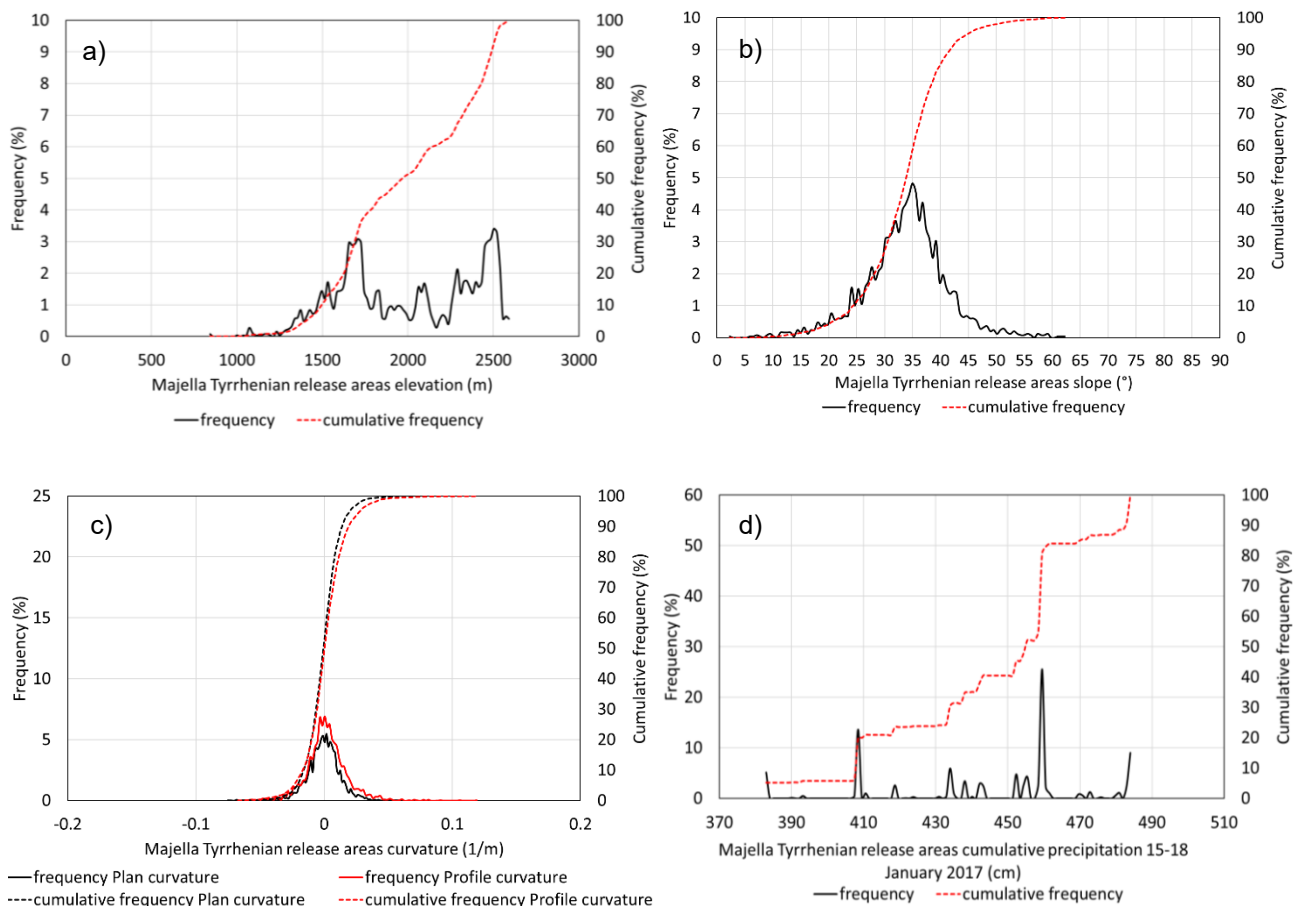


Fig. 4.52 Statistical analysis of the main topographic attributes a) elevation, b) slope, c) curvature d) cumulative snow precipitation and e) aspect carried out for Majella Adriatic release areas extracted from mapped snow avalanches

4.4.10 Majella, Tyrrhenian side, release areas

The statistical analysis carried out for release areas extracted in Majella Massif, Tyrrhenian side, is shown below in Fig. 4.53. Fig. 4.53 a) shows the distribution of release areas elevation in the interested side of the mountain sector. It is observed that detachment areas are found in a range of altitudes between 830 and 2600 m. It is observed that almost 51% of the cells have height values between 1000 and 2000 m. The remaining 49% shows values above 2000 m. Fig. 4.53 b) shows the distribution of release areas slope in Majella Tyrrhenian Massif. Slopes are included in a range from 2° to 63°. The median is located around 34°. About 80% of the cells manifests values between 28° and 60°, which is the optimal range for which detachment is believed to occur. The remaining cells, about 20%, present values lower than 28°. These values below 28° depending on low quality DEM. Fig. 4.53 c) shows the Plan and Profile curvatures frequencies distribution for Majella Tyrrhenian release areas. In detail, it is observed that about 5% of the cells have profile curvature values equal to 0, i.e., flat areas in the direction of maximum slope. The concave areas (negative values) are about 44% while the convex areas (positive values) are about 51%. With regard to Plan curvature, release areas present, in the direction perpendicular to the aspect, a 5% of flat cells, a 49% of concave cells and a 46% of convex cells. Thus a prevalence of concave cells in Plan curvature is observed. This data must be critically evaluated because of error propagation through second derivatives starting from a low quality DEM. For release areas, the frequency distribution of the cumulative snow precipitation, during the period January 15th-18th 2017, is reported in Fig. 4.53 d). It is observed that in these areas the cumulative snowfall varies in a range between 383 and 485 cm. Furthermore, snow depth values greater than 456 cm were found in half areas. In Fig. 4.53 e) the release areas aspect distribution is shown. The main aspect presented by release areas is S-W (about 80% of total cells shows values in 3rd quadrant), but there is also a 16% of cells that present values in 4th quadrant.



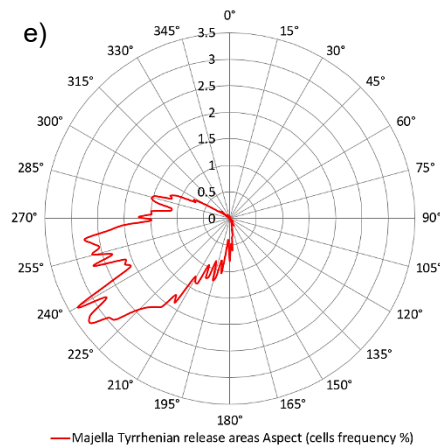


Fig. 4.53 Statistical analysis of the main topographic attributes a) elevation, b) slope, c) curvature d) cumulative snow precipitation (previous page) and e) aspect carried out for Majella Tyrrhenian release areas extracted from mapped snow avalanches.

4.4.11 Sibillini release areas

The statistical analysis carried out for release areas extracted in the Sibillini Mountains is shown below in Fig. 4.54. Fig. 4.54 a) shows the distribution of release areas elevation in the interested mountain sector. Firstly, it is observed that detachment areas are found in a range of altitudes between 1000 and 2450 m. It is observed that 77% of the cells have height values between 1000 and 2000 m. The remaining 23% shows values above 2000 m. Fig. 4.54 b) shows the distribution of release areas slope in Sibillini mountains. Slopes are included in a range from 0° to 65°. The median is located around 33°. About 72% of the cells manifests values between 28° and 60°, which is the optimal range for which detachment is believed to occur. The remaining cells, about 28 %, present values lower than 28°. Most likely, these values below 28° depending on low quality DEM. Fig. 4.54 c) shows the Plan and Profile curvatures frequencies distribution for Sibillini release areas. It is observed that Profile and Plan curvature are symmetrical with respect to 0, therefore, in the aspect direction, and in the perpendicular direction, the found structures are about 50% concave and about 50% convex. As already mentioned, this data must be critically evaluated. In fact, what is expected in correspondence to release areas is a prevalence of negative values curvature, which corresponds to concave areas. The result obtained, in fact, is indeed subject to error since the curvature corresponds to the second derivative of the DEM which, as described in paragraph 4.3, does not appear to be of excellent quality. For release areas, the frequency distribution of the cumulative snow precipitation, during the period January 15th-18th 2017, was also evaluated and reported in Fig. 4.54 d). It is observed that in these areas the cumulative snowfall varies in a range between 383 and 459 cm. Furthermore, after the 3 days considered, snow depth values greater than 459 cm were found in half areas. In Fig. 4.54 e) the release areas aspect distribution is reported. It is observed that there is no prevalent exposure of Sibillini release areas. During the days of interest, the perturbation mainly came from north-east/east with an average wind speed, at 2000 m, of 29 km/h. The axis of the mountain range turns out to be approximately tangent to the prevailing direction of perturbation. For this reason, all the mountain sides were loaded by huge layers of snow that caused the releases. There is a slight prevalence of release areas in the second and third quadrant (90°-270°).

The mountain sector of the Sibillini was subdivided into the Adriatic side and the Tyrrhenian side for which the same frequency analysis was performed. The statistical analysis carried out for different sides is reported in the following paragraphs.

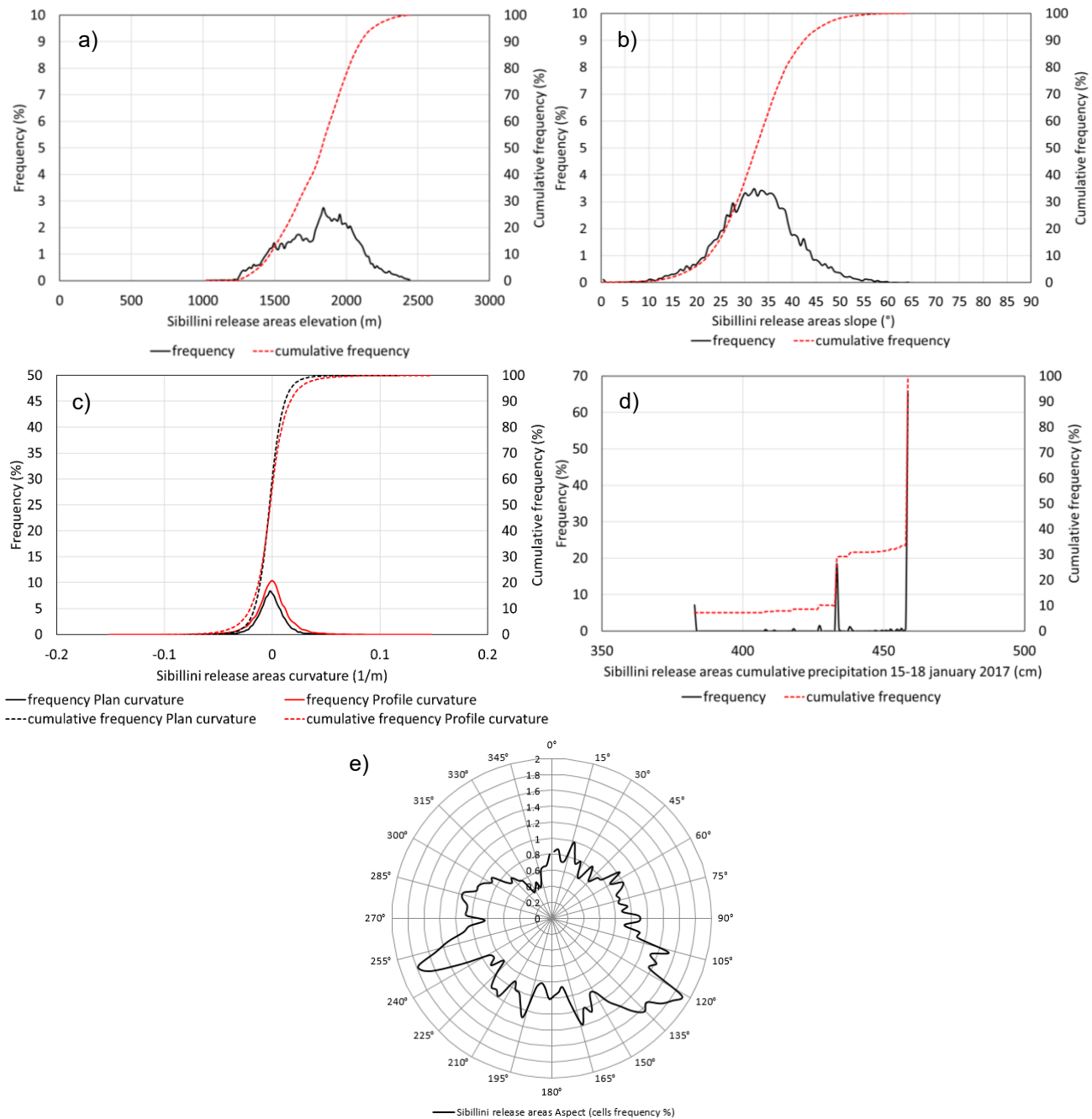


Fig. 4.54 Statistical analysis of the main topographic attributes a) elevation, b) slope, c) curvature d) cumulative snow precipitation and e) aspect carried out for Sibillini release areas extracted from mapped snow avalanches

4.4.12 Sibillini, Adriatic side, release areas

The statistical analysis carried out for release areas extracted in the Sibillini Mountains, Adriatic side, is shown below in Fig. 4.55. Fig. 4.55 a) shows the distribution of release areas elevation in the interested side of the mountain sector. It is observed that detachment areas are found in a range of altitudes between 1000 and 2450 m. It is observed that almost 73% of the cells have height values between 1000 and 2000 m. The remaining 27% shows values above 2000 m. Fig. 4.55 b) shows the distribution of release areas slope in Sibillini Adriatic mountains. Slopes are included in a range from 1° to 65°. The median is located around 34°. About 78% of the cells manifests values between 28° and 60°, which is the optimal range for which detachment is believed to occur. The remaining cells, about 22%, present values lower than 28°. Most likely, these values below 28° depending on low

quality DEM. Fig. 4.55 c) shows the Plan and Profile curvatures frequencies distribution for Sibillini Adriatic release areas. It is observed that Profile curvature is symmetrical with respect to 0, therefore, in the aspect direction, excluding plan areas, the found structures are about 50% concave and about 50% convex. Plan curvature presents a slight asymmetry for which about 60 % of total cells present a negative value, while the remaining 40% shows positive values. Therefore, in the aspect perpendicular direction, concave structures are prevalent. As already mentioned, this data must be critically evaluated because of error propagation through second derivatives starting from a low quality DEM. For release areas, the frequency distribution of the cumulative snow precipitation, during the period January 15th-18th 2017, is reported in Fig. 4.55 d). It is observed that in these areas the cumulative snowfall varies in a range between 408 and 459 cm. Furthermore, snow depth values greater than 459 cm were found in half areas. In Fig. 4.55 e) the release areas aspect distribution is shown. The main aspect presented by release areas is S-E (about 42 % of total cells shows values in 3rd quadrant), but there is also a 30 % of cells that present values in 1st quadrant.

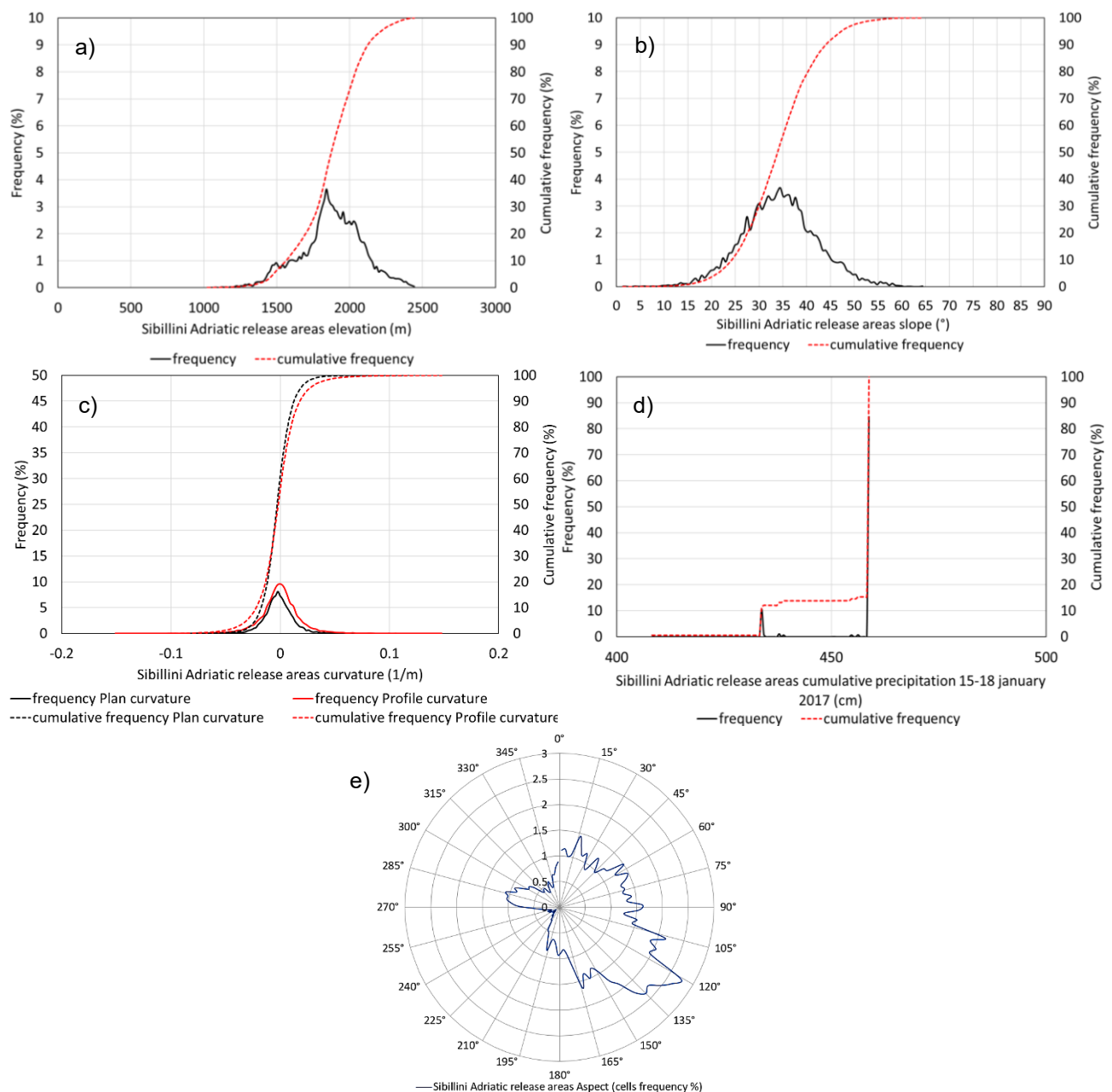
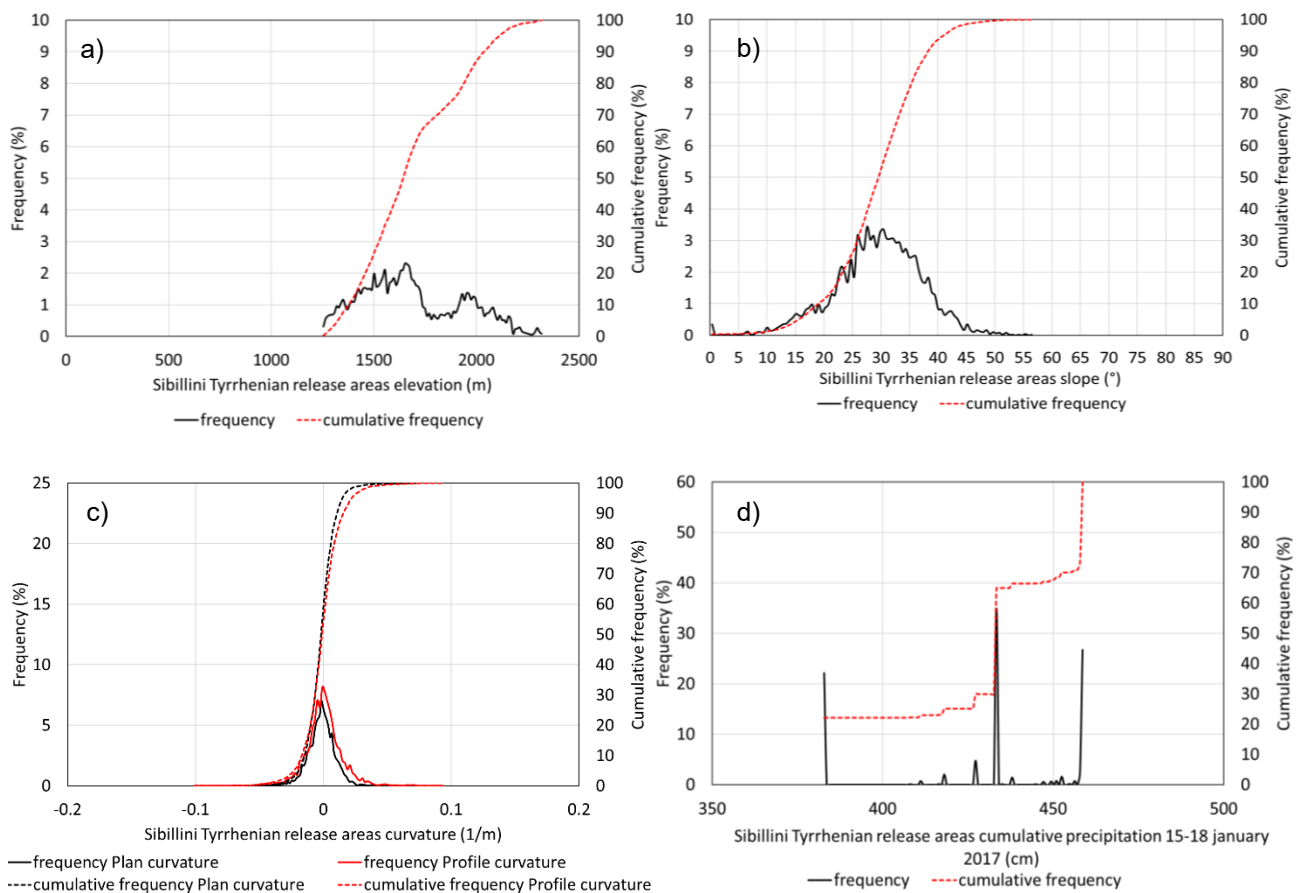


Fig. 4.55 Statistical analysis of the main topographic attributes a) elevation, b) slope, c) curvature d) cumulative snow precipitation and e) aspect carried out for Sibillini Adriatic release areas extracted from mapped snow avalanches

4.4.13 Sibillini, Tyrrhenian side, release areas

The statistical analysis carried out for release areas extracted in the Sibillini Mountains, Tyrrhenian side, is shown below in Fig. 4.56. Fig. 4.56 a) shows the distribution of release areas elevation in the interested side of the mountain sector. It is observed that detachment areas are found in a range of altitudes between 1250 and 2300 m. It is observed that almost 87% of the cells have height values between 1250 and 2000 m. The remaining 13% shows values above 2000 m. Fig. 4.56 b) shows the distribution of release areas slope in Sibillini Tyrrhenian mountains. Slopes are included in a range from 0° to 57°. The median is located around 30°. About 57% of the cells manifests values between 28° and 60°, which is the optimal range for which detachment is believed to occur. The remaining cells, about 43%, present values lower than 28°. These values below 28° depending on low quality DEM. Fig. 4.56 c) shows the Plan and Profile curvatures frequencies distribution for Sibillini Tyrrhenian release areas. In detail, it is observed that about 8% of the cells have Profile curvature values equal to 0, i.e., flat areas in the direction of maximum slope. The concave areas (negative values) are about 42% while the convex areas (positive values) are about 50%. With regard to Plan curvature, release areas present, in the direction perpendicular to the aspect, a 6% of flat cells, a 60% of concave cells and a 34% of convex cells. Thus a prevalence of concave cells in Plan curvature is observed. Anyhow, this data must be critically evaluated because of error propagation through second derivatives starting from a low quality DEM. For release areas, the frequency distribution of the cumulative snow precipitation, during the period January 15th-18th 2017, is reported in Fig. 4.56 d). It is observed that in these areas the cumulative snowfall varies in a range between 383 and 459 cm. Furthermore, snow depth values greater than 434 cm were found in half areas. In Fig. 4.56 e) the release areas aspect distribution is shown. The main aspect presented by release areas is S-W (about 66 % of total cells shows values in 3rd quadrant), but there is also a 21 % of cells that present values in 4th quadrant.



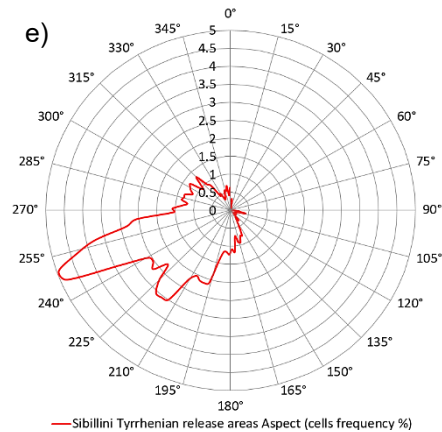


Fig. 4.56 Statistical analysis of the main topographic attributes a) elevation, b) slope, c) curvature d) cumulative snow precipitation (previous page) and e) aspect carried out for Sibillini Tyrrhenian release areas extracted from mapped snow avalanches

4.4.14 Sirente Velino release areas

The statistical analysis carried out for release areas extracted in the Sirente Velino Mountains is shown below in Fig. 4.57. Fig. 4.57 a) shows the distribution of release areas elevation in the interested mountain sector. Firstly, it is observed that detachment areas are found in a range of altitudes between 1415 and 2430 m. It is observed that 42% of the cells have height values between 1415 and 2000 m. The remaining 58% shows values above 2000 m. Fig. 4.57 b) shows the distribution of release areas slope in the Sirente Velino Mountains. Slopes are included in a range from 4° to 63°. The median is located around 32°. About 70% of the cells manifests values between 28° and 60°, which is the optimal range for which detachment is believed to occur. The remaining cells, about 30%, present values lower than 28°. Most likely, these values below 28° depending on low quality DEM. Fig. 4.57 c) shows the Plan and Profile curvatures frequencies distribution for Sirente Velino Mountains release areas. In detail, it is observed that about 12% of the cells have Profile curvature values equal to 0, i.e. flat areas in the direction of maximum slope. The concave areas (negative values) are about 40% while the convex areas (positive values) are about 48%. With regard to Plan curvature, release areas present, in the direction perpendicular to the aspect, a 5% of flat cells, a 46% of concave cells and a 49% of convex cells. Thus a prevalence of convex cells in Plan curvature is observed. This data must be critically evaluated because of error propagation through second derivatives starting from a low quality DEM. For release areas, the frequency distribution of the cumulative snow precipitation, during the period January 15th-18th 2017, is reported in Fig. 4.57 d). It is observed that in these areas the cumulative snowfall varies in a range between 280 and 408 cm. Furthermore, snow depth values greater than 316 cm were found in half areas. In Fig. 4.57 e) the release areas aspect distribution is shown. The main aspect presented by release areas is S-W (about 50% of total cells shows values in 3rd quadrant), but there are also a 15 % of cells in 1st quadrant. During the days of interest, the perturbation mainly came from the east with an average wind speed, at 2000 m, of 33 km/h. It is observed that part of release areas has opposite aspects with respect to the origin direction of the wind, but the greater part has S-W aspect. This is probably due to a wind velocity peak of 48 km/h coming from N-E.

Sirente Velino was not subdivided into the Adriatic and Tyrrhenian side because it is an internal massif so that, it can be considered as a Tyrrhenian massif.

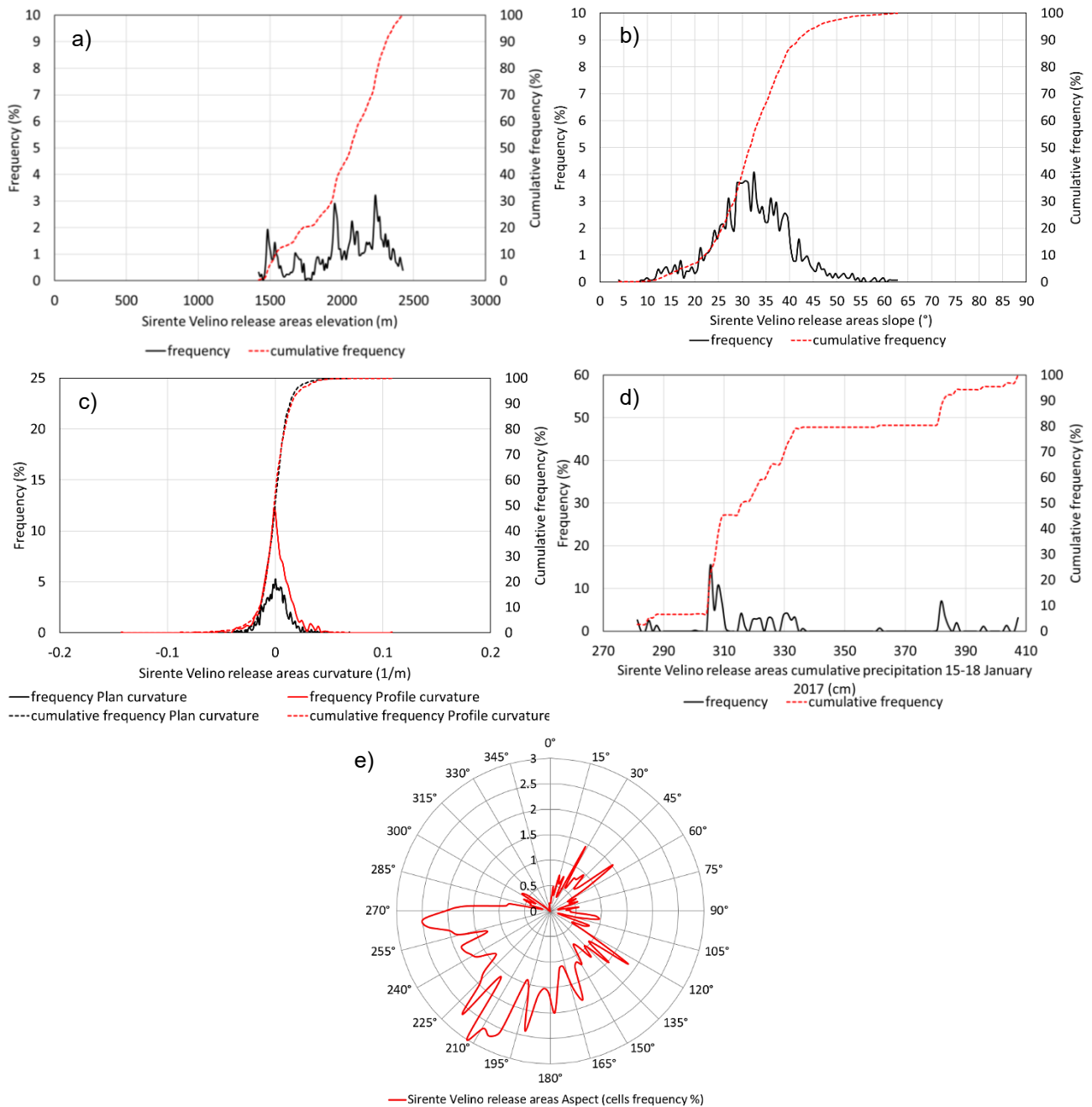


Fig. 4.57 Statistical analysis of the main topographic attributes a) elevation, b) slope, c) curvature d) cumulative snow precipitation and e) aspect carried out for Sirente Velino release areas extracted from mapped snow avalanches

4.4.15 Mountain sectors release areas compared

Following the statistical analysis of interested mountain sectors and their respective Adriatic and Tyrrhenian sides, it is possible to compare the different distributions obtained. Before doing so, however, it was evaluated the number of events that occurred in each mountain sector by relating it to the release areas extension, as reported in Fig. 4.58. It is observed that, except for Laga Mountains, the highest number of events were found on the Adriatic sides. Observing the trend of release areas extension, it is noted that where there are more events there is also a more significant release areas extension, but this data must be analyzed critically. In Sibillini Mountains the events number occurred on the Adriatic and Tyrrhenian sides is comparable, but release areas extension presents a difference of about 3 km². This means that snow avalanches of the Adriatic side were of greater magnitude, affecting large release areas. In Laga Mountains events number is

comparable on the two sides, but the most significant extension is found on the Tyrrhenian side (with a difference of about 2 km²). In this case, events of higher magnitude occurred on the Tyrrhenian side. In the Majella Massif, Adriatic side, there were 27 events more than the Tyrrhenian side. Despite this, release areas extension is comparable on both sides. This leads to say that the events of stronger magnitude occurred on the Tyrrhenian side. This reasoning cannot be conducted for the Gran Sasso Massif, since the difference in extension could merely be related to the higher number of events occurring on the Adriatic side (15 more compared to the Tyrrhenian side).

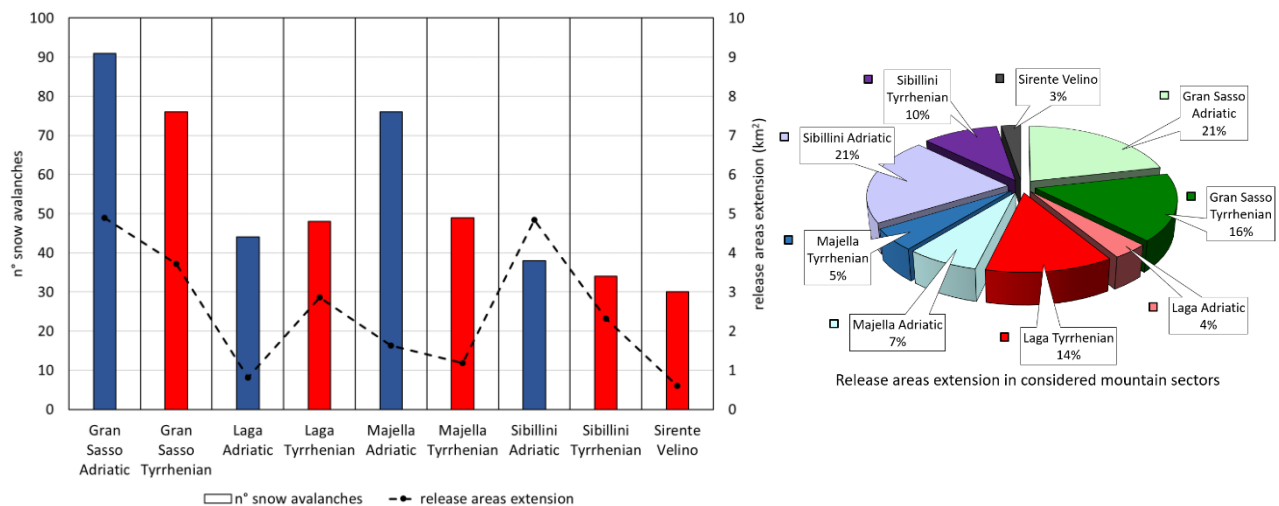


Fig. 4.58 Number of events that occurred in each mountain sector, Adriatic and Tyrrhenian sides, in relation with release areas extension (on the left) and distribution of release areas extension in considered mountain sectors (on the right)

Below is reported the comparison between the various mountain sectors with regard to the primary topographic attributes and the cumulative snow precipitation.

Elevation

In Fig. 4.59 is reported the comparison, through boxplots, between release areas elevation distributions of considered mountain sectors, also differencing for the Adriatic and Tyrrhenian side. From the comparison, it emerged that release areas at higher altitudes are those of Gran Sasso and Majella Massifs. This, in the first place, may be due to the fact that the two massifs intrinsically present higher altitudes than the others. It is noted that the trend of release areas maximum elevation follows the trend of mountain sectors maximum elevation. Regarding minimum values, despite the mountain sectors present a constant value (about 500 m following the altitude filter used), the trend of release areas minimum elevation shows some differences. This is, in part, an indicator of the altimetric areas where more snow layers were accumulated. As regards Gran Sasso, there are no significant differences between Adriatic and Tyrrhenian sides. In the Majella Massif it is observed that distributions are similar even if, on the Adriatic side, release areas are found at higher altitudes compared to the Tyrrhenian side. The same is true for Sibillini mountains. On the other hand, it is observed that the Laga Mountains present release areas at a lower elevation on the Adriatic side. Having regard to the direction of perturbation in the period of interest, coming from north-east/east, it is possible to explain a higher release areas elevation on the Tyrrhenian sector of Laga Mountains. Since the axis of the mountain range is substantially perpendicular to the perturbation, in the upwind sector the Stau effect is obtained while on the leeward sector a Fohn current is generated and it allowed

the snow accumulation in the higher part of the mountain range and, therefore, releases. This phenomenon is less pronounced for Majella and Sibillini Mountains because the main ridges are, on average, more aligned with the perturbation. Moreover, Sirente Velino, despite it shows elevation values below Gran Sasso and Majella, presents release areas with elevation comparable with those of the main massifs. It is noted that the altitude average values of release areas are always higher than the elevation average values of respective mountain sector. The difference between mean values is on average 650 m. Looking at every single massif, there is a good matching between altitude average values of release areas and those of the sector considered. In general, we can conclude that release areas elevation indeed depends on the intrinsic altitude of the mountain sector to which they belong, but in some cases, the meteorological context can lead to some variations.

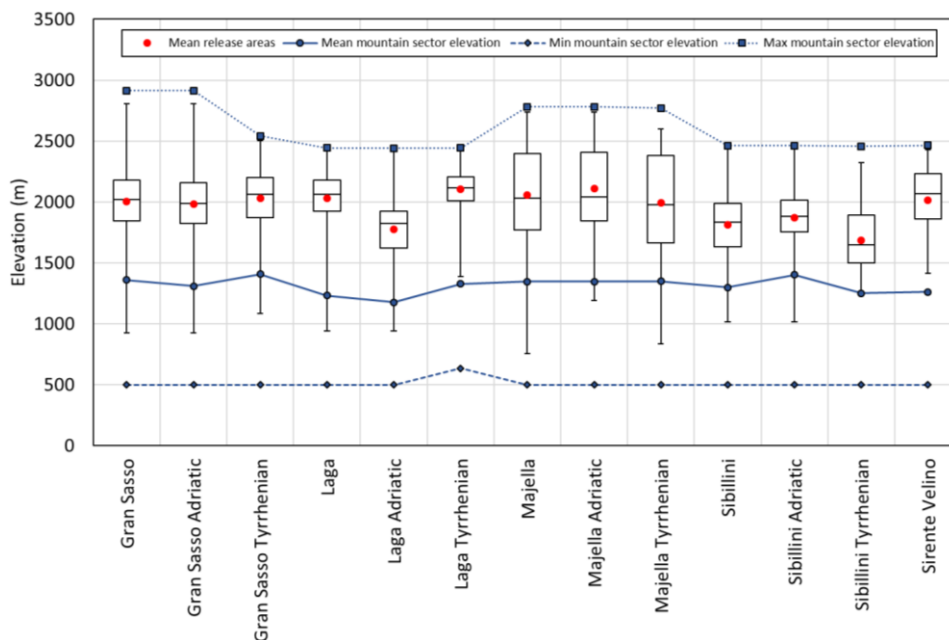


Fig. 4.59 Comparison, through boxplots (minimum, 1st quartile, median, 3rd quartile, maximum and mean) between elevation distributions of release areas in considered mountain sectors, also differencing for Adriatic and Tyrrhenian side. Min, Max and Mean values of mountain sectors elevation are reported for a further comparison

Slope

In Fig. 4.60 is reported the comparison, through boxplots, between release areas slope distributions of considered mountain sectors, also differencing for the Adriatic and Tyrrhenian side. Regarding slope, there are no significant differences between release areas of interested mountain sectors and, within the same sector, between release areas of the Adriatic and Tyrrhenian side. In general, there are higher slopes on the Adriatic sides release areas, except for the Majella Massif. In any case, any differences are merely due to the morphological structure of the slopes caused by the tectonic formation of the mountain range. In fact, observing maximum and average slope values for the mountain sectors, we see a good matching with the average slope values for release areas. The only exception is presented by the Majella Massif because, despite the Adriatic side is on average more sloping than the Tyrrhenian side, release areas with greater slope were found in this last sector. Four typical sections of the interested mountain sectors are represented in Fig. 4.61. These sections allow visualizing, on a large scale, the morphological structure of mountain sectors. Most of the release areas slope values are found, for all the distributions, in the range between 28° and 45°. It is considered, from literature, the optimal range that favors detachment. Slope data

above 60° (too steep) and below 28° (too flat), since this range is deeply consolidated, can be attributed to outliers due to a low quality DEM.

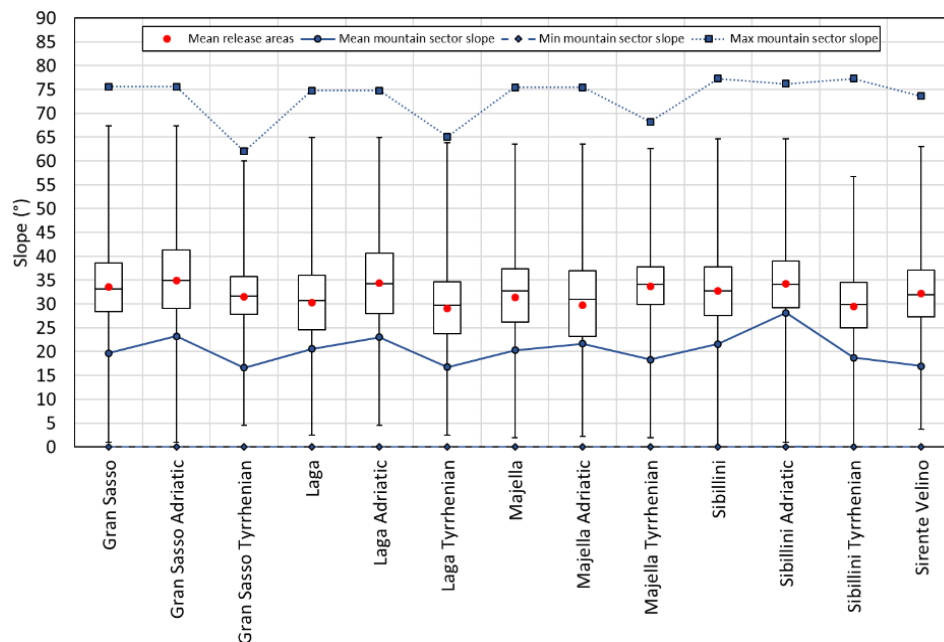


Fig. 4.60 Comparison, through boxplots (minimum, 1st quartile, median, 3rd quartile, maximum and mean) between slope distributions of considered mountain sectors, also differencing for Adriatic and Tyrrhenian side. Min, Max and Mean values of mountain sectors slope are reported for a further comparison

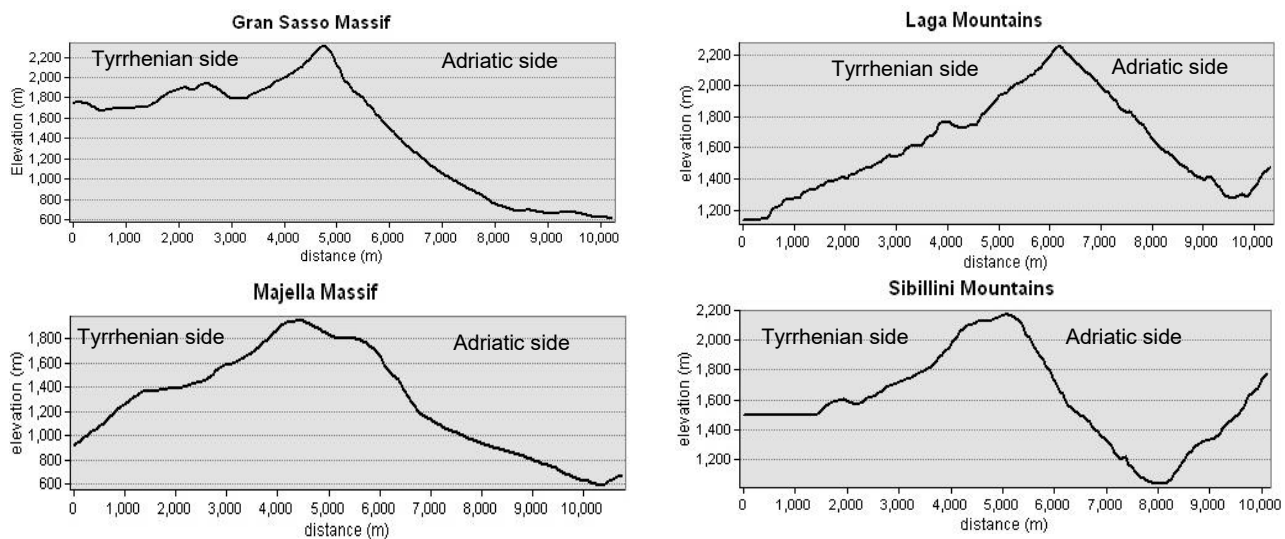


Fig. 4.61 Four typical sections of the interested mountain sectors. The distance 0 refers to a point in Tyrrhenian side of mountain range. As the distance increases, you are moving from the Tyrrhenian to the Adriatic side

Aspect

In Fig. 4.62 and in Fig. 4.63 are reported the comparisons, through boxplots and polar graphs, between release areas aspect distributions of considered mountain sectors, also differencing for the Adriatic and Tyrrhenian side. All the mountain sectors, considered as a whole, present release areas with an average exposure of about 180° (South). Another observation is that all the release areas in Tyrrhenian sectors present a much more concentrated distribution than the Adriatic ones. This is mainly due to the orographic constraint, present in downwind slopes, which leads to channeling of flows, loading with snow only areas that

intercept and obstruct such flows. In particular, it is noted that almost all the exposure values of release areas in the Tyrrhenian sides are between 180° and 270° (South-West). This is because flows were channeled mainly in the orographic structures with opposite exposure concerning the origin direction of perturbation. On the other hand, in the windward sides, more turbulence is generated and it leads to having release areas in an expanded range of aspects since more areas can intercept the flows. The average exposure of release areas in the Adriatic sides is between 90° and 180° (South-East) also if, especially in the Gran Sasso and Majella massifs, particularly expanded distributions can be seen on the Adriatic side. This can be attributed to many factors: in the first place, the turbulent regime, on the Adriatic side, leads to an indiscriminate loading of all areas, regardless of their exposure; in second place, it may also depend on the morphology of the mountain massif. Majella Massif, for example, is characterized by a rounded shape and, for this reason, it is more prone to homogeneous snow loading even if the prevailing direction of the perturbation varies. Finally, another simple reason is to be found in the extent and the orographic complexity of mountain massifs: Gransasso and Majella Massifs are indeed the largest massifs in Central Apennines and they include, more likely, areas with more varied exposures. As already mentioned, in the Sibillini Mountains there is not a common release areas aspect. In this case, the explanation can be found in the reciprocal position between the main ridge of the chain and the origin direction of the perturbation. Indeed, the winds, especially towards the end of the perturbation, rotated counterclockwise, blowing from North / North-East. The mountain range is roughly parallel to the perturbation direction, so the loading has been more homogeneous. Despite this, on the downwind side the channeling of flows has led to release areas with a concentrated exposure between 225° and 270°. It is also noted that release areas of Sirente Velino, despite it is an internal massif for which we expected a more concentrated distribution, present most of the exposure values in a reasonably wide range between 135° and 225°.

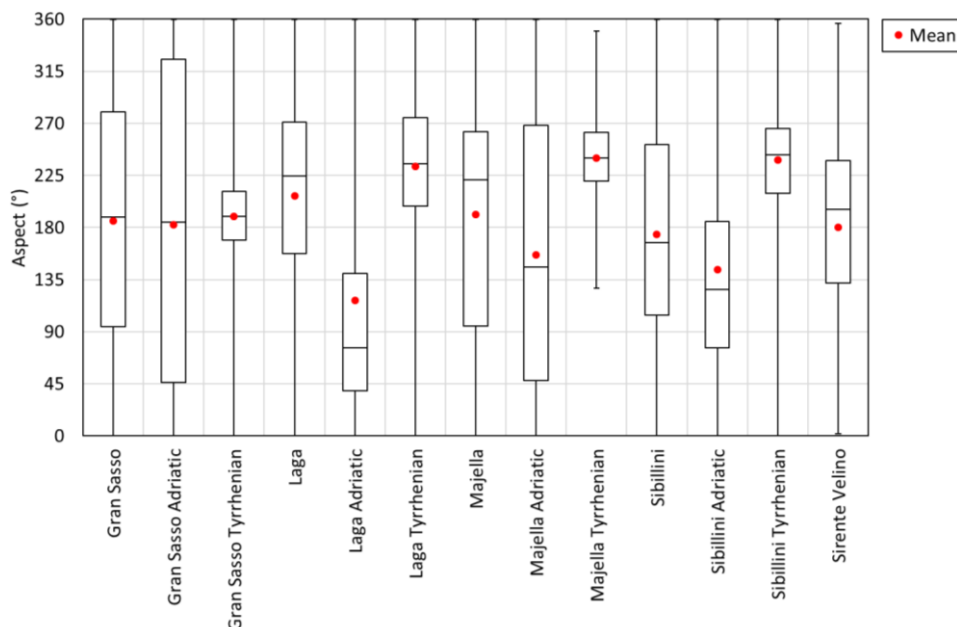


Fig. 4.62 Comparison, through boxplots (minimum, 1st quartile, median, 3rd quartile, maximum and mean) between aspect distributions of considered mountain sectors, also differencing for Adriatic and Tyrrhenian side.

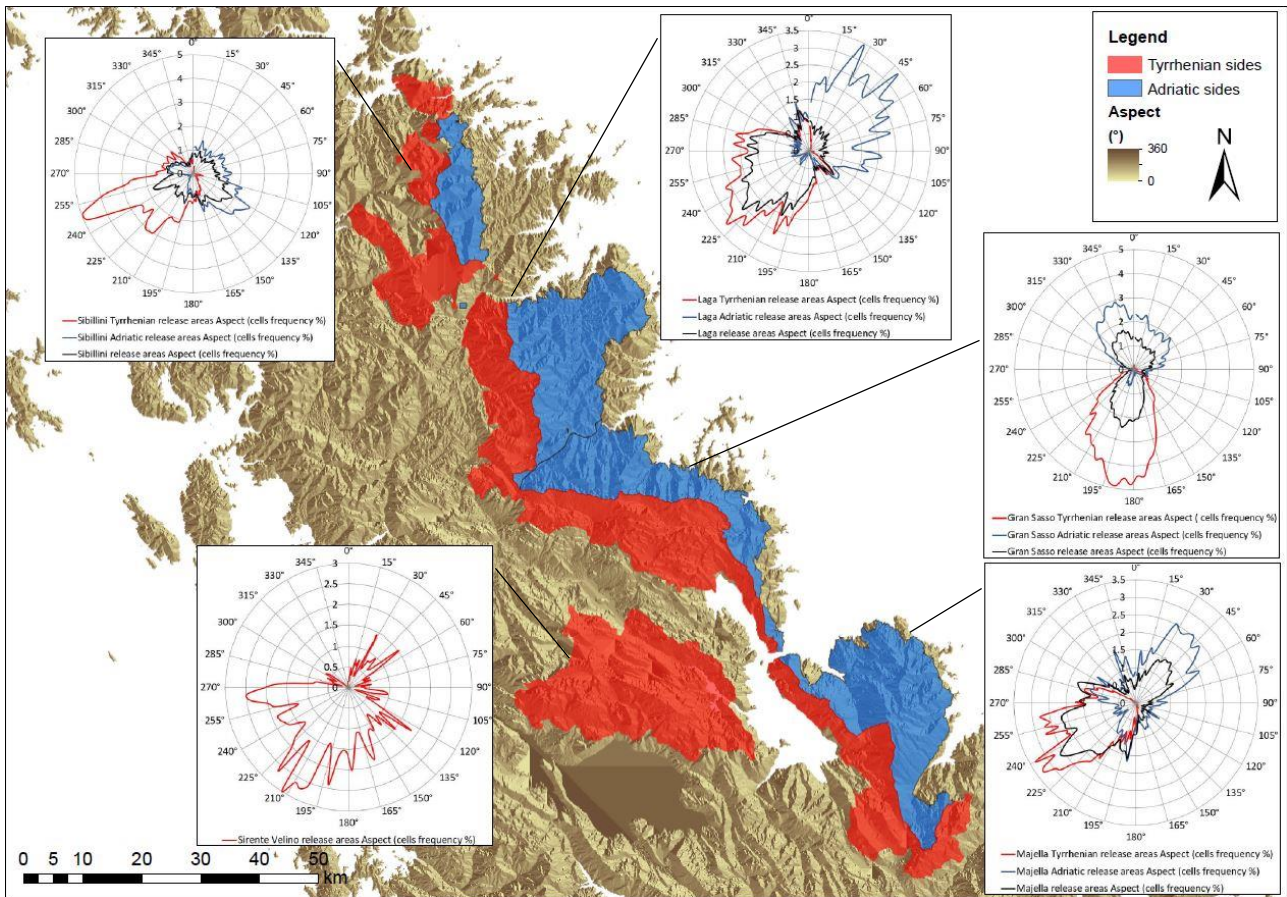


Fig. 4.63 Comparisons, through polar graphs, between release areas aspect distributions of considered mountain sectors, also differencing for Adriatic and Tyrrhenian side. The subdivision of mountain sectors in Adriatic and Tyrrhenian sides, performed for the calculation, is reported.

Curvature

In Fig. 4.64 and Fig. 4.65 is reported the comparison, through boxplots, between release areas Plan and Profile curvature distributions of considered mountain sectors, also differencing for the Adriatic and Tyrrhenian side.

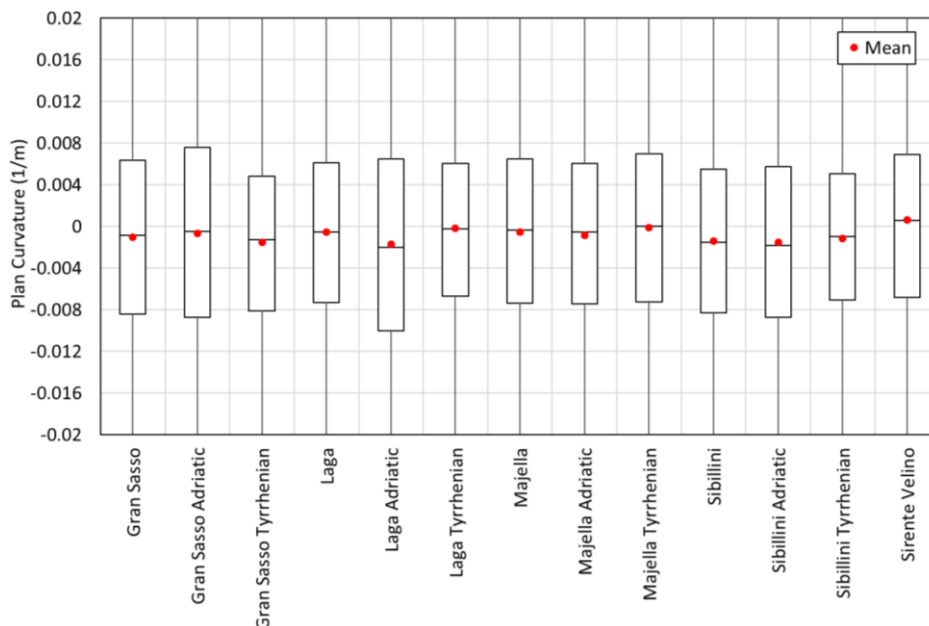


Fig. 4.64 Comparison, through boxplots (minimum, 1st quartile, median, 3rd quartile, maximum and mean) between Plan curvature distributions of considered mountain sectors, also differencing for Adriatic and Tyrrhenian side.

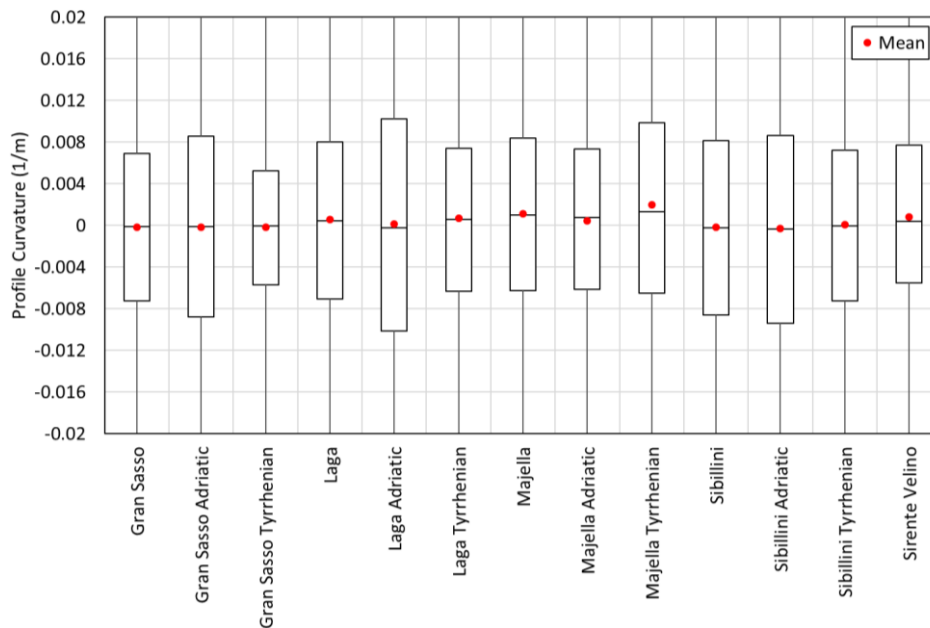


Fig. 4.65 Comparison, through boxplots (minimum, 1st quartile, median, 3rd quartile, maximum and mean) between Profile curvature distributions of considered mountain sectors, also differencing for Adriatic and Tyrrhenian side.

From an initial analysis of the data it is observed that release areas, in all the mountain sectors, present very similar values, not showing particular differences between Adriatic and Tyrrhenian side. So that data could be appropriately described, the boxplots must be displayed in the neighborhood of 0. Therefore, the minimum and maximum curvature values are not displayed. Regarding release areas Plan curvature, it is observed that almost all distributions have a negative median value. This means that more than 50% of values shows negative Plan curvature. These values correspond to concave areas, in the direction perpendicular to the maximum slope, which are the ones more appropriate to accumulate snow. In the Majella sector, Tyrrhenian side, there is a median practically equal to 0 and the first and third quartiles are practically symmetrical, while in the Sirente Velino the median is positive and therefore there is a prevalence of convex cells. As regards the values of Profile curvature, it is observed that in the Gran Sasso and in the Sibillini the median is practically equal to 0 and the first and third quartiles are practically symmetrical. In the mountains of Laga, Majella and Sirente Velino the median is instead slightly above 0: consequently, there is a prevalence of convex cells in the direction of steepest descent. Exceptions are the Laga Mountains, Adriatic side, where the median is negative. We expected, from these distributions, a significant presence of concave structures since, as already mentioned, they are the ones that allow the accumulation of snow and therefore the snow avalanches releases. It must, however, be stressed that this data must be critically evaluated because of error propagation through second derivatives starting from a low-quality DEM.

Cumulative snow precipitation

In Fig. 4.66 is reported the comparison, through boxplots, between release areas cumulative snow precipitation distributions of considered mountain sectors, also differencing for the Adriatic and Tyrrhenian side. The data obtained allow us to see those release areas in which the greatest cumulative snow precipitation values were recorded are those present in the Gran Sasso Massif and in Laga Mountains. Then follow, in order, release areas of the Majella Massif, Sibillini and finally those of Sirente Velino Mountains. As mentioned, release areas in which more snow was

accumulated are those of Gran Sasso Massif. This is due to the fact that the massif in question is very high, presenting peaks that reach even 2900 m. Being the chain very high, the phenomenon of the Stau is more accentuated allowing the formation of clouds and, therefore, of snowfall. According to this reasoning in the Majella Massif, there should be values comparable to those found in the Gran Sasso. This did not happen most likely due to the rounded shape of the massif that tends to force less the displacement of air upward. We can see instead that, in the Laga Mountains, the cumulative values are comparable to those of the Gran Sasso despite the lower altitudes. This can be caused by the fact that the massif has allowed a greater orographic elevation since the main ridge is perpendicular to the direction of the perturbation. By observing the number of snow avalanches mapped in each sector, a good matching can be found between the number of events and the cumulative precipitation values. There is, therefore, a higher number of events in sectors where there were more snowfalls. The only exception is found for events occurred in Laga Mountains, Adriatic and Tyrrhenian sides. Although on release areas of the Adriatic side there are higher cumulative values, in the Tyrrhenian side there are 4 more events. It's interesting as, considering individually the Sibillini, Tyrrhenian side, and the Serente Velino, despite very different cumulative values, the number of events is almost identical (even in this case there is a gap of only 4 events).

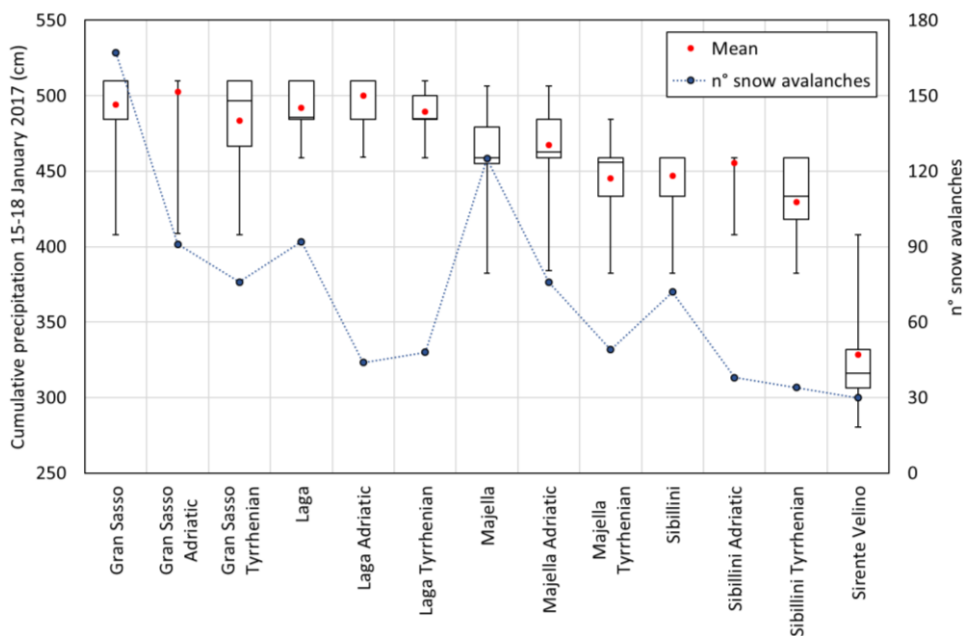


Fig. 4.66 Comparison, through boxplots (minimum, 1st quartile, median, 3rd quartile, maximum and mean) between cumulative snow precipitation distributions of considered mountain sectors, also differencing for Adriatic and Tyrrhenian side.

4.5 Potential Release Areas (PRA) delineation algorithms

The definition of semi-automatic procedures for the determination of Potential Release Areas (PRA) is crucial for the snow avalanche risk management. These areas can be used for prevention purposes and to evaluate the priority of protection works on the territory. Together with other evaluations, PRA can also be used to create hazard or risk maps. In the latter case, information on exposure and vulnerability (of structures) must be available. GIS techniques, together with a digital terrain model (DEM), lend themselves well to the creation of such procedures that can be applied to different regions (Maggioni, 2004). Below, two possible algorithms for PRA delineation, used in our case study, are described.

4.5.1 Maggioni (2004)

After having performed the snow avalanches real release areas characterization, obtained from events perimeters through photo-interpretation, a semi-automatic procedure that allows defining the potential release areas (PRA) was applied. This procedure is based on some topographic features. Basically, starting from the primary topographic attributes and the land cover, we follow a chain of consecutive filtering that leads to the definition of the PRA. The filtering criteria are chosen on the basis of the typical values, drawn from literature, of predisposing causes (Maggioni, 2004). The parameters that have been used are forest cover, slope, curvature, main ridges, size, aspect and height difference (Maggioni, 2004).

Assuming DEM as the starting point, the primary topographic attributes, i.e., slope, aspect and curvature, can be calculated. As already defined above, it is well known that forest cover leads to preventing detachment, so much that it can also act as a protective element for snow avalanches (Maggioni, 2004). For this reason, first filtering was carried out by subtracting all the areas covered by the forest from the starting DEM. To do this we used the Corine Land Cover 2012, IV level, retrieved from Geoportale Nazionale, and all areas corresponding to “boschi di conifere”, “boschi di latifoglie” and “boschi misti di conifere e latifoglie” were excluded from starting DEM. For remaining areas, slope values were extracted. It is known that typical slope values for release areas are those between 30° and 60°, so only areas that respect this criterion have been considered.

At this point, there will be a wide single release area consisting of areas without forest and with a slope between 30° and 60°. We tried to divide this area into smaller units that can refer, in principle, to individual snow avalanches events (Maggioni, 2004). To do this, the ridges have been calculated. The latter, in fact, separate the different basins and therefore are used as an element of separation. To calculate the ridges, we used a different algorithm than the one suggested by Maggioni (2004). The algorithm used to calculate the ridges basically involves the calculation of a negative DEM (allowing to invert ridges and valleys) and to use it as input for the usual procedure used for the calculation of the flow grids, which in this case will correspond to the ridges. The original procedure for the calculation of the ridges involved the construction of two TINs (Triangular Irregular Network) with a resolution of 10 and 50 m. Starting from these TINs, it is necessary to calculate the aspect using the TIN with a resolution of 10 m and the curvature employing the TIN with a resolution of 50 m. Subsequently the derivative of the aspect can be calculated. At this point the ridges are defined as the areas having an aspect variation greater than 40° and a curvature greater than 1 1/100 m. Among the two procedures for the calculation of the ridges it was decided to use the first because it has been shown that, in our case, it allows us to identify many more ridges. This is most likely due to the quality of the starting DEM. The comparison between ridges obtained with the two procedures is reported in Fig. 4.67. In this figure there is only an extract of the ridges raster, but it is possible to see how the geomorphological structures identified by the alternative algorithm are superior to those identified by the algorithm proposed by Maggioni (2004). Quantitatively, it has been calculated that the ridges identified by the alternative algorithm are 6.3 times higher than those identified by the algorithm proposed by Maggioni (2004). Snow avalanches perimeters were superimposed for showing how the alternative algorithm defines, within the limits of the quality of the initial DTM, the individual avalanche channels quite accurately. After calculating the ridges, they have been eliminated from the potential release areas.

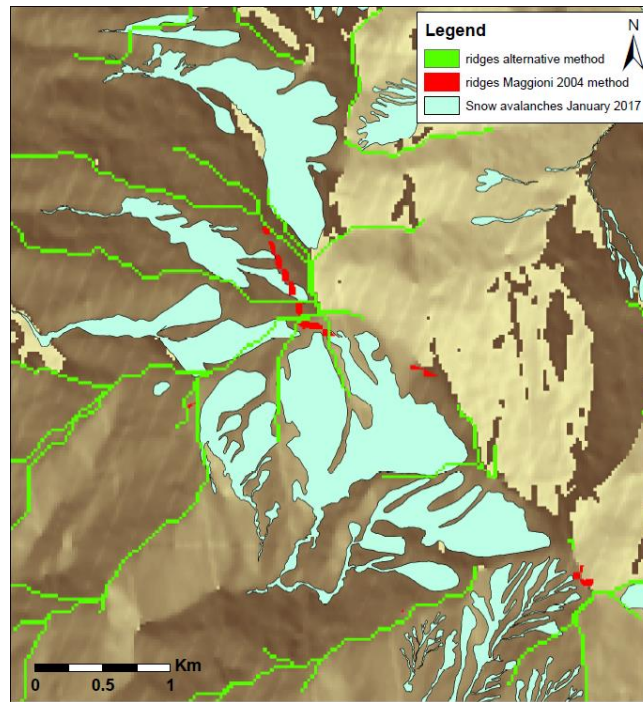


Fig. 4.67 Raster extract of comparison between ridges obtained with Maggioni 2004 method and alternative method. Ridges identified by the alternative algorithm are 6.3 times higher than those identified by the algorithm proposed by Maggioni (2004).

Another topographic parameter taken into account to obtain PRA is curvature. In particular, reference has been made to the plan curvatures because previous studies have shown that areas with a concave (negative) plan curvature are more likely to accumulate snow carried by the wind, while areas with a convex (positive) plan curvature do not have such propensity and they accumulate lower snow thicknesses (Maggioni, 2004). Using the Plan curvature criterion, the concave PRAs were then separated from the flat and convex ones. Areas with a Plan Curvature presenting values lower than or equal to -0.2 ($1/100$ m) were considered concave, while areas showing Plan Curvature values greater than -0.2 ($1/100$ m) were considered flat and convex. The Plan curvature was calculated starting from a 50 m re-sampled DEM in order to consider the large-scale curvature variations. The concave areas are also defined as self-contained, i.e., considered as the core of a single release area. At this point, for the PRA flat and convex, a dimensional criterion was used to define which PRA can be defined as self-contained and which are not. It has been defined that the PRA having a dimension higher than 5000 m² are considered self-contained, while those of smaller dimensions are considered not self-contained and they can act as expansion zones for the cores of the release area.

For all self-contained PRAs an additional filter is now applied to try to eliminate the avalanche track and deposition areas. Basically, the maximum height value within each PRA is calculated and only cells with a height greater than the difference (max altitude - 200 m) are considered to belong to the release area. The value of 200 m was chosen based on real events (Maggioni, 2004).

At this point, it is necessary to homogenize the results obtained because the DEM quality and the large-scale analysis return areas that may not be homogeneous. The self-contained PRA, to which the Altitude Range filter has been applied, are merged with the possible expansion areas (not self-contained PRA) and for their adjacent areas were evaluated the aspect and altitude differences. If in the adjacent areas the difference in height was less than 100 m and the aspect

difference is lower than 45° , then these areas were joined in the self-contained PRA while if the difference in height was less than 100 m and the difference in aspect higher than 45° the self-contained PRAs have been expanded in these areas. This procedure is repeated iteratively until a satisfactory result is obtained from the point of view of homogeneity. In this case, 4 iterations were performed. The entire procedure is summarized in the following flowchart (Fig. 4.68).

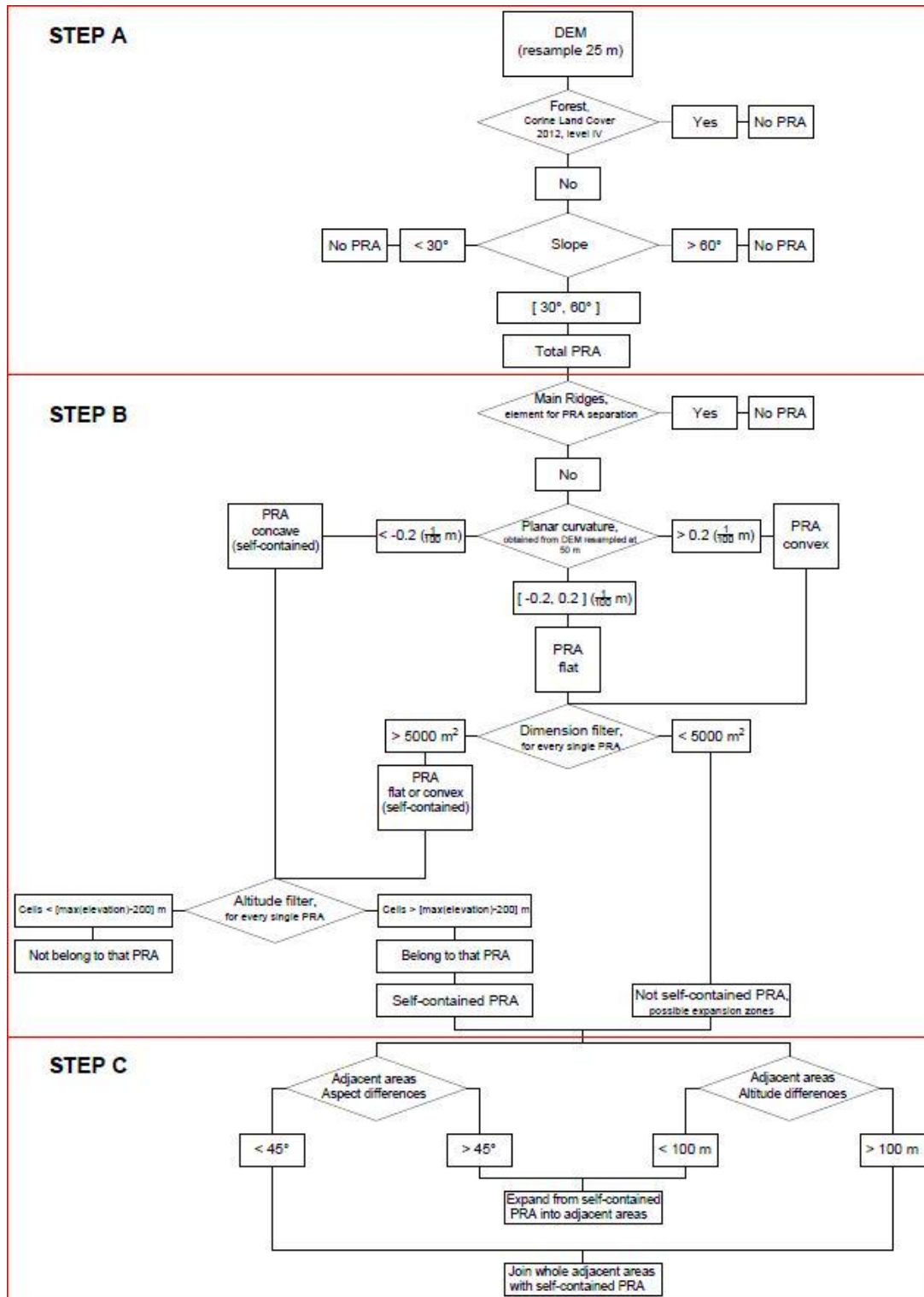


Fig. 4.68 Schematization of the procedure for obtaining PRAs. STEP A: Total PRA; STEP B: Identification of the individual release areas; STEP C: homogenization procedure. Whole ArcGIS passages are reported in [Appendix A](#). Modified after. Source: Maggioni (2004), p.30

As a result of the application of the previous procedure, it is therefore possible to obtain the Potential Release Areas (PRA). Once obtained, it is possible to compare the latter with the real release areas obtained from photo-interpretation. Before doing this, since the real detachment areas have been characterized, it is possible to follow some additional steps to clean up the result. In particular, it was found that all the real release areas lie above 750 m. For this reason, also the PRA obtained from Maggioni procedure have been filtered using this altimetric filter. The PRAs having an area lower than 5000 m² have been eliminated again, because some of these areas may have appeared as a consequence of the expansion procedure. Moreover, PRAs' cells that fell in known snow avalanches track zones were eliminated. At this point, a comparison between PRA obtained from the procedure and those obtained from photo-interpretation is possible. A sample of this comparison is reported in Fig. 4.69. The whole ArcGIS passages, to clarify this algorithm to GIS experts, are reported in **Appendix A**.

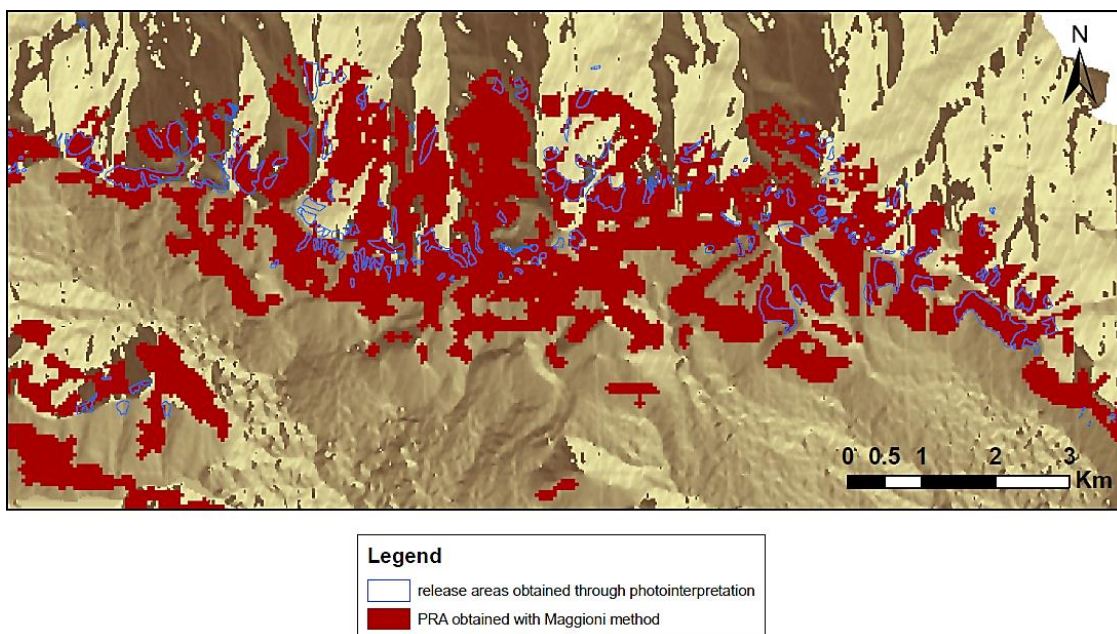


Fig. 4.69 A comparison between PRA obtained from the Maggioni (2004) procedure and release areas obtained from photo-interpretation

The first thing that catches the eye from the comparison is that PRA obtained through Maggioni algorithm are much more extensive than real release areas. It is also noted that, despite the large scale analysis and non-excellent quality DEM, the matching between PRA and real release areas can be considered more than satisfactory. Quantitatively, the real release areas extension is equal to 4% of the PRA identified through Maggioni algorithm. On the other hand, 75% of real release areas overlap with PRA identified by the semi-automatic procedure. The comparison between release area extensions is reported in Table 12.

Table 12 Comparison between real release areas (RRA) and potential release areas (PRA) extension

	Extension (Km ²)
Real release areas (RRA)	23.51
PRA, Maggioni (2004) algorithm	514.45
Overlapping between RRA and PRA	17.65

4.5.2 Bühler et al. (2018)

In addition to the algorithm just applied, there are others to determine the Potential Release Areas. A second algorithm, developed by Bühler et al. (2018) was applied. The applied method refers to what Bühler et al. (2018) define scenario frequent. Also in this case, the method takes into consideration some of the main topographic attributes to get PRA. The main parameters used are slope, plan curvature and ruggedness. As already described above, the slope is a parameter of primary importance for defining possible release areas. As for the previous algorithm, the areas with a slope between 30 ° and 60 ° were then extracted, but, before doing this, a mean filter with a 5x5 kernel, weighted with distance, was applied on a raster with 25 m resolution. In this way we try to homogenize the resulting areas since slope changes between the individual cells can lead to disconnected areas without a real physical reason (Bühler et al., 2018). Subsequently, the ruggedness (Sappington et al., 2007) was calculated using a window size of 2 cells (50 m). This parameter describes, in essence, the complexity of the topography. It is known that ridges, that are very rough terrain, can be used as an element of separation between PRA because they do not allow the continuity of the weak layer present inside the snowpack (Bühler et al., 2018 cum bibl.). It is, therefore, possible to use the value of ruggedness to extract ridges and subtract them from the areas falling within the slope values indicated above. In particular, cells having a ruggedness greater than 0.06 were extracted. A further element that allows identifying the ridges is the value of plan curvatures. Basically, by looking for convex structures, it is possible to identify areas where it is difficult to have large accumulations of snow and, consequently, release areas. In this case, the cells having a value of plan curvatures greater than 6 rad / 100 m were extracted. Subsequently, the extracted cells were removed from the previously defined areas. As already described above, the presence of forests acts as an element of protection and impediment to detachment. For this reason, using areas without the forest, previously obtained starting from Corine Land Cover 2012, level IV, only the PRA in these areas have been extracted. At this point, PRA having an area below a certain threshold have been excluded. It was decided to eliminate areas under 5000 m², as done for Maggioni algorithm. Finally, only the areas present in the mountain areas of interest were extracted, obtaining the final PRA.

Also in this case, it is reported in Fig. 4.70 a sample of comparison between PRA obtained from the algorithm and those obtained from photo-interpretation. As in the case of PRA obtained with Maggioni algorithm, areas obtained with the semi-automatic procedure are much more extensive than the real ones. The matching between PRA and real release areas can be considered satisfactory. Quantitatively, the real release areas extension is equal to 7.6 % of PRA identified through Bühler et al. algorithm. On the other hand, 62% of real release areas overlap with PRA identified by the semi-automatic procedure. It is noted that, in this case, a lower percentage of PRA cells falls within the real detachment areas. Given this fact, however, we must also consider the difference in extension of PRA identified by the two algorithms. In fact, the PRA extension obtained through Maggioni algorithm is about 1.7 times higher than that of PRA obtained with the Bühler et al. algorithm. The comparison between release area extensions is reported in Table 13.

Table 13 Comparison between real release areas (RRA) and potential release areas (PRA) extension

	Extension (Km ²)
Real release areas (RRA)	23.51
PRA, Bühler et al. (2018) algorithm	309.93
Overlapping between RRA and PRA	14.50

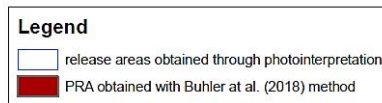
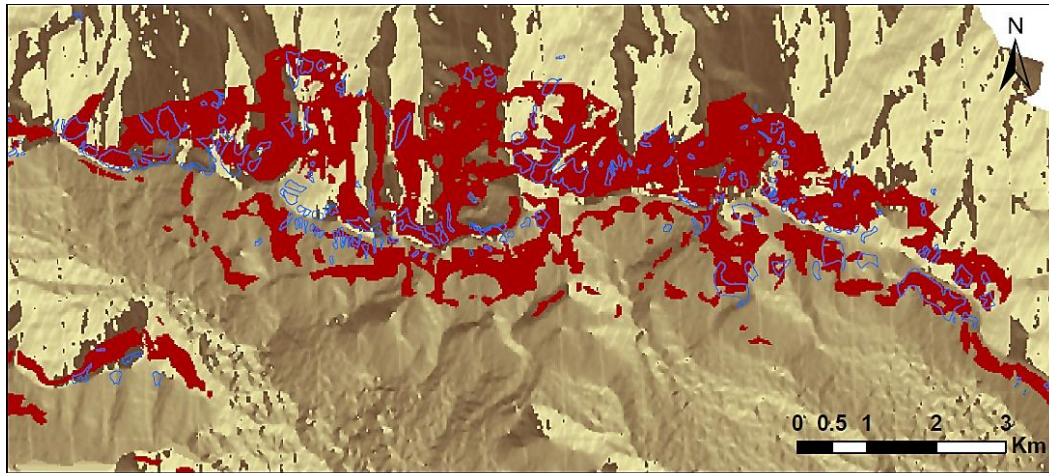


Fig. 4.70 A comparison between PRA obtained from the Bühler et al. (2018) procedure and release areas obtained from photo-interpretation.

Qualitatively, we can say that the Bühler algorithm, in this case, resulted more precise. We also note an 81% overlap between the Bühler and the Maggioni PRA. The entire procedure followed for obtaining PRA with Bühler et al. (2018) algorithm is summarized in the following flowchart (Fig. 4.71). PRA obtained with both Maggioni (2004) and Bühler et al. (2018) algorithms, for the mountain sectors of interest, are reported in **Attached 4**.

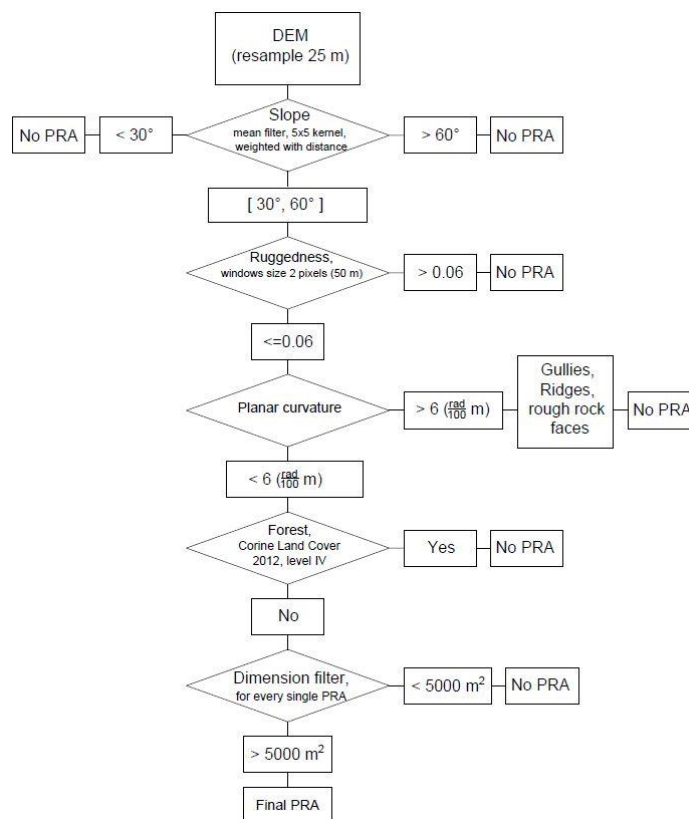


Fig. 4.71 Schematization of the procedure for obtaining PRAs with Bühler et al. (2018) algorithm.

4.6 Seismic analysis of release areas (January 2017)

On the basis of release areas extracted from mapped snow avalanches, it was possible to perform a statistical analysis of the seismic accelerations. This analysis has been developed both in the entire area of interest, as regards the PGA analysis reported by the seismic hazard map ($P_{VR} = 10\%$ $V_r = 50$ y), and on three selected mountain sectors, as regards both the analysis of the PGA and the acceleration values found in ShakeMaps for 4 events occurred in January 2017. ShakeMaps, obtained from INGV site, “have been determined automatically from the instrumentally recorded data by the seismic stations and are updated as more data become available” (INGV). They give only an indicative estimation of the shaking suffered by the ground. It is anticipated that since ShakeMaps are provided with discrete acceleration values, homogeneous within each band, and with intervals of 0.04 g, the frequency graphs will have only peaks corresponding to the acceleration values multiples of 0.04 g or equal to 0.02 g (minimum value). For more information on Shake Maps, see the publication “ShakeMap Manual: Technical Manual, User’s Guide, and Software Guide” By David J. Wald et al. (2005). Anyway, selected seismic events are reported in Table 14.

Table 14 Greater seismic events occurred in January 2017 used for the seismic analysis of snow avalanches release areas

Event ID (ID in Fig. 4.3)	mm/dd/yy	hh:min:sec UTC	Region	Epicenter	z [km]	M _L	M _w
12695491 (13)	01/18/17	9:25:40 AM	Abruzzo	L’Aquila	9.2	5.3	5.1
12697591 (12)	01/18/17	10:14:09 AM	Abruzzo	L’Aquila	9.1	5.4	5.5
12698071 (8)	01/18/17	10:25:23 AM	Abruzzo	L’Aquila	8.9	5.3	5.4
12707401 (5)	01/18/17	1:33:36 PM	Abruzzo	L’Aquila	10.0	5.1	5

These are earthquakes of greater entity occurred in January 2017; they verified on January 18th, 2017 and mainly in the morning. It is observed that magnitude values are all higher than 5. Therefore, selected earthquakes, according to Podolskiy et al. (2010), would correspond to events that could trigger landslides since the reference lower bound is $M_w = 5.1$. It is also noted that depths of such earthquakes are comparable to each other. In fact, according to what is reported in Fig. 4.3, these earthquakes were generated starting from the same fault, i.e. the Colfiorito-Campotosto fault (ITCS028) whose characteristics are reported in Table 9. Moreover, it is observed that almost all the earthquakes occurred in January 2017 were generated by this particularly active fault. Selected mountain sectors, in order to perform seismic analysis, are Sibillini Mountains, Laga Mountains and Gran Sasso Massif. The characterization of Majella and the Sirente Velino release areas has not been carried out as they fall entirely or almost entirely into a single acceleration band and, moreover, with the lowest values. The Shake Maps used, with the indication of the most affected mountain areas, are reported in Fig. 4.72. The three mountain sectors considered, due to their proximity to the epicenters and due to the seismic accelerations found, may, more likely, have manifested snow avalanches release caused by the action of earthquakes. In reality, it must be kept in mind that, in order to study the release of snow avalanches induced by earthquakes, it is necessary to know two critical parameters: seismic acceleration and snow height. Each considered mountain sector was further subdivided into the Adriatic and Tyrrhenian side to ascertain any differences. It is emphasized that the statistical analysis was performed on the totality of release areas cells falling into the interested mountain sector. The reasoning has therefore been made on a large scale and not considering every single release area.

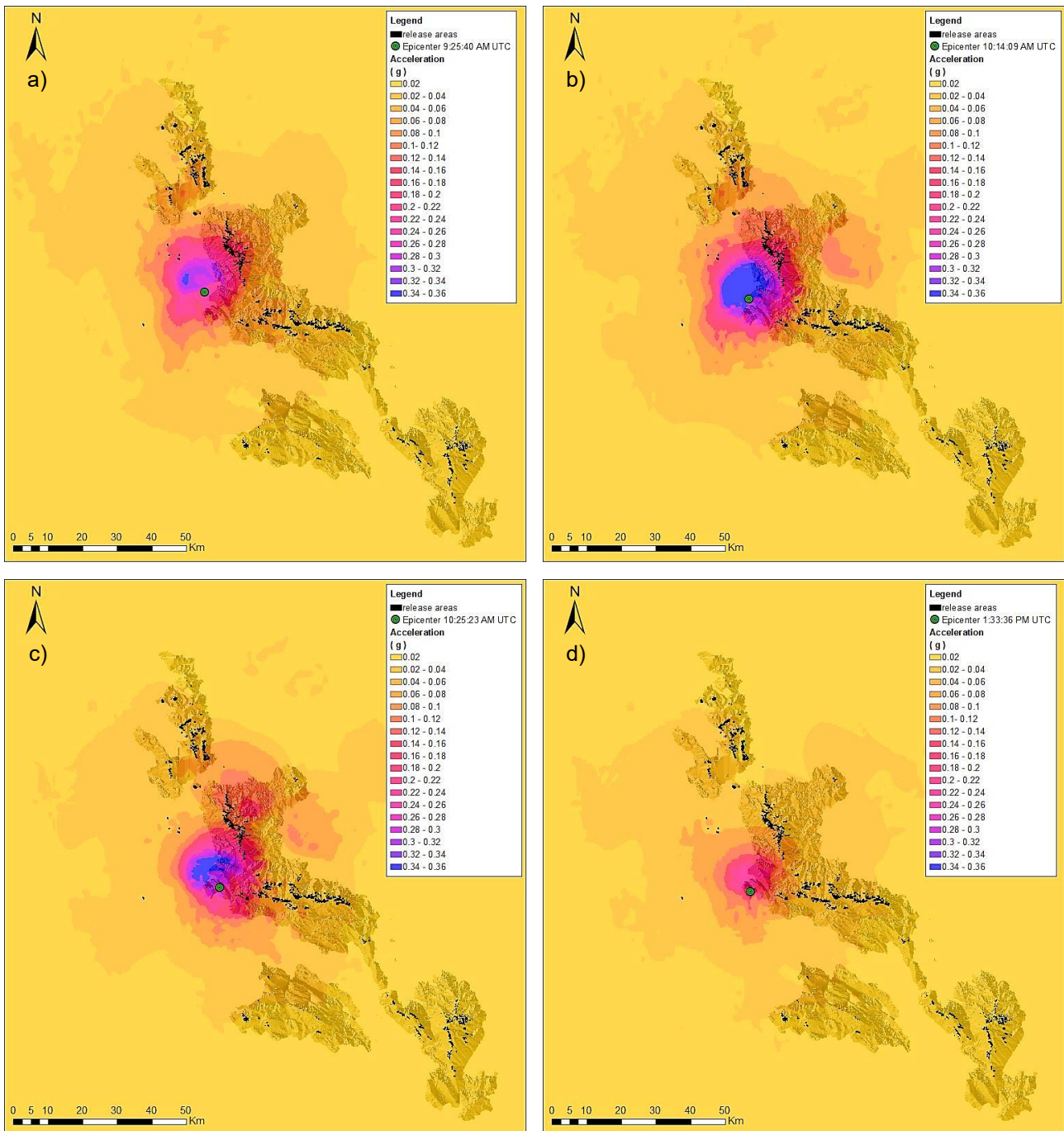


Fig. 4.72 Shake Maps used, with the indication of the most affected mountain areas: a) ShakeMap for the earthquake verified on January 18th, 2017 at 9:25:40 AM UTC b) ShakeMap for the earthquake verified on January 18th, 2017 at 10:14:09 AM UTC c) ShakeMap for the earthquake verified on January 18th, 2017 at 10:25:23 AM UTC d) ShakeMap for the earthquake verified on January 18th, 2017 at 1:33:36 PM UTC. Snow avalanches release areas are shown in black.

4.6.1 Total release areas

As already anticipated, the characterization of all snow avalanches release areas, within the area of interest, was carried out only concerning PGA values reported by the seismic hazard map ($P_{VR} = 10\%$ $V_r = 50$ y). Since the PGA values were found in the form of points on the INGV site, and because of they were distributed according to a regular grid of 0.02° (planar distance of about 3 km), it was necessary to transform points in raster and carry out a resampling so that the values of PGA, falling within release areas, could be extracted. The raster was

resampled at 25 m using, as resampling technique, a method that calculates PGA values weighting for distance. The obtained raster has already been reported in Fig. 4.1. At this point, the PGA values were extracted within the release areas perimeters. Performing the frequency analysis, the results reported in Fig. 4.73 were obtained.

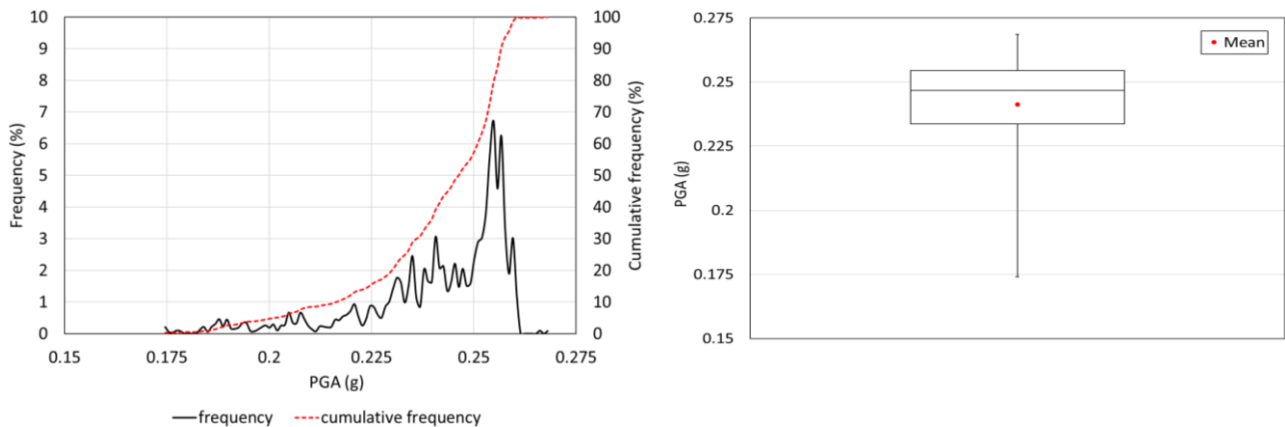


Fig. 4.73 Statistical analysis of the PGA values reported by the seismic hazard map ($P_{VR} = 10\%$ $V_r = 50$ y) carried out for all release areas extracted from mapped snow avalanches

It is observed that approximately 57% of release areas cells show values ranging from 0.15 to 0.25 g, corresponding to seismic zone 2. The remaining 43% of the cells show values higher than 0.25 g, corresponding to seismic zone 1. It is therefore observed that all the release areas fall into the two zones with the highest seismic hazard. It should be noted that the seismic hazard map presents PGA values about a rigid and plan soil, not taking into account the stratigraphic and topographic amplification phenomena which, for a single event, can lead to higher acceleration values. The comparison between accelerations obtained, for release areas, from earthquakes of January 2017 and seismic hazard map will be addressed, in the following paragraphs, for the considered mountain sectors.

4.6.2 Gran Sasso release areas

The statistical analysis carried out for release areas extracted in Gran Sasso Massif is shown below in Fig. 4.74. Fig. 4.74 a) shows the distribution of release areas acceleration for the earthquake verified on January 18th, 2017 at the time 9:25:40 AM UTC in the interested mountain sector. It is observed that about 13% of the cells of release areas include PGA values of 0.02 g, 48% equal to 0.04 g and the remaining 39% equal to 0.08 g. Fig. 4.74 b) shows the distribution of release areas acceleration for the earthquake verified on January 18th, 2017 at the time 10:14:09 AM UTC in the interested mountain sector. It is observed that about 12% of the cells of release areas include PGA values of 0.02 g, 62% equal to 0.04 g, 22% equal to 0.08 g, 3% equal to 0.12 g and the remaining 1% equal to 0.16 g. Fig. 4.74 c) shows the distribution of release areas acceleration for the earthquake verified on January 18th, 2017 at the time 10:25:23 AM UTC in the interested mountain sector. It is observed that about 5% of the cells of release areas include PGA values of 0.02 g, 60% equal to 0.04 g, 22% equal to 0.08 g, 5% equal to 0.12 g and the remaining 8% equal to 0.16 g. Fig. 4.74 d) shows the distribution of release areas acceleration for the earthquake verified on January 18th, 2017 at the time 1:33:36 PM UTC in the interested mountain sector. It is observed that about 11% of the cells of release areas include PGA values of 0.02 g, 78% equal to 0.04g,

11% equal to 0.08 g, and the remaining 0.1% equal to 0.12 g. Fig. 4.74 e) shows the distribution of release areas PGA extracted from seismic hazard map ($P_{VR} = 10\%$ $V_r = 50$ y). It is observed that approximately 39% of release areas cells show values ranging from 0.15 to 0.25 g, corresponding to seismic zone 2. The remaining 61% of the cells show values higher than 0.25 g, corresponding to seismic zone 1. It is therefore observed that all the release areas fall into the two zones with the highest seismic hazard.

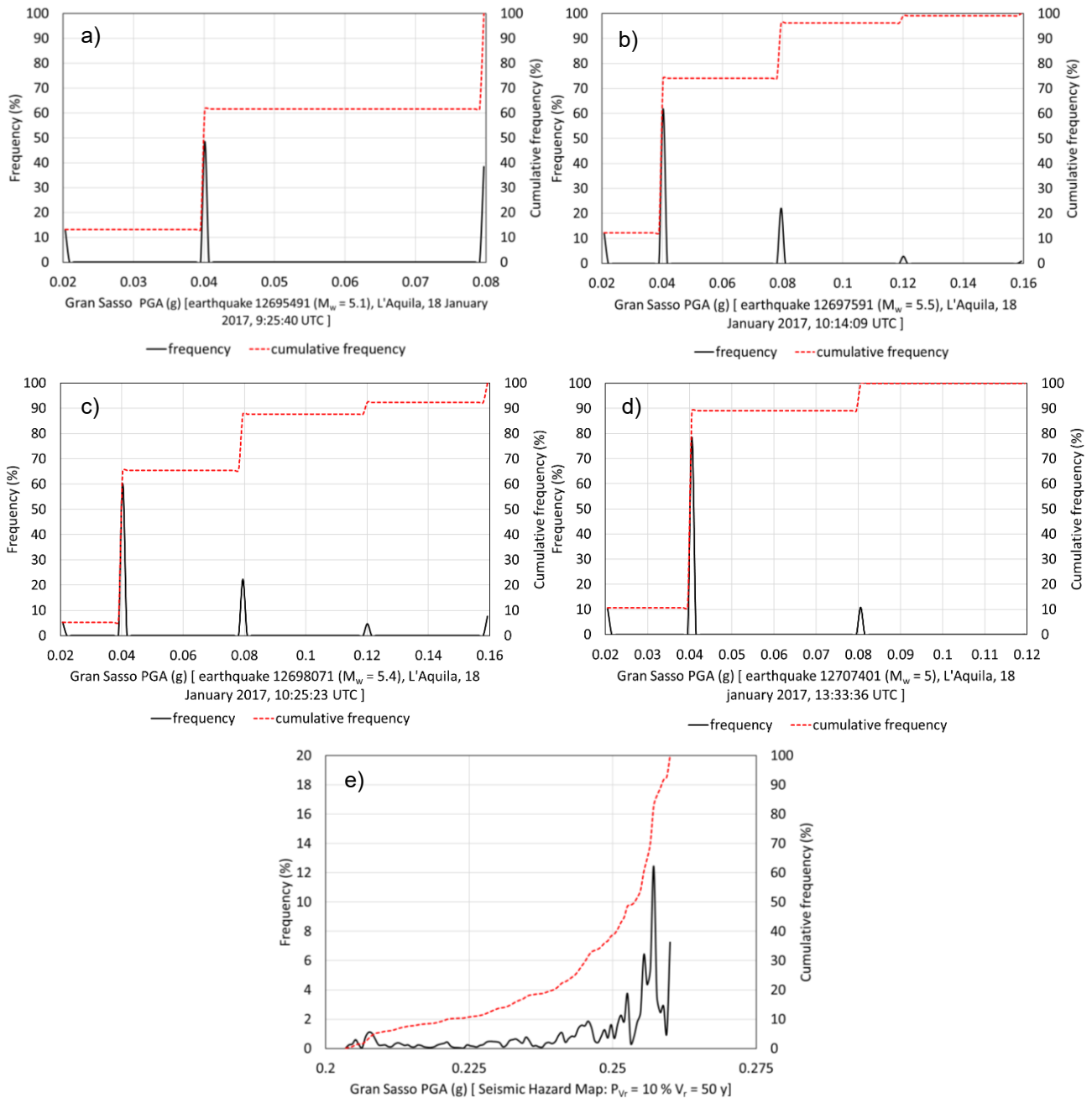
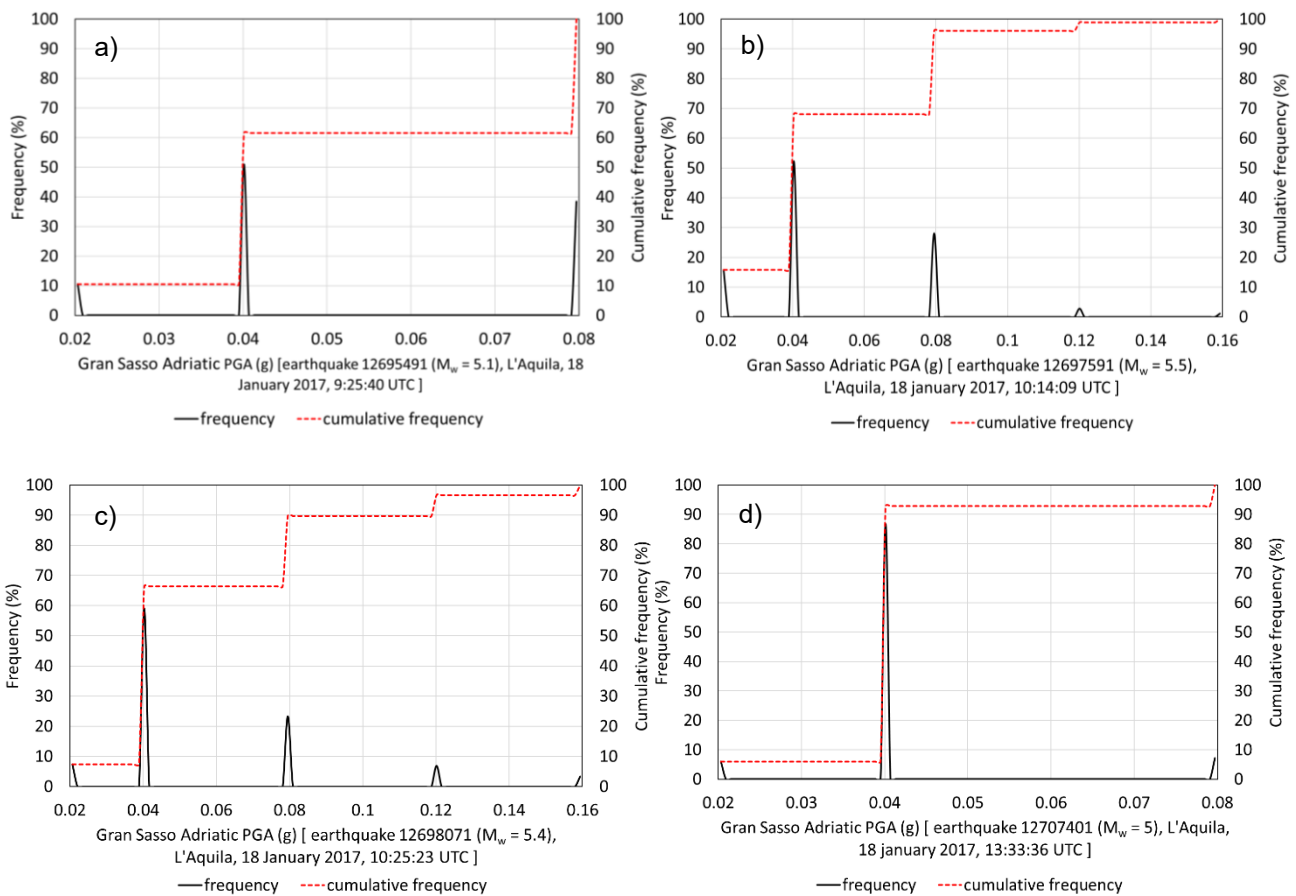


Fig. 4.74 Statistical analysis of accelerations for the earthquakes verified on January 18th, 2017 at the time a) 9:25:40 AM UTC b) 10:14:09 AM UTC c) 10:25:23 AM d) 1:33:36 PM and e) PGA extracted from seismic hazard map ($P_{VR} = 10\%$ $V_r = 50$ y) carried out for Gran Sasso release areas extracted from mapped snow avalanches

4.6.3 Gran Sasso, Adriatic side, release areas

The statistical analysis carried out for release areas extracted in Gran Sasso Massif, Adriatic side, is shown below in Fig. 4.75. Fig. 4.75 a) shows the distribution of release areas acceleration for the earthquake verified on January 18th, 2017 at the time 9:25:40 AM UTC in the interested mountain sector. It is observed that about 11% of the cells of release areas include PGA values of 0.02 g, 51% equal to 0.04 g and the remaining 38% equal to 0.08 g. Fig. 4.75 b) shows the distribution of release areas acceleration for the earthquake verified on January 18th, 2017 at the time 10:14:09 AM UTC in the interested mountain sector. It is observed that about 16% of the cells of release areas include PGA values of 0.02 g, 52% equal to 0.04 g, 28% equal to 0.08 g, 3% equal to 0.12 g and the remaining 1% equal to 0.16 g. Fig. 4.75 c) shows the distribution of release areas acceleration for the earthquake verified on January 18th, 2017 at the time 10:25:23 AM UTC in the interested mountain sector. It is observed that about 8% of the cells of release areas include PGA values of 0.02 g, 59% equal to 0.04 g, 23% equal to 0.08 g, 7% equal to 0.12 g and the remaining 3% equal to 0.16 g. Fig. 4.75 d) shows the distribution of release areas acceleration for the earthquake verified on January 18th, 2017 at the time 1:33:36 PM UTC in the interested mountain sector. It is observed that about 6% of the cells of release areas include PGA values of 0.02 g, 87% equal to 0.04g and the remaining 7% equal to 0.08 g. Fig. 4.75 e) shows the distribution of release areas PGA extracted from seismic hazard map ($P_{VR} = 10\%$ $V_r = 50$ y). It is observed that approximately 48% of release areas cells show values ranging from 0.15 to 0.25 g, corresponding to seismic zone 2. The remaining 52% of the cells show values higher than 0.25 g, corresponding to seismic zone 1. It is therefore observed that all the release areas fall into the two zones with the highest seismic hazard.



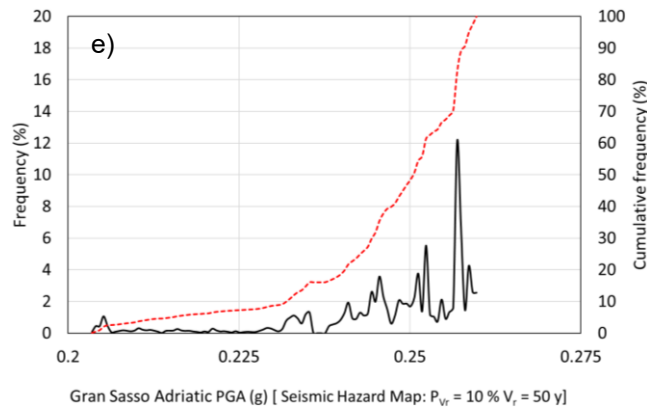
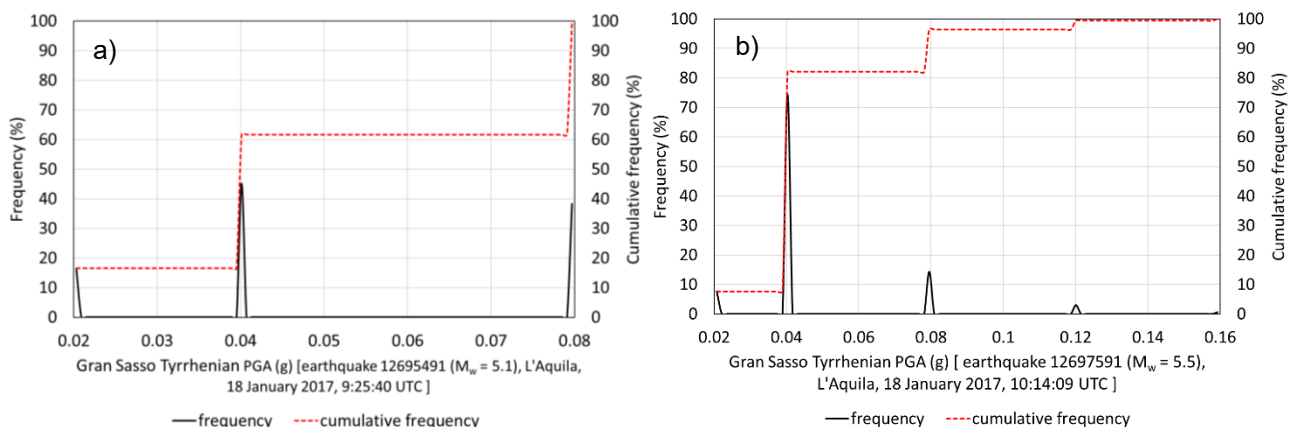


Fig. 4.75 Statistical analysis of accelerations for the earthquakes verified on January 18th, 2017 at the time a) 9:25:40 AM UTC b) 10:14:09 AM UTC c) 10:25:23 AM d) 1:33:36 PM (previous page) and e) PGA extracted from seismic hazard map ($P_{VR} = 10\%$ $V_r = 50$ y) carried out for Gran Sasso Adriatic release areas extracted from mapped snow avalanches.

4.6.4 Gran Sasso, Tyrrhenian side, release areas

The statistical analysis carried out for release areas extracted in Gran Sasso Massif, Tyrrhenian side, is shown below in Fig. 4.76. Fig. 4.76 a) shows the distribution of release areas acceleration for the earthquake verified on January 18th, 2017 at the time 9:25:40 AM UTC in the interested mountain sector. It is observed that about 17% of the cells of release areas include PGA values of 0.02 g, 45% equal to 0.04 g and the remaining 38% equal to 0.08 g. Fig. 4.76 b) shows the distribution of release areas acceleration for the earthquake verified on January 18th, 2017 at the time 10:14:09 AM UTC in the interested mountain sector. It is observed that about 8% of the cells of release areas include PGA values of 0.02 g, 74% equal to 0.04 g, 14% equal to 0.08 g, 3% equal to 0.12 g and the remaining 1% equal to 0.16 g. Fig. 4.76 c) shows the distribution of release areas acceleration for the earthquake verified on January 18th, 2017 at the time 10:25:23 AM UTC in the interested mountain sector. It is observed that about 2% of the cells of release areas include PGA values of 0.02 g, 62% equal to 0.04 g, 21% equal to 0.08 g, 2% equal to 0.12 g and the remaining 13% equal to 0.16 g. Fig. 4.76 d) shows the distribution of release areas acceleration for the earthquake verified on January 18th, 2017 at the time 1:33:36 PM UTC in the interested mountain sector. It is observed that about 17% of the cells of release areas include PGA values of 0.02 g, 67% equal to 0.04g, 16% equal to 0.08 g, and the remaining 0.2% equal to 0.12 g. Fig. 4.76 e) shows the distribution of release areas PGA extracted from seismic hazard map ($P_{VR} = 10\%$ $V_r = 50$ y). It is observed that approximately 25% of release areas cells show values ranging from 0.15 to 0.25 g, corresponding to seismic zone 2. The remaining 75% of the cells show values higher than 0.25 g, corresponding to seismic zone 1. It is therefore observed that all the release areas fall into the two zones with the highest seismic hazard.



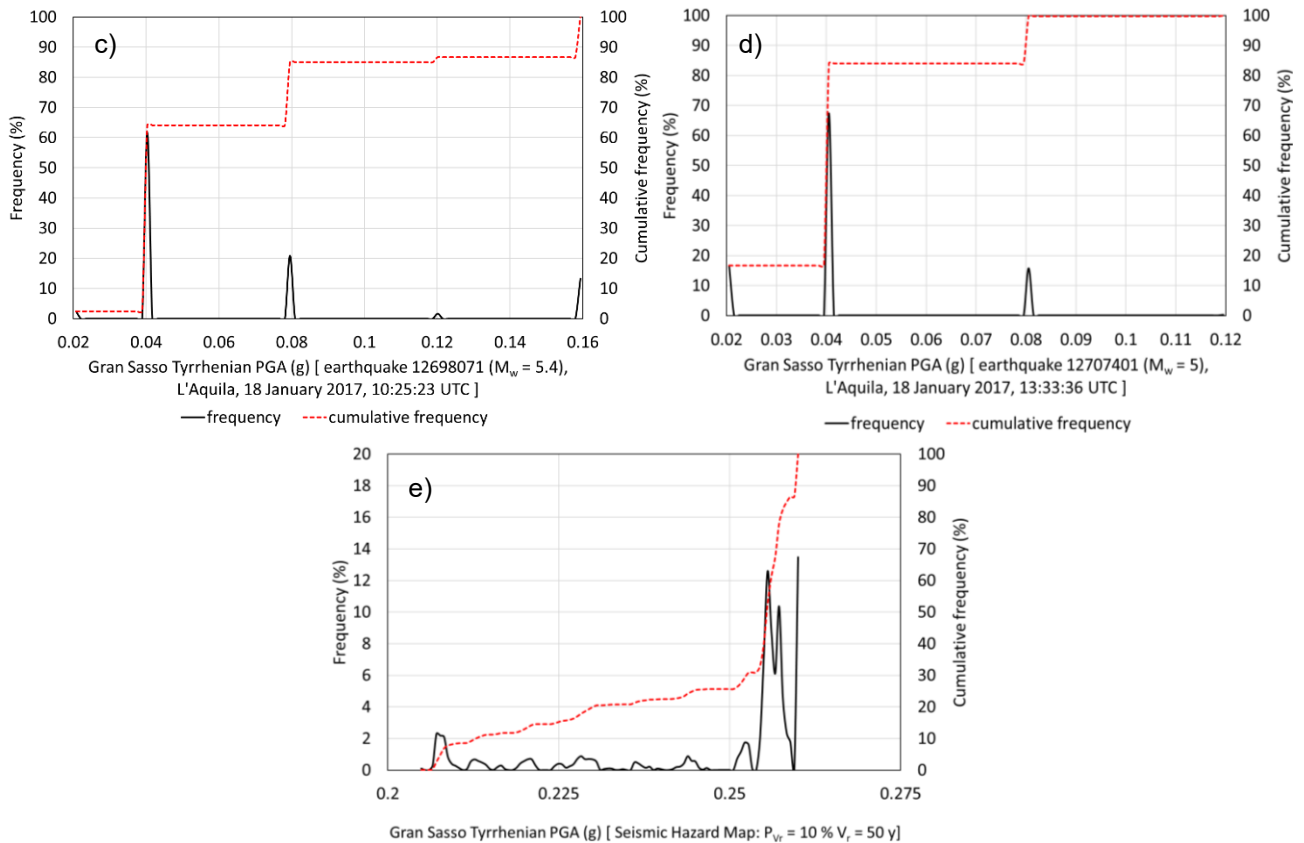


Fig. 4.76 Statistical analysis of accelerations for the earthquakes verified on January 18th, 2017 at the time a) 9:25:40 AM UTC b) 10:14:09 AM UTC (previous page) c) 10:25:23 AM d) 1:33:36 PM (previous page) and e) PGA extracted from seismic hazard map ($P_{VR} = 10\%$ $V_r = 50$ y) carried out for Gran Sasso Tyrrhenian release areas extracted from mapped snow avalanches.

4.6.5 Laga release areas

The statistical analysis carried out for release areas extracted in Laga Mountains is shown below in Fig. 4.77. Fig. 4.77 a) shows the distribution of release areas acceleration for the earthquake verified on January 18th, 2017 at the time 9:25:40 AM UTC in the interested mountain sector. It is observed that about 2% of the cells of release areas include PGA values of 0.04 g, 4% equal to 0.08 g, 28% equal to 0.12 g, 66% equal to 0.16 g and the remaining 0.03% equal to 0.2 g. Fig. 4.77 b) shows the distribution of release areas acceleration for the earthquake verified on January 18th, 2017 at the time 10:14:09 AM UTC in the interested mountain sector. It is observed that about 2% of the cells of release areas include PGA values of 0.04 g, 0.14% equal to 0.08 g, 16% equal to 0.12 g, 37% equal to 0.16 g, 36% equal to 0.2 g, 9% equal to 0.24 g and the remaining 0.3% equal to 0.28 g. Fig. 4.77 c) shows the distribution of release areas acceleration for the earthquake verified on January 18th, 2017 at the time 10:25:23 AM UTC in the interested mountain sector. It is observed that about 2% of the cells of release areas include PGA values of 0.04 g, 12% equal to 0.08 g, 68% equal to 0.12 g, 11% equal to 0.16 g, 7% equal to 0.2 g, and the remaining 0.5% equal to 0.24 g. Fig. 4.77 d) shows the distribution of release areas acceleration for the earthquake verified on January 18th, 2017 at the time 1:33:36 PM UTC in the interested mountain sector. It is observed that about 79% of the cells of release areas include PGA values of 0.04 g, 21% equal to 0.08 g and the remaining 0.02% equal to 0.12 g.

Fig. 4.77 e) shows the distribution of release areas PGA extracted from seismic hazard map ($P_{VR} = 10\%$ $V_r = 50$ y). It is observed that approximately 16% of release areas cells show values ranging from 0.15 to 0.25 g, corresponding to seismic zone 2. The remaining 84% of the cells show values higher than 0.25 g, corresponding to seismic zone 1. It is therefore observed that all the release areas fall into the two zones with the highest seismic hazard.

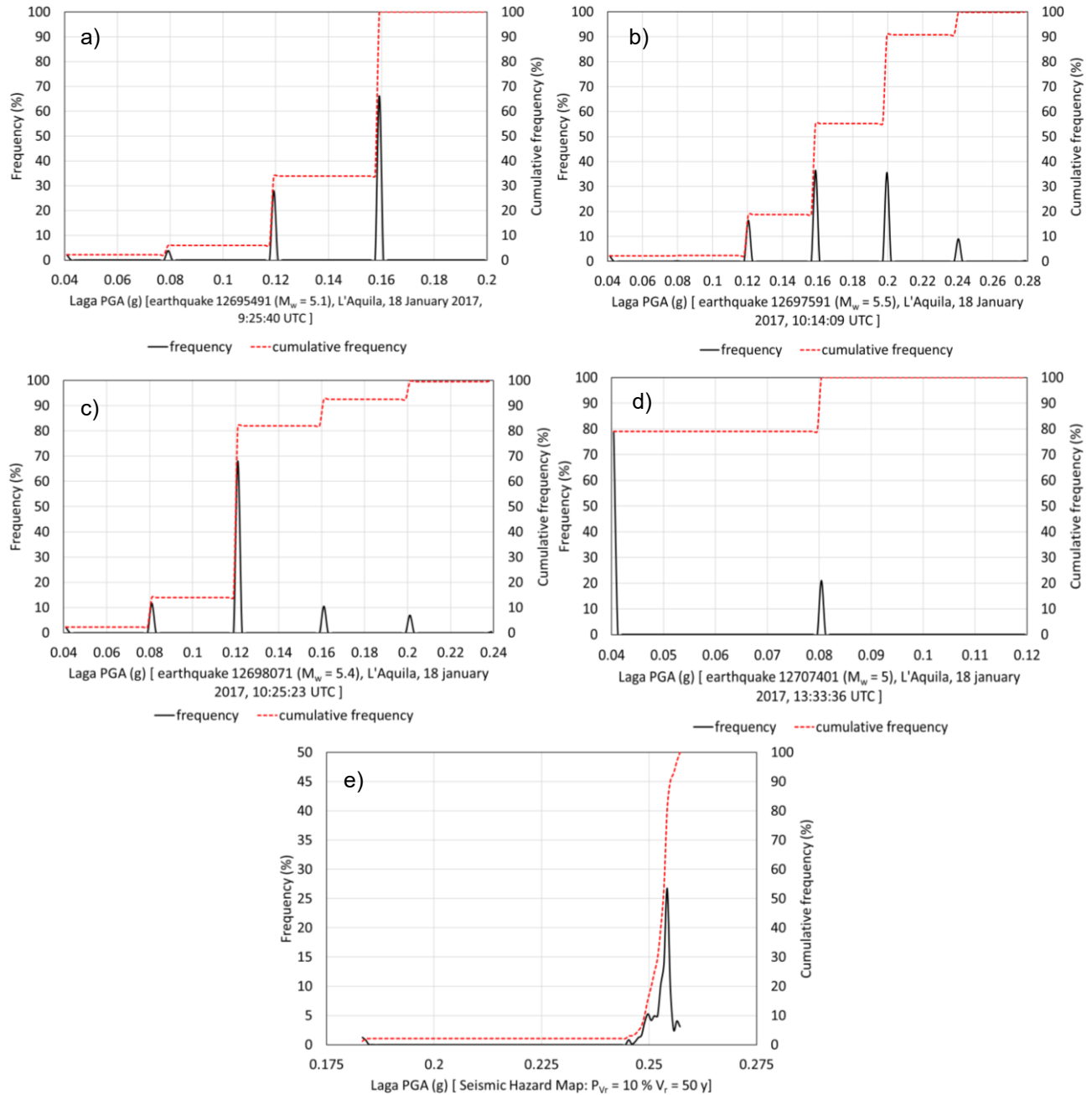
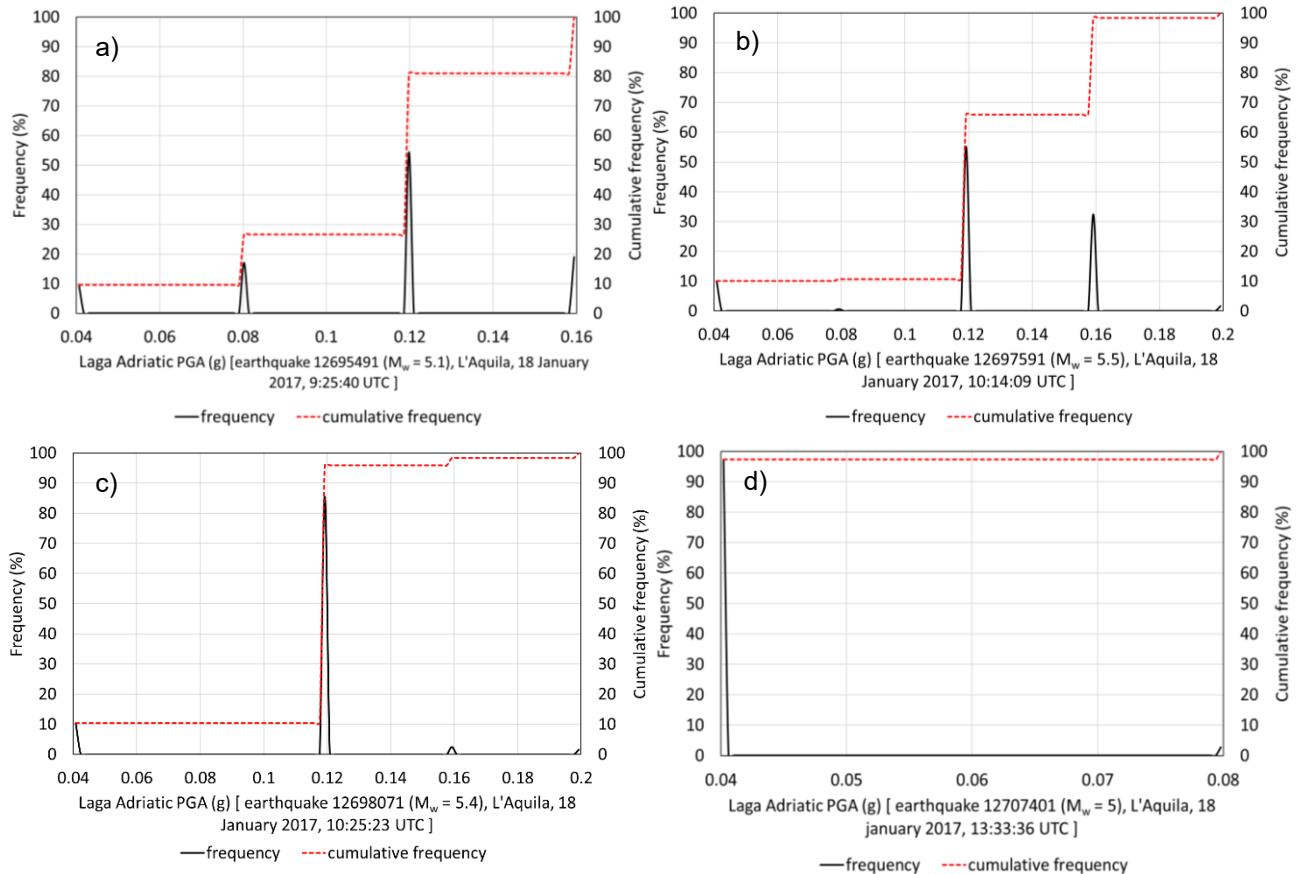


Fig. 4.77 Statistical analysis of accelerations for the earthquakes verified on January 18th, 2017 at the time a) 9:25:40 AM UTC b) 10:14:09 AM UTC c) 10:25:23 AM d) 1:33:36 PM and e) PGA extracted from seismic hazard map ($P_{VR} = 10\%$ $V_r = 50$ y) carried out for Laga release areas extracted from mapped snow avalanches

4.6.6 Laga, Adriatic side, release areas

The statistical analysis carried out for release areas extracted in Laga Mountains, Adriatic side, is shown below in Fig. 4.78. Fig. 4.78 a) shows the distribution of release areas acceleration for the earthquake verified on January 18th, 2017 at the time 9:25:40 AM UTC in the interested mountain sector. It is observed that about 10% of the cells of release areas include PGA values of 0.04 g, 17% equal to 0.08 g, 54% equal to 0.12 g, and the remaining 19% equal to 0.16 g. Fig. 4.78 b) shows the distribution of release areas acceleration for the earthquake verified on January 18th, 2017 at the time 10:14:09 AM UTC in the interested mountain sector. It is observed that about 10% of the cells of release areas include PGA values of 0.04 g, 0.6% equal to 0.08 g, 55% equal to 0.12 g, 33% equal to 0.16 g and the remaining 1.6% equal to 0.2 g. Fig. 4.78 c) shows the distribution of release areas acceleration for the earthquake verified on January 18th, 2017 at the time 10:25:23 AM UTC in the interested mountain sector. It is observed that about 10% of the cells of release areas include PGA values of 0.04 g, 86% equal to 0.12 g, 2.4% equal to 0.16 g and the remaining 1.6% equal to 0.2 g. Fig. 4.78 d) shows the distribution of release areas acceleration for the earthquake verified on January 18th, 2017 at the time 1:33:36 PM UTC in the interested mountain sector. It is observed that about 97% of the cells of release areas include PGA values of 0.04 g, while the remaining 3% equal to 0.08 g. Fig. 4.78 e) shows the distribution of release areas PGA extracted from seismic hazard map ($P_{VR} = 10\%$ $V_r = 50$ y). It is observed that approximately 77% of release areas cells show values ranging from 0.15 to 0.25 g, corresponding to seismic zone 2. The remaining 23% of the cells show values higher than 0.25 g, corresponding to seismic zone 1. It is therefore observed that all the release areas fall into the two zones with the highest seismic hazard.



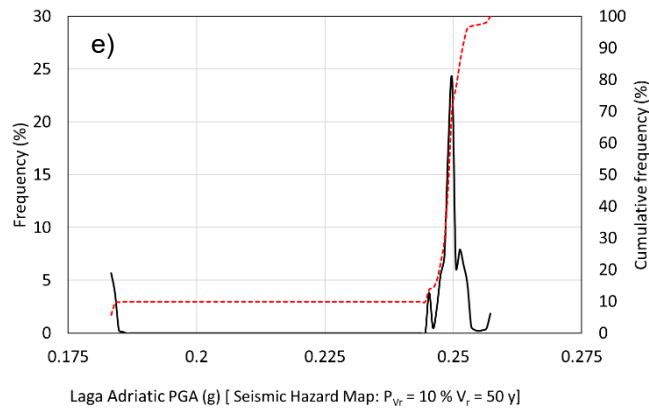
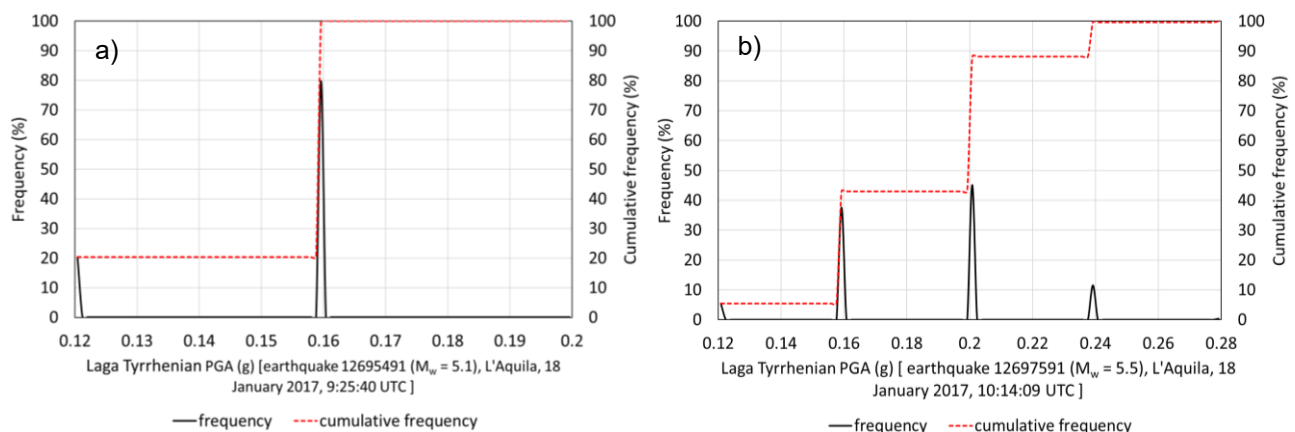


Fig. 4.78 Statistical analysis of accelerations for the earthquakes verified on January 18th, 2017 at the time a) 9:25:40 AM UTC b) 10:14:09 AM UTC c) 10:25:23 AM d) 1:33:36 PM (previous page) and e) PGA extracted from seismic hazard map ($P_{VR} = 10\%$ $V_T = 50$ y) carried out for Laga Adriatic release areas extracted from mapped snow avalanches

4.6.7 Laga, Tyrrhenian side, release areas

The statistical analysis carried out for release areas extracted in Laga Mountains, Tyrrhenian side, is shown below in Fig. 4.79. Fig. 4.79 a) shows the distribution of release areas acceleration for the earthquake verified on January 18th, 2017 at the time 9:25:40 AM UTC in the interested mountain sector. It is observed that about 20% of the cells of release areas include PGA values of 0.12 g, 80% equal to 0.16 g and the remaining 0.04% equal to 0.2 g. Fig. 4.79 b) shows the distribution of release areas acceleration for the earthquake verified on January 18th, 2017 at the time 10:14:09 AM UTC in the interested mountain sector. It is observed that about 5% of the cells of release areas include PGA values of 0.12 g, 38% equal to 0.16 g, 45% equal to 0.2 g, 12% equal to 0.24 g and the remaining 0.35% equal to 0.28 g. Fig. 4.79 c) shows the distribution of release areas acceleration for the earthquake verified on January 18th, 2017 at the time 10:25:23 AM UTC in the interested mountain sector. It is observed that about 15% of the cells of release areas include PGA values of 0.08 g, 63% equal to 0.12 g, 13% equal to 0.16 g, 9% equal to 0.2 g and the remaining 0.6% equal to 0.24 g. Fig. 4.79 d) shows the distribution of release areas acceleration for the earthquake verified on January 18th, 2017 at the time 1:33:36 PM UTC in the interested mountain sector. It is observed that about 74% of the cells of release areas include PGA values of 0.04 g, 26% equal to 0.08 g and the remaining 0.02% equal to 0.12 g. Fig. 4.79 e) shows the distribution of release areas PGA extracted from seismic hazard map ($P_{VR} = 10\%$ $V_T = 50$ y). It is observed that 100% of release areas cells show values greater than 0.25 g, corresponding to seismic zone 1.



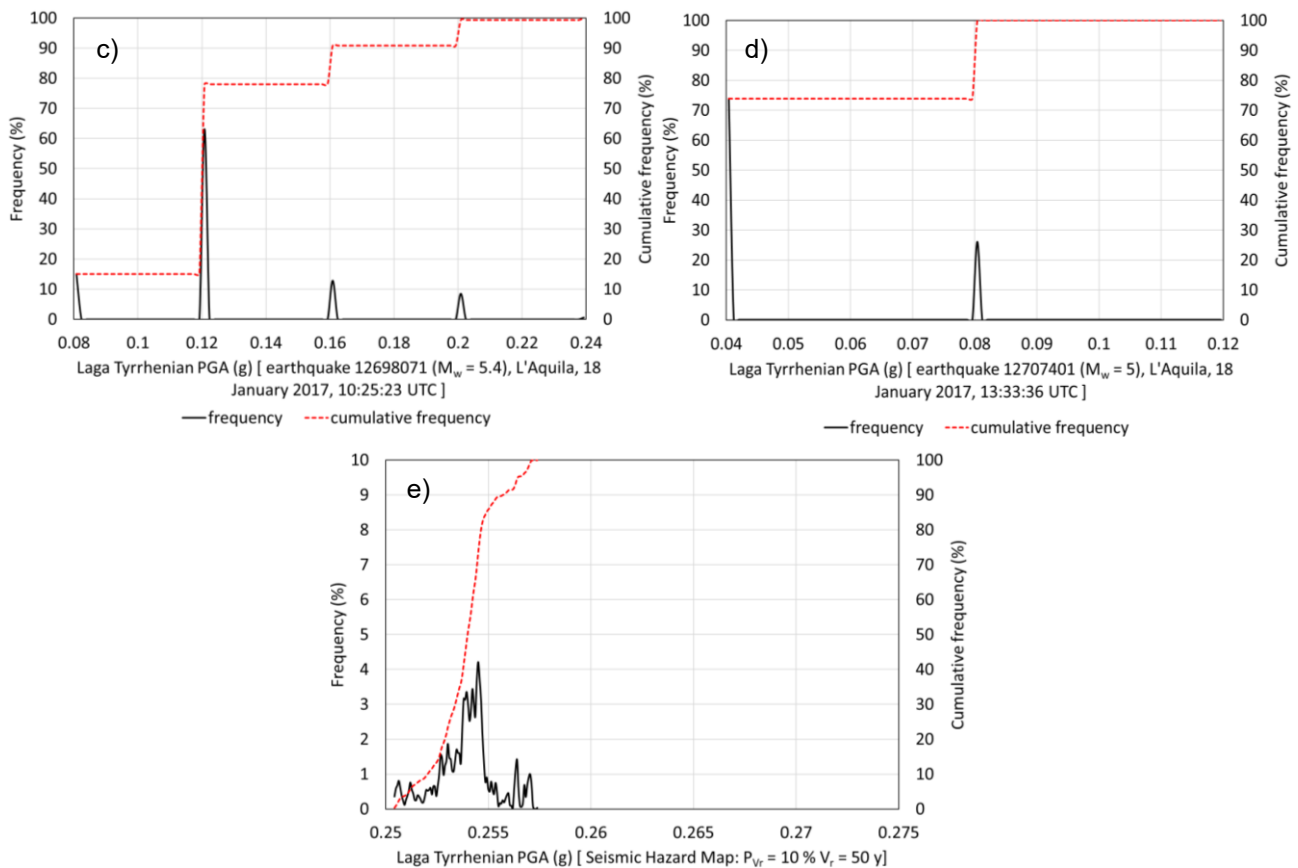


Fig. 4.79 Statistical analysis of accelerations for the earthquakes verified on January 18th, 2017 at the time a) 9:25:40 AM UTC b) 10:14:09 AM UTC (previous page) c) 10:25:23 AM d) 1:33:36 PM and e) PGA extracted from seismic hazard map ($P_{VR} = 10\%$ $V_r = 50$ y) carried out for Laga Tyrrhenian release areas extracted from mapped snow avalanches

4.6.8 Sibillini release areas

The statistical analysis carried out for release areas extracted in Sibillini Mountains is shown below in Fig. 4.80. Fig. 4.80 a) shows the distribution of release areas acceleration for the earthquake verified on January 18th, 2017 at the time 9:25:40 AM UTC in the interested mountain sector. It is observed that about 0.4% of the cells of release areas include PGA values of 0.02 g, 60% equal to 0.04 g and the remaining 40% equal to 0.08 g. Fig. 4.80 b) shows the distribution of release areas acceleration for the earthquake verified on January 18th, 2017 at the time 10:14:09 AM UTC in the interested mountain sector. It is observed that about 0.4% of the cells of release areas include PGA values of 0.02 g, 58% equal to 0.04 g, 41% equal to 0.08 g and the remaining 0.18% equal to 0.12 g. Fig. 4.80 c) shows the distribution of release areas acceleration for the earthquake verified on January 18th, 2017 at the time 10:25:23 AM UTC in the interested mountain sector. It is observed that about 0.4% of the cells of release areas include PGA values of 0.02 g, 77% equal to 0.04 g and the remaining 22.5% equal to 0.08 g. Fig. 4.80 d) shows the distribution of release areas acceleration for the earthquake verified on January 18th, 2017 at the time 1:33:36 PM UTC in the interested mountain sector. It is observed that about 48% of the cells of release areas include PGA values of 0.02 g while the remaining 52% is equal to 0.04 g. Fig. 4.80 e) shows the distribution of release areas PGA extracted from seismic hazard map ($P_{VR} = 10\%$ $V_r = 50$ y). It is observed that approximately 88% of release areas cells show values ranging from 0.15 to 0.25 g, corresponding to seismic zone 2. The remaining 12% of the cells show values higher than 0.25 g, corresponding to seismic zone 1. It is therefore observed that all the release areas fall into the two zones with the highest seismic hazard.

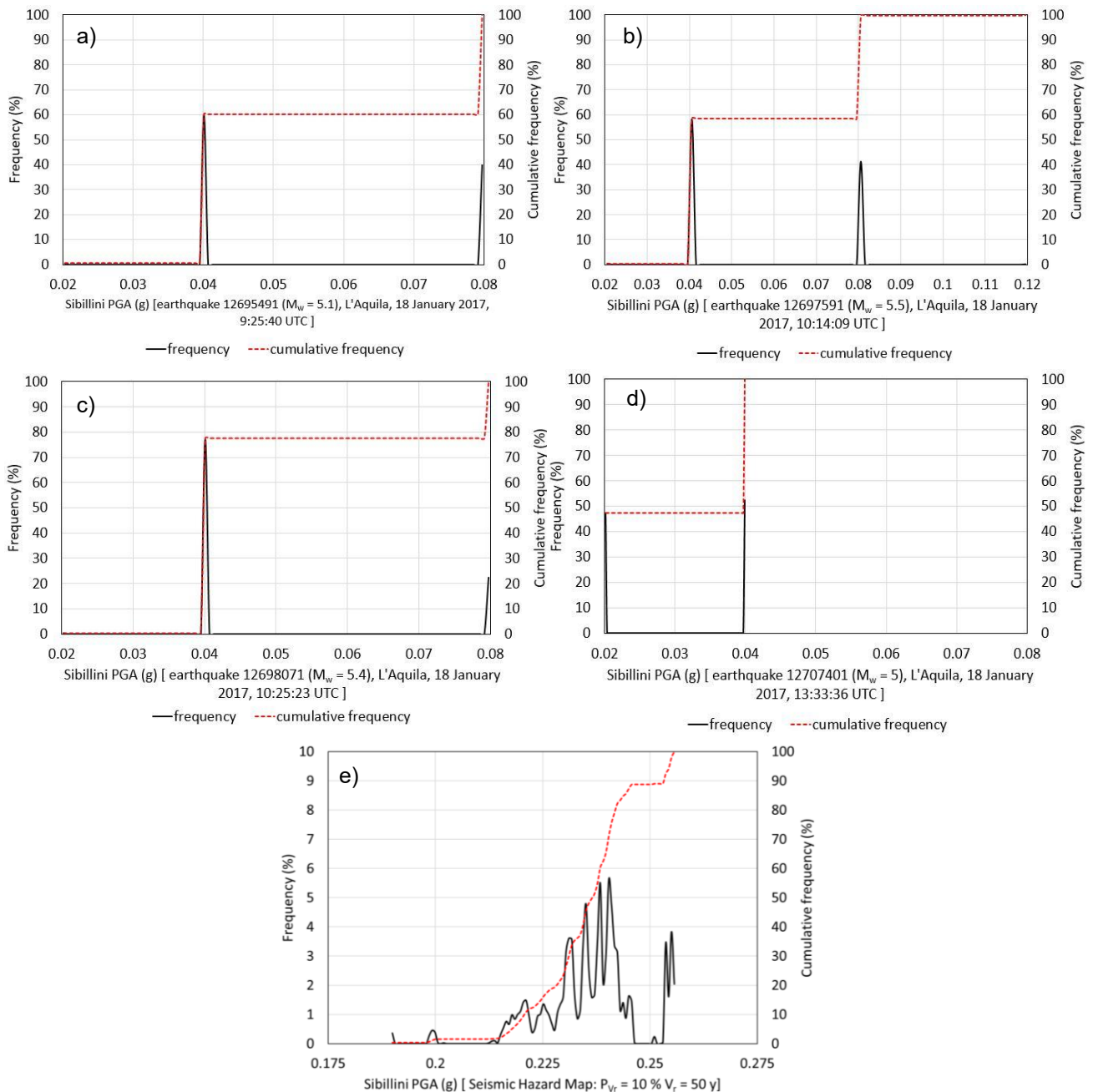


Fig. 4.80 Statistical analysis of accelerations for the earthquakes verified on January 18th, 2017 at the time a) 9:25:40 AM UTC b) 10:14:09 AM UTC c) 10:25:23 AM d) 1:33:36 PM and e) PGA extracted from seismic hazard map ($P_{VR} = 10\%$ $V_I = 50$ y) carried out for Sibillini release areas extracted from mapped snow avalanches

4.6.9 Sibillini, Adriatic side, release areas

The statistical analysis carried out for release areas extracted in the Sibillini Mountains, Adriatic side, is shown below in Fig. 4.81. Fig. 4.81 a) shows the distribution of release areas acceleration for the earthquake verified on January 18, 2017 at the time 9:25:40 AM UTC in the interested mountain sector. It is observed that about 0.6% of the cells of release areas include PGA values of 0.02 g, 64% equal to 0.04 g and the remaining 36% equal to 0.08 g. Fig. 4.81 b) shows the distribution of release areas acceleration for the earthquake verified on January 18, 2017 at the time 10:14:09 AM UTC in the interested mountain sector. It is observed that about 0.6% of the cells of release areas include PGA values of 0.02 g, 53% equal to 0.04 g, 46% equal to 0.08 g, and the remaining 0.1% equal to 0.12 g.

Fig. 4.81 c) shows the distribution of release areas acceleration for the earthquake verified on January 18th, 2017 at the time 10:25:23 AM UTC in the interested mountain sector. It is observed that about 0.6% of the cells of release areas include PGA values of 0.02 g, 75% equal to 0.04 g and the remaining 24.4% equal to 0.08 g. Fig. 4.81 d) shows the distribution of release areas acceleration for the earthquake verified on January 18th, 2017 at the time 1:33:36 PM UTC in the interested mountain sector. It is observed that about 48% of the cells of release areas include PGA values of 0.02 g, while the remaining 52% is equal to 0.04 g. Fig. 4.81 e) shows the distribution of release areas PGA extracted from seismic hazard map ($P_{VR} = 10\%$ $V_r = 50$ y). It is observed that approximately 99% of release areas cells show values ranging from 0.15 to 0.25 g, corresponding to seismic zone 2. The remaining 1% of the cells show values higher than 0.25 g, corresponding to seismic zone 1. It is therefore observed that all the release areas fall into the two zones with the highest seismic hazard.

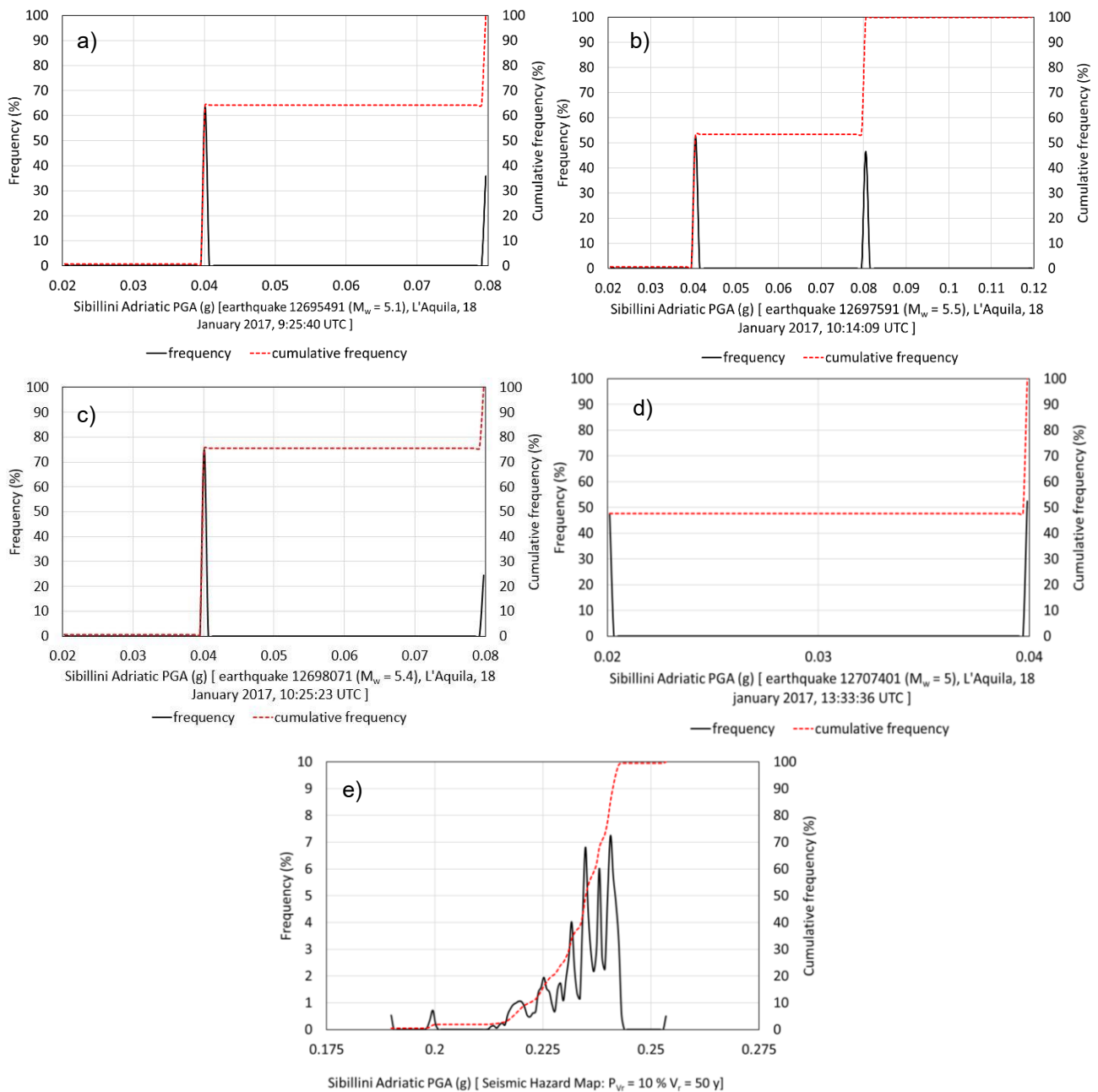
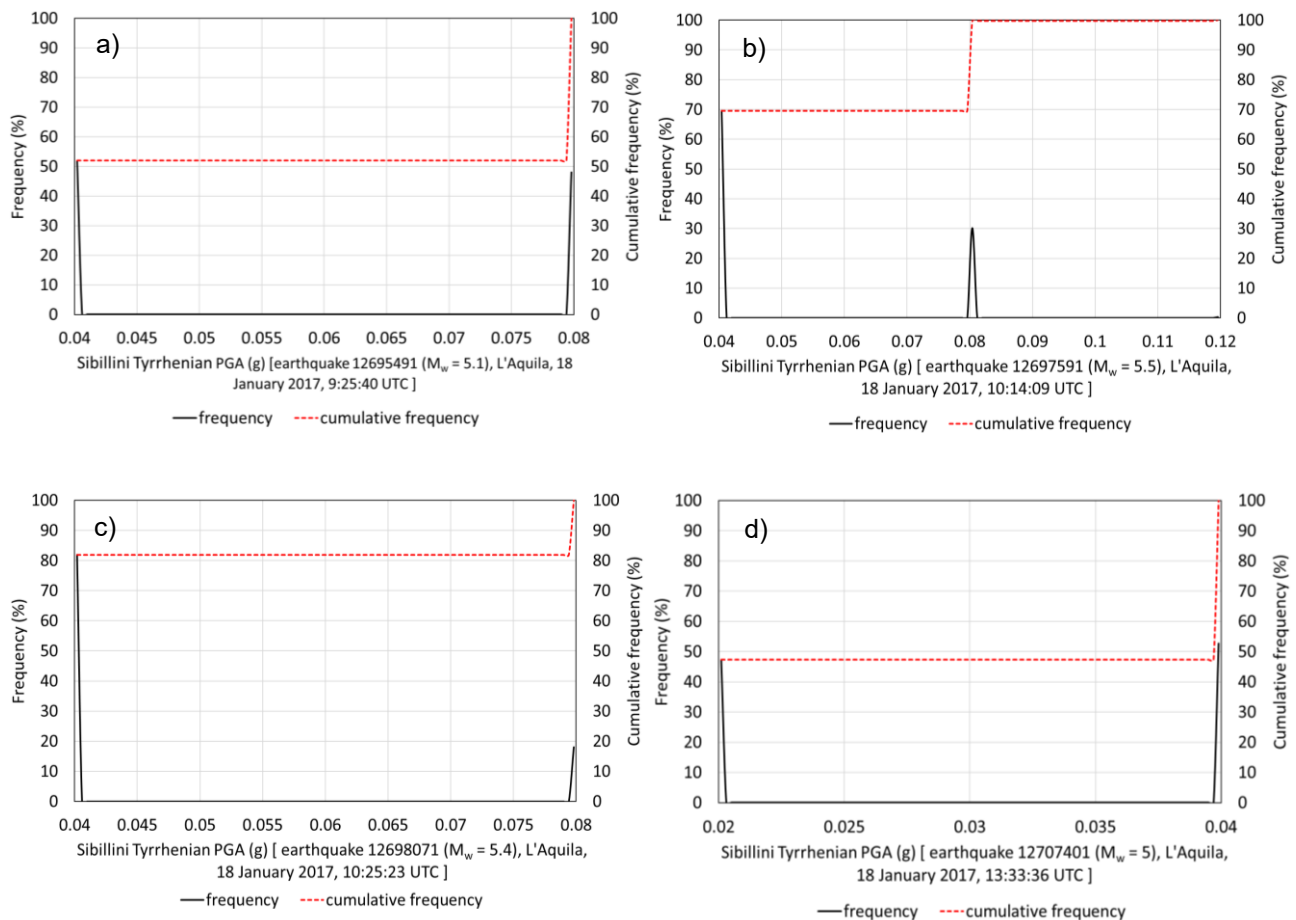


Fig. 4.81 Statistical analysis of accelerations for the earthquakes verified on January 18th, 2017 at the time a) 9:25:40 AM UTC b) 10:14:09 AM UTC c) 10:25:23 AM d) 1:33:36 PM and e) PGA extracted from seismic hazard map ($P_{VR} = 10\%$ $V_r = 50$ y) carried out for Sibillini Adriatic release areas extracted from mapped snow avalanches

4.6.10 Sibillini, Tyrrhenian side, release areas

The statistical analysis carried out for release areas extracted in the Sibillini Mountains, Tyrrhenian side, is shown below in Fig. 4.82. Fig. 4.82 a) shows the distribution of release areas acceleration for the earthquake verified on January 18th, 2017 at the time 9:25:40 AM UTC in the interested mountain sector. It is observed that about 52% of the cells of release areas include PGA values of 0.04 g, while the remaining 48% is equal to 0.08 g. Fig. 4.82 b) shows the distribution of release areas acceleration for the earthquake verified on January 18th, 2017 at the time 10:14:09 AM UTC in the interested mountain sector. It is observed that about 69.7% of the cells of release areas include PGA values of 0.04 g, 30% equal to 0.08 g and the remaining 0.3% equal to 0.12 g. Fig. 4.82 c) shows the distribution of release areas acceleration for the earthquake verified on January 18th, 2017 at the time 10:25:23 AM UTC in the interested mountain sector. It is observed that about 82% of the cells of release areas include PGA values of 0.04 g, while the remaining 18% is equal to 0.08 g. Fig. 4.82 d) shows the distribution of release areas acceleration for the earthquake verified on January 18th, 2017 at the time 1:33:36 PM UTC in the interested mountain sector. It is observed that about 47% of the cells of release areas include PGA values of 0.02 g, while the remaining 53% is equal to 0.04 g. Fig. 4.82 e) shows the distribution of release areas PGA extracted from seismic hazard map ($P_{VR} = 10\%$ $V_r = 50$ y). It is observed that approximately 66% of release areas cells show values ranging from 0.15 to 0.25 g, corresponding to seismic zone 2. The remaining 34% of the cells show values higher than 0.25 g, corresponding to seismic zone 1. It is therefore observed that all the release areas fall into the two zones with the highest seismic hazard.



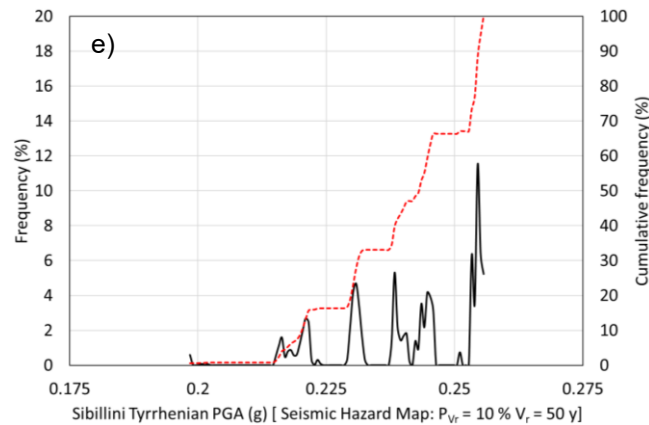
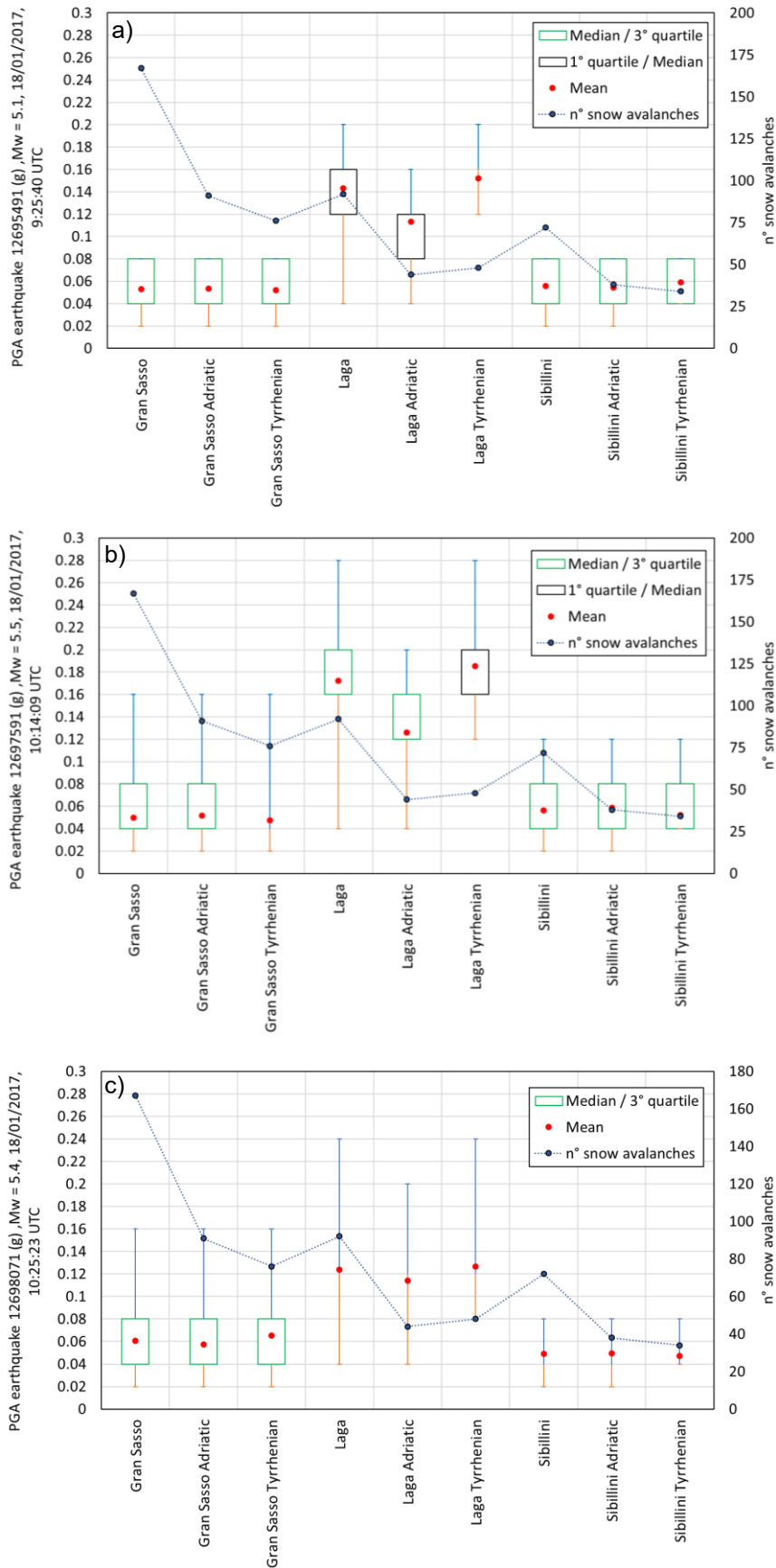


Fig. 4.82 Statistical analysis of accelerations for the earthquakes verified on January 18th, 2017 at the time a) 9:25:40 AM UTC b) 10:14:09 AM UTC c) 10:25:23 AM d) 1:33:36 PM 8previous page) and e) PGA extracted from seismic hazard map ($P_{VR} = 10\%$ $V_r = 50$ y) carried out for Sibillini Tyrrhenian release areas extracted from mapped snow avalanches.

4.6.11 Mountain sectors release areas compared

Regarding Fig. 4.83, it is observed that for earthquakes of January 18th, 2017, in Gran Sasso Massif, release areas have always shown roughly the same acceleration values. Only differences in the maximum values are noted: in the earthquakes occurred at the time 10:14:09 UTC and 10:25:23 UTC they reached a 0.16 g PGA. Maximums were lower for the other earthquakes. In general, comparing extracted values with those of seismic hazard map, accelerations lower or comparable with the minima shown on the map, have been reached. There were no particular differences between Adriatic and Tyrrhenian side both for earthquakes and the seismic hazard map. A behavior similar to that found in the Gran Sasso was also observed in the Sibillini mountains where, however, the acceleration values obtained in release areas are very similar during the 4 earthquakes. Also in this case, maximum values were found in the course of the earthquakes that took place at 10:14:09 UTC and 10:25:23 UTC. Compared to values extracted from the seismic hazard map, accelerations felt by release areas during earthquakes were much lower. For all earthquakes, release areas of Laga mountains presented the highest acceleration values. Most of these values, caused by earthquakes, fall below the first quartile reported, for the same areas, by the seismic hazard map. Moreover, these values are slightly higher than the minimum values of the seismic hazard map. In this case, we observe differences between Adriatic and Tyrrhenian side. Higher acceleration values are observed in the release areas of the Tyrrhenian side, which is the slope that is firstly affected by seismic waves. The same trend is observed starting from values extracted from seismic hazard map. During the earthquake that occurred at 13:33:36 UTC, a decrease and homogenization of accelerations felt by the release areas of different sectors is observed. The highest values are always found in the Laga Mountains, but they are much more comparable with values found for Gran Sasso and Sibillini release areas. Reporting in the boxplots also the number of snow avalanches occurred in each sector, it was observed that, in Gran Sasso and Sibillini Mountains, the events number does not seem to be related to the acceleration values found. In these sectors the number of snow avalanches was, instead, related to the snowfall data (Fig. 4.66). On the other hand, a similar trend between acceleration values and events number was noted in Laga Mountains. It is interesting to note that, looking at the Adriatic and Tyrrhenian sides of Laga Mountains, the higher number of events occurred on the Tyrrhenian side in which there is not the maximum of cumulative snow precipitation, found on the Adriatic side (Fig. 4.66), but the maximum of acceleration values.

This element may suggest that some events in the Laga Mountains may, in some way, be related to earthquakes, even if, as already mentioned, we must always take into account two critical parameters: acceleration and snow height.



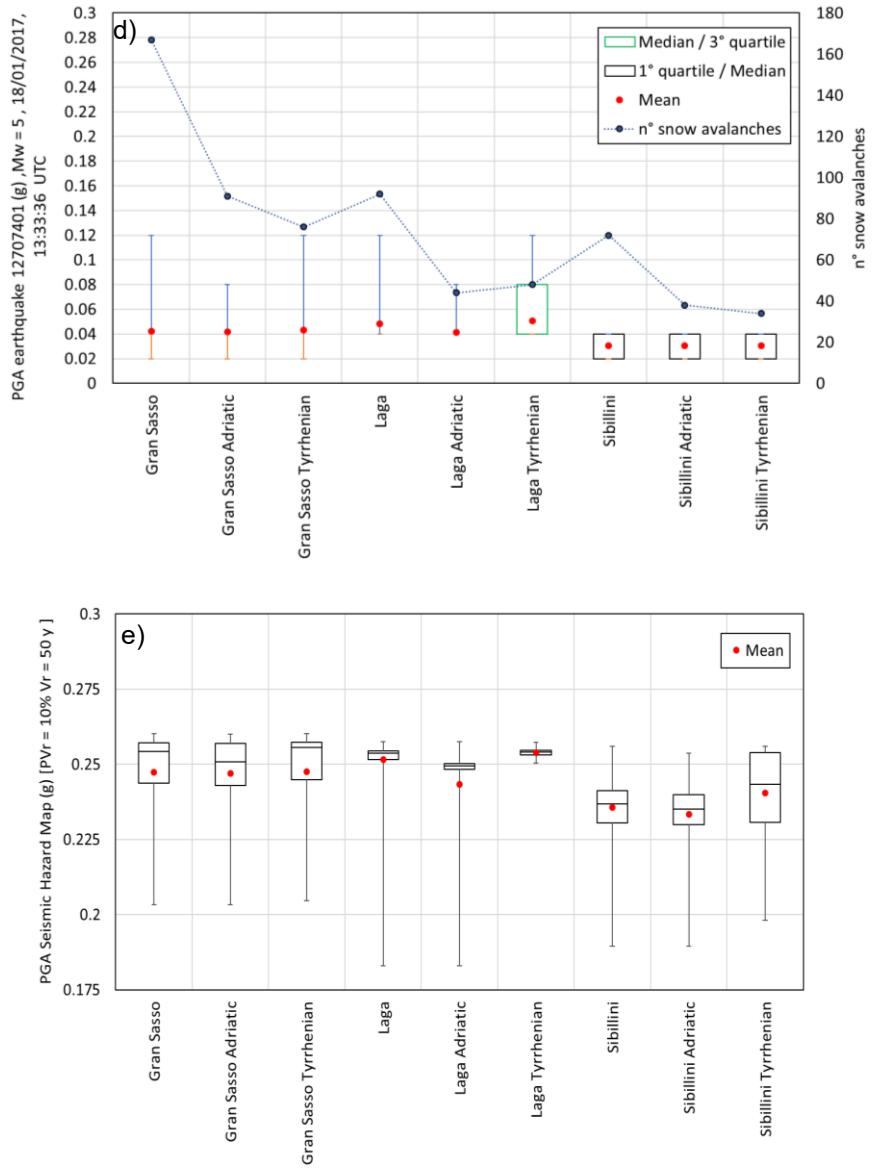


Fig. 4.83 Comparison among PGA distributions of release areas for earthquakes verified on January 18, 2017 at a) 9:25:40 AM UTC b) 10:14:09 AM UTC c) 10:25:23 AM UTC (previous page) d) 1:33:36 PM UTC and e) seismic hazard map. Dot line indicates number of events in each sector.

4.6.12 Snow avalanches potentially triggered by earthquakes

After the seismic characterization of release areas, we tried to understand which of these could have been triggered by earthquakes with $M_w \geq 5$ occurred on January 18th, 2017. To this end, the snow avalanche release model, proposed by Pérez-Guillén (2014) cum bibl. also reported in paragraph 3.2.2 was applied. The goal is the achievement of a critical acceleration value, produced by an earthquake, that can trigger snow avalanches. As already anticipated, the problem of the detachment induced by earthquake must take into account 2 parameters: the snowpack height and the acceleration. In our study, the first problem was to understand the snow height when the earthquakes occurred. This depends on the meteorological model that accumulates snow regardless of the occurrence of previous snow avalanches. As a consequence, on the day of interest, the cumulative values ranged from 400 to 500 cm in all the release areas. The Pérez-Guillén (2014) cum bibl. model would be inapplicable using these values, since the cumulative value is higher than the critical snow height for which snow avalanches would be detached, even without the earthquakes action. Having no further data available, we tried to estimate the average snow height present in each mountain sector, differentiating between Adriatic and Tyrrhenian side. Usually, when the snow avalanche release occurs, the whole snow thickness is hardly ever detached. Of the entire precipitous snow mass, only a part is considered unstable. A representative quantity of this mass is the detachment height H_d . The latter can be calculated using the indications provided by Swiss Directives (Salm et al., 1990), and it presents the following expression.

$$H_d(T; z) = [DH_{3gg}(T; z) + H_{sd}] \cdot \cos(28^\circ) * f(\vartheta) \quad (50)$$

$DH_{3gg}(T; z)$ is the increase in snowpack height (measured vertically), on three consecutive days of precipitation, and it is a function of the return time T and the average altitude of release area z . In this case, return time and altitude have not been taken into account. So, the cumulative precipitation data, as provided by the model, were used. H_{sd} is the snow height (measured vertically) transported by the wind. On the mountain sector scale, exposures vary a lot and there are many factors that can influence this variable. So, this parameter has been set equal to 0 because it is not possible to evaluate the wind effect. $f(\vartheta)$ is a descending function of the release area average slope, ϑ , having the following expression:

$$f(\vartheta) = \frac{0.291}{\sin(\vartheta) - 0.202 \cdot \cos(\vartheta)}, \text{ with } \vartheta \geq 28^\circ \quad (51)$$

The $DH_{3gg}(T; z)$ values used for mountain sectors, on both sides, are the average values. For the slope used, we need to make an anticipation. Critical acceleration value is highly sensitive with respect to slope variations. More details in paragraph "Model and results critical observations". Therefore, to be precautionary, we used the average slope value, to which one degree was subtracted. At this point, the model of Pérez-Guillén (2014) cum bibl. was used, but without considering the action of the earthquake. In this way, the critical snow height, for which spontaneous release occurs, was obtained. These calculations were made with 2 values of shear strength. Snow layers composed of decomposing forms and graupel were considered. To find the shear strength for decomposing forms, equation (29.1) was used. A snow density of 200 kg/m³ and ice density of 916.8 kg/m³ were considered. To find the shear strength for graupel, the following expression, suggested by Osamu Abe (2004), was used:

$$SFI = 82 \cdot \left(\frac{\rho}{\rho_{ice}} \right)^{2.8} \quad [kPa] \quad (52)$$

A snow density of 190 kg/m³ and ice density of 916.8 kg/m³ were used. We chose these two types of snow composition as they are the ones that best describe the snow with weak cohesion reported by bulletins. Subsequently, the critical height was iteratively subtracted from the H_d value. This operation was repeated until a value, lower than critical height, was obtained. It corresponds to an estimate of the snow height, stable, in the mountain sectors release areas for which calculations were performed. As anticipated, we calculated for both shear strength values. Now, we applied the Pérez-Guillén (2014) cum bibl. model, using the stable height as input, to find the critical earthquake acceleration that causes detachment. Input values (slope and $DH_{3gg}(T; z)$), H_d , critical snow height (h_c), stable snow height (h_{stab}) and critical acceleration (a_c) for graupel and decomposing forms are reported, respectively, in Table 15 and Table 16.

Table 15 Input values (slope and DH_{3gg}), H_d , critical snow height (h_c), stable snow height (h_{stab}) and critical acceleration (a_c) for graupel snow

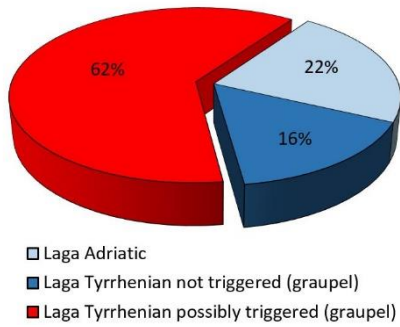
GRAUPEL	$\alpha = \theta$ (°)(mean -1)	DH_{3gg} (cm) (mean)	H_d (m)	h_c (m)	h_{stab} (m)	a_c (g)
Gran Sasso Adriatic	34	503	3.299	0.960	0.418	0.725
Gran Sasso Tyrrhenian	31	484	3.637	1.043	0.509	0.539
Laga Adriatic	33	500	3.424	0.986	0.466	0.608
Laga Tyrrhenian	28	490	4.325	1.144	0.893	0.132
Sibillini Adriatic	33	455	3.116	0.986	0.158	2.861
Sibillini Tyrrhenian	28	430	3.795	1.144	0.364	1.007

Table 16 Input values (slope and DH_{3gg}), H_d , critical snow height (h_c), stable snow height (h_{stab}) and critical acceleration (a_c) for decomposing forms snow

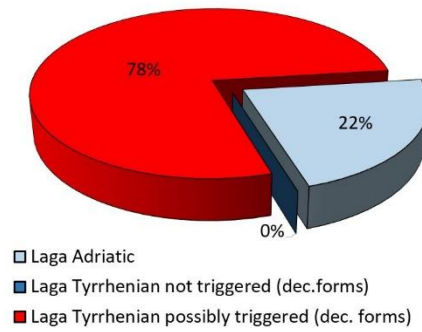
DECOMPOSING FORMS	$\alpha = \theta$ (°)(mean -1)	DH_{3gg} (cm) (mean)	H_d (m)	h_c (m)	h_{stab} (m)	a_c (g)
Gran Sasso Adriatic	34	503	3.299	0.950	0.450	0.621
Gran Sasso Tyrrhenian	31	484	3.637	1.031	0.544	0.461
Laga Adriatic	33	500	3.424	0.975	0.498	0.521
Laga Tyrrhenian	28	490	4.325	1.131	0.931	0.101
Sibillini Adriatic	33	455	3.116	0.975	0.190	2.246
Sibillini Tyrrhenian	28	430	3.795	1.131	0.401	0.853

The highest accelerations were found for graupel snow. Found accelerations are quite high because h_{stab} shows, in general, low values. Using the results obtained from the release areas seismic characterization for mountain sectors, reported in paragraph 4.6, and critical accelerations, it is possible to understand which areas can potentially be triggered by interested earthquakes. It was noted that only release areas in Laga Mountains, Tyrrhenian side, presented accelerations, manifested during earthquakes, higher than respective critical values. The scenario for graupel and decomposing forms, during the 4 events considered, is reported respectively in **Attached 5** and **Attached 6**. Each scenario is independent. Below are the pie charts that show, in the Laga Mountains and for the two shear strengths, the percentage of release areas extension that can potentially be triggered during the considered earthquakes (Fig. 4.84).

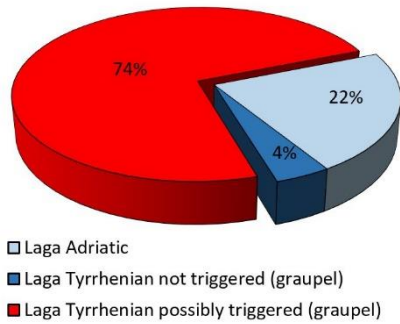
Earthquake 12695491 (M_w=5.1), L'Aquila, 18 January 2017,9:25:40 UTC



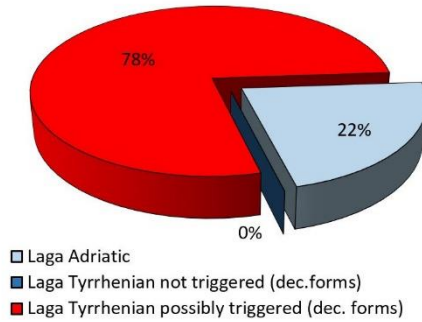
Earthquake 12695491 (M_w=5.1), L'Aquila, 18 January 2017,9:25:40 UTC



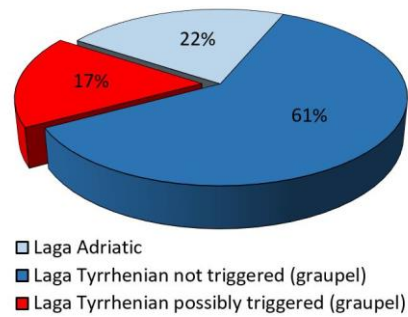
Earthquake 12697591 (M_w = 5.5), L'Aquila, 18 January 2017, 10:14:09 UTC



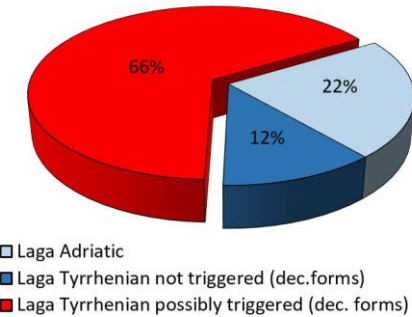
Earthquake 12697591 (M_w = 5.5), L'Aquila, 18 January 2017, 10:14:09 UTC



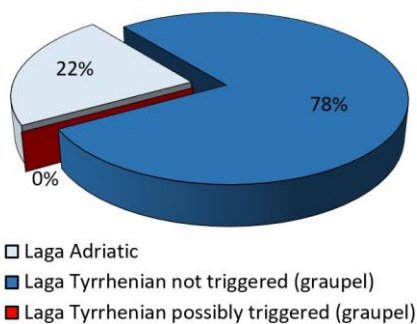
Earthquake 12698071 (M_w = 5.4), L'Aquila, 18 January 2017, 10:25:23 UTC



Earthquake 12698071 (M_w = 5.4), L'Aquila, 18 January 2017, 10:25:23 UTC



Earthquake 12707401 (M_w = 5), L'Aquila, 18 January 2017, 13:33:36 UTC



Earthquake 12707401 (M_w = 5), L'Aquila, 18 January 2017, 13:33:36 UTC

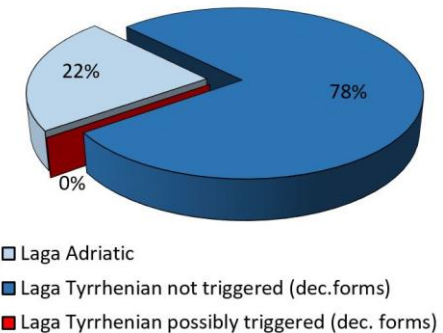


Fig. 4.84 Pie charts showing, in Laga Mountains and for the two shear strengths(graupel snow on the left, decomposing forms on the right), the percentage of release areas extension that can potentially be triggered during the considered earthquakes

There are some differences between scenarios obtained with the two shear strengths. For the first 3 earthquakes, a greater release areas extension can be triggered considering the decomposing forms shear strength respect to graupel snow. For the last earthquake, instead, the scenario obtained for decomposing forms is identical to that obtained for graupel snow. In this case, accelerations produced by the earthquake are not high enough to cause detachment. Considering the graupel snow, there is a slight increase in areas that can be triggered between the earthquake occurred at 9:25:40 UTC (62%) and that verified at 10:14:09 UTC (74%). On the contrary, a sharp decrease of possibly triggered areas is observed between the earthquake occurred at 10:14:09 UTC and that verified at 10:25:23 UTC (17%), despite the magnitude of the two events is comparable. Considering the decomposing forms, we observe an identical scenario between the first two earthquakes, in which all the release areas of Laga Mountains, Tyrrhenian side, can be potentially triggered. For the earthquake occurred at 10:25:23 UTC, a slight decrease in release areas extent, possibly triggered, was observed.

Model and results critical observations

It is necessary to make an important observation. These evaluations and results are carried out on the scale of mountain massifs; therefore, on the single slope the conditions can be significantly different. The model presents uncertainties related to input data. Release areas slope values were obtained from a low quality DEM. Moreover, a_c is very sensitive to slope changes. To be precautionary, as slope input (α) the average value (calculated for mountain sector release areas) minus 1 was used. The following table shows the critical accelerations that are obtained using average slope value with the reduction (%) respect to critical acceleration calculated using mean slope minus 1.

Table 17 a_c obtained using mean slope with indication of decrease (%) respect to a_c calculated using (mean slope -1)

	$a_c \alpha = \text{mean}$	$a_c \alpha = (\text{mean} - 1)$	decrease (%)
GRAUPEL	0.926 g	0.725 g	21.74%
	0.726 g	0.539 g	25.72%
	0.788 g	0.608 g	22.83%
	0.219 g	0.132 g	39.87%
	4.632 g	2.861 g	38.24%
	1.560 g	1.007 g	35.45%

	$a_c \alpha = \text{mean}$	$a_c \alpha = (\text{mean} - 1)$	decrease (%)
DEC. FORMS	0.791 g	0.621 g	21.55%
	0.622 g	0.461 g	25.79%
	0.675 g	0.521 g	22.82%
	0.179 g	0.101 g	43.74%
	3.368 g	2.246 g	33.32%
	1.290 g	0.853 g	33.85%

The choice of the snow composition, with relative densities, has been hypothesized since the stratigraphies were not accessible. To this, we add the meteorological model uncertainties for the definition of the cumulative snow precipitation. Moreover, the applied model is basic and we have not taken into account several factors that can significantly change the obtained scenarios. As already mentioned, the wind action, that could locally cause a snow load even higher than the values obtained, was not considered. The temperature variation was not regarded in the model. It can influence the critical height value for which the release occurs. Moreover, the model does not treat the release areas curvature: a greater concavity would allow a better capacity of accumulation and, therefore, increase the value of critical height. Finally, the stable height value, for which the calculations were developed, is only an approximate estimate of the height present at the time of earthquakes. Based on what previously described, the h_{stab} values could also be very different from those obtained. Also, no height variations were made between one earthquake and another. Therefore, the obtained scenarios are independent: the effects of the single earthquake were considered as if it was the only event

that occurred. We must also add the uncertainty of data extracted by ShakeMaps. As described in section 4.6, they give only an indicative estimation of the shaking suffered by the ground. For all these reasons, results obtained are indicative of which areas may have been, more likely, subject to a seismically induced snow avalanches during the earthquakes of interest. If the analysis was repeated, locally, for each snow avalanche release area, the results could be significantly different.

4.7 Rigopiano disaster (January 18th 2017)

The Rigopiano tragedy, in which 29 people died, occurred on January 18th, 2017, and it is part of a context of heavy snowfall and seismic activity in Central Italy. The Rigopiano Hotel was located in Farindola Municipality, province of Pescara, and it was destroyed by a snow avalanche defined by Frigo et al., (2018) a "fluidized dry snow avalanche" which was characterized by a particularly long channeled track zone (about 1500 m) despite the release area extension was not particularly wide. "The avalanche released approximately at 17:40 from Mount Siella", on the Adriatic side of Gran Sasso Massif (Frigo et al., 2018). The main features of the avalanche were its fluidity and the presence of trees and debris (Frigo et al., 2018). Upstream of the Hotel, there was a forest, and usually, forested areas should prevent or slow down the avalanche, but in this case, the flow was incredibly fast (about 30 m/s), and the presence of solid material led exclusively to avalanche density increasing (Frigo et al., 2018). In fact, the slab density can be considered equal to 250 kg/m³, but, because of fluidification, it can be reduced to 200 kg/m³. Debris and trees density was about 700 kg/m³, so the final snow avalanche density can reasonably be considered equal to 450 kg/m³ (Frigo et al., 2018). This scenario led to an impact pressure with the Hotel equal to 393 kPa (Frigo et al., 2018). Starting from DEM and cumulative precipitation data on the days January 15th-18th 2017, it was possible to characterize Rigopiano release area. Rigopiano release area shows an extension of approximately 25500 m² and it lies between 1846 and 1725 m altitude, with an average altitude of 1781 m. The Rigopiano Hotel was located downstream at an altitude of about 1150 m. The average slope obtained is about 34 °, but it presents maximums that reach even 47°. Release area aspect is between 18° and 108°, with an average value that is around 83°, so the area is exposed to the East. The distribution of Plan curvature cells values has a negative median. Therefore, more than 50% of the area has concave structures in the direction perpendicular to that of maximum slope. On the contrary, a prevalence of convex structures is observed in the direction of maximum slope. Always keep in mind that data must be evaluated based on the initial DEM quality. The meteorological model has returned, for Rigopiano release area, a cumulative value, for the days January 15th-18th 2017, equal to 485 cm. Considering a depth of the weak layer equal to 2 m (Frigo et al., 2018), it is possible to estimate that the snow volume, detached at the release area, is about 50000 m³. Considering that the total volume dragged by the avalanche is about 103000 m³ (Frigo et al., 2018), it can be observed that the volume has more than doubled. It is emphasized that data obtained are slightly different from data reported in Frigo et al., 2018 and Chiambretti et al., 2018. The main reasons are the different starting DEM, and the analysis carried out at a much larger scale. Following the event, the activity carried out by forensic engineering was significant. The most difficult data to obtain were those relating to the release area because of the time elapsed since the event. The perimeter of this area was obtained through the comparison of photographs, from days before the event, combined with data found in the field. The perimeter of the avalanche was obtained by GPS, and the rough height of the stream was obtained by observing the vegetation damages. On average, the height of the dense flow was

3-4 m, while that of the powder flow was of about 10 m. Furthermore, from snow and debris deposits near the trees, it was possible to evaluate the flow direction (Chiambretti et al., 2018). Below, in Fig. 4.85, the territorial classification, in the Gran Sasso Massif, of Rigopiano snow avalanche, and the detail of its release area and path are reported. Moreover, the section taken along the central axis of snow avalanche path is reported.

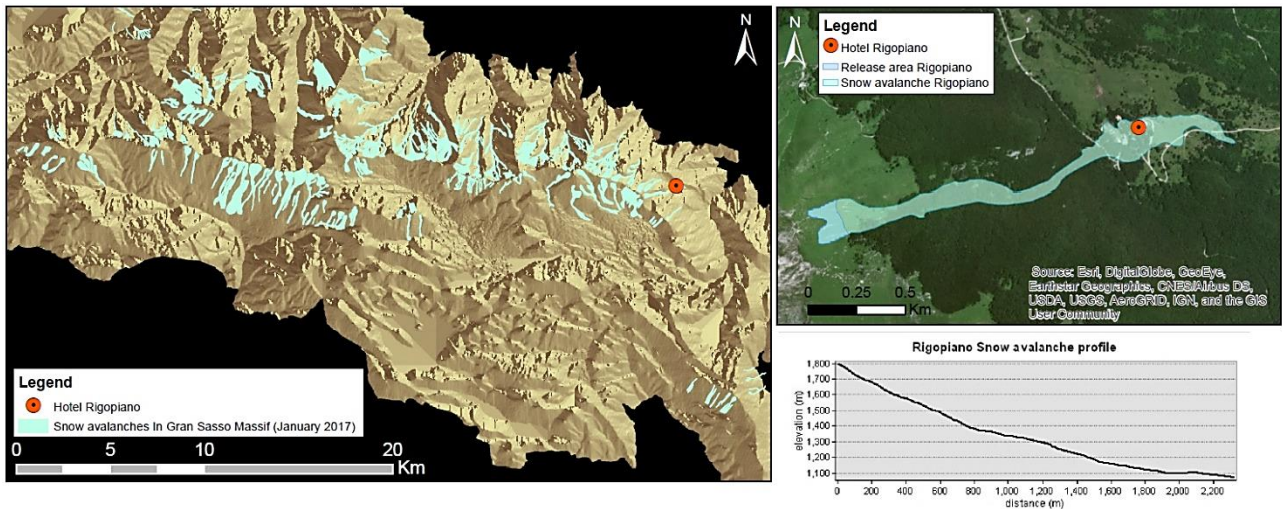


Fig. 4.85 territorial classification, in the Gran Sasso Massif, of Rigopiano snow avalanche and the detail of its release area, path and section taken along the central axis of snow avalanche path

As already mentioned, the Rigopiano release area is not indeed among the most relevant in terms of the extension, as shown in Fig. 4.86. Approximately 98% of the total release areas present an extension of less than 100,000 m². Only 2% are larger. Among these, the largest has an extension of approximately 575,000 m². The average extension is about 14000 m², so the Rigopiano release area presents an extension just above the average. This factor makes it possible to understand how even avalanches involving a lower volume can cause disastrous damage. Undoubtedly, in the risk assessment, exposure plays a key role. We want to underline that, with both the Maggioni and Bühler algorithms for the PRA delineation, the Rigopiano release area has been identified. Therefore, with such methods, it is possible to carry out a work of prevention and protection against snow avalanches.

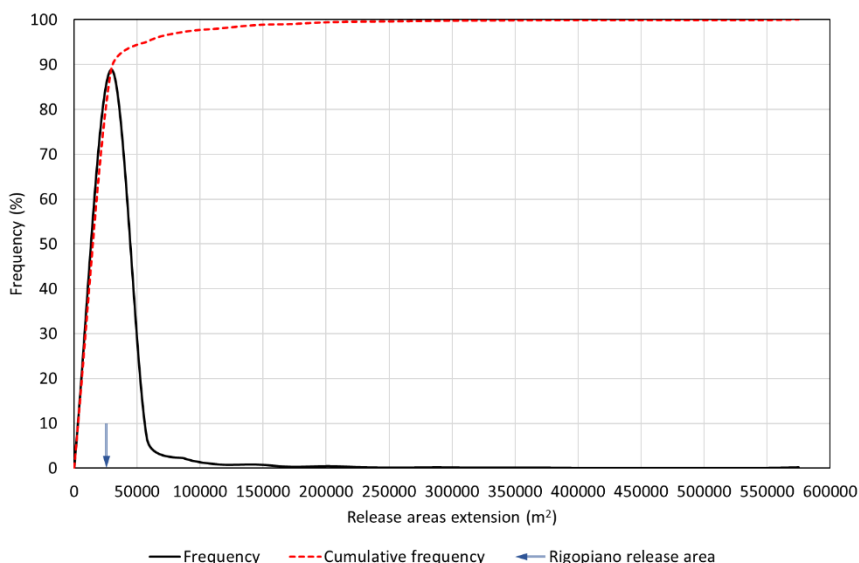


Fig. 4.86 Statistical distribution of release areas extension with the indication of Rigopiano release area.

The context that is being analyzed must take into account, in addition to the geomorphological and nivo-meteorological data, also the possible influence of earthquakes. In this study, the 4 earthquakes of magnitude higher than or equal to 5 occurred on January 18th, 2017 as reported in paragraph 4.6. In addition to these earthquakes, the seismic hazard map was used. Using the Rigopiano release area, acceleration values resented and seismic hazard map PGA values were extracted. The values obtained are shown in Table 18.

Table 18 Acceleration values (g) that affected Rigopiano release area on 18 January 2017 and PGA from seismic hazard map for the same release area

Event ID (ID in Fig. 4.3)	mm/dd/yy	hh:min:sec UTC	Rigopiano resented PGA (g)
12695491 (13)	1/18/2017	9:25:40 AM	0.02
12697591 (12)	1/18/2017	10:14:09 AM	0.04
12698071 (8)	1/18/2017	10:25:23 AM	0.04
12707401 (5)	1/18/2017	1:33:36 PM	0.02
Seismic Hazard Map ($P_{VR}= 10\%$ $V_R= 50$ y)	-	-	0.21

It is observed that the acceleration data obtained from the 4 earthquakes are of an order of magnitude lower than the value reported by the seismic hazard map. Starting from this last value, Rigopiano release area falls in seismic zone 2 (Table 8). For the Rigopiano snow avalanche it is possible to affirm that it is not a co-seismic event, in reference to the 4 earthquakes considered. In fact, the Rigopiano snow avalanche occurred many hours later compared to events with $M_w \geq 5$ of January 18th 2017. It is challenging to know if one of these earthquakes could, in some way, compromise the stability of the snowpack causing a delayed release over time. It is assumed that the model of Pérez-Guillén (2014) cum bibl. it is basic to obtain a precise result for the specific case of Rigopiano. As described in the paragraph 4.6.12 "Model and results critical observations", too many aspects that could make the difference would be overlooked. In general, however, it is possible to compare the accelerations resented by Rigopiano release area (Table 18) with the critical accelerations (for graupel snow and decomposing forms, respectively Table 16 and Table 18) found for the mountain sector to which it belongs: Gran Sasso, Adriatic side. From this comparison it is observed that the critical accelerations, in both cases, are more than one order of magnitude above those resented at Rigopiano release area. Consequently, considering the time gap between the Rigopiano avalanche and the earthquakes, and ascertaining the considerable difference between critical acceleration found for Gran Sasso, Adriatic side, and accelerations resented at Rigopiano release area, it can be concluded that the events with $M_w \geq 5$, verified on January 18th 2017, played a negligible role in the detachment of the Rigopiano snow avalanche.

4.8 Conclusions

This study can be subdivided into 2 parts:

In the first part the state of the art of snow avalanches monitoring, characterizing and forecasting methods was described. In particular, seismic and infrasonic methods were described. It was found that different parameters (speed, size, path, type, distance) of avalanches can be obtained through the study of such signals. It is possible to use seismic and infrasonic signals for the automatic detection of avalanches, even if this operation does not always produce good results due to the environmental noise. The mutual use of seismic and infrasonic methods is very important. Infrasonic signals are not subject to anelastic attenuation and geometric diffusion so that, they can be used for the detection of the initial phase of the avalanche. On the contrary, the final phase is only detected by seismic sensors since the powder cloud, origin of infrasonic signals, is drastically reduced. Precisely because these methods work well for the initial and final phase of the avalanche release, they allow to understand the total event duration. In essence, we have observed the complementarity of the two methods which can provide a great potential for monitoring snow avalanches. Also in the first part, the main literature notions about snow avalanches triggered by earthquakes were introduced. There are two types of snow avalanches induced by earthquakes. The first type is co-seismic snow avalanches, whose release occurred immediately or soon after the earthquake. The second type is snow packs that, because of seismic-induced stress changes, irremediably compromised their stability. Then, the release takes place with a certain delay time compared to the earthquake occurrence. Even now, the success of seismic and infrasonic methods complementarity, for the identification of seismic-induced snow avalanches, has been described. A fundamental concept has been emphasized: when studying the seismic-induced snow avalanches, the earthquake alone is not enough to cause detachment. Snowpack stability conditions are fundamental. In the first studies on the subject, a parallelism with landslides triggered by the earthquakes was often sought. What is valid for landslides, and that we expect for avalanches, is that as earthquake magnitude increases, the distance for which seismic-induced events occur and the number of such events, increases too. Again, in a comparison between avalanches and landslides, the minimum magnitude value that could trigger avalanches was investigated. From literature, the minimum M_w value that can trigger snow avalanches, for a 0 distance between site and source, is equal to 1.9 (corresponding to a PGA of 0.03 g). The first part of the work ends with the presentation of 3 snow avalanches release models with earthquake action. We highlight the model of Pérez-Guillén et al. (2014), to understand some results of this study described below, which takes into account the action of the earthquake, studying the relationship between the shear resistance of the snowpack, at the weak layer, and the shear stress acting on it. The whole is enclosed in a stability factor.

In the second part, core of this elaborate, the case study was presented: Central Apennines area. The objective of the study is a geomorphological, nivo-meteorological and seismic analysis of snow avalanches release areas in January 2017. The study area is defined by the administrative limits of Abruzzo, Lazio, Marche, Molise and Umbria regions. Initially, the seismic and nivo-meteorological framing, in January 2017, was presented. Central Apennines fall into seismic zones 1 and 2. Most of the earthquakes occurred in January 2017 (57% of those occurring throughout the whole year) were provoked by the CSS ITCS028 (Colfiorito-Campotosto). Among these, there are 4 earthquakes with $M_w \geq 5$ occurred on January 18th, 2017. They will be of particular interest for subsequent analyzes. The nivo-meteorological analysis was based mainly on official data reported by

Meteomont bulletins: sector 07 (Appennino Umbro-Marchigiano) and sector 04 (Grandi Massicci Appenninici and Appennino Abruzzese). These data are valid on a synoptic- regional scale, so results of cumulative snow precipitation (15th-18th January 2017) returned by the application of a meteorological model (Moloch), compared with NASA satellite images were examined too. Mountainous areas mainly affected by the perturbation are Laga Mountains, Gran Sasso and Majella Massifs. In these sectors the average cumulative value was between 400 and 500 cm, but the maximum values also exceeded 500 cm. However, the entire area of interest has been subject to strong perturbation in the examined period. After this general overview, the work can be divided into 5 subparts:

- 1) Geomorphological analysis of the entire study area
- 2) Geomorphological, nivo-meteorological analysis of snow avalanches release areas
- 3) Application of semi-automatic procedures for defining the Potential Release Areas (PRA)
- 4) Seismic analysis of snow avalanches release areas and definition of possible detachments due to earthquakes.
- 5) Rigopiano disaster (January 18th 2017)

1) To carry out the geomorphological analysis the SRTM (Shuttle Radar Topography Mission) DEM, with a resolution of 30 m, was used. It is emphasized that the shifting, resampling and interpolating data inherited, from the original DEM, and introduced artifacts in some topographic features. Therefore, the used DEM is not of excellent quality. This leads to uncertainties in the results obtained. The analysis was developed for areas at an altitude higher than 500 m. The Zevenbergen and Thorne (1987) algorithm was used for the calculation of slope, aspect profile and plan curvature. Slope distribution reveals that 50% of cells show values between 10° and 25°. There are no prevailing exposures on the entire study area. The distribution of the Plan curvature is practically symmetrical, while the profile curvature is slightly asymmetrical, and about 70% of total cells are concave. A classification of the curvatures was carried out using the Dikau criterion (1989). The most common structures are hollow foot and nose (about 30% of the total cells for each of them). Subsequently, different parameters were calculated for the identification of ridges and valleys. Using the TOPMODEL approach, we calculated the Total Catchment Area (TCA) and consequently the Specific Catchment Area (SCA). Subsequently, other topographic indices were calculated: Topographic Wetness Index (TWI), Stream Power Index (SPI) and Convergence Index (CI). The TCA classifies a higher number of cells as valleys. On the contrary, the TWI classifies a higher number of cells as ridges and it is better than the TCA in managing the flow for flat areas. The SPI classifies most of the cells as valleys, but the percentage of ridges does not differ much. The CI obtains a similar classification. The geomorphological analysis ends with the calculation of the Topographic Position Index (TPI). Also, in this case, the algorithm is used for differentiating ridges and valleys. In this case, the result depends on the chosen neighborhood size.

2) Snow avalanches, occurred in the Apennines (January 2017), perimeter of the largest events was obtained thanks to a work of photo-interpretation carried out on high-resolution satellite images. From these, release areas were extracted. It is anticipated that the timing of such avalanches is not known. The geomorphological analysis led to a statistical characterization of main topographic attributes (elevation, slope, aspect, and curvature) of snow avalanches release areas. Nivo-meteorological release areas analysis was based mainly on data of cumulative snow precipitation, during the period 15th-18th January 2017, deriving from a meteorological model.

In particular, the geomorphological and nivo-meteorological analyses were carried out on the totality of release areas and on Sibillini Mountains, Laga Mountains, Gran Sasso Massif, Majella Massif, and Sirente Velino Mountains release areas. For each mountain sector, release areas were also characterized by differentiating between Adriatic and Tyrrhenian side. Regarding the altitude, it is noted that all the release areas lie above 750 m elevation. Moreover, we can assert that release areas elevation certainly depends on the intrinsic altitude of the mountain sector to which they belong, but in some cases, the meteorological context can lead to some variations. Regarding slope, most of the release areas show values, for all the distributions, in the range between 28° and 45° . It is considered, from literature, the optimal range that favors detachment. Slope data above 60° (too steep) and below 28° (too flat), since this range is deeply consolidated, can be attributed to outliers due to a low DEM quality. Aspect is the parameter for which there are more variations and more things to say. The most interesting result is that all the release areas in the Tyrrhenian sectors present a much more concentrated distribution, between 180° and 270° , than the Adriatic ones. This is caused by the orographic constraints, present in downwind slopes, which lead to the channeling of flows loading with snow only areas that intercept and obstruct such flows coming from North-East. Regarding Plan curvature, it is observed that almost all distributions have a negative median value. This means that more than 50% of cells show concave structures. The distributions of the profile curvature are symmetric with respect to 0. We expected, from these distributions, a significant presence of concave cells. This data must be critically evaluated because of error propagation through second derivatives starting from a low-quality DEM. By observing the number of snow avalanches mapped in each sector, a good matching can be found between the number of events and the cumulative precipitation values. The only exception is found for events occurred in Laga Mountains, Adriatic and Tyrrhenian sides. Although on release areas of the Adriatic side there are higher cumulative values, in the Tyrrhenian side verified more events.

3) In the perspective of prevention, and construction of protective works, two semi-automatic procedures for delineating Potential Release Areas (PRA) were applied. Procedures are presented in Maggioni (2004) and Bühler (2018). The application of the first algorithm is more complex than the second one. In both cases, PRA were obtained starting from reasoning on main topographic attributes. The results were compared with real release areas obtained by photo-interpretation. In both cases, the algorithms identify an area extension that is decidedly superior to that of real events. The latter show an extension equal to 4% of PRA identified with Maggioni (2004) and equal to 7.6% of PRA identified with Bühler et al. (2018). The 75% of real release areas was correctly identified by Maggioni (2004), the 62% by Bühler et al. (2018). PRA extension obtained through Maggioni algorithm is 1.7 times higher than that of PRA obtained with the Bühler et al. algorithm. So, in our case, Bühler's algorithm showed higher precision. In both cases, considering the DEM quality, the results are more than satisfactory. Further possible use of these algorithms lies in the creation of hazard maps.

4) Starting from release areas extracted from mapped snow avalanches, a statistical analysis of the seismic accelerations was performed. This analysis was developed both in the entire area of interest, as regards the PGA reported by the seismic hazard map ($P_{VR} = 10\%$ $V_R = 50$ y), and on three selected mountain sectors (Sibillini Mountains, Laga Mountains and Gran Sasso Massif), as regards both the the PGA and accelerations found in ShakeMaps for events with $M_w \geq 5$ occurred in January 18th 2017. For all earthquakes, except for the one that occurred at 13:33:36 UTC, release areas of Laga mountains presented the highest acceleration values. Higher acceleration values are observed in the release areas of the Laga Mountains, Tyrrhenian side. In Gran Sasso and Sibillini Mountains, the events number is not related to the accelerations found. In these sectors the snow

avalanches number was, instead, related to the snowfall data. On the other hand, a similar trend between acceleration and events number was noted in Laga Mountains. Looking at Adriatic and Tyrrhenian sides of Laga Mountains, the higher number of events occurred on the Tyrrhenian side in which there is not the maximum of cumulative snow precipitation, found on the Adriatic side, but the maximum of accelerations. Accelerations resented by release areas during the earthquakes were lower than those indicated by the seismic hazard map. Now, we tried to understand which release areas could be triggered by earthquakes of interest. To this end, the snow avalanche release model, proposed by Pérez-Guillén (2014) cum bibl. was applied. The goal is the achievement of a critical acceleration value that can trigger snow avalanches. Calculations were made with 2 values of shear strength corresponding to graupel snow and decomposing forms. It was noted that only release areas in Laga Mountains, Tyrrhenian side, could present accelerations for seismic-induced snow avalanches. Critical accelerations found respectively for graupel and decompsing forms are 0.132 g and 0.101 g. For each earthquake, the scenario is independent. It is important to underline that we used a basic model and that these evaluations are carried out on the scale of mountain massifs. Therefore, on the single slope the conditions can be significantly different.

5) The Rigopiano disaster was analyzed. Also, Rigopiano release area was statistically characterized by the geomorphological, nivo-meteorological and seismic viewpoint. Rigopiano release area shows an extension of approximately 25500 m² and it lies at an average altitude of 1781 m. The average slope is about 34 °. Release area aspect is exposed to the East. More than 50% of cells show concave structures in the direction perpendicular to that of maximum slope. On the contrary, a prevalence of convex structures is observed in the direction of steepest descent. The meteorological model has returned, for Rigopiano release area, a cumulative value, for the days January 15th-18th 2017, equal to 485 cm. Rigopiano release area is not among the most relevant in terms of extension: it is just above the average. It should be noted that with the application of both the algorithms described at point 3); despite the low DEM quality, the Rigopiano release area was correctly identified. Accelerations suffered by Rigopiano release area during earthquakes (from 0.02 g to 0.04 g) were compared with the critical acceleration found for Gran Sasso, Adriatic side sector (0.725 g and 0.621 g respectively for graupel snow and decomposing forms), to which the snow avalanche belongs. From this comparison, and considering the time gap between the earthquakes and the avalanche, we concluded, with the highest probability, that earthquake had a marginal role in the detachment of the Rigopiano snow avalanche.

Bibliography and sitography

- #italiasicura. *Il piano nazionale di opere e interventi e il piano finanziario per la riduzione del rischio idrogeologic.* Roma: Invitalia, 2017.
- Abe. «Shear strength and angle of repose of snow layers including graupel.» *Annals of Glaciology* 38 (2004): 305-308.
- AINEVA. AINEVA - Associazione delle Regioni e Province autonome dell'arco alpino italiano. s.d. <http://www.aineva.it/>.
- Bessason, Eiriksson, Thorarinsson, Thorarinsson, Einarsson. «Automatic detection of avalanches and debris flows by seismic methods.» *Journal of Glaciology* 53, n. 182 (2007): 461-472.
- Biescas, Dufour, Furdada, Khazaradze and Suriñach. «Frequency content evolution of snowavalanche seismic signals.» *Surveys in Geophysics* 24 (2003): 447-464.
- Böhner, Selige. «Spatial prediction of soil attributes using terrain analysis and climate regionalisation.» *Göttinger geographische abhandlungen* 115 (2006): 13-28.
- Bühler, von Rickenbach, Stoffel, Margreth, Stoffel, Christen. «Automated snow avalanche release area delineation - validation of existing algorithms and proposition of a new object-based approach for large scale hazard indication mapping.» *Natural Hazards and Earth System Sciences*, 2018: 1-24.
- Bulajića, Bajić, Stojnić. «The effects of geological surroundings on earthquake-induced snow avalanche prone areas in the Kopaonik region.» *Cold Regions Science and Technology* 149 (2018): 29-45.
- Chiambretti, Chiaia, Frigo, Marellò, Maggioni, Fantucci, Bernabei. «The 18th January 18th 2017 Rigopiano avalanche disaster in Italy - Analysis of the applied forensic field investigation techniques.» *Proceedings, International Snow Science Workshop*. Innsbruck, Austria, 2018. 1208-1212.
- Chiambretti, Sofia. «Winter 2016-2017 snowfall and avalanche emergency management in Central Italy .» *Proceedings, International Snow Science Workshop, Innsbruck, Austria, 2018*, 2018: 1445-1449.
- Comey, Mendenhall. «Recent studies using infrasound sensors to remotely monitor avalanche activity.» *Proceeding of International Snow Science Workshop*, 2004: 640–646.
- ESRI. *Curvature function - Help | ArcGIS for Desktop*. s.d. <http://desktop.arcgis.com/en/arcmap/10.5/manage-data/raster-and-images/curvature-function.htm>.
- Fierz, Armstrong, Durand, Etchevers, Greene, McClung. «The International Classification for Seasonal Snow on the Ground.» *IHP-VII Technical Documents in Hydrology*, 2009: 8.
- Frigo, Chiaia, Chiambretti, Bartelt, Maggioni, Freppaz. «The January 18th 2017 Rigopiano disaster in Italy - Analysis of the avalanche dynamics.» *Proceedings, International Snow Science Workshop*. Innsbruck, Austria, 2018. 6-10.
- Fujita, Inoue, Izumi, Yamaguchi, Sadakane, Sunako, Nishimura, Immerzeel, Shea, Kayastha, Sawagaki, Breashears, Yagi, Sakai. «Anomalous winter-snow-amplified earthquake-induced disaster of the 2015 Langtang avalanche in Nepal.» *Nat. Hazards Earth Syst. Sci.* 17 (2017): 749-764.
- Goudie. *Encyclopedia of Geomorphology*. New Fetter Lane, London: Routledge Ltd, 2004.
- Gruber, Peckam. «Land-Surface Parameters and Object in Hydrology.» *Developments in Soil Science* 33 (2008): 171-194.
- Hammer, Fah, Ohrnberger. «Automatic detection of wet-snow avalanche seismic signals.» *Nat Hazards* 86 (2017): 601-618.
- Horn. «Hill Shading and the Reflectance Map.» *Proceedings of the IEEE* 69, n. 1 (1981): 14-47.
- INGV. «"DISS Working Group (2018). Database of Individual Seismogenic Sources (DISS), Version 3.2.1: A compilation of potential sources for earthquakes larger than M 5.5 in Italy and surrounding areas.» <http://diss.rm.ingv.it/diss/>, s.d.
- . *Itaca- Italian Accelerometric Archive*. s.d. <http://itaca.mi.ingv.it>.
- Kogelnig, Surinach, Vilajosana, Hubl, Sovilla, Hiller and Dufour. «On the complementariness of infrasound and seismic sensors for monitoring snow avalanches.» *Nat. Hazards Earth Syst. Sci* 11 (2011): 2355–2370.
- Lacroix, Grasso, Roule, Giraud, Goetz, Morin, Helmstetter. «Monitoring of snow avalanches using a seismic array: Location, speed estimation, and relationships to meteorological variables.» *Journal of geophysical research* 117 (2012): 1-15.
- Maggioni. «Avalanche release areas and their influence on uncertainty in avalanche hazard mapping.» *Ph.D. Thesis - University of Zurich*, 2004: 1-139.
- Marchetti, Ripepe, Ulivieri, Kogelnig. «Infrasound array criteria for automatic detection and front velocity estimation of snow avalanches: towards a real-time early-warning system.» *Nat. Hazards Earth Syst. Sci* 15 (2015): 2545–2555.
- Matsushita, Ikeda, Ito, Matsuzawa, Nakamura. «Avalanches induced by earthquake in North Tochigi prefecture on 25 February 2013.» *International Snow Science Workshop*. Grenoble – Chamonix Mont-Blanc, 2013. 1122-1129.
- McClung, Schaerer. *The Avalanche Handbook*. Seattle: The Mountaineers Books, 2006.

- Ministero delle Infrastrutture, Trasporti. «Aggiornamento delle "Norme tecniche per le costruzioni".» *Gazzetta Ufficiale della Repubblica Italiana*, n. 42 (febbraio 2018): 45-51.
- Moore, Grayson, Ladson. «Digital terrain Modelling: a review of hydrological, geomorphological and biological applications.» *Hydrological processes* 5 (1991): 3-30.
- NASA, NGA, German space agency, Italian space agency. «The Shuttle Radar Topography Mission (SRTM) Collection User Guide.» October 2015: 1-15.
- Pérez- Guillén, Sovilla , Suriñach , Tapia , Köhler. «Deducing avalanche size and flow regimes from seismic measurements.» *Cold Regions Science and Technology* 121 (2016): 25-41.
- Peréz-Guillen, supervised by Surinach Cornet. *Advanced seismic methods applied to the study of snow avalanche dynamics and avalanche formation (Ph.D. Thesis)*. Barcellona, 2016.
- Pérez-Guillén, Tapia, Furdada, Suriñach, McElwaine, Steinkogler, Hiller. «Evaluation of a snow avalanche possibly triggered by a local earthquake at Vallée de la Sionne, Switzerland.» *Cold Regions Science and Technology* 108 (2014): 149-162.
- Podolskiy, Nishimura, Abe, Chernous. «Earthquake-induced snow avalanches: I. Historical case studies.» *Journal of Glaciology* 56, n. 197 (2010): 431-446.
- Podolskiy, Nishimura, Abe, Chernous. «Earthquake-induced snow avalanches: II. Experimental study.» *Journal of Glaciology* 56, n. 197 (2010): 447-458.
- Quinn, Beven, Chevallier, Planchon. «The prediction of hillslope flow paths for distributed Hydrological Modelling using digital terrain models.» *Hydrological processes* 5 (1991): 59-79.
- Salm, Burkard, Gubler. «Berechnung von Fliesslawinen : eine Anleitung fuer Praktiker mit Beispielen.» *Mitteilungen des Eidgenössischen Institutes für Schnee und Lawinenforschung* 47 (1990).
- Sappington, Longshore, Thompson. «Quantifying landscape ruggedness for animal habitat analysis: A case study using bighorn sheep in the Mojave Desert.» *Journal of Wildlife Management*, 2007: 1419-1426.
- Schaerer, Salway. «Seismic and Impact-Pressure Monitoring of Flowing Avalanches.» *Journal of Glaciology* 26, n. 94 (1980): 179-187.
- Schweizer, Bartelt, van Herwijnen. *Snow and Ice-Related Hazards, Risks, and Disasters*. Amsterdam, Waltham, Kidlington: John F. Shroder (University of Nebraska at Omaha, US), Colin Whiteman (University of Brighton, UK), Wilfried Haeblerli (University of Zurich, Switzerland), 2015.
- Scott, Hayward, Kubichek, Hamann, Pierre, Comey, Mendenhall. «Single and multiple sensor identification of avalanche-generated infrasound.» *Cold Regions Science and Technology* 47 (2007): 159-170.
- SIN. *Servizio Meteomont*. A cura di Comando Truppe Alpine, Centro Meteorologico dell'Aeronautica Militare di Milano Linate, ActionImage, De Maria, Canon, Corpo Forestale dello Stato. s.d. <http://www.meteomont.gov.it>.
- Surinach, Sabot, Furdada, Vilaplana. «On the characterization of seismic signals generated by snow avalanches for monitoring purposes.» *Annals of Glaciology* 32 (2001): 268-274.
- Surinach, Sabot, Furdada, Vilaplana. «Study of Seismic Signals of Artificially Released Snow Avalanches for Monitoring Purposes.» *Phys. Chem. Earth (B)*, 25, n. 9 (2000): pp. 721-727.2.
- Surinach, Vilajosana, Khazaradze, Biescas, Furdada, Vilaplana. «Seismic detection and characterization of landslides and other mass movements.» *Natural Hazards and Earth System Sciences* 5 (2005): 791-798.
- Thommeret, Bailly, Puech. «Robust Extraction of Thalwegs Networks from DTMs for Topological Characterisation: A Case Study on Badlands.» *Proceedings of Geomorphometry 2009. Zurich, Switzerland*, 2009: 218-223.
- Thüring, Schoch, van Herwijnen, Schweizer. «Robust snow avalanche detection using supervised machine learning with infrasonic sensor arrays.» *Cold Regions Science and Technology* 111 (2015): 60-66.
- Ulivieri, Marchetti, Ripepe, Chiambretti, De Rosa, Segor. «Monitoring snow avalanches in Northwestern Italian Alps using an infrasound array.» *Cold Regions Science and Technology* 69 (2011): 177-183.
- van Herwijnen, Schweizer. «Monitoring avalanche activity using a seismic sensor.» *Cold Regions Science and Technology* 69 (2011): 165-176.
- van Herwijnen, Heck, Schweizer. «Forecasting snow avalanches using avalanche activity data obtained through seismic monitoring.» *Cold Regions Science and Technology* 132 (2016): 68-80.
- Vilajosana, Khazaradze , Suriñach , Lied , Kristensen. «Snow avalanche speed determination using seismic methods.» *Cold Regions Science and Technology* 49 (2007): 2-10.
- Vilajosana, Suriñach , Khazaradze , Gauer. «Snow avalanche energy estimation from seismic signal analysis.» *Cold Regions Science and Technology* 50 (2007): 72-85.
- Wald, Worden, Quitariano, Pankow. *ShakeMap Manual: Technical Manual, User's Guide, and Software Guide*. USGS science for a changing world, 2005.
- Wang, Liu. «An efficient method for identifying and filling surface depressions in digital elevation models for hydrologic analysis and modelling.» *International Journal of Geographical Information Science* 20, n. 2 (2006): 193-213.
- Weiss. «Topographic Position and Landforms analysis.» *The Nature Conservancy*, s.d.: 1.

Wilson, Gallant. *Terrain Analysis, Principles and Applications*. John Wiley & Sons, Inc, 2000.
Zevenbergen, Thorne. «Quantitative analysis of land surface topography.» *Earth Surface Processes and Landforms* 12 (1987): 47-56.

Appendix A

ArcGIS passages for determining PRA: Maggioni (2004)

For the application of the algorithm reported in Maggioni (2004), the ArcGIS software was used. So, slope (Slope – Spatial Analyst tool), aspect (Aspect – Spatial Analyst tool) and Planar curvature (Curvature – Spatial Analyst tool) rasters were recalculated for the study area using different algorithms than those described in paragraph X. The reason is that in Maggioni (2004) the author uses this software to obtain PRA. In this way the results were obtained with the same algorithms used by the author.

Step A

- Resampling of input DEM at 25 m (Resample – Data Management tool). DEM must have already been preprocessed (see Geomorphological analysis section)
- Download CLC 2012 level IV from Geoportale Nazionale (WFS Service) and extraction of all areas, except for “boschi di conifere”, “boschi di latifoglie” and “boschi misti di conifere e latifoglie”. (Selection by Attributes and Export selected features)
- Extract slope raster using exported no forested areas as mask. (Extract by Mask – Spatial Analyst tool)
- Export, from the latter result, areas with $30^\circ \leq \text{slope} \leq 60^\circ$. Raster calculator expression: `Con (“Slope_raster” <= 60°) & (“Slope_raster” >= 30°),1)`
- Convert the latter raster in polygon for subsequent processing. (Raster to Polygon – Conversion tool)

Step B

- Calculation of ridges with algorithm given by literature:
- Calculate the negative DEM (Raster calculator expression: `“DTM_raster” * (-1)`)
- Calculate flow direction with negative DEM as input data. (Flow Direction – Spatial Analyst tool). Check “Force all edge cells to flow outward”.
- Calculate flow accumulation using flow direction raster as input. (Flow Accumulation – Spatial Analyst tool). Set the output data type as INTEGER.
- Create the flow network. (Raster Calculator expression: `Con (“FlowAccumulation_raster”, 1, 0, “Value >= 500”)`). Ridgelines are obtained.
- Convert the latter raster in polygon (Raster to Polygon – Conversion tool)

[It is possible to convert the latter raster into a vector through the Stream Order (Stream Order – Spatial Analyst tool). Use as “input stream raster” the ridgelines raster and, as “input flow direction raster” the flow direction raster calculated above. Use as Stream ordering method STRAHLER. In the end, use the Stream to feature tool (Spatial analyst tool) using as “input stream raster” and “input flow direction raster” the rasters previously calculated.]

- Use the command Erase (Analysis tool) for subtracting polygonal ridges from polygon representing no forested areas and slope areas between 30° and 60° previously computed.

- Use the latter polygon for extract (Extract by Mask – Spatial Analyst tool) the Planar curvature with a resolution of 50 m. Therefore, before the extraction, resample the Planar curvature raster at 50 m (Resample – Data Management tool)
- Split the curvature raster into the following classes using raster calculator. Raster calculator expressions:
 - A. $\text{Con}(\text{"Plan_Curvature"} \leq (-0.2), 1)$: PRA, self-contained (concave)
 - B. $\text{Con}(\text{"Plan_Curvature"} > (-0.2), 1)$: PRA, flat e convex.
- Group PRA, flat e convex using an adjacency criterion (Region Group – Spatial Analysis tool). Use FOUR cells as “number of neighbors to use” and the grouping method WITHIN. The adjacency with 4 cells ensures that areas that are divided by the intermediate presence of a ridge are not considered adjacent. Performing this tool, in the raster attribute table it is present the field COUNT which indicates the number of cells within each group found.
- It is, therefore, possible to calculate the area (m^2) of each group by adding the "AREA" field and using the Field calculator. Field calculator expression: $[\text{COUNT}] * 50 * 50$.
- Use the group dimension (“AREA”) for determining PRA (flat e convex), self-contained and not. For this purpose, a threshold of 5000 m^2 was used. Areas below 5000 m^2 are the not self-contained PRA, while those above 5000 are the PRA, self-contained, flat or convex. It is possible doing this using the Raster Calculator. Raster calculator expressions:
 - C. $\text{Con}(\text{Lookup}(\text{"Raster_Group_Name"}, \text{"AREA"}) \leq 5000), 1)$, obtaining not self-contained PRA
 - D. $\text{Con}(\text{Lookup}(\text{"Raster_Group_Name"}, \text{"AREA"}) \geq 5000), 1)$, obtaining PRA, self-contained-flat or convex.)
- The raster obtained by the last expression D., together with the raster of the PRA, self-contained (concave), obtained with the expression A., are subjected to a filtering process based on Altitude Range. Only cells with an altitude value higher than “maximum value in every PRA minus 200 m” are considered to belong to that PRA. For obtaining the result, consisting in Self-contained PRA, the following procedure can be applied. The procedure will be applied first to the PRA, self-contained (concave) and then to the PRA, self-contained, flat or convex.
- Group PRA raster using an adjacency criterion (Region Group – Spatial Analysis tool). Use FOUR cells as number of neighbors to use and the grouping method WITHIN. The adjacency with 4 cells ensures that areas that are divided by the intermediate presence of a ridge are not considered adjacent.
- Convert Raster PRA in Polygon through Raster to Polygon (Conversion tool)
- Execute, for obtained polygon, the Dissolve tool (Data Management tool). Use “gridcode” as dissolve field for obtaining a layer with indexed groupings in the attribute table.
- Resampling of input DEM at 50 m (Resample – Data Management tool). DEM must have already been preprocessed (see Geomorphological analysis section)
- Use the Dissolve output as Mask for an extracting operation (Extract by Mask – Spatial Analyst tool) executed on raster DEM with a resolution of 50 m.

- The Extract by Mask output will be a floating type raster. With this raster type, it is not possible to open the raster attribute table. Therefore, convert it in an integer raster type (Int – Spatial Analyst tool). Now, the attribute table can be opened. It is present a “gridcode” field in which altitude values are reported.
- Use the command Raster to Point (Conversion tool) to convert each DEM raster cell in a point, maintaining altitude values.
- Use the polygon obtained with the previously Dissolve operation and join it spatially with the point layer just created. In Spatial join settings set the checkbox Maximum. In this way for each polygon will be given the maximum of numeric attributes of the points that fall inside it. This value is shown in the "Max_grid_c" field. By adding a field “Threshold” in the attribute table and using the field calculator (Field calculator expression: ["Max_grid_c"] –200) it is possible to find the threshold above which cells are considered to belong to the PRA.
- Execute a spatial joining between the DEM point layer and the output of the previous join. In this way all area attributes, in which a point falls in, are associated with it. Therefore, in the output point layer attribute table the “grid code” (altitude values) and the “Threshold” field are present.
- Use Selection by attributes for the point layer created by using the spatial join and compile the following query: “grid code” > “Threshold”. In this way, all points with an altitude value higher than the threshold are identified. Export selected features.
- Use Point to Raster (Conversion Tool) for obtaining PRA, self-contained (concave) and PRA, self-contained (flat or convex) rasters.
- Merge raster through Raster calculator for obtaining Self Contained PRA raster. Raster Calculator Expression:

$$\text{Con}((\text{Con}(\text{IsNull}(\text{"PRA_1_name"}),0,\text{"PRA_1_name"})+\text{Con}(\text{IsNull}(\text{"PRA_2_name"}),0,\text{"PRA_2_name"}),1)$$

Step C

- Unit Self Contained PRA raster with Not Self Contained PRA raster. Raster Calculator Expression:

$$\text{Con}((\text{Con}(\text{IsNull}(\text{"Self_Cont_PRA_name"}),0,\text{"Self_Cont_PRA_name"})+\text{Con}(\text{IsNull}(\text{"Not_Self_Cont_PRA_name"}),0,\text{"Not_Self_Cont_PRA_name"}),1)$$
- Use this raster for extracting DEM and Aspect values (both with a resolution of 50 m). (Extract by Mask – Spatial Analyst tool). So, resample aspect raster at 50 m (Resample – Data Management tool).
- Use Euclidean Distance (Spatial Analyst tool), using as input raster the merge raster obtained with the first passage of Step C, setting as maximum distance the cellsize value (50). Beyond this value, the output raster will have cells with a value of NoData. In this way raster will expand, along its entire perimeter, of one cellsize. Expanded cells have all value 50.
- Use Raster calculator for extracting only the expanded cells. Raster Calculator expression:

$$\text{Con}(\text{"Expanded_raster_name"} == 50), 1)$$
- Extract with raster of expanded cells the initial DEM and the Aspect rasters, both with a resolution of 50 m. (Extract by Mask – Spatial Analyst tool)

- Unit DEM, extracted with PRA, with DEM extracted with expanded cells using Raster calculator. Repeat the same procedure for extracted Aspect rasters. Raster calculator expression:
- E. `Con(IsNull("dtm_cells_exp_name"), 0, "dtm_cells_exp_name") + Con(IsNull("DTM_SelfC_PRA_name"), 0 , "DTM_SelfC_PRA_name")`
- F. `Con(IsNull("Aspect_cells_exp_name"), 0, "Aspect_cells_exp_name") + Con(IsNull("Aspect_SelfC_PRA_name"), 0 , "Aspect_SelfC_PRA_name")`
- Use Focal Statistics (Spatial Analyst tool), using as input raster the merging obtained at the previously passage and set as statistic type RANGE. In this way the tool calculates the range (difference between largest and smallest value) of the cells in the neighborhood. For the calculation, use a rectangular kernel of 3x3 (cell unit). Check "Ignore NoData in calculations". Use this tool for both outputs obtained from E. and F. expressions.
- Extract with the raster of expanded cells the Focal Statistics output raster. Use this tool for both outputs obtained from the previous tool. (Extract by Mask – Spatial Analyst tool)
- Use Raster calculator for evaluating adjacent areas in which the altitude difference is less than 100 m and the aspect difference is higher than 45°. Raster calculator expression:
`Con((("Clipped_Focal_Statistics_altitude_name"<100)&("Clipped_Focal_Statistics_aspect_name" > 45)), 1)`
- Expand from self contained PRA into adjacent areas that respect this condition. Raster calculator expression:
`Con(IsNull("SelfC_PRA_name"), 0, " SelfC_PRA_name ") + Con(IsNull("Adjacent_100_45_name"), 0 , " Adjacent_100_45_name ")`
- Use Raster calculator for evaluating adjacent areas in which the altitude difference is less than 100 m and the aspect difference is less than 45°. Raster calculator expression:
`Con((("Clipped_Focal_Statistics_altitude_name"<100)&("Clipped_Focal_Statistics_aspect_name" < 45)), 1)`
- Join the whole adjacent areas with self-contained PRA. Raster calculator expression:
`Con(IsNull(" Adjacent_100_45_name "), 0, "Adjacent_100_45_name ") + Con(IsNull(" SelfC_PRA_name "), 0 , " SelfC_PRA_name ")`
- Repeat all the Step C procedure using the new PRA obtained.
- Remove again areas with extension less than 5000 m² as described in Step B.
- Filter the PRA using a 750 m altimeter filter (value obtained from the characterization of the real release areas) after the extraction of DEM values with PRA raster. Raster calculator expression:
`Con((("Final_PRA_DEM">750, 1)`
- Remove PRA cells that intersect note track zones. Raster calculator expression:
`Con(IsNull("Track_zones_raster"), "PRA_raster")`
- Extract only PRA in interested mountain sectors.

Acknowledgments - Ringraziamenti

Con questo lavoro termina la mia carriera da studente al Politecnico di Torino. Al raggiungimento di questo traguardo la sensazione che provo è ben descritta da alcune parole di Luciano Ligabue in una canzone che, per restare in tema, si intitola "La neve se ne frega": "...Sembra tutto pulito, sembra tutto più chiaro, tutto quanto più morbido senza più spigoli da arrotondare...". Durante questo percorso gli spigoli non sono mancati, ma per fortuna ho sempre avuto al mio fianco qualcuno che, come la neve, è riuscito ad arrotondarli.

Ringrazio di cuore i miei genitori. Mamma e papà mi sono stati vicini in ogni momento e sempre mi hanno aiutato e sostenuto durante questo percorso. Hanno vissuto insieme a me i momenti ricchi di soddisfazioni, ma soprattutto quelli più difficili. Tutte le pagine di questa tesi non basterebbero per ringraziarli adeguatamente per quello che ogni giorno fanno per me. A loro in particolare dedico questo lavoro e questo traguardo, a significare che tutti i sacrifici che hanno fatto per me hanno portato i loro frutti. Ringrazio Toschina per essere sempre stata al mio fianco e per aver sempre creduto in me, nelle mie capacità e nella mia persona. La ringrazio perché nei periodi in cui sono stato giù di morale mi è sempre stata vicina e con il suo amore, la sua semplicità e la sua dolcezza è sempre riuscita a farmi tornare il sorriso e la spensieratezza. Ringrazio le mie nonne. Nonna Titina per tutte le preghiere che ha detto per me, soprattutto durante il periodo degli esami, e per quelle che dice quotidianamente. Nonna Luisa perché, nonostante la lontananza, chiede sempre di me ogni volta che sente papà al telefono e, riguardo al percorso universitario, mi ha sempre ricordato che tutto arriva ad una fine. Ringrazio i miei nonni Pasquale e Vincenzo per tutto il loro affetto e perché so che da lassù mi sono sempre vicini. Ringrazio tutti i miei familiari e in particolare quelli che hanno vissuto più da vicino il mio percorso universitario. Ringrazio zia Rosanna, zio Mimmo e Matteo perché non è mai mancato il loro incoraggiamento. Ringrazio Paola e Valter per il loro affetto, il loro sostegno e per essere sempre stati disponibili ad un aiuto. Ringrazio gli amici che ci sono sempre stati: Mirko, Alessandro, Alessio, Domenico, Gianluca. Chiedo scusa loro se, spesso per il grande impegno che lo studio ha richiesto, ho rinunciato a trascorrere del tempo insieme a loro, ma li ringrazio proprio perché, nonostante tutto, credono nella mia amicizia. Ringrazio tutti i colleghi che hanno vissuto con me l'avventura del Politecnico. In particolare, ringrazio chi è diventato un po' più di un collega: Davide, Andrea, Valentina, Vincenzo, Antonio, Angela, Simone; Cenzino, e i Foppi. Un ringraziamento sentito va all' Ing. Frigo e al Dott. Geol. Chiambretti che mi hanno seguito con dedizione e professionalità durante la redazione di questo elaborato. Li ringrazio per i consigli, la disponibilità e la pazienza. Un ultimo pensiero va al Politecnico di Torino. Non è stato facile il passaggio dalla scuola superiore all'università, ma con il trascorrere degli anni ho imparato ad apprezzare un ambiente che porta spesso ad incontrare i propri limiti, stimolando una crescita della persona sia dal punto di vista professionale che umano, affinché questi limiti possano essere superati.

Ricorderò con nostalgia i miei anni da studente trascorsi al Politecnico di Torino.

Alessio Gentile